Linking local dynamics to network organization in the human brain

GOLIA SHAFIEI
Integrated Program in Neuroscience
McGill University, Montréal, QC, Canada
August 2022

A thesis submitted to McGill University in partial fulfillment
of the requirements of the degree of
Doctor of Philosophy

Abstract

The human brain is a complex network of anatomically connected and functionally interacting neuronal populations. Neural activity and functional interactions between brain areas are naturally variable from moment to moment, resulting in dynamic configurations of brain activity. Connectome architecture shapes the functional associations between brain areas, constraining both local and global brain dynamics. Contemporary theories of brain structure and function also emphasize systematic variations in cortical micro-architecture that are concomitant with macroscale variation in anatomical connectivity and functional interactions among neuronal populations. How the confluence of microscale gradients and macroscale network architecture manifests as dynamic neural activity remains unknown. This thesis explores the dynamical signature of haemodynamic and electromagnetic regional spontaneous neural activity and its association with cortical micro-architecture and large-scale network organization. Chapters 1 and 2 provide a brief introduction on spontaneous neural activity in the human brain and outline the main research questions presented throughout this thesis. Chapter 3 examines the interplay of local dynamics and global network interactions, using a single time-series property. Specifically, this chapter investigates how pharmacological manipulation of dopamine affects regional neural dynamics and how the observed changes in dynamics relate to global functional connectivity. The results demonstrate that disruption in normal levels of dopamine leads to increased haemodynamic signal variability and decreased functional connectivity, consistent with the stabilizing effects of dopamine on neural signaling. Chapter 4 takes an exploratory, data-driven approach to characterize the topographic organization of intrinsic dynamics across the cortex. Specifically, I derive a comprehensive, unbiased list of time-series features to quantify the dynamical fingerprint of spontaneous haemodynamic brain activity. The findings demonstrate a link between microscale gradients and macroscale connectivity, intrinsic dynamics, and cognition. Chapter 5 expands on the previous chapter and studies regional dynamics using neurophysiological activity with high temporal resolution instead

of slower haemodynamic fluctuations. This chapter assesses the relationship between fast-oscillating neural activity and network embedding and determines the micro-architectural basis of neurophysiological activity. Chapter 6 seeks to jointly consider haemodynamic and neurophysiological activity by investigating the cross-modal correspondence between functional network architectures recovered from these two types of neural activity. The presented analyses indicate that the cross-modal coupling is regionally heterogeneous, reflecting cortical functional hierarchy and laminar differentiation. Finally, Chapter 7 provides an overview of the primary findings of this thesis and discusses their significance and implications for future research on human neural dynamics.

Résumé

Le cerveau humain est un réseau complexe de populations neuronales anatomiquement connectées et interagissant fonctionnellement. L'activité neuronale et les interactions fonctionnelles entre les aires cérébrales varient naturellement à travers le temps, entraînant des reconfigurations dynamiques de l'activité cérébrale. L'architecture du connectome façonne les associations fonctionnelles entre les aires cérébrales, contraignant les dynamique cérébrales locales et globales. Les théories contemporaines de la structure et de la fonction du cerveau mettent également l'accent sur des variations systématiques de la micro-architecture corticale concomitantes à des variations à grande échelle de la connectivité anatomique et des interactions fonctionnelles entre les populations neuronales. La manière dont la confluence des gradients à petite échelle et de l'architecture du réseau cérébral à grande échelle se manifeste sous forme d'activité neuronale dynamique demeure inconnue. Cette thèse explore la signature dynamique de l'activité neuronale hémodynamique et électromagnétique spontanée évaluée au niveau régional, ainsi que son association avec la micro-architecture corticale et l'organisation à grande échelle du réseau cérébral. Les chapitres 1 et 2 fournissent une brève introduction sur l'activité neuronale spontanée dans le cerveau humain et décrivent les principales questions de recherche présentées tout au long de cette thèse. Le chapitre 3 examine la relation entre les dynamiques locales et les interactions globales au sein du réseau cérébral en utilisant une seule propriété des séries temporelles. Spécifiquement, ce chapitre étudie comment la manipulation pharmacologique de la dopamine affecte les dynamiques neuronales régionales et comment les changements de dynamiques observés sont liés à la connectivité fonctionnelle globale. Les résultats démontrent que la perturbation des niveaux normaux de dopamine entraîne une augmentation de la variabilité du signal hémodynamique et une diminution de la connectivité fonctionnelle, conformément aux effets stabilisateurs de la dopamine sur la signalisation neuronale. Le chapitre 4 adopte une approche exploratoire

axée sur les données pour caractériser l'organisation topographique des dynamiques intrinsèques à travers le cortex. Spécifiquement, je développe une liste exhaustive et objective de caractéristiques de séries temporelles pour quantifier l'empreinte dynamique de l'activité cérébrale hémodynamique spontanée. Les résultats présentent un lien entre les gradients à petite échelle et la connectivité à grande échelle, ainsi qu'entre les dynamiques intrinsèques et la cognition. Le chapitre 5 développe les idées présentées au chapitre précédent et étudie les dynamiques régionales en utilisant l'activité neurophysiologique, qui a une résolution temporelle plus élevée que les fluctuations hémodynamiques. Ce chapitre évalue le lien entre les oscillations rapides de l'activité neuronale et l'intégration du réseau cérébral, et identifie la base micro-architecturale de l'activité neurophysiologique. Le chapitre 6 vise à considérer conjointement l'activité hémodynamique et neurophysiologique en étudiant la correspondance intermodale entre les architectures de réseaux fonctionnels reconstruits à partir de ces deux types d'activité neuronale. Les analyses présentées indiquent que le couplage intermodal est régionalement hétérogène, reflétant la hiérarchie fonctionnelle et la différenciation laminaire du cortex. Finalement, le chapitre 7 donne un aperçu des principaux résultats de cette thèse et discute de leur importance et de leurs incidences sur les recherches futures portant sur les dynamiques neuronales humaines.

Contents

List of Figures

List of Tables

Acknowledgements

First and foremost, I would like to thank my supervisor, Dr. Bratislav Misic, an exceptional scientist and mentor without whose guidance and support none of this work would have been possible. Bratislav: I cannot thank you enough for everything you have done for me. I am extremely grateful for all the lessons you have taught me over the past years. Thank you for being such a wonderful person and for showing me how to be a kind human while maintaining a high work standard. I could not have asked for a better mentor. It has been an absolute privilege and honor to work with you, I will always be grateful for that. My heartfelt thanks to my past and present colleagues in the Network Neuroscience Lab: Ross, Estefany, Bertha, Zhen-Qi, Vincent, Justine, and Filip. I truly appreciate your friendship and support throughout the years. I have learned so much from you. Thank you for being such amazing people. It has been a great pleasure to work alongside you all. I would like to express my deepest gratitude to my committee members, Drs. Sylvain Baillet and Alain Dagher for their continued mentorship, guidance and support over the past years. I was lucky to have such brilliant scientists as my role models. I would also like to thank all my collaborators and co-authors for their invaluable help with my research. To my brother Shahin, my parents, and my grandparents: thank you for your endless love and for having faith in me. I cannot express how grateful I am for your unconditional support from afar. And finally, my sincere love and gratitude to Pooya. I cannot find words to describe how thankful I am for your constant support. Thank you for always being there for me and for believing in me even when I doubted myself.

Contribution of authors

As the lead author on the manuscripts presented in chapters 3 through 6, I was responsible for overseeing all aspects of the research, including: conceptualization, experimental design, data processing, statistical analysis, visualization, interpretation of results, and writing of the manuscripts. Contributions of co-authors for these chapters are outlined below:

Chapter 3

- Yashar Zeighami: data collection, data processing, and editing of the manuscript
- Crystal A. Clark: data collection and editing of the manuscript
- Jennifer T. Coull: data collection and editing of the manuscript
- Atsuko Nagano-Saito: data collection and editing of the manuscript
- Marco Leyton: experimental design, data collection, and editing of the manuscript
- Alain Dagher: conceptualization, experimental design, data collection, and writing of the manuscript
- Bratislav Misic: conceptualization, experimental design, interpretation of results, and writing of the manuscript

Chapter 4

- Ross D. Markello: data processing and editing of the manuscript
- Reinder Vos de Wael: data processing and editing of the manuscript
- Boris C. Bernhardt: editing of the manuscript
- Ben D. Fulcher: interpretation of results and editing of the manuscript
- Bratislav Misic: conceptualization, experimental design, interpretation of results, and writing of the manuscript

Chapter 5

- Sylvain Baillet: editing of the manuscript
- Ben D. Fulcher: editing of the manuscript
- Bratislav Misic: conceptualization, experimental design, interpretation of results, and writing of the manuscript

Chapter 6

- Sylvain Baillet: editing of the manuscript
- Bratislav Misic: conceptualization, experimental design, interpretation of results, and writing of the manuscript

Chapter 1

Introduction

1.1 General context

The human brain is a complex network of interacting neuronal populations. Connectome architecture and its spatial embedding shape global network interactions and local dynamics. Inter-regional anatomical projections promote signaling among remote neuronal populations, resulting in patterned neuronal co-activation and coherent dynamics. The dynamic neural activity is reflected in regional neurophysiological and haemodynamic time-series and can be measured at different timescales, from milliseconds to several seconds, using magneto- and electro-encephalography (MEG/EEG) and functional magnetic resonance imaging (fMRI), respectively. Moreover, the functional organization of the human cortex—as well as anatomical markers such as intracortical myelin, cortical thickness, and gene expression—display a hierarchical organization, principally along an axis that spans unimodal sensory areas and higher order transmodal regions (Huntenburg et al., 2018). However, the dynamic consequences of these microscale gradients and macroscale network organization remains unclear.

Multiple lines of evidence suggest that local computations in the brain reflect systematic variation in microscale properties and macroscale network embedding, manifesting as diverse temporal properties of regional activity. The objective of this thesis is to comprehensively assess intrinsic temporal dynamics across the human brain and to characterize the link between regional brain dynamics and network embedding using temporal properties of localized brain activity measured at different timescales. Most of the conventional computational analyses use a single measure or a few specific, manually selected measures of intrinsic dynamics to characterize regional brain activity from haemodynamic

and electrophysiological signals. However, the time-series analysis literature is vast and interdisciplinary, providing additional metrics of temporal structure of regional brain activity. In this thesis, I use commonly used measures of intrinsic dynamics as well as near-exhaustive, unbiased lists of time-series features to map the dynamical signature of regional haemodynamic and electromagnetic neural activity to microscale gradients and macroscale network architecture. Specifically, I use non-invasive neuroimaging techniques such as fMRI with high spatial precision and MEG with high temporal precision to study human brain function at rest. These modalities are two of the commonly used techniques to quantify neural activity at multiple scales and to examine the large-scale brain network organization. In the work presented here, I leverage the complementary strengths of fMRI and MEG in imaging spatiotemporal brain dynamics and investigate the dynamical properties of slow- and fast-fluctuating neural activity, respectively, and their association with cortical micro-architecture and multi-modal brain networks.

1.2 Objectives

Chapter 3

Chapter 3 examines the interplay of local dynamics and global network interactions, using a single, commonly used time-series property. Specifically, this chapter investigates how disruption in normal levels of dopamine, caused by pharmacological manipulation of dopamine precursor, influences regional neural dynamics and how the observed changes in dynamics relate to global functional interactions. Moreover, this study examines the stabilizing effects of dopamine on neural signaling in the system level.

Chapter 4

Chapter 4 applies an exploratory, data-driven approach to characterize the topographic organization of intrinsic dynamics across the cortex. Rather than manually selecting a single or a few measures of intrinsic dynamics, I derive a comprehensive, unbiased list of time-series features to quantify the dynamical fingerprint of spontaneous haemodynamic brain activity. I then examine the link between microscale gradients and macroscale connectivity, intrinsic dynamics, and cognition.

Chapter 5

Chapter 5 extends the previous chapter and examines regional neural dynamics using spontaneous neurophysiological activity with high temporal resolution instead of slower haemodynamic fluctuations. I use both conventional measures of neurophysiological intrinsic dynamics and data-driven, comprehensive list of time-series properties to assess the relationship between fast-oscillating neural activity and network embedding and identify the micro-architectural basis of neurophysiological activity.

Chapter 6

Chapter 6 presents a joint analysis of slow haemodynamic and fast neurophysiological fluctuations and investigates the cross-modal correspondence between functional network architectures recovered from these two types of neural activity. I map electromagnetic networks to haemodynamic networks and examine the relationship between the regionally heterogeneous cross-modal coupling and macroscale network embedding and cortical cytoarchitecture.

1.3 Contributions to original knowledge

Collectively, the research presented in this thesis provides important insight into fundamental aspects of brain function and integration and elucidates how neural communication patterns are organized across multiple scales, from regional dynamics to global functional interactions. Distinct scientific contributions of each research project are highlighted below.

Chapter 3

- Dopamine signaling modulates the stability and integration of intrinsic brain networks.
- Dopamine-related increases in haemodynamic signal variability appear to be concomitant with decreased functional connectivity and localized to specific intrinsic networks.
- Findings support a link between local node dynamics and network architecture.

Chapter 4

- Dynamic fingerprint of regional brain activity is related to the macroscale network embedding.
- Regional dynamics are hierarchically organized across cortex, recapitulating the unimodal-transmodal hierarchy.
- Spatial gradients of intrinsic dynamics reflect functional and microstructural hierarchical organization and support distinct functional activation patterns.

Chapter 5

- Topographic organization of dominant neurophysiological intrinsic dynamics reflects variations in characteristics of power spectral density.
- Long-term memory in neurophysiological activity follows large-scale gradients of micro-architecture.
- Dynamic signature of neurophysiological activity reflects the anatomical hierarchy and cortical metabolic demands.
- Findings emphasize the importance of conventional approaches in studying the characteristics of neurophysiological dynamics and introduce novel ones.

Chapter 6

- Superposition of electromagnetic functional connectivity in multiple rhythms predicts haemodynamic functional connectivity.
- Cross-modal correspondence is regionally heterogeneous, reflecting the macroscale unimodal-transmodal cortical hierarchy and cytoarchitectural variation.
- Hierarchical decoupling of haemodynamic and electromagnetic connectivity suggests that the two modalities may capture partially non-overlapping functional patterns.

Chapter 2

Review of the literature

2.1 Macroscale brain networks

The brain is a complex network of anatomically connected and perpetually interacting neuronal populations that collectively support perception, cognition and action (Sporns, 2011; Sporns and Betzel, 2016; Sporns et al., 2005). This complex network of neuronal populations and synaptic projections are organized into a hierarchical organization, forming increasingly polyfunctional neural circuits (Bazinet et al., 2021; Hilgetag and Goulas, 2020; Jones and Powell, 1970; Mesulam, 1998). The macroscale hierarchy of processing reflects the topographic distributions of microscale molecular and cellular properties and spans the unimodal—transmodal cortices (Huntenburg et al., 2018). Neuronal populations receive the incoming signals and integrate those signals based on the neuron's specific cellular and molecular characteristics, such as its resting membrane potential and its threshold to generate action potentials (Kandel et al., 2000). The transformed neuronal signal is then transmitted to other neuronal populations through synaptic projections, either through electronic synapses via gap junction channels or chemical synapses via neurotransmitter release and postsynaptic neurotransmitter receptors (Kandel et al., 2000). The information flow and neural signaling on microscale circuits manifests as patterned, macroscale neurophysiological activity and can be measured using neuroimaging techniques, including electromagnetic and haemodynamic imaging modalities (Baillet, 2017; Fries, 2005; Sadaghiani et al., 2022). Variations in microscale cellular and molecular properties are also reflected in cortical gradients of gene expression (Burt et al., 2018; Fulcher et al., 2019), neurotransmitter receptors and transporters (Hansen et al., 2021), intracortical myelin (Huntenburg et al., 2017), cortical thickness (Wagstyl et al., 2015) and laminar

and cytoarchitectonic profiles (Paquola et al., 2019, 2021; Wagstyl et al., 2020). Recent advances in noninvasive neuroimaging techniques (Raichle, 2009), have coincided with the large-scale data collection and data sharing initiatives (DuPre et al., 2020; Frauscher et al., 2018; Gordon et al., 2017; Griffa et al., 2019; Hansen et al., 2021; Hawrylycz et al., 2012; Miller et al., 2016; Niso et al., 2016; Sudlow et al., 2015; Taylor et al., 2017; Van Essen et al., 2013). These efforts have resulted in large samples of increasingly detailed maps of brain structure and function, making it possible to comprehensively study microscale circuit properties and macroscale network architecture (Eickhoff et al., 2018; Glasser et al., 2016; Markello et al., 2022; Paquola et al., 2021; Schaefer et al., 2018).

2.1.1 Graph reconstruction of the brain

One of the most common approaches in modeling and studying the brain as a complex system is to reconstruct a graph model of the brain (Bassett et al., 2018; Khambhati et al., 2018; Sporns et al., 2005). Data sharing efforts and growing number of advanced analytical tools and image processing techniques allow for building high-quality models of the brain (Griffa et al., 2019; Tournier et al., 2019; Van Essen et al., 2013). In the graph representation of the brain, network nodes correspond to grey matter that is subdivided into parcels or regions and network edges correspond to white matter, anatomical pathways connecting brain regions to each other (Sporns, 2011). The anatomical organization of the brain, namely the "structural connectivity" or the "connectome" can be reconstructed using non-invasive neuroimaging techniques, such as diffusion weighted imaging and streamline tractography (Hagmann et al., 2007), and has unique properties that distinguishes it from random networks. For example, brain networks are small-world networks with short path lengths, such that distant regions are connected to each other with only a few connections, and high clustering coefficients, such that neighbours of a region tend to be neighbours of each other (Bassett and Bullmore, 2006; Watts and Strogatz, 1998). The small-world topology of brain networks facilitates information processing by minimizing wiring costs and maximizing local and global efficiency (Bassett and Bullmore, 2006; Betzel and Bassett, 2018; Watts and Strogatz, 1998). Moreover, the structural connectivity network has a power-law degree distribution with a long tail, suggesting that some regions make disproportionately large number of connections with the rest of the brain (Hagmann et al., 2007). These highly connected and central regions tend to form a densely inter-connected hub complex, commonly referred to as a "rich club" or backbone of the connectome, and have a key role in exchanging signal and integrating information in brain networks (Hagmann et al., 2008; Van Den Heuvel et al., 2012).

The distinct connectome architecture supports, and simultaneously constrains, local and global communication processes and dynamics. Regional neural dynamics and long-range functional associations between distant regions are shaped by inter-regional connectivity that promotes signaling through anatomical pathways (Avena-Koenigsberger et al., 2018; Suárez et al., 2020). Neural activity is reflected in haemodynamic or blood oxygen level-dependent (BOLD) signals as well as electromagnetic signals and can be measured by different modalities such functional as magnetic resonance imaging (MRI) (Poldrack and Farah, 2015; Raichle, 2009) and electro- and magneto-encephalography (EEG/MEG) (Baillet, 2017; Hämäläinen et al., 1993; Niedermeyer and Silva, 2005), respectively. Given the inter-regional coupling imposed by the underlying anatomical connections, activity of distant neural populations may fluctuate synchronously (Baillet, 2017; Baillet et al., 2001; Biswal et al., 1995). This generates spatiotemporal patterns of correlated dynamics that can be quantified as statistical dependencies between time courses of pairs of brain regions, resulting in functional connectivity networks. Spontaneous regional neural activity at different timescales is inferred from resting-state or intrinsic functional patterns that are highly organized (Baker et al., 2014; Bellec et al., 2006; Brookes et al., 2011a,b; De Pasquale et al., 2010; Power et al., 2011; Yeo et al., 2011), reproducible (Brookes et al., 2012; Colclough et al., 2016; Gordon et al., 2017; Noble et al., 2019) and comparable to task-driven co-activation patterns (Brookes et al., 2012; Cole et al., 2014; Smith et al., 2009). Numerous studies have investigated the relationship between structural and functional networks using intrinsic brain activity (Damoiseaux and Greicius, 2009; Suárez et al., 2020).

2.1.2 Structure-function relationship in brain networks

The network representation of the brain has been previously employed to explore the relationship between large-scale structural and functional networks (Damoiseaux and Greicius, 2009; Honey et al., 2010; Suárez et al., 2020). Previous studies have reported moderate structure-function coupling using whole-brain associative analysis and predictive modeling, where the inter-regional connection strengths were compared with each other (Cabral et al., 2014; Deco and Jirsa, 2012; Deco et al., 2014b; Honey et al., 2007; Honey et al., 2009; Mišić et al., 2016). Structural and functional networks have also been investigated at the regional level, identifying a regionally heterogeneous correspondence between the two along a cortical hierarchy that spans unimodal, sensory areas and transmodal, higher order regions (Baum et al., 2020; Preti and Van De Ville, 2019; Vázquez-Rodríguez et al., 2019; Zamani Esfahlani et al., 2022). Moreover, both structural and functional networks have modular organizations, such that partially over-lapping modules or communities

can be identified in both networks (Mišić et al., 2015; Power et al., 2011; Suárez et al., 2020; Van Den Heuvel et al., 2009b; Yeo et al., 2011). Specifically, lower order intrinsic functional networks, namely visual and somatomotor networks, are consistently recovered from structural and functional connectivity networks as they consist of regions that are densely inter-connected with direct anatomical pathways (Betzel et al., 2018, 2017; Mišić et al., 2015), whereas intrinsic networks consisting of distant regions with no direct anatomical connections, such as default mode network, can only be partially recovered by structural networks (Betzel et al., 2017; Honey et al., 2010; Mišic et al., 2015). Thus, the correspondence between structural and functional networks may be constrained by network geometry and spatial embedding of brain regions, given that proximal regions tend to be anatomically connected and as a result have stronger functional associations compared to distant areas (Bettinardi et al., 2017; Liu et al., 2021; Roberts et al., 2016). The large-scale network organization, particularly functional networks, has also been used to study individual variations in behaviour and cognition both in resting-state and task-based experimental settings (Bassett et al., 2011; Mirchi et al., 2018; Mišić and Sporns, 2016; Rosenberg et al., 2016; Smith et al., 2015; Van Den Heuvel et al., 2009a).

Altogether, as mentioned above, graph reconstruction of the brain is one of the most common approaches in studying the brain as a complex system (Bullmore and Sporns, 2009). However, in the graph model of the brain, brain areas are usually treated as identical nodes that are connected with weighted edges based on the strength of structural or functional connections. While this type of graph notation of the brain has proven to be useful in various research areas in neuroscience, it lacks information regarding local properties of brain areas that are essential in understanding the function and integrity of the brain (Khambhati et al., 2018; Suárez et al., 2020).

2.2 Regional heterogeneity of cortical properties

More recently there has been a growing interest in incorporating a wide range of local properties in studies of large-scale brain networks (Khambhati et al., 2018; Suárez et al., 2020). Adding local attributes to the network nodes and constructing "annotated networks" help to better understand the structure-function relationships by linking microscale and macroscale brain organization (Khambhati et al., 2018; Suárez et al., 2020). Large-scale network architecture both shapes, and is shaped by, the regional microscale properties such that regions with similar local properties are more likely to have inter-regional anatomical connections and functional interactions (Beul et al., 2017; Goulas et al., 2019; Hilgetag et al.,

2019; Wei et al., 2018). Examples of these local attributes are cellular (Anderson et al., 2020; Hansen et al., 2021; Müller et al., 2020; Scholtens et al., 2014), molecular (Anderson et al., 2018; Fulcher and Fornito, 2016; Richiardi et al., 2015; Zheng et al., 2019) and temporal (Fallon et al., 2020; Gao et al., 2020; Sethi et al., 2017; Shafiei et al., 2020) properties.

Previous studies report a hierarchical organization in the neural systems that reflects the systematic variations in regional cytoarchitectonic properties, such as neuron density, spine count, branching and neurotransmitter receptor profiles (Hansen et al., 2021; Hilgetag and Goulas, 2020; Margulies et al., 2016; Mesulam, 1998). Macroscale gradients of structural and functional attributes mirror such variations in the underlying laminar architecture (Huntenburg et al., 2018). For example, large-scale hierarchical cortical organization was found in gene expression (Burt et al., 2018; Fulcher et al., 2019; Hansen et al., 2020), cortical thickness (Wagstyl et al., 2015), intracortical myelin (Huntenburg et al., 2017), laminar differentiation (Paquola et al., 2019; Wagstyl et al., 2020) and excitability (Demirtaş et al., 2019; Markicevic et al., 2020; Straub et al., 2020; Wang, 2020).

The hierarchical organization of micro-architectural properties is thought to manifest as spatial variation in characteristics of regional neural activity (Gao et al., 2020; Murray et al., 2014; Shafiei et al., 2020; Vinck and Bosman, 2016; Wang, 2020). Regional intrinsic dynamics are associated with local excitation and inhibition ratios (Deco et al., 2014a, 2021; Wang et al., 2019; Wang, 2020) and reflect microscale and macroscale cortical hierarchies, including measures of intracortical myelin (Demirtaş et al., 2019; Gao et al., 2020; Shafiei et al., 2020), cytoarchitecture and recurrent subcortical inputs (Wang et al., 2019) and functional hierarchy (Shafiei et al., 2020). In particular, multiple studies have reported faster timescales of intrinsic neural activity in unimodal sensory cortex, and slower timescales in transmodal cortex (Gao et al., 2020; Ito et al., 2020; Kiebel et al., 2008; Mahjoory et al., 2020; Murray et al., 2014; Raut et al., 2020). This hierarchy of timescales is thought to support a hierarchy of temporal receptive windows: time windows in which a newly arriving stimulus will modify processing of previously presented, contextual information (Baldassano et al., 2017; Chaudhuri et al., 2015; Chien and Honey, 2020; Hasson et al., 2008; Honey et al., 2012; Huntenburg et al., 2018). As a result, unimodal cortex needs to adapt to rapid, uncertain changes in sensory input, while transmodal cortex sustains its activity for a longer period of time, resulting in greater sensitivity to contextual information. The hierarchical organization of neural circuit properties and cortical micro-architecture both influence and are influence by spatial embedding and network architecture. Neural circuit properties, however, are mainly quantified using a small number of manually selected time-series features, potentially precluding the possibility that different types of local

computations, that may be better captured by other, less commonly used time-series properties, manifest as different topographic organizations (Fulcher, 2018; Sethi et al., 2017; Shafiei et al., 2020).

2.3 Interplay of local attributes and global network organization

Previous literature suggests that regional heterogeneity in microscale properties of the brain is associated with macroscale network organization (Huntenburg et al., 2018; Suárez et al., 2020). For example, regional cytoarchitectonic features of the macaque cortex are correlated with large-scale structural connectivity (Scholtens et al., 2014). Moreover, highly connected hub complexes in the mouse connectome display a unique transcriptomic signature, reflecting the regional metabolic demands and macroscale network embedding (Fulcher and Fornito, 2016). Patterns of covariation in regional transcriptomic properties are also associated with large-scale functional connectivity (Richiardi et al., 2015). Several studies have also reported significant relationships between local microstructural and circuit properties and large-scale structural and functional networks in humans, using neurotransmitter receptors and transporters (Hansen et al., 2021), gene expression (Burt et al., 2018; Richiardi et al., 2015), laminar differentiation and cytoarchitecture (Paquola et al., 2019), intracranial myelin (Huntenburg et al., 2017), morphometric properties (Seidlitz et al., 2018) and intrinsic dynamics (Baracchini et al., 2021; Demirtaş et al., 2019; Gao et al., 2020; Shafiei et al., 2020).

Regional neural dynamics are shaped by the spatial embedding of neural circuits in macroscale networks and gradients of the underlying molecular and cellular properties (Cocchi et al., 2016; Gollo et al., 2015; Kiebel et al., 2008; Murray et al., 2014; Wang, 2020). Local micro-architecture and global network interactions together influence the neural signals generated by neuronal populations as well as the communication patterns between groups of neuronal populations. Particularly, heterogeneity of local circuit properties reflect cytoarchitectural variations and cell type compositions of brain regions, which have a crucial role in signal generation, transmission and integration (Murray et al., 2018; Payeur et al., 2019). Indeed, neural activity captured by electromagnetic and haemodynamic recordings is influence by cytoarchitecture and the laminar organization of brain regions (Bastos et al., 2020; Scheeringa and Fries, 2019; Scheeringa et al., 2016). Previous reports suggest that cortical rhythms have distinct laminar origins, such that deep infragranular cortical layers (layers V-VI) facilitate the top-down, feedback projections from higher-order

transmodal regions to sensory unimodal areas via alpha and beta rhythms, while bottom-up feedforward signals are transferred through superficial cortical layers (supragranular layers I-III and granular layer IV) via gamma oscillations (Bastos et al., 2018, 2020; Bastos et al., 2015; Buffalo et al., 2011; Maier et al., 2011, 2010; Smith et al., 2013). Haemodynamic activity is also associated with the cortical laminar structure and microvascular density of cortical layers (Drew, 2019; Scheeringa and Fries, 2019; Schmid et al., 2019). Specifically, the BOLD response appears to be more sensitive to neural activity from the highly vascularized cortical layer IV (Uludağ and Blinder, 2018). This is consistent with the notion that the BOLD response mainly reflects local field potentials from feedforward projections that mainly target layer IV (Douglas and Martin, 2004; Harel et al., 2006).

Therefore, regional neural activity and the characteristics of electromagnetic and haemodynamic signals mirror the cytoarchitectonic and microstructural gradients. Cortical micro-architectural properties can be directly measured using histological data (Amunts et al., 2013) or indirectly inferred from other measurements, such as microarray gene expression (Hawrylycz et al., 2012), neurotransmitter systems (Hansen et al., 2021), cortical thickness (Wagstyl et al., 2015) and intracortical myelin (Burt et al., 2018; Huntenburg et al., 2017). This has made it possible to characterize neural signal properties and regional brain dynamics with respect to microscale circuit properties and macroscale network topology (Cocchi et al., 2016; Deco et al., 2014b, 2021; Demirtaş et al., 2019; Gao et al., 2020; Ito et al., 2020; Mahjoory et al., 2020; Murray et al., 2018, 2014; Raut et al., 2020; Shine et al., 2019; Wang, 2020).

Previous reports have also examined the relationship between global network organization and regional brain dynamics (Suárez et al., 2020). An emerging literature suggests that spontaneous neural activity is inexorably linked with brain function and integration (Baracchini et al., 2021; Burzynska et al., 2013; Garrett et al., 2011, 2013b, 2018; Misic et al., 2011; Shafiei et al., 2019, 2020; Sorrentino et al., 2021; Uddin, 2020) and supports complex behaviour and cognition (Gao et al., 2020; Garrett et al., 2013b, 2015; Uddin, 2020; Waschke et al., 2021). Highly organized patterns of intrinsic dynamics have also been associated with inter-individual differences in cognitive function across the adult lifespan (Garrett et al., 2013a, 2015, 2022; Grady and Garrett, 2018; Reinhart and Nguyen, 2019; Uddin, 2020; Voytek et al., 2015; Waschke et al., 2017, 2021). For example, signal variability of brain regions, usually quantified as standard deviations or temporal entropy of inherent neural activity, used to be disregarded as noise (Garrett et al., 2013b; Uddin, 2020). However, previous studies found that signal variability of the BOLD signal changes with working memory task demands and varies between younger and older adults (Garrett et al., 2015;

Grady and Garrett, 2018; Waschke et al., 2021). Moreover, variability of electromagnetic neural activity increases during development and healthy aging (McIntosh et al., 2008; Mišić et al., 2010; Waschke et al., 2017, 2021). Other measures of neural dynamics, such as properties of power spectral density, have also been reported to reflect task demand and cognitive performance and vary across the lifespan (Dave et al., 2018; Gao et al., 2020; Voytek et al., 2015).

More generally, local temporal features of BOLD signal have been related to the topological characteristics of structural brain networks (Fallon et al., 2020; Sethi et al., 2017), demonstrating that signals generated by regions with greater connectivity have greater autocorrelation or self-affinity (Fallon et al., 2020; Sethi et al., 2017). The relationship between magnitude of the BOLD signal and large-scale functional connectivity, and its influence on modular organization of the human brain, has been studied using using task-based functional MRI data in a motor learning paradigm (Murphy et al., 2016). Power spectral properties of resting state magnetoencephalography (MEG) signal have unique properties that distinguish the intrinsic functional networks (Keitel and Gross, 2016) and can be used to identify individuals from a larger group with high accuracy using "finger printing" analysis (Silva Castanheira et al., 2021). Moreover, the heterogeneous temporal organization in the brain, that follows the anatomical and functional hierarchy (Baldassano et al., 2017; Cocchi et al., 2016; Gao et al., 2020; Honey et al., 2012; Huntenburg et al., 2018; Ito et al., 2020; Kiebel et al., 2008; Raut et al., 2020), have been incorporated in large-scale computational and biophysical modeling of large-scale network organization (Demirtaş et al., 2019; Gollo et al., 2015; Murray et al., 2018). Computational models of structurally coupled neuronal populations (Breakspear, 2017) have found that highly interconnected hub regions exhibit slow dynamic fluctuations whereas sensory areas that are tightly coupled to changes in the environment exhibit fast fluctuating neural activity (Gollo et al., 2015). Multiple studies have demonstrated that considering heterogeneity of local circuit properties in predictive models of functional brain networks improves the model fit to the empirical networks (Burt et al., 2021; Cocchi et al., 2016; Deco et al., 2021; Demirtaş et al., 2019; Wang et al., 2019).

Altogether, earlier work has examined the relationship between regionally heterogeneous cortical properties, including local circuit properties, and global network organization. However, most of the conventional computational analyses have often used a single or a small number of manually selected features-of-interest, linking a single dynamical feature to measures of micro-architecture and network embedding. This potentially obscures contributions of other important measures of intrinsic dynamics from the wider

time-series literature that may reflect different types of local computations and circuit properties. Recent advances in modern neuroimaging techniques and increasing number of data sharing initiatives offer new opportunities to comprehensively study local and global brain dynamics. The work presented in this thesis builds on previous research and explores the characteristics of regional spontaneous neural activity, and offers a comprehensive mapping between dynamic signatures of brain activity and gradients of cortical micro-architecture and network organization. In Chapter 3, I first examine regional neural activity and its relationship with large-scale functional interactions using a pharmacological manipulation that affects the stability of neural dynamics. Focusing on a commonly used characteristic of neural activity, I find that regional neural dynamics and large-scale network organization are indeed related to one another, such that perturbations in one results in changes in the other. Next, in Chapter 4, I expand on the previous chapter and use an unbiased, data-driven set of measures of intrinsic dynamics from time-series literature to comprehensively characterize spontaneous haemodynamic activity. I find that the dynamic fingerprint of haemodynamic activity mirrors systematic variations in multiple microstructural properties and is associated with macroscale network embedding. In Chapter 5, directly inspired by the work presented in the previous chapter, I investigate the properties of fast-oscillating neural activity using intrinsic neurophysiological recordings. Using a comprehensive list of time-series properties and multiple micro-architectural maps, I find that the dynamic signature of neurophysiological activity predominantly reflects characteristics of power spectral density and follows gradients of cortical circuit properties and metabolic demands. Finally, in Chapter 6, I identify commonalities between haemodynamic and neurophysiological networks by examining the correspondence between the inter-regional functional associations recovered from the two modalities. I find that the correspondence between the two network architectures is regionally heterogeneous, reflecting the unimodal-transmodal cortical hierarchy and the underlying cytoarchitecture.

2.4 Summary and conclusions

In summary, previous studies report that the local characteristics of brain areas, including micro-architectural properties as well as intrinsic neuronal dynamics, are highly associated with the large-scale structural and functional organization of brain networks. Multiple lines of evidence suggest that gradients of molecular and microstructural properties and macroscale network embedding reflect systemic patterns of variation in local circuit properties. Local computations are reflected in haemodynamic and electromagnetic signals

and manifest as diverse time-series features of regional neural activity. How microscale gradients of cellular and molecular properties and macroscale network embedding shape regional dynamic fingerprint of neural activity across the cortex remains unclear. The current thesis builds on previous literature and investigates the relationship between micro-architectural gradients, large-scale network organization and dynamical signatures of neural activity. Comprehensive mapping between regional time-series properties and microscale and macroscale gradients provides important insight into fundamental aspects of brain function and integration and offers new avenues for future research on mechanistic links between neural dynamics and human cognition and complex behaviour.

Chapter 3

Dopamine signaling modulates the stability and integration of intrinsic brain networks

Golia Shafiei[1], Yashar Zeighami[1], Crystal A. Clark[1], Jennifer T. Coull[2,3], Atsuko Nagano-Saito[1,4,5], Marco Leyton[1,5], Alain Dagher[1] & Bratislav Misic[1]

[1]McConnell Brain Imaging Centre, Montréal Neurological Institute, McGill University, Montréal, Canada

[2]Laboratoire des Neurosciences Cognitives UMR 7291, Federation 3C, Aix-Marseille University, France

[3]Centre National de la Recherche Scientifique (CNRS), Paris, France

[4]Centre de Recherche, Institut Universitaire de Gériatrie de Montréal, Montréal, Canada

[5]Department of Psychiatry, McGill University, Montréal, Canada

Published in:

Cerebral Cortex: https://doi.org/10.1093/cercor/bhy264

3.1 Preface

A prominent feature of brain function is the dynamic repertoire of neural activity. Regional neural dynamics are highly variable and inter-regional functional interactions perpetually reconfigure to support a wide range of sensory, motor and cognitive functions. How these local and global functional properties are linked and modulated remains unknown. A prominent hypothesis holds that dopamine signaling serves to stabilize neural activity, and may therefore mediate how individual areas are integrated into the wider network.

However, the stabilizing influence of dopamine has not been demonstrated at the systems level. The work presented here examines the relationship between regional neural dynamics and large-scale functional interactions and investigates the effects of dopamine precursor depletion on local and global functional architecture. The results highlight the stabilizing influence of dopamine signaling at the systems level and demonstrate that the local dynamics of a brain region are inseparable from its embedding in large-scale networks. This work was published in Cerebral Cortex in 2019 (Shafiei et al., 2019).

3.2 Abstract

Dopaminergic projections are hypothesized to stabilize neural signaling and neural representations, but how they shape regional information processing and large-scale network interactions remains unclear. Here we investigated effects of lowered dopamine levels on within-region temporal signal variability (measured by sample entropy) and between-region functional connectivity (measured by pairwise temporal correlations) in the healthy brain at rest. The acute phenylalanine and tyrosine depletion (APTD) method was used to decrease dopamine synthesis in 51 healthy participants who underwent resting-state functional MRI (fMRI) scanning. Functional connectivity and regional signal variability were estimated for each participant. Multivariate partial least squares (PLS) analysis was used to statistically assess changes in signal variability following APTD as compared with the balanced control treatment. The analysis captured a pattern of increased regional signal variability following dopamine depletion. Changes in haemodynamic signal variability were concomitant with changes in functional connectivity, such that nodes with greatest increase in signal variability following dopamine depletion also experienced greatest decrease in functional connectivity. Our results suggest that dopamine may act to stabilize neural signaling, particularly in networks related to motor function and orienting attention towards behaviorally-relevant stimuli. Moreover, dopamine-dependent signal variability is critically associated with functional embedding of individual areas in large-scale networks.

3.3 Introduction

The brain is a complex network of interacting neuronal populations that collectively support perception, cognition, and action. Transient episodes of synchrony establish brief windows for communication among remote neuronal populations, manifesting as patterns

of functional connectivity and large-scale resting state networks (Damoiseaux et al., 2006; Power et al., 2011; Yeo et al., 2011). Thus, regional neural activity reflects computations that result from network interactions, but also drives those interactions (Avena-Koenigsberger et al., 2018; Deco et al., 2011). Greater connectivity may promote greater signal exchange, leading to variable dynamics (Mišić et al., 2011; Rubinov et al., 2009); alternatively, densely interconnected regions may be more likely to synchronize, rendering their dynamics less variable and more stable (Gollo et al., 2015). How the balance between local dynamics and global functional interactions (connectivity) is modulated remains a fundamental question in systems neuroscience.

Dopamine is thought to stabilize neuronal signaling by modulating synaptic activity and signal gain (Seamans and Yang, 2004). Dopamine, acting in cortex or striatum, could regulate cortical representations by facilitating or suppressing neural signaling. These effects may also play a role in reinforcement learning, based on the theory of dopaminergic reward prediction error signaling (Schultz, 2002). In humans, transient decreases in dopamine synthesis (which we term *"dopamine depletion"*) have been shown to disrupt multiple aspects of perception, motor control, and executive function (Coull et al., 2012; Nagano-Saito et al., 2008, 2012; Ramdani et al., 2015), consistent with a role in the regulation of sustained cortical activity (Seamans and Yang, 2004). Similar effects have also been demonstrated in various animal models including rodents and monkeys (Seamans and Robbins, 2010). Furthermore, death of dopamine neurons in Parkinson's disease (PD) leads to unstable and increasingly variable motor output (Björklund and Dunnett, 2007; McAuley, 2003). Thus, by stabilizing neuronal signaling, dopamine may influence the stability of regional activity and its potential for functional interactions at a network level.

Here we use resting-state functional magnetic resonance imaging (fMRI) to investigate the effects of dopamine depletion on within region signal variability and intrinsic brain networks in healthy brain at rest. We applied acute phenylalanine and tyrosine depletion (APTD) to transiently decrease dopamine levels in healthy participants (Carbonell et al., 2014; Leyton et al., 2000; Leyton et al., 2004; McTavish et al., 1999b; Montgomery et al., 2003; Palmour et al., 1998). We hypothesized that dopamine depletion would destabilize regional haemodynamic activity, manifesting as increased signal variability. We further hypothesized that regions with increased signal variability may be less likely to interact with other regions, resulting in decreased functional connectivity defined by temporal statistical association of fMRI time series.

3.4 Materials and methods

3.4.1 Participants

Altogether, $n = 51$ healthy young individuals (right-handed, 23.6 $\pm$ 5.9 years old, 32 male/19 female) participated in 3 separate dopamine precursor depletion studies (two published (Coull et al., 2012; Nagano-Saito et al., 2012) and one unpublished studies). The protocol, acquisition site, scanner and sequence were identical across the 3 studies. Participants with a history of drug abuse, neurological or psychiatric disorder were excluded. Informed consent was obtained from all participants.

3.4.2 Dopamine depletion

The acute phenylalanine and tyrosine depletion (APTD) technique (Leyton et al., 2000; McTavish et al., 1999b; Palmour et al., 1998) was used to reduce dopamine synthesis in healthy participants, following the procedure described previously (Coull et al., 2012; Nagano-Saito et al., 2012). In short, each participant was tested twice on 2 separate days, once following administration of a nutritionally balanced amino acid mixture (BAL) and once following acute phenylalanine/tyrosine depletion (APTD), in a randomized, double-blind manner, such that neither the participants nor the experiment conductors had any information regarding the label of the condition (BAL vs. APTD) being tested on each day. It should be noted that although APTD leads to depletion of dopamine precursors and only reduces the dopamine synthesis and availability, the term *"dopamine depletion"* is used throughout this manuscript to refer to *"dopamine precursor depletion"* and APTD. Although APTD might also theoretically decrease norepinephrine synthesis, several reports have shown that the release of norepinephrine is not affected under resting state conditions (Le Masurier et al., 2014; McTavish et al., 1999a).

3.4.3 Data acquisition and preprocessing

T1-weighted, three-dimensional structural MRIs were acquired for anatomical localization (1-mm^3 voxel size), as well as two resting-state echoplanar T2-weighted images with blood oxygenation level-dependent (BOLD) contrast (3.5-mm isotropic voxels, TE 30 ms, TR 2 s, flip angle 90°) from all participants using a Siemens MAGNETOM Trio 3T MRI system at the Montréal Neurological Institute (MNI) in Montréal, Canada. Each participant was scanned for 5 minutes (150 volumes) with eyes open, on 2 separate days,

once following administration of a nutritionally balanced amino acid mixture (BAL) and once following acute phenylalanine/tyrosine depletion (APTD). The resting state fMRI data was preprocessed through the following steps: slice timing correction, rigid body motion correction, removal of slow temporal drift using a high-pass filter with 0.01 Hz cut-off, physiological noise correction. Head motion parameters were estimated by spatially re-aligning individual time points with the median volume, which was then aligned with the anatomical T1 image of the individual. Further motion correction was done by scrubbing (Power et al., 2012): time points with excessive in-scanner motion (>0.5mm framewise displacement) were identified and removed from time series, along with the two volumes before and two volumes after. All preprocessing steps were performed using the Neuroimaging Analysis Kit (NIAK) (Bellec et al., 2010, 2012).

Anatomical MRI data was parcelled into 83 cortical and subcortical areas using the Desikan-Killiany atlas (Desikan et al., 2006), and then further subdivided into 129, 234, 463 and 1015 approximately equally sized parcels following the procedure described by Cammoun and colleagues (Cammoun et al., 2012). The Desikan-Killiany atlas is a commonly-used, anatomical (as opposed to functional), automated labeling system, where nodes are delineated according to anatomical landmarks. It has been shown that the Desikan-Killiany atlas is comparably reliable to manual parcellations of human cortex (Desikan et al., 2006). The atlas exists at 5 progressively coarser resolutions (the so-called "Lausanne" parcellation (Cammoun et al., 2012)), allowing us to verify the experimental effects on various spatial scales. The parcellations were used to extract BOLD time series from functional MRI data. The time series of each parcel were estimated as the mean of all voxels in that parcel. All analyses were repeated at each resolution to ensure that none of the conclusions were idiosyncratic to a particular spatial scale.

3.4.4 Sample entropy

Sample entropy (SE) analysis was used to estimate within-region signal variability (Richman and Moorman, 2000). The algorithm quantifies the conditional probability that any two sequences of time points with length of $m + 1$ will be similar to each other, given that the first m points of these sequences were similar (Figure 3.1). SE is then measured as the natural logarithm of this quantity, such that large values are assigned to unpredictable signals, and small values to predictable signals. The algorithm is subject to two parameters: the pattern length (m), which determines the segment length used to find repeating patterns, and the similarity criterion (r), which is the tolerance for accepting matches in the time series. The sample entropy of a time series with length N is estimated as

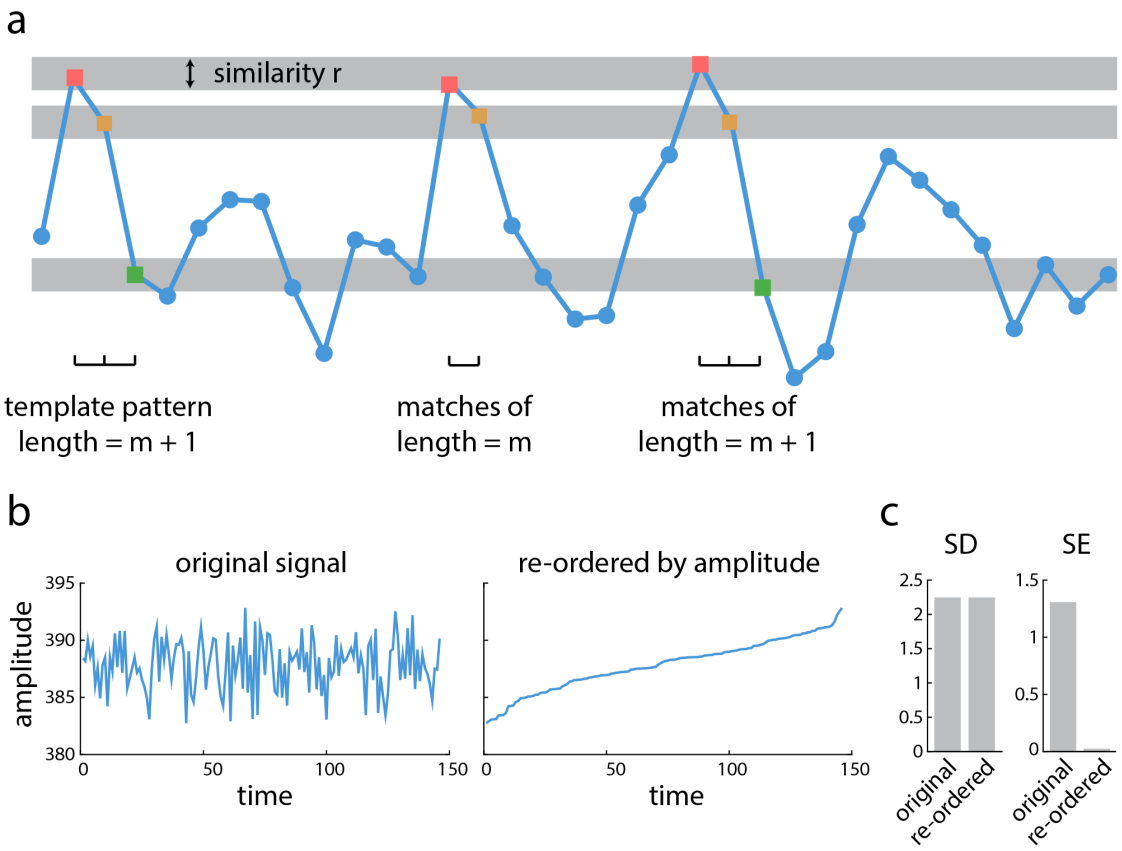

Figure 3.1: **Sample entropy of a time series** | (a) An example of a BOLD signal is shown, where the x-axis is time and the y-axis is the amplitude. Signal variability is calculated using sample entropy analysis. Sample entropy (SE) measures the conditional probability that any two sequences of data points with length $m + 1$ will be similar to one another under the condition that they were similar for the first m points. The similarity criterion r represents the tolerance of algorithm to accept matches in the time series. (b) An example of a BOLD signal in its original form (left). The same signal, with the time points re-ordered by amplitude (right). (c) Standard deviation of the signal is the same for both the original and reordered signal; however, sample entropy of the re-ordered signal drastically decreases compared to sample entropy of the original signal.

$$\mathrm{SE}(m, r, N) = \ln \frac{\sum_{i=1}^{N-m} n_i^m}{\sum_{i=1}^{N-m} n_i^{m+1}} \tag{3.1}$$

where n_i^m is the number of m-length segment of time series (e.g. segment j with length m) that are similar to the m-length segment i within to the similarity criterion, excluding self-matches ($i \neq j$; i.e., the algorithm does not compare patterns with themselves) (Costa et al., 2005). The sample entropy of a time series corresponds to 'scale 1' of the well-known multi-scale entropy analysis procedure (Costa et al., 2005).

Following the optimization proposed by Small & Tse (Small and Tse, 2004), we set $m = 2$

as the pattern length. We set the similarity criterion to $r = 0.5$ times the standard deviation (SD) of the time series following the method proposed by Richman & Moorman (Richman and Moorman, 2000). Although these values of m and r have been used extensively in previous reports (Beharelle et al., 2012; Heisz et al., 2012; McIntosh et al., 2008; Mišić et al., 2016), we sought to ensure that the reported results were robust across multiple choices of m and r. We therefore re-calculated SE using different values for m and r and re-ran the PLS analysis described below (see *Statistical assessment*). Figure S3.2 shows the correlation between new bootstrap ratios (i.e., changes in signal variability) with bootstrap ratios that were originally estimated by setting $m = 2$ and $r = 0.5 \times SD$. The correlations were generally greater than 0.7 across a range of similarity criteria r, and greater than 0.3 across a range of pattern lengths m, suggesting that the results were relatively insensitive to choice of parameters.

We operationalized signal variability using SE rather than other popular measures, such as standard deviation (SD). The primary reason for this choice is that SE is sensitive to temporal dependencies in the signal, while variance-based measures, such as SD, are not. This distinction is illustrated in Figure 3.1b and Figure 3.1c. Figure 3.1b (left) shows a typical BOLD signal from the present study (a randomly selected condition, participant and node). Figure 3.1b (right) shows the same signal, but with the time points reordered by amplitude. The sample entropy and standard deviation of the original and reordered signals were then measured (Figure 3.1c). Sample entropy is sensitive to this change, because the reordered signal monotonically increases and is trivially predictable. Critically, standard deviation is blind to this change; although the temporal complexity of the signal has been profoundly altered by reordering, standard deviation measures only the dispersion of points and cannot detect any temporal change (Figure 3.1c).

3.4.5 Statistical assessment

We used partial least squares (PLS) analysis to investigate within-participant changes in regional signal variability following the BAL versus APTD conditions. PLS analysis is a multivariate statistical technique that is used to analyze two "blocks" or sets of variables (McIntosh and Mišić, 2013; McIntosh and Lobaugh, 2004). In neuroimaging studies, one set may represent neural activity, while the other may represent behaviour or experimental design (e.g. condition and/or group assignments). PLS analysis seeks to relate these two data blocks by constructing linear combinations of the original variables such that the new latent variables have maximum covariance (Krishnan et al., 2011).

In the present report, one block (**X**) corresponded to regional signal variability in each participant estimated by sample entropy of BOLD time series following BAL versus APTD conditions. The rows of matrix **X** correspond to observations (participants nested within conditions) and the columns correspond to variables (regional signal variability). For p participants, c conditions, and v variables, matrix **X** will have $p \times c$ rows and v columns. Within-condition means are computed for each column and centered to give the matrix **M**. Singular value decomposition (SVD) is applied to **M**

$$\mathbf{USV}' = \mathbf{M} \tag{3.2}$$

resulting in a set of orthonormal left singular vectors, **U**, and right singular vectors, **V**, and a diagonal matrix of singular values, **S**. The number of latent variables is equal to the rank of the mean-centered matrix (here c), so **U** will have c columns and v rows, and **V** and **S** will both have c columns and c rows.

The decomposition results in a set of latent variables that are composed of columns of singular vectors, **U** and **V**, and a set of singular values from the diagonal matrix of **S**. In the present study, the v elements of column vectors of **U** are the weights of original brain activity variables (i.e., signal variability) that contribute to the latent variable and demonstrate a pattern of changes in signal variability following dopamine depletion. The c elements of column vectors of **V** are the weights of experimental design variables that contribute to the same latent variable and are interpreted as a contrast between experimental conditions. The latent variables are mutually orthogonal and express the shared information between the two data blocks with maximum covariance. This covariance is reflected in the singular values from the diagonal elements of matrix **S** that are associated with each given latent variable.

We assessed the statistical significance of each latent variable using permutation tests (Edgington and Onghena, 2007). During each permutation, condition labels for each participant are randomized by reordering the rows of matrix **X**. The new permuted data matrices were then mean-centered and subjected to SVD as before. The procedure was repeated 10,000 times to generate a distribution of singular values under the null hypothesis that there is no relationship between neural activity and study design. A p-value was estimated for each latent variable as the proportion of permuted singular values greater than or equal to the original singular value.

We assessed the reliability of singular vector weights using bootstrap resampling. Here, the rows of data matrix **X** were randomly resampled with replacement while keeping the original condition assignments. Mean-centering and SVD were then applied to the

resampled data matrices as before. The results were used to build a sampling distribution for each weight in the singular vectors **U** and **V**. A "bootstrap ratio" was then calculated for each original variable (i.e., for each node) as the ratio of the singular vector weight to its bootstrap-estimated standard error. Bootstrap ratios are designed to be large for variables that have a large weight (i.e., large contribution) as well as a small standard error (i.e., are stable). Bootstrap ratios are equivalent to z-scores if the bootstrap distribution is approximately unit normal (Efron and Tibshirani, 1986). In this case, 95% and 99% confidence intervals correspond to bootstrap ratios of ± 1.96 and ± 2.58, respectively.

PLS was chosen as the primary analytic method (instead of univariate statistical techniques) because we sought to identify patterns of nodes whose signal variability collectively changes due to dopamine depletion. However, the results of PLS analysis were nearly identical with the results obtained by a more conventional univariate paired t-test (correlation between t-values and bootstrap ratios; $r \approx 1$).

3.4.6 Community detection

Functional networks were partitioned into communities or intrinsic networks using the assignment derived in (Mišić et al., 2015), which we describe below. As we show in the *Results* section, the main conclusions also hold for the partitions reported by Yeo and colleagues (Yeo et al., 2011) and Power and colleagues (Power et al., 2011).

A Louvain-like greedy algorithm was used to identify a community assignment that maximized the quality function, Q (Newman and Girvan, 2004; Rubinov and Sporns, 2011)

$$\begin{aligned} Q(\gamma) = \frac{1}{m^+} \sum_{ij} (W_{ij}^+ - \gamma p_{ij}^+) \delta(\sigma_i, \sigma_j) \\ - \frac{1}{m^+ + m^-} \sum_{ij} (W_{ij}^- - \gamma p_{ij}^-) \delta(\sigma_i, \sigma_j) \end{aligned} \tag{3.3}$$

where W_{ij}^+ and W_{ij}^- are the functional connectivity (correlation) matrices that contain only positive and only negative coefficients of correlation, respectively. $p_{ij}^{\pm}$ is the expected density of only positive or only negative connectivity matrices according to the configuration null model and is given as $p_{ij}^{\pm} = (s_i^{\pm} s_j^{\pm})/2m^{\pm}$. $m^{\pm} = \sum_{i,j>i} W_{ij}^{\pm}$ is the total weight of all positive or negative connections of $W_{ij}^{\pm}$ (note that the summation is taken over $i, j > i$ to ensure that each connection is only counted once). The total weights of positive or negative connections of i and j are given by $s_i^{\pm} = \sum_i W_{ij}^{\pm}$ and $s_j^{\pm} = \sum_j W_{ij}^{\pm}$, respectively.

The resolution parameter γ scales the importance of the null model and effectively controls the size of the detected communities: larger communities are more likely to be detected when $\gamma < 1$ and smaller communities (with fewer nodes in each community) are more likely to be detected when $\gamma > 1$. Furthermore, σ_i defines the community assignment of node i. The Kronecker function $\delta(\sigma_i, \sigma_j)$ is equal to 1 if $\sigma_i = \sigma_j$ and is equal to zero otherwise ($\sigma_i \neq \sigma_j$), ensuring that only within-community connections contribute to Q.

Multiple resolutions γ were assessed, from 0.5 to 10 in steps of 0.1. The Louvain algorithm was repeated 250 times for each γ value (Blondel et al., 2008). The resolution $\gamma = 1.5$ was chosen based on the similarity measures (Rand index) of pairs of partitions for each γ value, such that the similarity measures of a more stable set of partitions for a given γ value would have a larger mean and smaller standard deviation compared to similarity measures at other γ values (i.e., larger z-score of similarity measure) (Red et al., 2011). Finally, a consensus partition was found from the 250 partitions at $\gamma = 1.5$ following the method described in Bassett et al., 2013. Eight communities or networks were detected, including visual (VIS), temporal (TEM), default mode (DMN), dorsal attention (DA), ventral attention (VA), somatomotor (SM) and salience (SAL) (Mišić et al., 2015). The subcortical areas (SUB) were added to the list as a separate network based on the anatomical Desikan-Killiany parcellation.

3.4.7 Cohesion and integration

Connectivity between and within modules was assessed as the participation coefficient and within-module degree z-score (Guimera and Amaral, 2005), using Brain Connectivity Toolbox (BCT) (Rubinov and Sporns, 2010). The participation coefficient quantifies how evenly distributed a node's connections are to all modules. Values close to 1 indicate that a node is connected to many communities, while values close to 0 indicate that a node is connected to few communities. The participation coefficient of node i, P_i, is given by:

$$P_i = 1 - \sum_{m \in M} \left(\frac{k_i(m)}{k_i} \right)^2 \tag{3.4}$$

where m is a module from a set of modules M, k_i is the weighted degree (i.e., connection strength) of node i, and $k_i(m)$ is the number of connections between node i and all other nodes in module m (Guimera and Amaral, 2005; Rubinov and Sporns, 2010). To find participation coefficients of resting state networks, we first found the average participation coefficient of each node across all participants and then compared the participation

coefficients of the nodes that belong to the same module following the BAL versus APTD conditions.

The within-module degree is estimated as the weighted degree (i.e., strength) of the connections that node i makes to other nodes within the same module. The measure is then z-scored, expressing a node's weighted degree in terms of standard deviations above or below the mean degree of the nodes in the given module (Z_i). A positive within-module degree z-score indicates that a node is highly connected to other nodes within the same module, while a negative within-module z-score indicates a node participates in less than average connections within its own module. We estimated the within-module degree z-score of each node for each participant and then calculated the average Z_i over all participants. Finally, we compared the within-module degree z-scores of the nodes of a given module following the BAL and APTD conditions.

3.5 Results

Task-free, eyes-open resting-state fMRI was recorded in $n = 51$ healthy young participants on two separate days, once following administration of a nutritionally balanced amino acid mixture (BAL) and once following acute phenylalanine/tyrosine depletion (APTD). Anatomical MRI data were parcelled into five progressively finer resolutions, comprising 83, 129, 234, 463 and 1015 nodes (Cammoun et al., 2012)), which were used for extraction of blood-oxygen-level dependent (BOLD) time series. We investigated how dopamine depletion affects (a) local, region-level haemodynamic activity, (b) global, between-region temporal statistical association of BOLD time series (termed as *functional connectivity*) and (c) the relationship between the two.

3.5.1 Dopamine depletion increases signal variability

We estimated within region signal variability using sample entropy (SE), a measure of the unpredictability of a time series (Richman and Moorman, 2000). Briefly, the SE algorithm quantifies the conditional probability that any two sequences of $m + 1$ time points will be similar to each other given that the first m points were similar (Figure 3.1). We then used multivariate partial least squares (PLS) analysis to statistically assess within-participant changes in signal variability at each brain region following administration of the BAL versus APTD mixtures (McIntosh and Mišić, 2013). PLS results in a set of latent variables (LV), that are weighted combinations of experimental design (i.e., a contrast) and signal variability patterns that optimally covary with each other. The analysis revealed a single

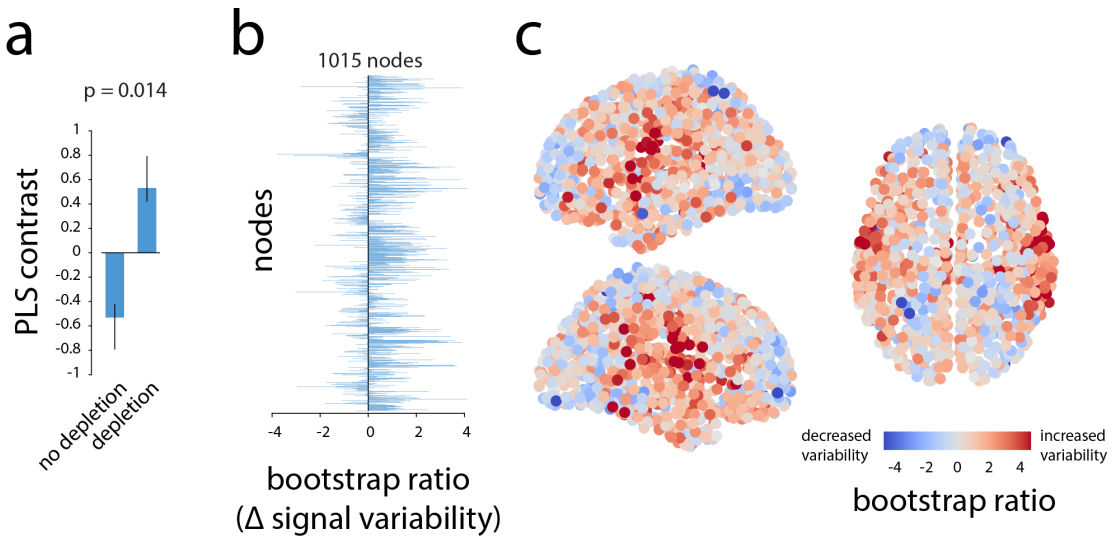

Figure 3.2: **Dopamine depletion increases signal variability** | (a) PLS analysis identified a significant contrast between patterns of signal variability in depletion (APTD) versus non-depletion (BAL) conditions (permuted $p = 0.014$). (b) The change in signal variability of each node is given by a bootstrap ratio for that node: such that a positive bootstrap ratio shows increase in signal variability of the node following dopamine depletion, while a negative bootstrap ratio shows the opposite. Bootstrap ratios are depicted at the finest resolution (1015 nodes), showing that dopamine depletion increases signal variability at most nodes. (c) Bootstrap ratios are shown in 3D space sagittally and axially. Corresponding results are shown for all resolutions in Figure S3.1

statistically significant latent variable (permuted $p = 0.014$ for the finest parcellation resolution with 1015 nodes), showing broadly increased signal variability following dopamine depletion (Figure 3.2). Bootstrap resampling was used to estimate the reliability with which individual nodes contribute to the overall multivariate pattern. Specifically, the weight or loading associated with each node was divided by its bootstrap-estimated standard error, yielding a measure ("bootstrap ratio") that is high for nodes with large weights (i.e., large contributions) and small standard errors (i.e., are stable) (McIntosh and Lobaugh, 2004). Note that bootstrap ratios may be interpreted as z-scores if the sampling distribution is approximately unit normal (Efron and Tibshirani, 1986). Positive bootstrap ratios indicate an increase in signal variability, while negative bootstrap ratios indicate decreased variability. Figure 3.2c depicts a brain projection of this statistical pattern, showing that the greatest increase in signal variability was observed in somatomotor cortex. This effect (increased regional haemodynamic variability following depletion) and the spatial pattern were consistent across all five spatial resolutions (Figure S3.1).

3.5.2 Increased signal variability in somatomotor and salience networks

We next investigated the effect of APTD on resting state networks (Power et al., 2011; Yeo et al., 2011). Figure 3.3a depicts the nodes displaying the greatest increase in signal variability following dopamine depletion in descending order and colour-coded by resting state network membership (Mišić et al., 2015). The most affected nodes appear to belong primarily to the somatomotor (yellow) and salience (green) networks suggesting that the signal variability may selectively affect certain large-scale networks.

To directly investigate the network-selectivity of dopamine depletion, we first estimated the mean change in signal variability across all nodes in a given network, using PLS-derived bootstrap ratios for the finest resolution (1015 nodes). To determine which network-level changes were statistically significant and not due to differences in network size, spatial contiguity or lateralization, we used a label permuting procedure. Network labels were randomly permuted within each hemisphere (preserving the number of nodes assigned to each network) and network means were recomputed 10,000 times, generating a distribution under the null hypothesis that network assignment does not influence the overall change in signal variability. A p-value was estimated for each network as the proportion of cases when the mean for the permuted network assignment exceeded the mean for the original empirical network assignment. Figure 3.3b,c shows that changes in signal variability were observed for all intrinsic networks, but that increased variability was greatest and statistically significant for the somatomotor and salience networks ($p < 10^{-4}$, FDR corrected (Benjamini and Hochberg, 1995)).

To ensure that these results are independent of how intrinsic networks are defined, we repeated the procedure using partitions reported by Yeo and colleagues (Yeo et al., 2011) and by Power and colleagues (Power et al., 2011) (Figure S3.3). The results were consistent across the three partitions, indicating significant increased signal variability in somatomotor and ventral attention networks among Yeo networks (note that the "ventral attention network" overlaps with the "salience network" shown in Figure 3.3), and in somatosensory and auditory networks among Power networks. No significant decrease in signal variability was observed in any intrinsic networks, regardless of which network assignments were used.

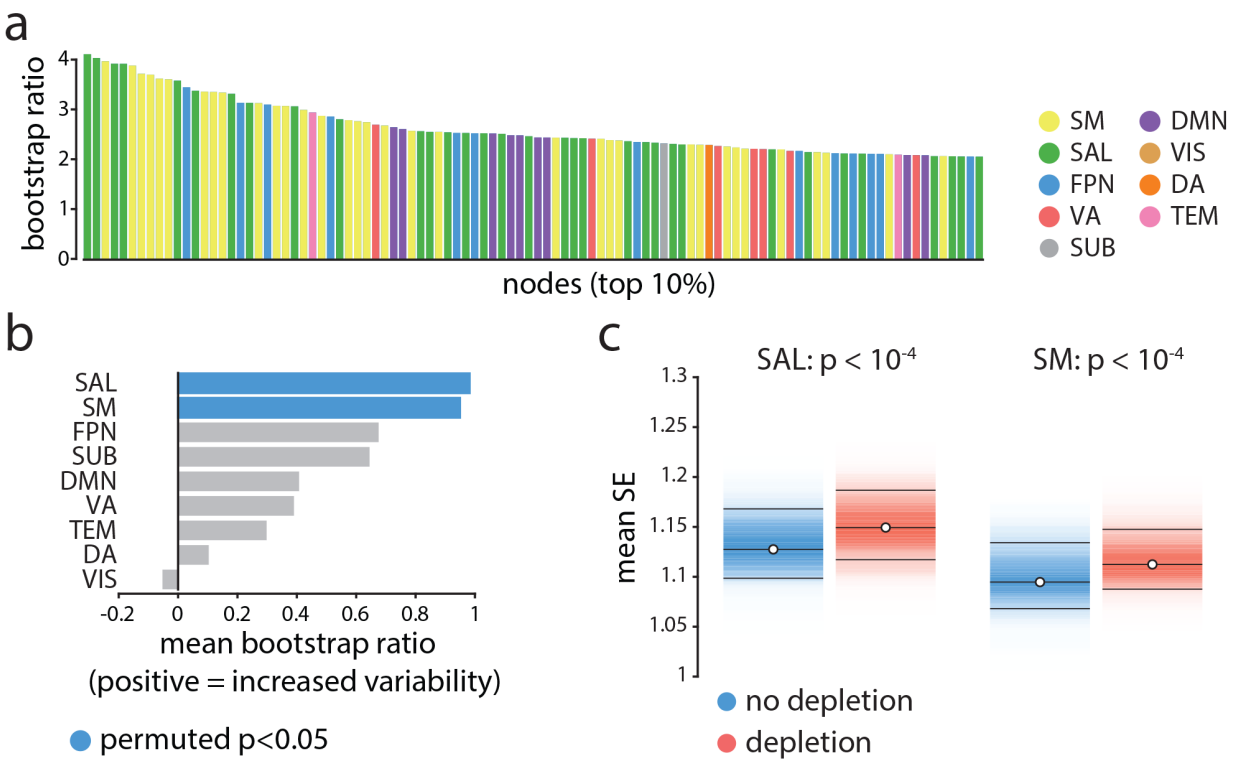

Figure 3.3: **Node- and network-level effects of dopamine depletion** | (a) The top 10% of the nodes (i.e., top 100 nodes) that had the largest increase in signal variability (largest bootstrap ratios) following dopamine depletion. Each bar shows the magnitude of bootstrap ratio of a node and is colored based on the community assignment of that node (Mišić et al., 2015). Somatomotor (yellow) and salience (green) networks appear over-represented compared with other networks. (b) The mean change in signal variability is calculated for each network and assessed by permutation tests (10,000 repetitions). Signal variability increases most in the salience and somatomotor networks following dopamine depletion, and these are the only two networks where this effect is statistically significant. (c) Changes in mean signal variability are depicted for somatomotor and salience networks (significance obtained by permutation tests; FDR corrected (Benjamini and Hochberg, 1995)). SM = somatomotor, SAL = salience, FPN = fronto-parietal, VA = ventral attention, SUB = subcortical areas, DMN = default mode, VIS = visual, DA = dorsal attention, TEM = temporal.

3.5.3 Increased signal variability correlates with decreased functional connectivity

Given that changes in signal variability were highly network dependent, we next investigated whether increased signal variability is related to patterns of functional connectivity. Functional connectivity was estimated as a zero-lag Pearson correlation coefficient between regional time series for each participant in each condition. To relate patterns of signal variability with functional connectivity, we estimated a group-average functional connectivity matrix by calculating the mean connectivity of each pair of brain regions across all

participants. We then estimated the mean connectivity (i.e., strength of the functional correlations) for each brain region.

We observed a weak relationship between increased signal variability and decreased functional connectivity, such that nodes with the greatest increase in signal variability following dopamine depletion also experienced the greatest decrease in functional connectivity ($r = -0.23$, $R^2 = 0.053$, $p = 1.04 \times 10^{-13}$; Figure 3.4a). Although statistically significant, effect was small, suggesting that the relationship was not sustained over the bulk of data points (nodes), but that it may have been driven by a subset of nodes instead.

To investigate this possibility, we assessed mean dopamine-dependent changes in functional connectivity in each of the intrinsic networks separately and correlated the network specific changes in functional correlation with the network specific changes in signal variability. Note that these analyses did not estimate subject error, but modeled group-averaged effects. Although there is a significant negative correlation between changes in functional connectivity and signal variability in more than half of the participants (29 out of 51), positive or no correlation was observed in others (7 and 15 out of 51 participants, respectively). In other words, the group-level effect is consistent with individual-level effects in the majority of participants. This result is broadly consistent with previous studies of group- versus individual-level effects of dopaminergic manipulations (Alavash et al., 2018; Garrett et al., 2015) and indicates that further investigation is required to assess the effects of dopamine depletion at the individual participant level. The results provided in the present work mainly address the group-level effects of dopamine depletion.

Thus, on the group-level, we observed an anti-correlation between the two measures such that the networks with greatest increase in haemodynamic signal variability also experience the great decrease in functional correlations ($r = -0.59$; Figure 3.4b). Changes in functional connectivity were statistically assessed using the same label permuting procedure outlined above (randomly permuting the network label of all nodes and re-computing network means, with 10 000 repetitions). Mean functional connectivity significantly decreased in 3 intrinsic networks: temporal, salience, and somatomotor networks connectivity ($p = 9.0 \times 10^{-4}$, $p < 10^{-4}$ and $p = 9.0 \times 10^{-4}$ respectively; FDR corrected; Figure 3.4c,d). Critically, the salience and somatomotor networks also experienced the greatest increase in signal variability after APTD (Figure 3.3), suggesting that changes in signal variability and functional connectivity may be related. Overall, these results suggest that the effects of dopamine depletion are stronger in specific large-scale systems, and that changes in local dynamics are related to global functional interactions.

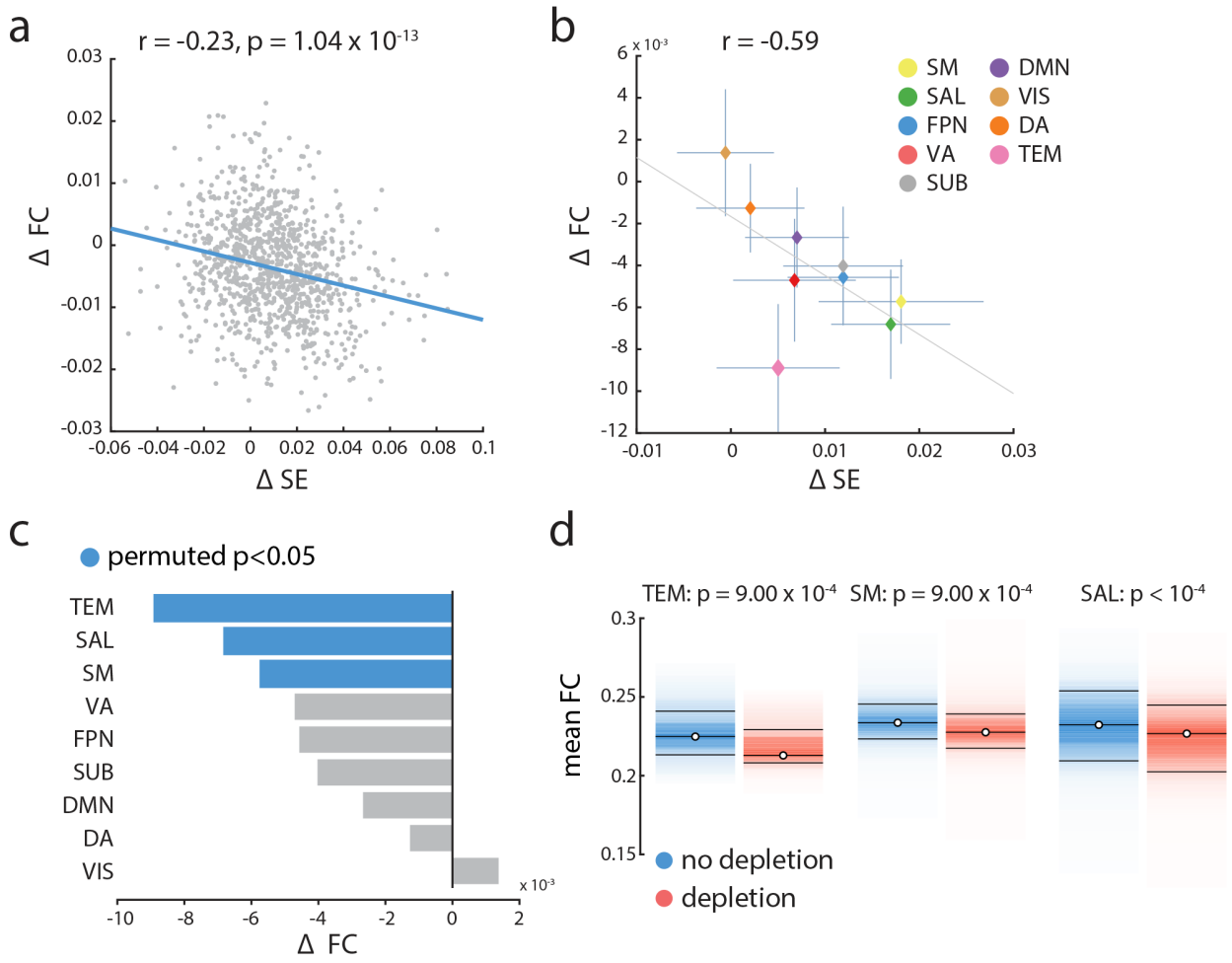

Figure 3.4: **Relating signal variability and functional connectivity** | (a) Mean changes in functional connectivity following dopamine depletion were estimated across all nodes and correlated with changes in within-region signal variability. Changes in functional connectivity are related to changes in signal variability, such that the larger the increase in signal variability, the larger the decrease in functional connectivity. (b) Mean changes in functional connectivity for intrinsic networks are correlated with mean changes in local signal variability in those networks. There is a clear anti-correlation between the two, consistent with the result in part (a). (c) The mean changes in functional connectivity was calculated for each network and assessed by permutation tests (10,000 repetitions). Mean connectivity significantly decreases in temporal, salience and somatomotor networks. Somatomotor and salience networks also experience significant increase in local variability (Figure 3.3). (d) Mean functional connectivity in depletion (APTD) vs. non-depletion (BAL) conditions, shown for nodes belonging to the temporal (TEM), somatomotor (SM) and salience (SAL) networks. Functional connectivity decreases in all instances (permutation test; FDR corrected).

3.5.4 Selective disconnection of intrinsic networks

Dopamine-related increases in signal variability appear to be concomitant with decreased functional connectivity and localized to specific intrinsic networks. However, it is unclear

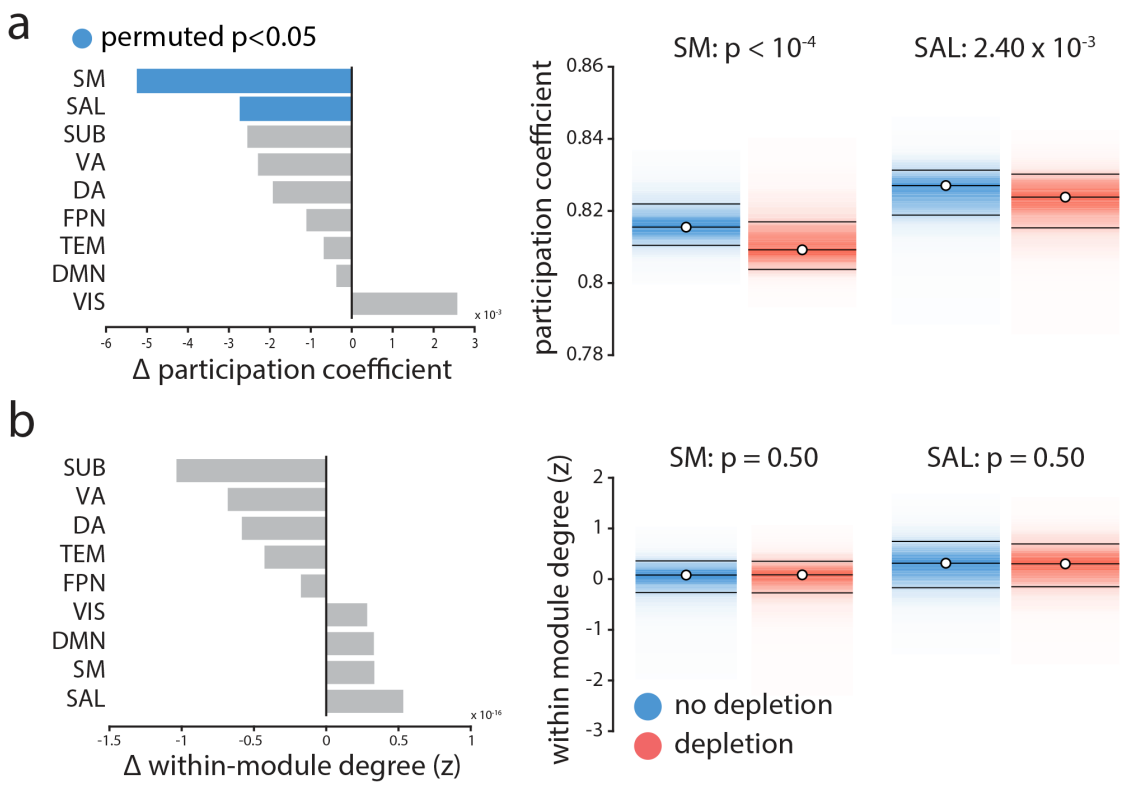

Figure 3.5: **Effects of dopamine depletion on cohesion and integration of specific intrinsic networks** | (a) Mean participation coefficient, indexing the diversity of inter-network connectivity, significantly decreases in somatomotor (SM) and salience (SAL) networks after dopamine depletion (using 10,000 permutation tests; FDR corrected). (b) Within-module degree z-score, indexing within-network connectivity, remains unaffected.

whether decreased connectivity in the somatomotor and salience networks is driven by weakened within-network or between-network connections, or both. To address this question, we calculated the participation coefficient and within-module degree z-score of every node (Guimera and Amaral, 2005). The participation coefficient quantifies the diversity of a node's connectivity profile. A participation coefficient with a value close to 1 indicates that a node's connections are evenly distributed across communities, while a value close to 0 indicates that most of the node's connections are within its own community. The within-module degree z-score of a node is a normalized measure of the strength of connections a node makes within its own community.

Figure 3.5 shows that the participation coefficient significantly decreases in somatomotor and salience networks following dopamine depletion ($p < 10^{-4}$ and $p = 2.4 \times 10^{-3}$ respectively, assessed by label permuting (see above); FDR corrected), while the within-module degree z-score does not ($p > 0.5$). In other words, dopamine depletion selectively

reduced functional interactions between these networks and the rest of the brain (participation coefficient; Figure 3.5a), but did not affect within-network cohesion (within-module degree z-score; Figure 3.5b). Overall, these results suggest that dopamine depletion effectively segregates these intrinsic networks from the rest of the brain, but does not affect their internal cohesion. Note that the two networks with significantly decreased participation coefficient are also the ones with greatest increases in signal variability. We also investigated average changes in participation coefficient and within-module degree z-score in other intrinsic networks, where we did not observe any significant changes in either of the two measures.

3.5.5 No systematic effect of study

The data used in this study were consolidated from three different experiments (two published (Coull et al., 2012; Nagano-Saito et al., 2012) and one unpublished studies), so it is possible that the observed effects were idiosyncratic to one or two of the constituent datasets and do not necessarily generalize across all three studies. To investigate this possibility, we used a multi-way ANOVA to assess differences between studies: participant-specific scores were calculated for the signal variability pattern and the three studies were treated as separate groups. The analysis did not reveal any significant difference among the three studies ($F(2,45) = 1.7$, $p = 0.19$), nor any condition by study interaction ($F(2,45) = 0.68$, $p = 0.51$). There was a significant condition difference, with greater scores in the depletion versus non-depletion condition ($F(1,45) = 131.06$, $p \approx 0$), but this is expected given that the scores were derived by PLS to maximize this condition difference.

3.5.6 Comparing sample entropy and standard deviation

A popular alternative measure of signal variability is the simple standard deviation (SD). Although we opted to use SE over SD because the latter is not sensitive to temporal dependencies in the signal (see Figure 3.1), for completeness we directly compared the effects of depletion using the two measures. *A priori*, we expect the two measures to be anti-correlated, because sample entropy estimation explicitly incorporates the SD of a given signal to define the similarity criterion r (the tolerance of the algorithm to accept matches in the time series). For a deeper discussion of this practice, including potential limitations, see Grandy et al., 2016. In other words, the similarity criterion for the sample entropy algorithm will be greater for a signal with a greater SD. Consequently, the sample entropy algorithm is more likely to identify matches in signals with a larger SD, resulting

in a lower sample entropy value. To demonstrate this claim, we correlated the SD and sample entropy of regional time series for both APTD (depletion) and BAL (no depletion) conditions, as well as the changes in each measure following dopamine depletion. The results are shown in Figure S3.4, confirming the anti-correlation between sample entropy and SD of a given signal at a brain region in the (a) no depletion condition, (b) depletion condition. Panel (c) further shows that depletion-driven changes in signal variability are also anti-correlated with changes in standard deviation.

To further assess whether the effects of dopamine depletion are specific to SE or SD, or both, we repeated the PLS analysis using the SD of the BOLD time series before and after dopamine depletion. The analysis revealed no significant effects of dopamine depletion on SD (permuted $p = 0.38$). We then regressed out SD from SE in each region for each participant and condition using a linear regression model and repeated the PLS analysis on the SD-residualized SE values. No statistically significant differences were detected using the SD-residualized SE values (permuted $p = 0.9$), indicating that SD and SE are not wholly independent of each other. Altogether the results suggest that SD and SE are both sensitive to the variance of the signal, but that SE captures additional temporal irregularities, making it more likely to detect the effects of dopamine depletion.

3.6 Discussion

We investigated the effect of dopamine depletion on the balance between local node properties and global network architecture. We report 2 key results: (1) dopamine depletion selectively destabilizes neural signaling, measured at the haemodynamic level, in salience and somatomotor networks, and (2) increased local variability in these intrinsic networks is accompanied by their disconnection from the global functional architecture. Altogether, these results point to a stabilizing influence of dopamine on neural signaling and highlight the link between local, node-level properties and global network architecture.

3.6.1 Linking local and global dynamics

The present results highlight the relationship between local haemodynamic signal variability and functional embedding. Increased variability in salience and somatomotor networks was concomitant with decreased functional connectivity with the rest of the brain. It is possible that low dopamine states disrupt local neuronal signaling, making it less likely for remote populations to synchronize. Alternatively, dopamine depletion may disrupt inter-regional synchrony through a separate mechanism, resulting in greater local variability.

The correlative nature of the results cannot be used to disambiguate these two possibilities and further causal experiments are necessary. The within-condition relationship between local variability and global connectivity remains an open question. In any case, the present report demonstrates that functional interactions span multiple topological scales, such that local and global dynamical properties cannot be fully appreciated in isolation (Bolt et al., 2018; Cabral et al., 2011).

Interestingly, dopamine depletion was associated with reduced between-module connectivity but not with within-module connectivity (Figure 3.5). The effect was highly specific: reduced between-module connectivity was significantly observed only in networks that also experienced increased regional signal variability. In other words, dopamine depletion affected how nodes within these networks communicated with the rest of the brain, but did not affect their internal cohesion. A recent study demonstrated a similar effect at the level of resting state networks: networks with greater temporal variability displayed greater within-network cohesion and lower between-network integration (Lee and Frangou, 2017). Altogether, the present results highlight a simple principle: the tendency for nodes to form functional networks depends on their ability to synchronize with one another. Thus, functional interactions between regions must be studied together with the temporal properties of their local signals.

Recent theories emphasize dynamic over static brain function. At the network level, reconfiguration of functional interactions is increasingly recognized as an informative attribute of healthy brain function and dysfunction (Calhoun et al., 2014). Functional reconfiguration has been observed across multiple temporal scales, both at rest (Betzel et al., 2016; Zalesky et al., 2014) and with respect to a variety of cognitive functions (Shine et al., 2016b), including learning (Bassett et al., 2015; Mohr et al., 2016), attention (Shine et al., 2016a) and working memory (Kitzbichler et al., 2011), and even conscious awareness (Barttfeld et al., 2015; Godwin et al., 2015). In parallel, the dynamic range of local signal fluctuations has emerged as a node-level marker of brain function (Garrett et al., 2013b; Roberts et al., 2017). Traditionally disregarded as "noise", changes in signal variability have been reported across the lifespan (Garrett et al., 2011; Guitart-Masip et al., 2015; McIntosh et al., 2008; Nomi et al., 2017), in multiple perceptual, cognitive and affective tasks (Garrett et al., 2013a; Mišić et al., 2010; Pfeffer et al., 2018; Samanez-Larkin et al., 2010) and in a variety of psychiatric and neurological diseases (Bertrand et al., 2016; Mišic et al., 2015; Mišić et al., 2016).

While most methods for estimating variability focus on node-level time series, several

recent studies have conceptualized variability with respect to functional network embedding (Mišić et al., 2016; Shen et al., 2015b). For instance, local variability can be defined as the tendency for a node to switch network allegiance or to interact with multiple networks (Braun et al., 2015; Zhang et al., 2016). This dynamic network switching is conditioned by an underlying anatomy (Shen et al., 2015a; Zhang et al., 2016), but is also likely to be influenced by a variety of neurotransmitters. A prominent hypothesis is that dopamine modulates signal-to-noise ratio (Mohr and Nagel, 2010; Samanez-Larkin et al., 2010). We turn to the specific role of dopamine next.

3.6.2 Dopamine and signal dynamics

Our results suggest that dopamine may act to stabilize neural signaling at the haemodynamic level, particularly in networks associated with motor control (somatomotor network) and orienting attention towards behaviorally-relevant stimuli (salience network). Dopamine depletion was simultaneously associated with increased within region signal variability and decreased extrinsic connectivity, indicating that dopaminergic signaling influences both local information processing and network-wide interactions. Importantly, the effects of depletion were not confined to a single locus but distributed over two large-scale networks, suggesting that even transient decreases in dopamine availability can disrupt local neuronal signaling and have far-reaching effects on synchrony among multiple systems.

There are two possible mechanisms by which dopamine depletion could cause the observed changes in cortical signal variability. The first possibility is that depletion modulates synaptic activity and signal gain directly via cortical receptors (Seamans and Yang, 2004). Mechanistic studies *in vitro* have demonstrated that dopamine influences intrinsic ionic currents and synaptic conductance (Durstewitz et al., 2000; Kroener et al., 2009). These modulatory effects may facilitate or suppress neural signaling, helping to stabilize neural representations. In addition, dose–response effects of dopamine release may be both tonic and phasic (Goto et al., 2007), with the two modes thought to be mediated by distinct signaling pathways and receptors, and manifesting in distinct behavioral outcomes (Cox et al., 2015). For instance, striatal medium spiny neurons of the direct pathway express D_1 receptors and are thought to promote movement and the selection of rewarding actions. Neurons in the indirect pathway mainly express D_2 receptors and are thought to inhibit cortical patterns that encode maladaptive or non-rewarding actions (Surmeier et al., 2011). Although our results are consistent with the broad notion that dopamine stabilizes neural representations to facilitate reward learning and movement,

further experiments are necessary to determine whether the observed effects can be attributed to tonic or phasic modulation, and to D_1 or D_2 receptor transmission.

The second possibility is that the effects of dopamine depletion may originate in the striatum, an area with dense dopaminergic afferents as well as projections to both the somatomotor and salience networks (Alexander and Crutcher, 1990; Alexander et al., 1986; Zhang et al., 2017). Prominent projections from dorsal striatum terminate in the somatomotor system (forming the motor loop), while projections ventral striatum terminate in the salience system. A dopaminergically-depleted striatum may therefore disrupt ongoing cortico-striatal signaling, resulting in downstream cortical effects, such as increased variability. Importantly, the two accounts are not mutually exclusive, and it is possible that the observed effects depend on both mechanisms.

Dopamine depletion can thus have local and global consequences, influencing a range of sensory-motor and higher cognitive functions. Age-related decline in dopaminergic transmission is hypothesized to lead to greater signal variability, influencing the distinctiveness of neural representations and, ultimately, performance (Mohr and Nagel, 2010; Samanez-Larkin et al., 2010). The stabilizing role of dopamine can also be observed in diseases associated with dopaminergic dysfunction, such as Parkinson's disease (PD), attention deficit hyperactivity disorder (ADHD), and schizophrenia. In PD for instance, cell death in substantia nigra leads to reduced dopaminergic transmission, with extensive motor symptoms. Intriguingly, dopamine depletion in PD is associated with reduced cortico-striatal functional connectivity patterns and reduced gait automaticity (Gilat et al., 2017). Similarly, in ADHD, reduced dopamine signaling is associated with deficits in goal-directed behavior and reward learning (Campo et al., 2013).

Finally, the present results draw attention to an overlooked assumption of graph-based models of brain structure and function: that all nodes are identical, except for their connectivity patterns. In other words, graph representations often ignore important inter-regional differences that could influence neural activity and synchrony, including morphology, cytoarchitectonics, gene expression, and receptor densities (Lariviere et al., 2019). How dopaminergic modulation interacts with modulation by other neurotransmitters is an exciting open question (Shine et al., 2018).

3.6.3 Measuring signal variability

Finally, we note that several recent reports have also investigated the role of dopaminergic signaling in the context of local signal dynamics, but drew an altogether different conclusion: that dopamine up-regulation "increases" signal variance. Specifically, Alavash et al.,

2018 reported that L-dopa administration increased BOLD standard deviation during an auditory working memory task (a syllable pitch discrimination task). Similarly, Garrett et al., 2015 reported that d-amphetamine administration also increased signal standard deviation during a working memory task (a visual letter n-back task). Although we used a different method to manipulate dopamine (APTD vs. L-dopa and d-amphetamine) and to record haemodynamic activity (resting state vs. task), we believe that the primary difference between these studies and our own is how signal variability was operationalized. Namely, both Alavash et al., 2018 and Garrett et al., 2015 defined signal variability in terms of standard deviations. The results shown in Figure 3.1 and Figure S3.4 demonstrate that sample entropy and variance based measures (e.g., standard deviation) capture different aspects of signal variability. Most importantly, because of the way that sample entropy is used to detect repeating patterns in a signal, we find that in practice, the two measures are often anti-correlated, which explains the seemingly different results. Altogether, these studies demonstrate a need to further refine the concept of signal variability and for greater plurality of methods (Fulcher and Jones, 2017). While some measures are sensitive to signal dispersion (e.g., standard deviation), others are sensitive to temporal regularity (e.g., sample entropy).

3.6.4 Methodological considerations

Our results may depend on a number of methodological choices and potential limitations, which we consider in detail here. Methodological choices include the type of parcellation and resolution, intrinsic network definition, and parameter settings for SE. The reported effects are consistent across 5 resolutions (from 83 to 1015 nodes; Figure S3.1), three network partitions (detected using clustering, Infomap, and Louvain methods; Figure S3.3) and a range of parameter settings (Figure S3.2). Although we took steps to mitigate concerns about these choices, the present results are based on a finite sampling of a multifactorial methodological space.

More generally, we studied the effects of dopamine depletion in the context of task-free, resting state fMRI, which presents 3 significant challenges for interpretation. First, dopaminergic transmission is inherently related to specific cognitive functions, which may be accessible without overt task demands. We find evidence that dopamine depletion affects information transfer in two intrinsic networks with specific functional properties, but more research is necessary to investigate how dopamine affects the function of these networks in the presence of task demands. Second, dopaminergic transmission within specific subcortical and cortical circuits occurs at time scales that may be inaccessible

with BOLD imaging. The present results can be used to draw conclusions about slow, modulatory effects of dopamine, but more electrophysiological evidence is necessary to relate these effects to faster phasic dopaminergic responses. Third, the present data were collected during an eyes-open resting state scan, which may potentially entail different neurocognitive demands than eyes-closed, including recruitment of visuomotor and attention networks (Jao et al., 2013; Patriat et al., 2013).

3.6.5 Summary

Our results support a link between local node dynamics and network architecture. Pharmacological perturbation may selectively target and disconnect specific networks without altering their internal cohesion. These results demonstrate that the effect of dopamine on synaptic signaling ultimately manifests at the level of large-scale brain networks.

3.7 Acknowledgments

This research was undertaken thanks in part to funding from the Canada First Research Excellence Fund, awarded to McGill University for the Healthy Brains for Healthy Lives initiative. BM acknowledges support from the Natural Sciences and Engineering Research Council of Canada (NSERC Discovery Grant RGPIN #017-04 265) and from the Fonds de recherche du Québec - Santé (Chercheur Boursier). G.S. acknowledges support from the Healthy Brains for Healthy Lives (HBHL) initiative at McGill University. The authors gratefully acknowledge code from Dr. Richard F. Betzel (University of Pennsylvania, PA, USA) and Dr. Andrea Avena-Koenigsberger (Indiana University, IN, USA) to create the boxplot and scatter plot figures, respectively. Conflict of Interest: The authors declare no competing interests.

3.8 Bibliography

Alavash, M. et al. (2018). “Dopaminergic modulation of hemodynamic signal variability and the functional connectome during cognitive performance”. *NeuroImage*, 172, pp. 341–356.

Alexander, G. E. and M. D. Crutcher (1990). “Functional architecture of basal ganglia circuits: neural substrates of parallel processing”. *Trends in neurosciences*, 13(7), pp. 266–271.

Alexander, G. E., M. R. DeLong, and P. L. Strick (1986). "Parallel organization of functionally segregated circuits linking basal ganglia and cortex". *Annual review of neuroscience*, 9(1), pp. 357–381.

Avena-Koenigsberger, A., B. Mišić, and O. Sporns (2018). "Communication dynamics in complex brain networks". *Nature Reviews Neuroscience*, 19(1), p. 17.

Barttfeld, P. et al. (2015). "Signature of consciousness in the dynamics of resting-state brain activity". *Proc Natl Acad Sci USA*, 112(3), pp. 887–892.

Bassett, D. S. et al. (2013). "Robust detection of dynamic community structure in networks". *Chaos: An Interdisciplinary Journal of Nonlinear Science*, 23(1), p. 013142.

Bassett, D. S. et al. (2015). "Learning-induced autonomy of sensorimotor systems". *Nat Neurosci*, 18(5), pp. 744–751.

Beharelle, A. R. et al. (2012). "Brain signal variability relates to stability of behavior after recovery from diffuse brain injury". *NeuroImage*, 60(2), pp. 1528–1537.

Bellec, P. et al. (2010). "Multi-level bootstrap analysis of stable clusters in resting-state fMRI". *Neuroimage*, 51(3), pp. 1126–1139.

Bellec, P. et al. (2012). "The pipeline system for Octave and Matlab (PSOM): a lightweight scripting framework and execution engine for scientific workflows". *Frontiers in neuroinformatics*, 6.

Benjamini, Y. and Y. Hochberg (1995). "Controlling the false discovery rate: a practical and powerful approach to multiple testing". *Journal of the royal statistical society. Series B (Methodological)*, pp. 289–300.

Bertrand, J.-A. et al. (2016). "Brain Connectivity Alterations Are Associated with the Development of Dementia in Parkinson's Disease". *Brain Conn*, 6(3), pp. 216–224.

Betzel, R. F. et al. (2016). "Dynamic fluctuations coincide with periods of high and low modularity in resting-state functional brain networks". *NeuroImage*, 127, pp. 287–297.

Björklund, A. and S. B. Dunnett (2007). "Fifty years of dopamine research". *Trends in neurosciences*, 30(5), pp. 185–187.

Blondel, V. D. et al. (2008). "Fast unfolding of communities in large networks". *Journal of statistical mechanics: theory and experiment*, 2008(10), P10008.

Bolt, T. et al. (2018). "Combining region-and network-level brain-behavior relationships in a structural equation model". *NeuroImage*, 165, pp. 158–169.

Braun, U. et al. (2015). "Dynamic reconfiguration of frontal brain networks during executive cognition in humans". *Proc Natl Acad Sci USA*, 112(37), pp. 11678–11683.

Cabral, J. et al. (2011). "Role of local network oscillations in resting-state functional connectivity". *Neuroimage*, 57(1), pp. 130–139.

Calhoun, V. D. et al. (2014). "The chronnectome: time-varying connectivity networks as the next frontier in fMRI data discovery". *Neuron*, 84(2), pp. 262–274.

Cammoun, L. et al. (2012). "Mapping the human connectome at multiple scales with diffusion spectrum MRI". *J Meth*, 203(2), pp. 386–397.

Campo, N. del et al. (2013). "A positron emission tomography study of nigro-striatal dopaminergic mechanisms underlying attention: implications for ADHD and its treatment". *Brain*, 136(11), pp. 3252–3270.

Carbonell, F. et al. (2014). "Dopamine precursor depletion impairs structure and efficiency of resting state brain functional networks". *Neuropharmacology*, 84, pp. 90–100.

Costa, M., A. L. Goldberger, and C.-K. Peng (2005). "Multiscale entropy analysis of biological signals". *Physical review E*, 71(2), p. 021906.

Coull, J. T. et al. (2012). "Dopamine precursor depletion impairs timing in healthy volunteers by attenuating activity in putamen and supplementary motor area". *Journal of Neuroscience*, 32(47), pp. 16704–16715.

Cox, S. M. et al. (2015). "Striatal D1 and D2 signaling differentially predict learning from positive and negative outcomes". *Neuroimage*, 109, pp. 95–101.

Damoiseaux, J. et al. (2006). "Consistent resting-state networks across healthy subjects". *Proceedings of the national academy of sciences*, 103(37), pp. 13848–13853.

Deco, G., V. K. Jirsa, and A. R. McIntosh (2011). "Emerging concepts for the dynamical organization of resting-state activity in the brain". *Nature Reviews Neuroscience*, 12(1), p. 43.

Desikan, R. S. et al. (2006). "An automated labeling system for subdividing the human cerebral cortex on MRI scans into gyral based regions of interest". *Neuroimage*, 31(3), pp. 968–980.

Durstewitz, D., J. K. Seamans, and T. J. Sejnowski (2000). "Dopamine-mediated stabilization of delay-period activity in a network model of prefrontal cortex". *J Neurophysiol*, 83(3), pp. 1733–1750.

Edgington, E. and P. Onghena (2007). *Randomization tests*. CRC Press.

Efron, B. and R. Tibshirani (1986). "Bootstrap methods for standard errors, confidence intervals, and other measures of statistical accuracy". *Statistical science*, pp. 54–75.

Fulcher, B. D. and N. S. Jones (2017). "hctsa: A Computational Framework for Automated Time-Series Phenotyping Using Massive Feature Extraction". *Cell systems*, 5(5), pp. 527–531.

Garrett, D. D., A. R. McIntosh, and C. L. Grady (2013a). "Brain signal variability is parametrically modifiable". *Cerebral Cortex*, 24(11), pp. 2931–2940.

Garrett, D. D. et al. (2011). "The importance of being variable". *J Neurosci*, 31(12), pp. 4496–4503.

Garrett, D. D. et al. (2013b). "Moment-to-moment brain signal variability: A next frontier in human brain mapping?" *Neuroscience & Biobehavioral Reviews*, 37(4), pp. 610–624.

Garrett, D. D. et al. (2015). "Amphetamine modulates brain signal variability and working memory in younger and older adults". *Proc Natl Acad Sci USA*, 112(24), pp. 7593–7598.

Gilat, M. et al. (2017). "Dopamine depletion impairs gait automaticity by altering cortico-striatal and cerebellar processing in Parkinson's disease". *NeuroImage*, 152, pp. 207–220.

Godwin, D., R. L. Barry, and R. Marois (2015). "Breakdown of the brain's functional network modularity with awareness". *Proc Natl Acad Sci USA*, 112(12), pp. 3799–3804.

Gollo, L. L. et al. (2015). "Dwelling quietly in the rich club: brain network determinants of slow cortical fluctuations". *Phil Trans R Soc B*, 370(1668), p. 20140165.

Goto, Y., S. Otani, and A. A. Grace (2007). "The Yin and Yang of dopamine release: a new perspective". *Neuropharmacology*, 53(5), pp. 583–587.

Grandy, T. H. et al. (2016). "On the estimation of brain signal entropy from sparse neuroimaging data". *Scientific reports*, 6(1), pp. 1–16.

Guimera, R. and L. A. N. Amaral (2005). "Cartography of complex networks: modules and universal roles". *Journal of Statistical Mechanics: Theory and Experiment*, 2005(02), P02001.

Guitart-Masip, M. et al. (2015). "BOLD variability is related to dopaminergic neurotransmission and cognitive aging". *Cereb Cortex*, 26(5), pp. 2074–2083.

Heisz, J. J., J. M. Shedden, and A. R. McIntosh (2012). "Relating brain signal variability to knowledge representation". *NeuroImage*, 63(3), pp. 1384–1392.

Jao, T. et al. (2013). "Volitional eyes opening perturbs brain dynamics and functional connectivity regardless of light input". *Neuroimage*, 69, pp. 21–34.

Kitzbichler, M. G. et al. (2011). "Cognitive effort drives workspace configuration of human brain functional networks". *J Neurosci*, 31(22), pp. 8259–8270.

Krishnan, A. et al. (2011). "Partial Least Squares (PLS) methods for neuroimaging: a tutorial and review". *Neuroimage*, 56(2), pp. 455–475.

Kroener, S. et al. (2009). "Dopamine modulates persistent synaptic activity and enhances the signal-to-noise ratio in the prefrontal cortex". *PLoS ONE*, 4(8), e6507.

Lariviere, S. et al. (2019). "Microstructure-informed connectomics: enriching large-scale descriptions of healthy and diseased brains". *Brain connectivity*, 9(2), pp. 113–127.

Le Masurier, M. et al. (2014). "Tyrosine-free amino acid mixtures reduce physiologically-evoked release of dopamine in a selective and activity-dependent manner". *Journal of Psychopharmacology*, 28(6), pp. 561–569.

Lee, W. H. and S. Frangou (2017). "Linking functional connectivity and dynamic properties of resting-state networks". *Sci Rep*, 7(1), p. 16610.

Leyton, M et al. (2000). "Effects on mood of acute phenylalanine/tyrosine depletion in healthy women". *Neuropsychopharmacology*, 22(1), pp. 52–63.

Leyton, M. et al. (2004). "Decreasing amphetamine-induced dopamine release by acute phenylalanine/tyrosine depletion: a PET/[11C] raclopride study in healthy men". *Neuropsychopharmacology*, 29(2), p. 427.

McAuley, J. (2003). "The physiological basis of clinical deficits in Parkinson's disease". *Progress in neurobiology*, 69(1), pp. 27–48.

McIntosh, A. R. and B. Mišić (2013). "Multivariate statistical analyses for neuroimaging data". *Annual review of psychology*, 64, pp. 499–525.

McIntosh, A. R., N. Kovacevic, and R. J. Itier (2008). "Increased brain signal variability accompanies lower behavioral variability in development". *PLoS Comput Biol*, 4(7), e1000106.

McIntosh, A. R. and N. J. Lobaugh (2004). "Partial least squares analysis of neuroimaging data: applications and advances". *Neuroimage*, 23, S250–S263.

McTavish, S. F., P. J. Cowen, and T. Sharp (1999a). "Effect of a tyrosine-free amino acid mixture on regional brain catecholamine synthesis and release". *Psychopharmacology*, 141(2), pp. 182–188.

McTavish, S. et al. (1999b). "Attenuation of some subjective effects of amphetamine following tyrosine depletion". *Journal of Psychopharmacology*, 13(2), pp. 144–147.

Mišić, B. et al. (2010). "Brain noise is task dependent and region specific". *J Neurophysiol*, 104(5), pp. 2667–2676.

Mišić, B. et al. (2011). "Functional embedding predicts the variability of neural activity". *Frontiers in systems neuroscience*, 5, p. 90.

Mišić, B. et al. (2015). "Cooperative and competitive spreading dynamics on the human connectome". *Neuron*, 86(6), pp. 1518–1529.

Mišic, B. et al. (2015). "Coordinated information generation and mental flexibility: large-scale network disruption in children with autism". *Cereb Cortex*, 25(9), pp. 2815–2827.

Mišić, B. et al. (2016). "Post-traumatic stress constrains the dynamic repertoire of neural activity". *J Neurosci*, 36(2), pp. 419–431.

Mohr, H. et al. (2016). "Integration and segregation of large-scale brain networks during short-term task automatization". *Nat Commun*, 7, p. 13217.

Mohr, P. N. and I. E. Nagel (2010). "Variability in brain activity as an individual difference measure in neuroscience?" *J Neurosci*, 30(23), pp. 7755–7757.

Montgomery, A. J. et al. (2003). "Reduction of brain dopamine concentration with dietary tyrosine plus phenylalanine depletion: an [11C] raclopride PET study". *American Journal of Psychiatry*, 160(10), pp. 1887–1889.

Nagano-Saito, A. et al. (2008). "Dopamine depletion impairs frontostriatal functional connectivity during a set-shifting task". *Journal of Neuroscience*, 28(14), pp. 3697–3706.

Nagano-Saito, A. et al. (2012). "From anticipation to action, the role of dopamine in perceptual decision making: an fMRI-tyrosine depletion study". *Journal of neurophysiology*, 108(2), pp. 501–512.

Newman, M. E. and M. Girvan (2004). "Finding and evaluating community structure in networks". *Physical review E*, 69(2), p. 026113.

Nomi, J. S. et al. (2017). "Moment-to-moment BOLD signal variability reflects regional changes in neural flexibility across the lifespan". *Journal of Neuroscience*, 37(22), pp. 5539–5548.

Palmour, R. M. et al. (1998). "An amino acid mixture deficient in phenylalanine and tyrosine reduces cerebrospinal fluid catecholamine metabolites and alcohol consumption in vervet monkeys". *Psychopharmacology*, 136(1), pp. 1–7.

Patriat, R. et al. (2013). "The effect of resting condition on resting-state fMRI reliability and consistency: a comparison between resting with eyes open, closed, and fixated". *Neuroimage*, 78, pp. 463–473.

Pfeffer, T. et al. (2018). "Catecholamines alter the intrinsic variability of cortical population activity and perception". *PLoS Biology*, 16(2), e2003453.

Power, J. D. et al. (2011). "Functional network organization of the human brain". *Neuron*, 72(4), pp. 665–678.

Power, J. D. et al. (2012). "Spurious but systematic correlations in functional connectivity MRI networks arise from subject motion". *Neuroimage*, 59(3), pp. 2142–2154.

Ramdani, C. et al. (2015). "Dopamine precursors depletion impairs impulse control in healthy volunteers". *Psychopharmacology*, 232(2), pp. 477–487.

Red, V. et al. (2011). "Comparing community structure to characteristics in online collegiate social networks". *SIAM review*, 53(3), pp. 526–543.

Richman, J. S. and J. R. Moorman (2000). "Physiological time-series analysis using approximate entropy and sample entropy". *American Journal of Physiology-Heart and Circulatory Physiology*, 278(6), H2039–H2049.

Roberts, J. A., K. J. Friston, and M. Breakspear (2017). "Clinical applications of stochastic dynamic models of the brain, part II: A review". *Biological psychiatry: cognitive neuroscience and neuroimaging*, 2(3), pp. 225–234.

Rubinov, M. and O. Sporns (2010). "Complex network measures of brain connectivity: uses and interpretations". *Neuroimage*, 52(3), pp. 1059–1069.

— (2011). "Weight-conserving characterization of complex functional brain networks". *Neuroimage*, 56(4), pp. 2068–2079.

Rubinov, M. et al. (2009). "Symbiotic relationship between brain structure and dynamics". *BMC neuroscience*, 10(1), p. 55.

Samanez-Larkin, G. R. et al. (2010). "Variability in nucleus accumbens activity mediates age-related suboptimal financial risk taking". *J Neurosci*, 30(4), pp. 1426–1434.

Schultz, W. (2002). "Getting formal with dopamine and reward". *Neuron*, 36(2), pp. 241–263.

Seamans, J. K. and T. W. Robbins (2010). "Dopamine modulation of the prefrontal cortex and cognitive function". *The dopamine receptors*, pp. 373–398.

Seamans, J. K. and C. R. Yang (2004). "The principal features and mechanisms of dopamine modulation in the prefrontal cortex". *Prog Neurobiol*, 74(1), pp. 1–58.

Shafiei, G. et al. (2019). "Dopamine signaling modulates the stability and integration of intrinsic brain networks". *Cerebral Cortex*, 29(1), pp. 397–409.

Shen, K. et al. (2015a). "Network structure shapes spontaneous functional connectivity dynamics". *J Neurosci*, 35(14), pp. 5579–5588.

Shen, K. et al. (2015b). "Stable long-range interhemispheric coordination is supported by direct anatomical projections". *Proc Natl Acad Sci USA*, 112(20), pp. 6473–6478.

Shine, J. M., O. Koyejo, and R. A. Poldrack (2016a). "Temporal metastates are associated with differential patterns of time-resolved connectivity, network topology, and attention". *Proc Natl Acad Sci USA*, p. 201604898.

Shine, J. M. et al. (2016b). "The dynamics of functional brain networks: Integrated network states during cognitive task performance". *Neuron*, 92(2), pp. 544–554.

Shine, J. M. et al. (2018). "Catecholaminergic manipulation alters dynamic network topology across cognitive states". *Network Neuroscience*, 2(3), pp. 381–396.

Small, M. and C. K. Tse (2004). "Optimal embedding parameters: a modelling paradigm". *Physica D: Nonlinear Phenomena*, 194(3-4), pp. 283–296.

Surmeier, D. J., L. Carrillo-Reid, and J. Bargas (2011). "Dopaminergic modulation of striatal neurons, circuits, and assemblies". *Neuroscience*, 198, pp. 3–18.

Yeo, B. T. et al. (2011). "The organization of the human cerebral cortex estimated by intrinsic functional connectivity". *Journal of neurophysiology*.

Zalesky, A. et al. (2014). "Time-resolved resting-state brain networks". *Proc Natl Acad Sci USA*, 111(28), pp. 10341–10346.

Zhang, J. et al. (2016). "Neural, electrophysiological and anatomical basis of brain-network variability and its characteristic changes in mental disorders". *Brain*, 139(8), pp. 2307–2321.

Zhang, Y. et al. (2017). "Anatomical and functional organization of the human substantia nigra and its connections". *eLife*, 6.

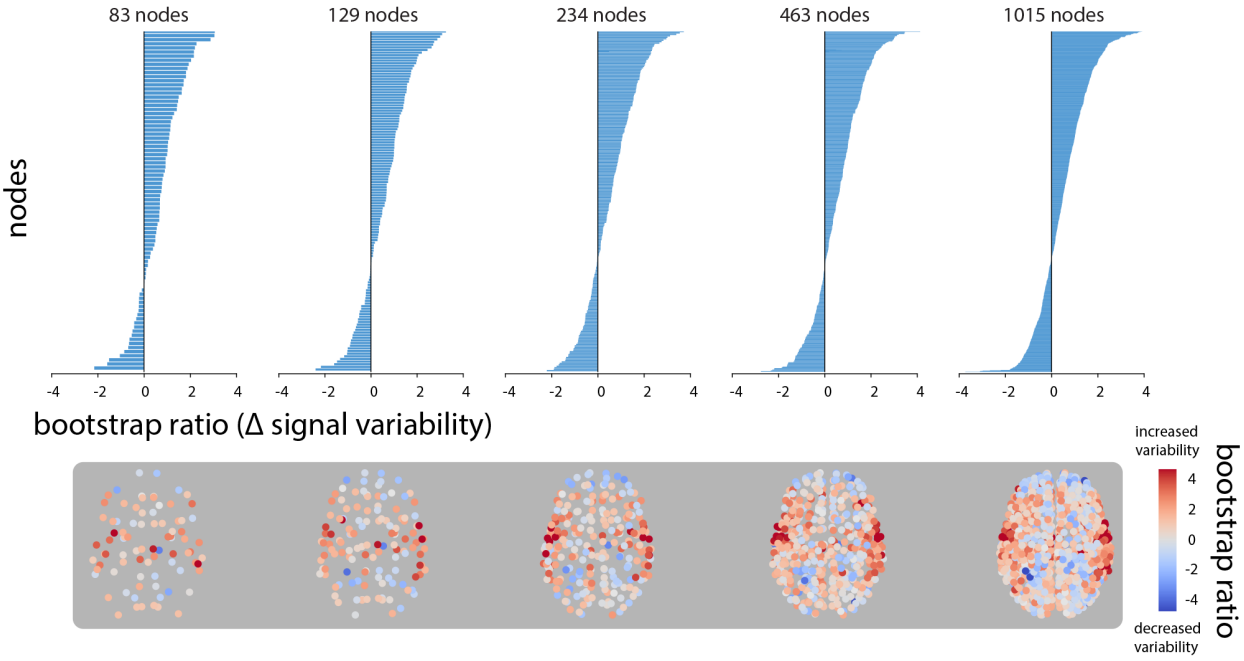

Figure S3.1: **Replicating results using alternative parcellation resolutions** | In all parcellation resolutions, PLS analysis identifies a contrast between the patterns of signal variability in depletion (APTD) vs. non-depletion (BAL) conditions, (permuted p-values for the 5 resolutions from 83 nodes to 1015 nodes are as following: $p = 0.047$, $p = 0.023$, $p = 0.006$, $p = 0.013$, and $p = 0.014$). Changes in signal variability of each node is given by a bootstrap ratio for that node, such that a positive bootstrap ratio shows increased variability of the node following dopamine depletion, while a negative bootstrap ratio shows the opposite. The bootstrap ratios are ordered and depicted at all resolutions by bar graphs (first row) and on each node of the brain network (second row).

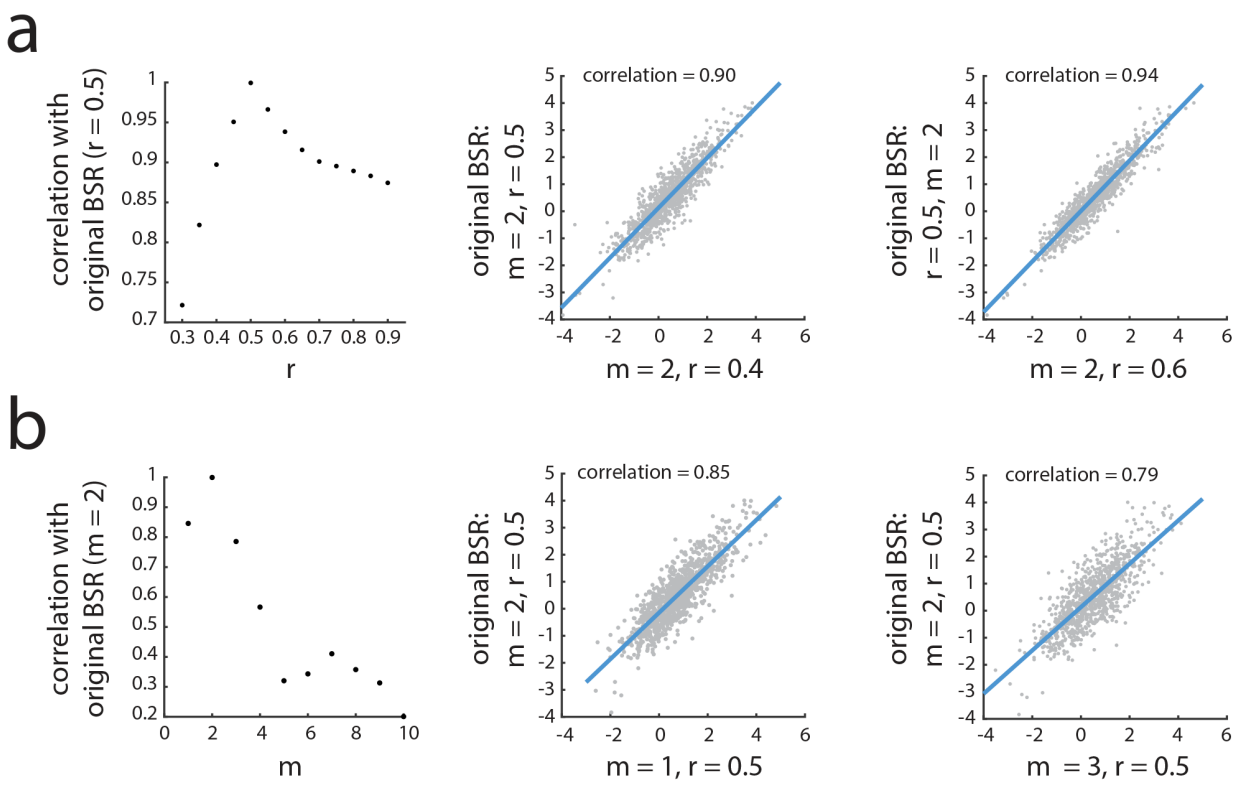

Figure S3.2: **Choosing parameters for sample entropy analysis** | The whole analysis was repeated several times to ensure that results are not affected by the choice of parameters used to estimate signal variability. For this purpose, signal variability was calculated for various m and r values. Results of each m and r value were subjected to PLS analysis and new bootstrap ratios were estimated each time. (a) New bootstrap ratios estimated for varying similarity criterion, r, were correlated with original bootstrap ratios that were estimated with $r = 0.5 \times SD$. The correlation coefficient at each r is shown in this figure. Note that pattern length was kept constant as $m = 2$. The correlation of bootstrap ratios for $r = 0.4 \times SD$ and $r = 0.6 \times SD$ with the original bootstrap ratios ($r = 0.5 \times SD$) are shown as examples. (b) Keeping similarity criterion unchanged at $r = 0.5 \times SD$, the correlation coefficients of new bootstrap ratios for varying pattern length, m, with original bootstrap ratio with $m = 2$ were estimated. Correlation of bootstrap ratios for $m = 1$ and $m = 3$ with original bootstrap ratios ($m = 2$) are depicted to show examples of varying m.

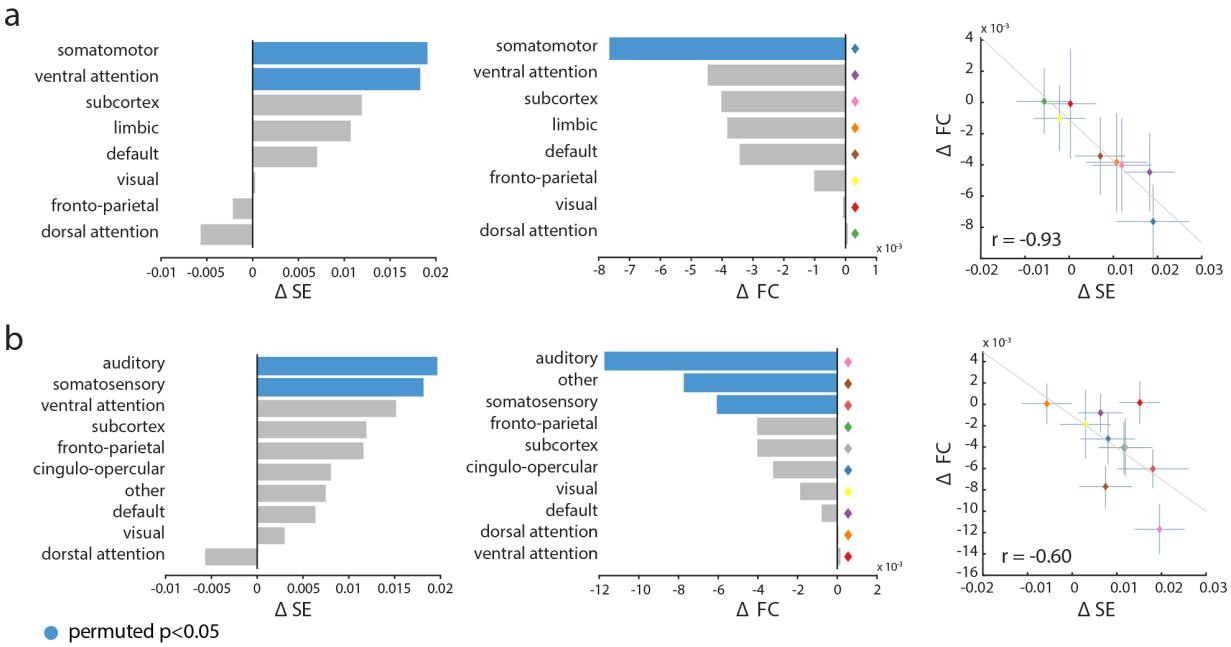

Figure S3.3: **Replicating results using alternative network partitions** | Mean local signal variability and mean functional connectivity across nodes were estimated at each resting state brain network using two of other well-known community assignments defined by (a) Yeo and colleagues (Yeo et al., 2011), and (b) Power and colleagues (Power et al., 2011). The significance of the mean signal variability and functional connectivity in each network was determined by 10,000 permutation tests. Mean network-wise changes in functional connectivity and local variability were correlated (scatter plots; $r = -0.93$ in (a) and $r = -0.60$ in (b)). The results are consistent with Figure 3.3 and Figure 3.4, confirming that our analysis is independent from the methods used to identify community assignments.

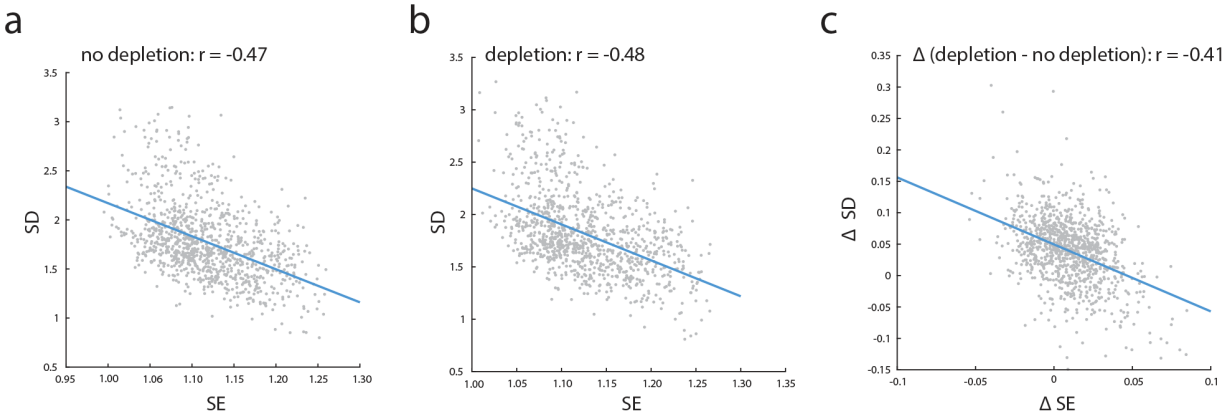

Figure S3.4: **Sample entropy versus standard deviation** | Sample entropy (SE) and standard deviation (SD) of the BOLD signal at each brain region were calculated and correlated for (a) BAL (no dopamine depletion) and (b) APTD (dopamine depletion) conditions. SE and SD are anti-correlated in both conditions, such that larger SE of the BOLD signal in a brain region corresponds to smaller SD. (c) Changes in sample entropy (ΔSE) and standard deviation (ΔSD), following dopamine depletion, are also anti-correlated.

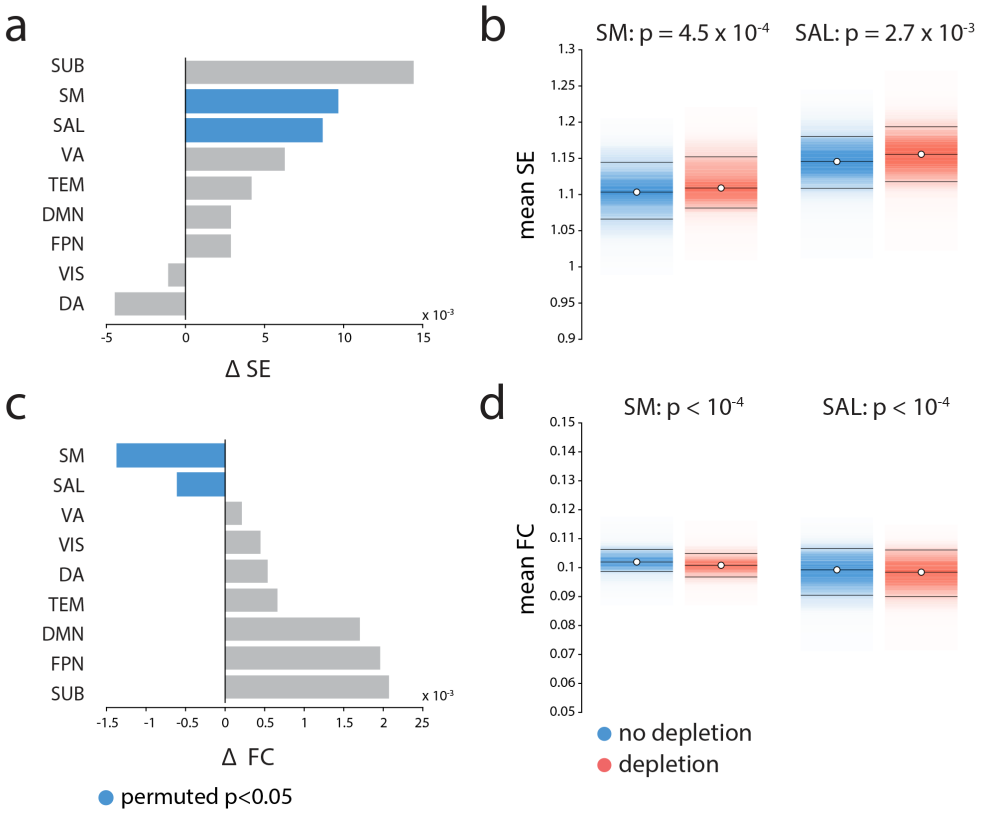

Figure S3.5: **Replicating results after performing global signal regression** | The analysis was repeated following global signal regression. The results are consistent with the ones shown before: (a) Mean signal variability increases significantly in the somatomotor and salience networks following dopamine depletion. (b) Changes in mean signal variability are depicted for somatomotor and salience networks (significance obtained by permutation tests; FDR corrected). (c) Mean functional connectivity significantly decreases in somatomotor and salience networks following dopamine depletion. (d) Changes in mean functional connectivity are depicted for somatomotor and salience networks (significance obtained by permutation tests; FDR corrected). SM = somatomotor, SAL = salience, FPN = fronto-parietal, VA = ventral attention, SUB = subcortical areas, DMN = default mode, VIS = visual, DA = dorsal attention, TEM = temporal.

Chapter 4

Topographic gradients of intrinsic dynamics across neocortex

Golia Shafiei[1], Ross D. Markello[1], Reinder Vos de Wael[1], Boris C. Bernhardt[1], Ben D. Fulcher[2] & Bratislav Misic[1]

[1]McConnell Brain Imaging Centre, Montréal Neurological Institute, McGill University, Montréal, Canada

[2]School of Physics, The University of Sydney, NSW 2006, Australia

Published in:

eLife: https://doi.org/10.7554/elife.62116

4.1 Preface

Contemporary theories of brain structure and function emphasize systematic variation in cytological properties across the cortex, including neuron density, dendritic branching and excitability. These microscale gradients are concomitant with macroscale variation in anatomical connectivity and functional interactions among neuronal populations. However, the dynamic consequences of these microscale and macroscale gradients remain unknown. Most of the conventional computational analyses use a single measure or a few specific, manually selected measures of intrinsic dynamics to characterize regional neural activity. However, the time-series analysis literature is vast and interdisciplinary, providing additional metrics of temporal structure of regional brain activity. The work presented here expands on Chapter 3 and, rather than manually selecting a few measures, attempts to comprehensively chart intrinsic dynamics across the cerebral cortex, mapping

temporal organization to structural and functional brain organization. This work was published in eLife in 2020 (Shafiei et al., 2020b).

4.2 Abstract

The intrinsic dynamics of neuronal populations are shaped by both microscale attributes and macroscale connectome architecture. Here we comprehensively characterize the rich temporal patterns of neural activity throughout the human brain. Applying massive temporal feature extraction to regional haemodynamic activity, we systematically estimate over 6,000 statistical properties of individual brain regions' time-series across the neocortex. We identify two robust spatial gradients of intrinsic dynamics, one spanning a ventromedial-dorsolateral axis and dominated by measures of signal autocorrelation, and the other spanning a unimodal-transmodal axis and dominated by measures of dynamic range. These gradients reflect spatial patterns of gene expression, intracortical myelin and cortical thickness, as well as structural and functional network embedding. Importantly, these gradients are correlated with patterns of meta-analytic functional activation, differentiating cognitive *versus* affective processing and sensory *versus* higher-order cognitive processing. Altogether, these findings demonstrate a link between microscale and macroscale architecture, intrinsic dynamics, and cognition.

4.3 Introduction

The brain is a complex network of anatomically connected and perpetually interacting neuronal populations (Sporns et al., 2005). Inter-regional connectivity promotes signaling via electrical impulses, generating patterned electrophysiological and haemodynamic activity (Avena-Koenigsberger et al., 2018; Suárez et al., 2020). Neuronal populations are organized into a hierarchy of increasingly polyfunctional neural circuits (Bazinet et al., 2020; Hilgetag and Goulas, 2020; Jones and Powell, 1970; Mesulam, 1998), manifesting as topographic gradients of molecular and cellular properties that smoothly vary between unimodal and transmodal cortices (Huntenburg et al., 2018). Recent studies have demonstrated cortical gradients of gene transcription (Burt et al., 2018; Fulcher et al., 2019), intracortical myelin (Huntenburg et al., 2017), cortical thickness (Wagstyl et al., 2015) and laminar profiles (Paquola et al., 2019).

The topological and physical embedding of neural circuits in macroscale networks and microscale gradients influence their dynamics (Gollo et al., 2015; Kiebel et al., 2008; Wang,

2020). For a neuronal population, the confluence of local micro-architectural properties and global connectivity shapes both the generation of local rhythms, as well as its propensity to communicate with other populations. Specifically, cell type composition, their morphology and their configuration in local circuits determine how signals are generated, transmitted and integrated (Payeur et al., 2019). These micro-architectural properties – increasingly measured directly from histology or inferred from other measurements, such as microarray gene expression – provide a unique opportunity to relate circuit architecture to temporal dynamics and computation. Indeed, multiple studies have focused on how intrinsic timescales vary in relation to microscale and macroscale attributes (Gao et al., 2020; Ito et al., 2020; Mahjoory et al., 2019; Murray et al., 2014; Raut et al., 2020; Shine et al., 2019). The primary functional consequence of this hierarchy of timescales is thought to be a hierarchy of temporal receptive windows: time windows in which a newly arriving stimulus will modify processing of previously presented (i.e. contextual) information (Baldassano et al., 2017; Chaudhuri et al., 2015; Chien and Honey, 2020; Hasson et al., 2008; Honey et al., 2012; Huntenburg et al., 2018). Thus, areas at the bottom of the hierarchy preferentially respond to immediate changes in the sensory environment, while responses in areas at the top of the hierarchy are modulated by prior context. Altogether, previous work highlights a hierarchy of a small number of manually selected time-series features, but it is possible that different types of local computations manifest as different organizational gradients.

The relationship between structure and dynamics is also observed at the network level (Suárez et al., 2020). Intrinsic or "resting state" networks possess unique spectral fingerprints (Keitel and Gross, 2016). The signal variability of brain areas, measured in terms of standard deviations or temporal entropy, is closely related to their structural and functional connectivity profiles (i.e. network embedding) (Burzynska et al., 2013; Garrett et al., 2017; Misic et al., 2011; Shafiei et al., 2019). More generally, the autocorrelation of blood oxygenation level-dependent (BOLD) signal is correlated with topological characteristics of structural brain networks, such that areas with greater connectivity generate signals with greater autocorrelation (Fallon et al., 2020; Sethi et al., 2017). Finally, in computational models of structurally coupled neuronal populations (neural mass and neural field models (Breakspear, 2017)), highly interconnected hubs exhibit slower dynamic fluctuations, while sensory areas exhibit fast fluctuating neural activity (Gollo et al., 2015). Indeed, these models offer better fits to empirical functional connectivity if they assume heterogeneous local dynamics (Cocchi et al., 2016; Deco et al., 2020; Demirtaş et al., 2019; Wang et al., 2019).

Altogether, multiple lines of evidence suggest that local computations may reflect

Figure 4.1: **Temporal phenotyping of regional dynamics** | The highly comparative time-series analysis toolbox, `hctsa` (Fulcher and Jones, 2017; Fulcher et al., 2013), was used to extract 6,441 time-series features of the parcellated time-series for each brain region and participant, including measures of autocorrelation, variance, spectral power, entropy, etc. Regional time-series profiles were then entered into two types of analyses. In the first analysis, pairs of regional time-series feature vectors were correlated to generate a region $\times$ region temporal profile similarity network. In the second analysis, principal component analysis (PCA) was performed to identify orthogonal linear combinations of time-series features that vary maximally across the cortex.

systematic variation in microscale properties and macroscale network embedding, manifesting as diverse time-series features of regional neural activity. How molecular, cellular and connectomic architecture precisely shapes temporal dynamics, and ultimately, cortical patterns of functional specialization, is poorly understood. A significant limitation is that conventional computational analysis is based on specific, manually selected time-series features, such as the decay of the autocorrelation function, bands of the Fourier power spectrum, or signal variance. Yet the time-series analysis literature is vast and interdisciplinary; how do other metrics of temporal structure vary across the brain and what can they tell us about cortical organization?

Here we comprehensively chart summary features of spontaneous BOLD signals across the cerebral cortex (hereafter referred to as "intrinsic dynamics"), mapping temporal organization to structural organization. We apply massive temporal feature extraction to resting state BOLD signals to derive a near-exhaustive time-series profile for each brain region. We then systematically investigate the relationship between local time-series features and gene expression, microstructure, morphology, structural connectivity and functional connectivity. Finally, we map time-series features to a meta-analytic atlas of cognitive ontologies to investigate how temporal dynamics shape regional functional specialization. We show that intrinsic dynamics reflect molecular and cytoarchitectonic

gradients, as well as patterns of structural and functional connectivity. These spatial variations in intrinsic dynamics ultimately manifest as patterns of distinct psychological functions.

4.4 Results

All analyses were performed on four resting state fMRI runs from the Human Connectome Project (Van Essen et al., 2013). The data were pseudorandomly divided into two samples of unrelated participants to form *Discovery* and *Validation* samples with $n = 201$ and $n = 127$, respectively (Wael et al., 2018). External replication was then performed using data from the Midnight Scan Club (Gordon et al., 2017). Massive temporal feature extraction was performed using highly comparative time-series analysis, `hctsa` (Fulcher and Jones, 2017; Fulcher et al., 2013), yielding 6,441 features per regional time-series, including measures of frequency composition, variance, autocorrelation, fractal scaling and entropy (Figure 4.1). The results are organized as follows. We first investigate whether regions that are structurally and functionally connected display similar intrinsic dynamics. We then characterize the topographic organization of time-series features in relation to microstructural attributes and cognitive ontologies.

4.4.1 Inter-regional temporal profile similarity reflects network geometry and topology

We first assessed the extent to which intrinsic dynamics depend on inter-regional physical distance, anatomical connectivity and functional connectivity. We estimated similarity between inter-regional dynamics by computing Pearson correlation coefficients between regional time-series feature vectors (Figure 4.1). Two regional time-series are judged to be similar if they have similar temporal profiles, estimated across a comprehensive and diverse set of time-series features (e.g. similar entropy, stationarity, linear correlation properties) (Fulcher, 2018). This measure of similarity identifies pairs of regions that have similar dynamical features, but not necessarily coherent or synchronous dynamics (Figure 4.2a). We refer to correlations between regional time-series feature profiles as "temporal profile similarity".

Figure 4.2b shows a negative exponential relationship between spatial proximity and temporal profile similarity, meaning that regions that are spatially close exhibit similar intrinsic dynamics. Interestingly, regions that share an anatomical projection have greater

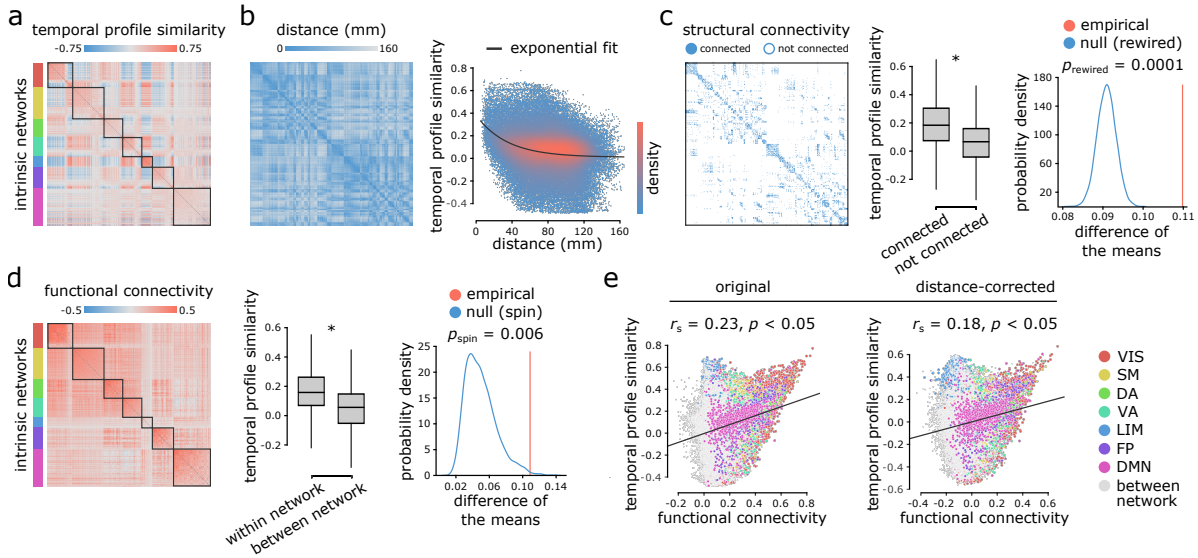

Figure 4.2: **Inter-regional temporal profile similarity reflects network geometry and topology** | (a) Temporal profile similarity networks are constructed by correlating pairs of regional time-series feature vectors. Brain regions are ordered based on their intrinsic functional network assignments (Schaefer et al., 2018; Yeo et al., 2011). (b) Temporal profile similarity between regions significantly decreases as a function of Euclidean distance between them. The black line represents an exponential fit as $y = 0.37e^{-0.03x} + 0.01$, where y is temporal profile similarity and x is Euclidean distance. (c, d) Regional time-series features are compared between pairs of cortical areas using their structural and functional connectivity profiles. Pairwise temporal profile similarity is significantly higher among structurally-connected areas (c), and among regions that belong to the same intrinsic functional networks (d). Asterisks denote a statistically significant difference of the means (two-tailed t-test; $p \approx 0$). For structural networks, statistical significance of the difference of the mean temporal profile similarity of connected and unconnected node pairs is also assessed against a null distribution of differences generated from a population degree- and edge length-preserving rewired networks (Betzel and Bassett, 2018)(c, right-most panel). For functional networks, statistical significance of the difference of the mean temporal profile similarity of within and between intrinsic networks is also assessed against a null distribution of differences generated by spatial autocorrelation-preserving label permutation ("spin tests"; (Alexander-Bloch et al., 2018))(d, right-most panel). (e) Temporal profile similarity is positively correlated with functional connectivity. This relationship remains after partialling out Euclidean distance between regions from both measures using exponential trends. r_s denotes the Spearman rank correlation coefficient; linear regression lines are added to the scatter plots for visualization purposes only. Connections are colour-coded based on the intrinsic network assignments (Schaefer et al., 2018; Yeo et al., 2011). VIS = visual, SM = somatomotor, DA = dorsal attention, VA = ventral attention, LIM = limbic, FP = fronto-parietal, DMN = default mode.

temporal profile similarity than those that do not (Figure 4.2c; two-tailed t-test; $t(79,798) = 40.234$, $p \approx 0$). To test whether this anatomically-mediated similarity of time-series features is not due to spatial proximity, we performed two additional comparisons. First, we regressed out the exponential trend identified above from the temporal profile similarity matrix, and repeated the analysis on the residuals, yielding a significant difference in temporal profile similarity between connected and non-connected regions (two-tailed

t-test; $t(79,798) = 9.916$, $p \approx 0$). Second, we generated an ensemble of 10,000 degree- and edge length-preserving surrogate networks (Betzel and Bassett, 2018), and compared the difference of the means between connected and non-connected pairs in the empirical and surrogate networks. Again, we observe a significant difference in temporal profile similarity between connected and non-connected regions (two-tailed; $p_{\text{rewired}} = 0.0001$; Figure 4.2c).

Likewise, regions belonging to the same intrinsic functional network have greater temporal profile similarity compared to regions in different networks (Figure 4.2d; two-tailed t-test; $t(79,798) = 61.093$, $p \approx 0$). To confirm this finding is not driven by spatial proximity, we repeated the analysis with distance-residualized values (Mišić et al., 2014), finding a significant difference (two-tailed t-test; $t(79,798) = 47.112$, $p \approx 0$). We also repeated the analysis using a nonparametric label-permutation null model with preserved spatial autocorrelation (10,000 repetitions) (Alexander-Bloch et al., 2018; Markello and Misic, 2020), again finding significantly greater within- compared to between-network temporal profile similarity (two-tailed; $p_{\text{spin}} = 0.006$; Figure 4.2d). These results are consistent when applying the 17 network partition of intrinsic networks (Schaefer et al., 2018; Yeo et al., 2011) (Figure S4.1).

More generally, we find a weak positive correlation between temporal profile similarity and functional connectivity (original: Spearman rank $r_s = 0.23$, $p \approx 0$; distance-corrected: $r_s = 0.18$, $p \approx 0$; Figure 4.2e), suggesting that areas with similar time-series features exhibit coherent spontaneous fluctuations, but that the two are only weakly correlated. Figure 4.2e shows the correlation between temporal profile similarity and functional connectivity; points represent node pairs and are coloured by their membership in intrinsic networks (Schaefer et al., 2018; Yeo et al., 2011). The results are consistent when functional connectivity is estimated using partial correlations (Figure S4.2). In other words, two regions could display similar time-series features, but they do not necessarily fluctuate coherently. Thus, representing time-series using sets of features provides a fundamentally different perspective compared to representing them as the raw set of ordered BOLD measurements.

As a final step, we sought to assess the distinct contributions of distance, structural connectivity and functional connectivity to temporal profile similarity. Dominance analysis revealed the relative importance of each predictor (collective $R^2 = 0.28$; distance = 56%, structural connectivity = 20.4%, functional connectivity = 23.6%; Table S4.1), suggesting that distance contributes the most to temporal profile similarity, while structural and functional connectivity make distinct but approximately even contributions (Azen and Budescu,

2003; Budescu, 1993) (https://github.com/dominance-analysis/dominance-analysis). Altogether, we find that the organization of intrinsic dynamics is closely related to both the geometric and topological embedding of brain regions in macroscale networks.

4.4.2 Two distinct spatial gradients of intrinsic dynamics

We next investigate the topographic organization of time-series features. The `hctsa` library generates 6,441 time-series features, with the aim of being comprehensive in coverage across scientific time-series analysis algorithms and, as a result, contains groups of features with correlated outputs (Fulcher et al., 2013). We therefore sought to identify groups of correlated features that explain maximal variance and that span different conceptual types of time-series properties. Applying principal component analysis (PCA; `Scikit-learn` (Pedregosa et al., 2011)) to the region $\times$ feature matrix yielded mutually orthogonal patterns of intrinsic dynamics (Figure 4.1), with the top two components collectively accounting for more than 70% of the variance in time-series features (Figure 4.3a). Figure 4.3a shows the spatial distribution of the top two components. The first component (PC1) mainly captures differential intrinsic dynamics along a ventromedial-dorsolateral gradient, separating occipital-parietal cortex and anterior temporal cortex. The second component (PC2) captures a unimodal-transmodal gradient, reminiscent of recently reported miscrostructural and functional gradients (Huntenburg et al., 2018). Both components show considerable hemispheric symmetry. In the following sections, we focus on these two components because of their (a) effect size (percent variance accounted for), (b) close resemblance to previously reported topographic gradients, and (c) reproducibility (only the first two components were reproducible in both the HCP and MSC datasets; see *Sensitivity and replication analyses* below). Note that neither spatial maps were significantly correlated with temporal signal-to-noise ratio map, computed as the ratio of the time-series mean to standard deviation (tSNR; PC1: $r_s = 0.28$, $p_{spin} = 0.19$; PC2: $r_s = 0.21$, $p_{spin} = 0.16$).

Which time-series features contribute most to these topographic gradients of intrinsic dynamics? To address this question, we systematically assess the feature composition of PC1 and PC2. We compute univariate correlations (i.e. loadings) between individual time-series feature vectors and PC scores (Figure 4.3b). Each loading is assessed against 10,000 spin tests and the results are corrected for multiple comparisons by controlling the false discovery rate (FDR (Benjamini and Hochberg, 1995); $\alpha = 0.001$). The top 5% positively and negatively correlated features are shown in word clouds. The complete list of features (ranked by loading), their definitions, loadings and p-values for both components is presented in machine-readable format in online Supplementary Files 3,4. Altogether,

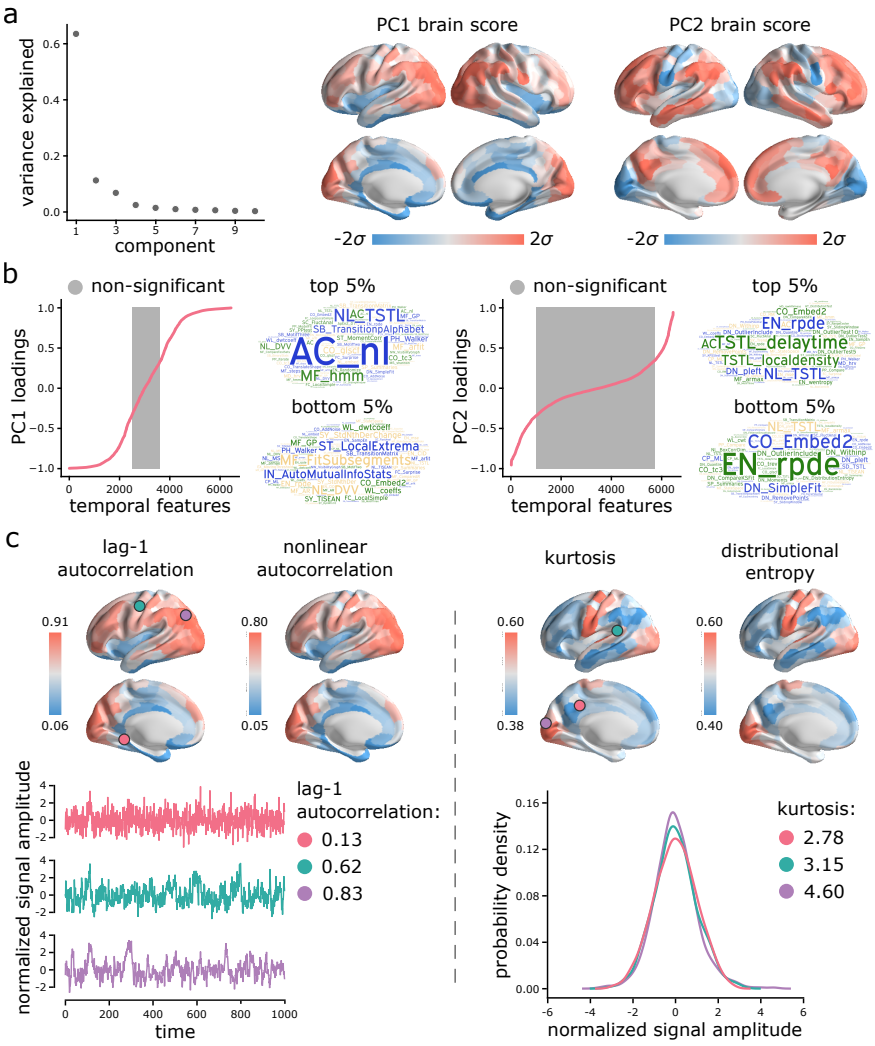

Figure 4.3: **Topographic gradients of intrinsic dynamics** | (a) PCA analysis identified linear combinations of time-series features with maximum variance across the cortex. Collectively, the first two components (PC1 and PC2) account for 75% of the total variance. To estimate the extent to which cortical regions display the patterns of intrinsic dynamics, `hctsa` matrices were projected back onto the PC weights (eigenvectors), yielding spatial maps of brain scores. Spatial maps are depicted based on the standard deviation σ of their respective distributions. (b) To understand the feature composition of the intrinsic dynamic patterns, feature loadings were computed by correlating individual `hctsa` feature vectors with the PC score maps. Time-series features are ordered by their individual loadings. Grey indicates non-significance based on 10,000 spatial permutation tests (FDR corrected). Features corresponding to the top and bottom 5% are visualized using word clouds. Complete lists of features, their definitions, correlations and p-values are presented in machine-readable format in online Supplementary Files 3,4. Feature nomenclature in `hctsa` is organized such that the term prefix indicates the broad class of measures (e.g. AC = autocorrelation, DN = distribution) and the term suffix indicates the specific measure (for a complete list, see https://hctsa-users.gitbook.io/hctsa-manual). (c) Spatial distributions of two high-loading representative time-series features are depicted for each component, including lag-1 linear autocorrelation (AC_1) and lag-[0,2,3] nonlinear autocorrelation (AC_nl_023, estimated as average $< x_t{}^2 x_{t-2} x_{t-3} >$ across time-series x) for PC1; and kurtosis (DN_Moments_4) and entropy (EN_DistributionEntropy_ks__02) of the time-series points distribution for PC2. To build intuition about what each component reflects about regional signals, three regional time-series from one participant are selected based on their lag-1 autocorrelation and kurtosis (circles on the brain surface: pink = 5^{th} percentile, green = 50^{th} percentile, purple = 95^{th} percentile).

we find that PC1 is sensitive to temporal dependencies in BOLD signals, while PC2 is sensitive to the distribution shape of time-series amplitudes. For PC1, in line with previous reports, we observe strong contributions from multiple measures of autocorrelation (e.g. linear autocorrelation; nonlinear autocorrelation; automutual information). Short-lag autocorrelation measures load positively, while long-lag autocorrelation measures load negatively, consistent with the notion that autocorrelation decays with increasing time lag (Gao et al., 2020; Murray et al., 2014; Raut et al., 2020) (Figure S4.3). For PC2, we observe strong contributions from measures of distribution shape, captured by measures of distributional entropy (e.g. entropy of kernel-smoothed distribution; kurtosis; distribution balance about the mean). In other words, PC2 captures the spread of time-series amplitudes away from the mean. Interestingly, none of the odd moments (distribution asymmetry) are high in the PC2 loading list, just even moments, suggesting that PC2 captures the shape of the deviations of time-series data points in both directions from the mean. Thus, PC2 indexes the range or diversity of values that a regional time-series can realize. Hereafter, we refer to the time-series profile of PC1 as "autocorrelation" and PC2 as "dynamic range".

To illustrate the spatial organization and time-series attributes of these components, Figure 4.3c shows the spatial distributions of two high-loading representative time-series features for each component. Ventromedial areas (lower in the PC1 gradient) have lower linear and nonlinear autocorrelation, while doroslateral areas (higher in the PC1 gradient) have greater autocorrelation. Sensory areas (lower in the PC2 gradient) have greater distributional entropy and kurtosis, while transmodal areas (higher in the PC2 gradient) have lower distributional entropy and kurtosis. Finally, to build intuition about what each component reflects about regional signals, we select three regional time-series from one participant based on their lag-1 autocorrelation and kurtosis (Figure 4.3c; pink = 5^{th} percentile, green = 50^{th} percentile, purple = 95^{th} percentile). For the former, going from low-ranked to high-ranked regions results in a slowing down of BOLD fluctuations. For the latter, going from low-ranked to high-ranked regions results in increasingly heavier symmetric tails of the signal amplitude distributions.

4.4.3 Intrinsic dynamics reflect microscale and macroscale hierarchies

To assess whether the dominant variation in time-series features of BOLD dynamics varies spatially with structural and functional gradients, we next quantify the concordance between PC1/PC2 and multiple microstructural and functional attributes (Figure 4.4). Specifically, we compare PC1 and PC2 with the following microscale and macroscale features: (1) the first component of microarray gene expression computed

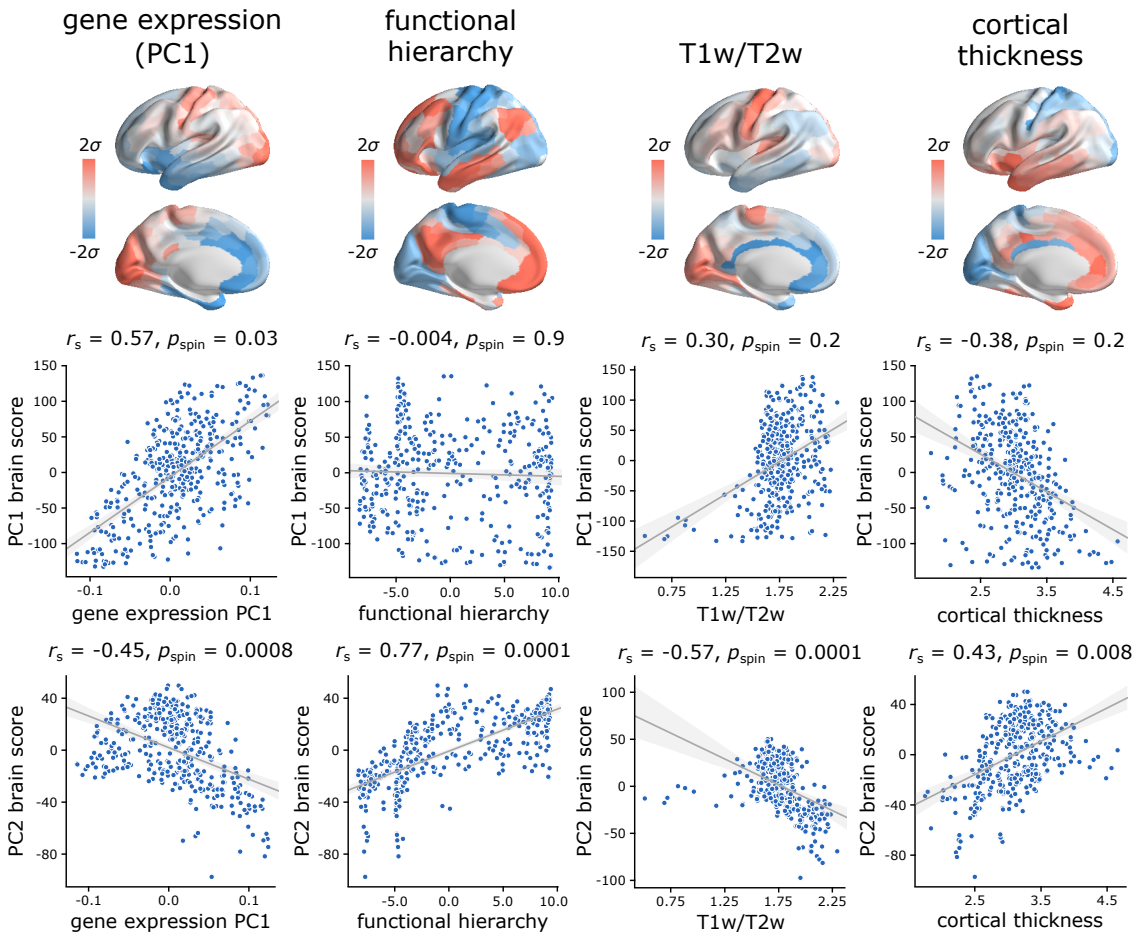

Figure 4.4: **Hierarchical organization of intrinsic dynamics** | PC1 and PC2 brain score patterns are compared with four molecular, microstructural and functional maps. These maps include the first principal component of microarray gene expression data from the Allen Human Brain Atlas (Burt et al., 2018; Hawrylycz et al., 2012), the first (principal) gradient of functional connectivity estimated using diffusion map embedding (Coifman et al., 2005; Langs et al., 2015; Margulies et al., 2016), group-average T1w/T2w ratio, and group-average cortical thickness. The three latter indices were computed from the HCP dataset (Van Essen et al., 2013). Statistical significance of the reported Spearman rank correlation r_s is assessed using 10,000 spatial permutations tests, preserving the spatial autocorrelation in the data ("spin tests"; (Alexander-Bloch et al., 2018)). Linear regression lines are added to the scatter plots for visualization purposes only.

from the Allen Institute Human Brain Atlas (Burt et al., 2018; Hawrylycz et al., 2012) using PCA analysis, (2) the principal gradient of functional connectivity estimated using diffusion map embedding (Coifman et al., 2005; Langs et al., 2015; Margulies et al., 2016) (`https://github.com/satra/mapalign`), (3) T1w/T2w ratio, a putative proxy for intracortical myelin (Huntenburg et al., 2017), (4) cortical thickness (Wagstyl et al., 2015). We use Spearman rank correlations (r_s) throughout, as they do not assume a linear relationship among variables. Given the spatially autocorrelated nature of both `hctsa` features and

other imaging features, we assess statistical significance with respect to nonparametric spatial autocorrelation-preserving null models (Alexander-Bloch et al., 2018; Markello and Misic, 2020).

PC1 topography is correlated with the first principal component of gene expression ($r_s = 0.57$, $p_{spin} = 0.03$), but no other attributes. PC2 topography is significantly correlated with the first principal component of gene expression ($r_s = -0.45$, $p_{spin} = 0.0008$), with the principal gradient of functional connectivity ($r_s = 0.77$, $p_{spin} = 0.0001$), with T1w/T2w ratio ($r_s = -0.57$, $p_{spin} = 0.0001$), and with cortical thickness ($r_s = 0.43$, $p_{spin} = 0.008$). Altogether, the two topographic gradients of intrinsic dynamics closely mirror molecular and microstructural gradients, suggesting a link between regional structural properties and regional dynamical properties. Figure S4.4 further confirms this intuition, showing the mean score of each component for three well-known cortical partitions, including intrinsic functional networks (Schaefer et al., 2018; Yeo et al., 2011), cytoarchitectonic classes (Economo and Koskinas, 1925; Economo et al., 2008; Vértes et al., 2016) and laminar differentiation levels (Mesulam, 2000).

For completeness, we also tested associations with two maps that were previously related to cortical hierarchies: evolutionary expansion (indexing enlargement of cortical areas in the human relative to the macaque) (Baum et al., 2020; Hill et al., 2010) and node-wise functional participation coefficient (indexing the diversity of a node's links) (Baum et al., 2020; Bertolero et al., 2017). PC2 is significantly correlated with evolutionary expansion ($r_s = 0.52$, $p_{spin} = 0.0002$), but neither component is correlated with participation coefficient (Figure S4.5).

4.4.4 Spatial gradients of intrinsic dynamics support distinct functional activations

Given that topographic patterns of intrinsic dynamics run parallel to microstructural and functional gradients, and are marked by specific time-series features, we next asked whether these topographic patterns of intrinsic dynamics are related to patterns of functional activation and psychological processes. To address this question, we used Neurosynth to derive probability maps for multiple psychological terms (Yarkoni et al., 2011). The term set was restricted to those in the intersection of terms reported in Neurosynth and in the Cognitive Atlas (Poldrack et al., 2011), yielding a total of 123 terms (Table S4.2). Each term map was correlated with the PC1 and PC2 score maps to identify topographic

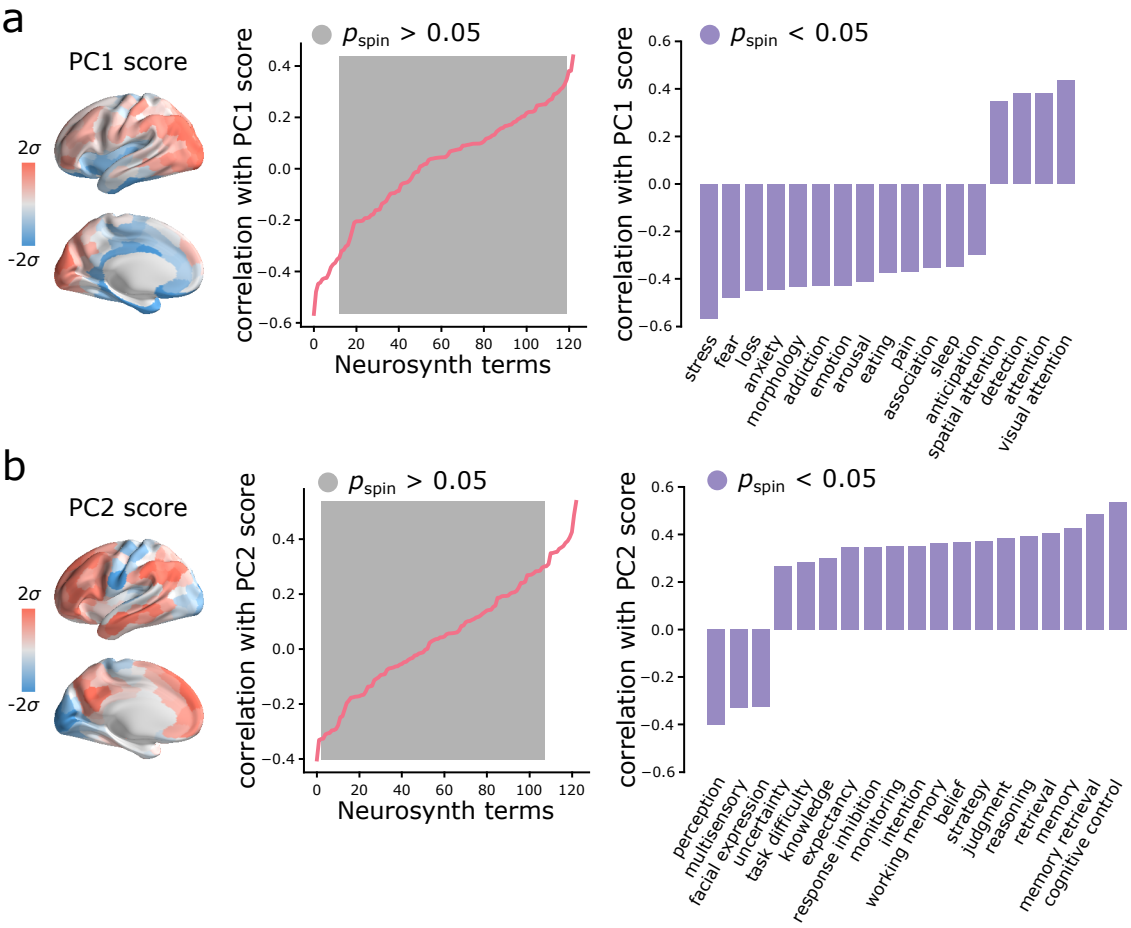

Figure 4.5: **Spatial gradients of intrinsic dynamics support distinct functional activations** | We used Neurosynth to derive probability maps for multiple psychological terms (Yarkoni et al., 2011). The term set was restricted to those in the intersection of terms reported in Neurosynth and in the Cognitive Atlas (Poldrack et al., 2011), yielding a total of 123 terms (Supplementary File S4.2). Each term map was correlated with the PC1 (a) and PC2 (b) score maps to identify topographic distributions of psychological terms that most closely correspond to patterns of intrinsic dynamics. Grey indicates non-significance based on 10,000 spatial permutation tests (Bonferroni correction, $\alpha = 0.05$). Statistically significant terms are shown on the right.

distributions of psychological terms that most closely correspond to patterns of intrinsic dynamics (Bonferroni corrected, $\alpha = 0.05$; Figure 4.5). Consistent with the intuition developed from comparisons with intrinsic networks, PC1 intrinsic dynamics mainly defined a cognitive-affective axis (e.g. "attention" *versus* "stress", "fear", "loss", "emotion"; Figure 4.5a), while PC2 dynamics defined a sensory-cognitive axis (e.g. "perception", "multisensory", "facial expression" *versus* "cognitive control", "memory retrieval", "reasoning"; Figure 4.5b).

4.4.5 Sensitivity and replication analyses

As a final step, we sought to assess the extent to which the present findings are replicable under alternative processing choices and in other samples (Figure 4.6). For all comparisons, we correlated PC1 and PC2 scores and weights obtained in the original analysis and in each new analysis. Significance was assessed using spatial autocorrelation preserving nulls as before. We first replicated the results in individual subjects in the *Discovery* sample by applying PCA to individual region $\times$ feature matrices and aligning PCA results through an iterative process using Procrustes rotations (`https://github.com/satra/mapalign` (Langs et al., 2015)). The mean individual-level PC scores and weights were then compared to the original findings (Figure 4.6a). We next replicated the results by repeating the analysis after grey-matter signal regression (similar to global signal regression as the global signal is shown to be a grey-matter specific signal following sICA+FIX) (Glasser et al., 2016, 2018), with near identical results (Figure 4.6b). To assess the extent to which results are influenced by choice of parcellation, we repeated the analysis using the 68-region Desikan-Killiany anatomical atlas (Desikan et al., 2006), which were then further divided into 200 approximately equally-sized cortical areas. Again, we find near-identical results (Figure 4.6c).

In the last two analyses we focused on out-of-sample validation. We first repeated the analysis on the held-out *Validation* sample of $n = 127$ unrelated HCP subjects, with similar results (Figure 4.6d). Finally, we repeated the analysis using data from the independently collected Midnight Scan Club (MSC) dataset, again finding highly consistent results (Figure 4.6e).

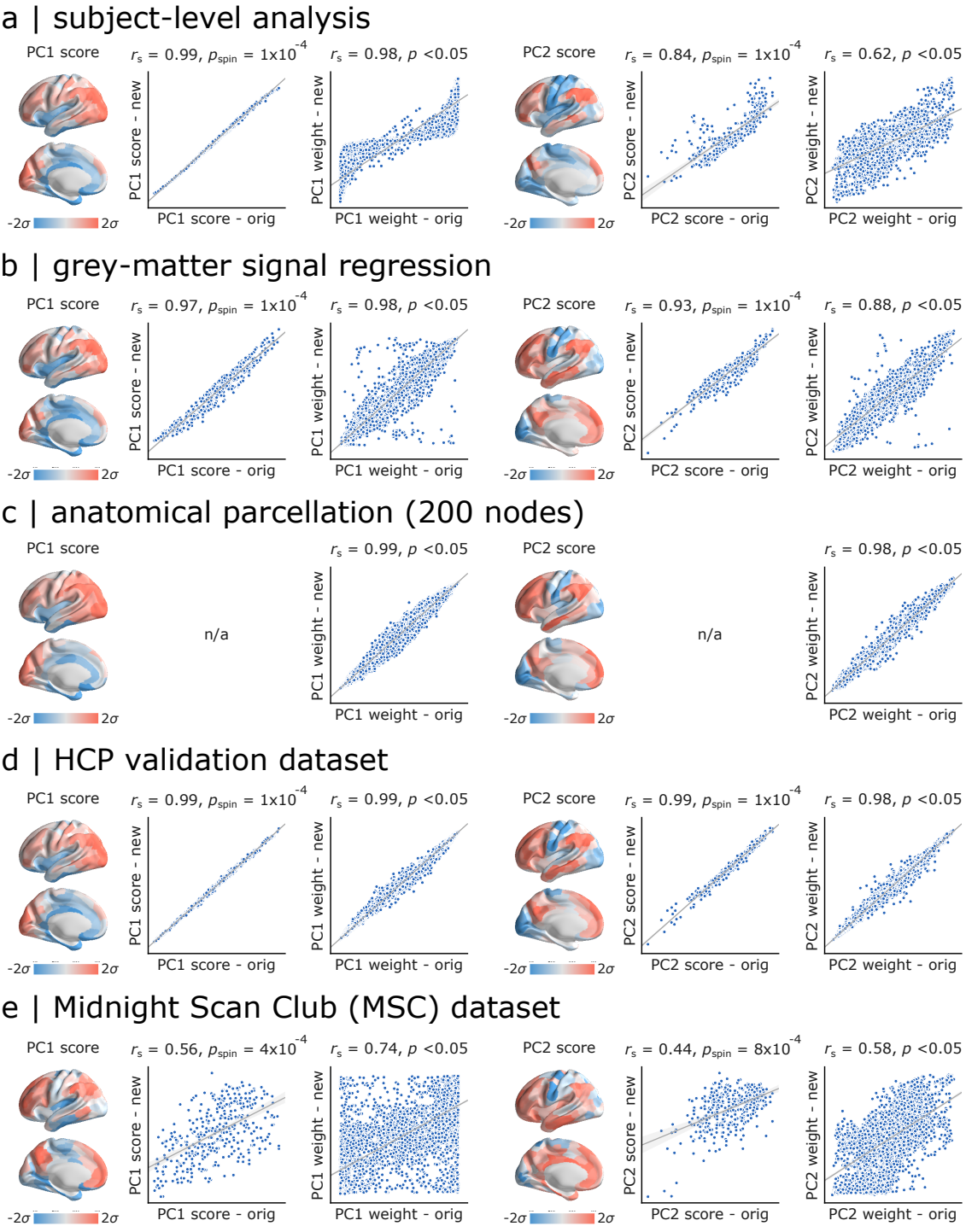

Figure 4.6: **Sensitivity and replication analyses** | For all comparisons, we correlated PC1 and PC2 scores and weights obtained in the original analysis and in each new analysis. Significance was assessed using spatial autocorrelation preserving nulls. Specific analyses include: (a) comparing group-level and individual subject-level results, (b) comparing data with and without grey-matter signal regression, (c) comparing functional (Schaefer) and anatomical parcellations (Desikan-Killiany), (d) comparing HCP *Discovery* and *Validation* datasets, (e) comparing HCP *Discovery* and Midnight Scan Club datasets.

4.5 Discussion

In the present report, we comprehensively characterize intrinsic dynamics across the cortex, identifying two robust spatial patterns of time-series features. The patterns, capturing spatial variation in signal autocorrelation and dynamic range, follow microscale gradients and macroscale network architecture. Importantly, the two patterns underlie distinct psychological axes, demonstrating a link between brain architecture, intrinsic dynamics, and cognition. These findings are robust against a wide range of methodological choices and were validated in two held-out samples.

Our results demonstrate that regional haemodynamic activity, often overlooked in favour of electrophysiological measurements with greater temporal resolution, possesses a rich dynamic signature (Bolt et al., 2018; Garrett et al., 2013; Li et al., 2019; Lurie et al., 2020; Preti et al., 2017; Uddin, 2020). While multiple reports have suggested the existence of a timescale or temporal receptive window hierarchy (Golesorkhi et al., 2020; Hasson et al., 2008; Honey et al., 2012; Ito et al., 2020; Kiebel et al., 2008; Murray et al., 2014; Watanabe et al., 2019), these investigations typically involved (a) incomplete spatial coverage, making it difficult to quantitatively assess correspondence with other microscale and macroscale maps, and (b) *a priori* measures of interest, such as spectral power or temporal autocorrelation, potentially obscuring other important dynamical features. Here we comprehensively benchmark the entire dynamic profile of the brain, by near-exhaustively estimating 6000+ features from the wider time-series literature. We identify a much broader spectrum of time-series features that relate to microstructure, connectivity and behavior. As we discuss below, feature-based time-series phenotyping offers a powerful, fundamentally new and entirely data-driven method to quantify and articulate neural dynamics.

Applying a data-driven feature extraction method to high-resolution BOLD fMRI, we decompose regional signals into two intrinsic modes, with distinct topographic organization and time-series features. One pattern, characterized by variation in signal autocorrelation, follows a ventromedial-dorsolateral gradient, separating the limbic and paralimibic systems from posterior parietal cortex. Another pattern, characterized by dynamic range, follows a unimodal-transmodal gradient, separating primary sensorymotor cortices from association cortex. The first is closely associated with gene expression PC1 (itself closely related to cell type composition, synaptic physiology and cortical cytoarchitecture (Burt et al., 2018)), suggesting a molecular and cellular basis for regional differences in temporal autocorrelation. The second is closely associated with the principal

functional gradient, as well as with intracortical myelin and cortical thickness, suggesting that the dynamic range of BOLD signals is related to regional variation in macroscale circuit organization. Taken together, we find evidence that molecular and cellular properties (gene expression PC1) relate to regional autocorrelation, while micro-circuit properties (T1w/T2w, cortical thickness) and macroscale network embedding (principal functional gradient) relate to regional dynamic range.

An emerging literature emphasizes the hierarchical organization of neural systems, whereby systematic variation in laminar architecture across the cortical sheet is mirrored by multiple cytological properties, including neuron density, spine count, branching and neurotransmitter receptor profiles (Hilgetag and Goulas, 2020; Margulies et al., 2016; Mesulam, 1998). These variations manifest as spatially ordered gradients of structural and functional attributes (Huntenburg et al., 2018), including gene expression (Burt et al., 2018; Fulcher et al., 2019; Hansen et al., 2020), cortical thickness (Wagstyl et al., 2015), intracortical myelin (Huntenburg et al., 2017), laminar differentiation (Paquola et al., 2019; Wagstyl et al., 2020) and excitability (Demirtaş et al., 2019; Markicevic et al., 2020; Straub et al., 2020; Wang, 2020). Indeed, we find that the two patterns of intrinsic dynamics are closely related to gene expression, intracortical myelin and cortical thickness. Our results build on this literature, demonstrating that microscale and connectional hierarchies leave an indelible mark on intrinsic dynamics (Lurie and D'Esposito, 2020), perhaps through variation in local excitability (Deco et al., 2020; Demirtaş et al., 2019; Wang et al., 2019; Wang, 2020). How these patterns are related to underlying cell types and subcortical afferent input – in particular, thalamocortical feedback – is an important ongoing question (Abeysuriya et al., 2015; Garrett et al., 2018; Muller et al., 2020; Paquola et al., 2020; Shine et al., 2019; Wang et al., 2019).

Importantly, the two patterns are related to two dominant axes of meta-analytic functional activation. We show that topographic variations in microcircuitry and connectomic embedding yield variations in intrinsic dynamics and may explain regional differences in functional specialization. The ventromedial-dorsolateral autocorrelation pattern differentiates affective versus cognitive activation (mainly visual cognition and visuo-spatial attention), whereas the unimodal-transmodal dynamic range pattern differentiates primary sensory versus higher-order cognitive processing. Collectively, these results provide evidence that local computations reflect systematic variation in multiple anatomical circuit properties, and can be measured as unique temporal signatures in regional activity and patterns of functional specialization.

More generally, the present findings are part of a larger trend in the field to understand

structure-function relationships by considering molecular (Anderson et al., 2018; Fulcher and Fornito, 2016; Richiardi et al., 2015; Zheng et al., 2019), cellular (Anderson et al., 2020; Muller et al., 2020; Scholtens et al., 2014; Shafiei et al., 2020a) and physiological (Fallon et al., 2020; Sethi et al., 2017) attributes of network nodes, thereby conceptually linking local and global brain organization (Khambhati et al., 2018; Suárez et al., 2020). In such "annotated networks", macroscale network architecture is thought to reflect similarity in local properties, and *vice versa*, such that areas with similar properties are more likely to be anatomically connected and to functionally interact with one another (Beul et al., 2017; Goulas et al., 2019; Hilgetag et al., 2019; Wei et al., 2018). Indeed, we find that two regions are more likely to display similar intrinsic dynamics if they are anatomically connected and if they are part of the same functional community, suggesting that network organization and local intrinsic dynamics are intertwined (Cocchi et al., 2016; Gollo et al., 2015). A significant corollary of the present work is that functional connectivity – presently conceptualized as coherent fluctuations in neural activity and operationalized as correlated BOLD values over time – misses out on an important set of inter-regional relationships. Namely, two regions may display identical time-series profiles, suggesting common circuit dynamics and function, but unless they also display time-locked activity, current methods would miss out on this potentially biologically meaningful inter-regional relationship.

The present results are consistent with contemporary theories linking brain structure and function, but they must be interpreted with respect to several methodological caveats. First, all analyses were performed on BOLD time-series with lower sampling rate compared to electromagnetic recordings, potentially obscuring more subtle dynamics occurring on faster timescales. To mitigate this concern, all analyses were performed in high-resolution multiband HCP data with multiple runs, and replicated in MSC data, but in principle, these analyses could be repeated and validated in magnetoencephalographic recordings (Watanabe et al., 2019). Second, all analyses were performed on haemodynamic time courses that may not completely reflect the underlying neuronal population dynamics. Despite this caveat, we observe a close correspondence between the isolated patterns of intrinsic dynamics and molecular, structural, functional, and psychological gradients. Third, the pattern of temporal signal-to-noise ratio in the BOLD is known to be non-uniform, but it is not correlated with the intrinsic dynamics patterns observed in the present report. Fourth, the analysis included all features from `hctsa`, potentially biasing results towards specific properties of BOLD signals. We attempted to mitigate this challenge by applying PCA to directly examine correlation patterns among features, but PCA components may still lend greater weight to over-represented feature classes (Fulcher

et al., 2013). This may obscure the contribution of under-represented feature classes, and should be investigated further in future work.

Altogether, the present results point towards highly patterned intrinsic dynamics across the neocortex. These patterns reflect prominent molecular and microstructural gradients, as well as macroscale structural and functional organization. Importantly, spatial variation of intrinsic dynamics parallels spatial variation of meta-analytic cognitive functional activation. These findings demonstrate that structural organization of the brain shapes patterns of intrinsic dynamics, ultimately manifesting as distinct axes of psychological processes.

4.6 Methods

4.6.1 Dataset: Human Connectome Project (HCP)

Following the procedure described in (Wael et al., 2018), we obtained structural and functional magnetic resonance imaging (MRI) data of two sets of healthy young adults (age range 22-35 years) with no familial relationships (neither within nor between sets) as *Discovery* ($n = 201$) and *Validation* ($n = 127$) sets from Human Connectome Project (HCP; S900 release (Van Essen et al., 2013)). All four resting state fMRI scans (two scans (R/L and L/R phase encoding directions) on day 1 and two scans (R/L and L/R phase encoding directions) on day 2, each about 15 minutes long; $TR = 720$ ms), as well as structural MRI and diffusion weighted imaging (DWI) data were available for all participants.

4.6.2 HCP Data Processing

All the structural and functional MRI data were pre-processed using HCP minimal pre-processing pipelines (Glasser et al., 2013; Van Essen et al., 2013). We provide a brief description of data pre-processing below, while detailed information regarding data acquisition and pre-processing is available elsewhere (Glasser et al., 2013; Van Essen et al., 2013). The procedure was separately repeated for *Discovery* and *Validation* sets.

4.6.2.1 Structural MRI

T1- and T2- weighted MR images were corrected for gradient nonlinearity, and when available, the images were co-registered and averaged across repeated scans for each individual. The corrected T1w and T2w images were co-registered and cortical surfaces

were extracted using FreeSurfer 5.3.0-HCP (Dale et al., 1999; Fischl et al., 1999; Wael et al., 2018). For each individual, cortical thickness was estimated as the difference between pial and white matter surfaces and T1w/T2w ratio was calculated as a putative proxy for intracortical myelin content. The pre-processed data were parcellated into 400 cortical areas using Schaefer parcellation (Schaefer et al., 2018).

4.6.2.2 Resting state functional MRI

All 3T functional MRI time-series were corrected for gradient nonlinearity, head motion using a rigid body transformation, and geometric distortions using scan pairs with opposite phase encoding directions (R/L, L/R) (Wael et al., 2018). Further pre-processing steps include co-registration of the corrected images to the T1w structural MR images, brain extraction, normalization of whole brain intensity, high-pass filtering ($>$ 2000s FWHM; to correct for scanner drifts), and removing additional noise using the ICA-FIX process (Salimi-Khorshidi et al., 2014; Wael et al., 2018). The pre-processed time-series were then parcellated into 400 areas as described above. The parcellated time-series were used to construct functional connectivity matrices as a Pearson correlation coefficient between pairs of regional time-series for each of the four scans of each participant. A group-average functional connectivity matrix was constructed as the mean functional connectivity across all individuals and scans.

4.6.2.3 Diffusion weighted imaging (DWI)

DWI data was pre-processed using the MRtrix3 package (Tournier et al., 2019) (https://www.mrtrix.org/). More specifically, fiber orientation distributions were generated using the multi-shell multi-tissue constrained spherical deconvolution algorithm from MRtrix (Dhollander et al., 2016; Jeurissen et al., 2014). White matter edges were then reconstructed using probabilistic streamline tractography based on the generated fiber orientation distributions (Tournier et al., 2010). The tract weights were then optimized by estimating an appropriate cross-section multiplier for each streamline following the procedure proposed by Smith and colleagues (Smith et al., 2015) and a connectivity matrix was built for each participant using the same parcellation as described above. Finally, we used a consensus approach to construct a binary group-level structural connectivity matrix, preserving the edge length distribution in individual participants (Betzel et al., 2018; Mišić et al., 2015, 2018; Shafiei et al., 2020a).

4.6.3 Replication dataset: Midnight Scan Club (MSC)

We used resting state fMRI data of $n = 10$ healthy young adults, each with 10 scan sessions of about 30 minutes long, from Midnight Scan Club (MSC (Gordon et al., 2017)) dataset as an independent replication dataset. Details about the participants, MRI acquisition, and data pre-processing are provided by Gordon and colleagues elsewhere (Gordon et al., 2017). We obtained the surface-based, pre-processed resting state fMRI time courses in CIFTI format through OpenNeuro (https://openneuro.org/datasets/ds000224/versions/1.0.0). The pre-processing steps include motion correction and global signal regression (Gordon et al., 2017). Following the pre-processing methods suggested by Gordon and colleagues (Gordon et al., 2017), we smoothed the surface-level time-series data with geodesic 2D Gaussian kernels ($\sigma = 2.55$mm) using the Connectome Workbench (Marcus et al., 2011). Finally, we censored the motion-contaminated frames of time-series for each participant separately, using the temporal masks provided with the dataset. The pre-processed data were parcellated into 400 cortical regions using Schaefer parcellation (Schaefer et al., 2018). One participant (MSC08) was excluded from subsequent analysis due to low data reliability and self-reported sleep as described in (Gordon et al., 2017). The parcellated time-series were then subjected to the same analyses that were performed on the HCP *Discovery* and *Validation* datasets.

4.6.4 Microarray expression data: Allen Human Brain Atlas (AHBA)

Regional microarray expression data were obtained from six post-mortem brains provided by the Allen Human Brain Atlas (AHBA; http://human.brain-map.org/) (Hawrylycz et al., 2012). We used the `abagen` (https://github.com/netneurolab/abagen) toolbox to process and map the data to 400 parcellated brain regions from Schaefer parcellation (Schaefer et al., 2018).

Briefly, genetic probes were reannotated using information provided by (Arnatkevičiūtė et al., 2019) instead of the default probe information from the AHBA dataset. Using reannotated information discards probes that cannot be reliably matched to genes. The reannotated probes were filtered based on their intensity relative to background noise levels (Quackenbush, 2002); probes with intensity less than background in $\geq$50% of samples were discarded. A single probe with the highest differential stability, $\Delta_S(p)$, was selected to represent each gene (Hawrylycz et al., 2015), where differential stability was calculated as:

$$\Delta_S(p) = \frac{1}{\binom{N}{2}} \sum_{i=1}^{N-1} \sum_{j=i+1}^{N} \rho[B_i(p), B_j(p)] \tag{4.1}$$

Here, ρ is Spearman's rank correlation of the expression of a single probe p across regions in two donor brains, B_i and B_j, and N is the total number of donor brains. This procedure retained 15,656 probes, each representing a unique gene.

Next, tissue samples were mirrored across left and right hemispheres (Romero-Garcia et al., 2018) and then assigned to brain regions using their corrected MNI coordinates (`https://github.com/chrisfilo/alleninf`) by finding the nearest region, up to 2mm away. To reduce the potential for misassignment, sample-to-region matching was constrained by hemisphere and cortical/subcortical divisions (Arnatkevičiūtė et al., 2019). If a brain region was not assigned any sample based on the above procedure, the sample closest to the centroid of that region was selected in order to ensure that all brain regions were assigned a value. Samples assigned to the same brain region were averaged separately for each donor. Gene expression values were then normalized separately for each donor across regions using a robust sigmoid function and rescaled to the unit interval (Fulcher and Fornito, 2016). Scaled expression profiles were finally averaged across donors, resulting in a single matrix with rows corresponding to brain regions and columns corresponding to the retained 15,656 genes. The expression values of 1,906 brain-specific genes were used for further analysis (Burt et al., 2018).

4.6.5 Massive temporal feature extraction using `hctsa`

We used the highly comparative time-series analysis toolbox, `hctsa` (Fulcher and Jones, 2017; Fulcher et al., 2013), to perform a massive feature extraction of the time-series of each brain area for each participant. The `hctsa` package extracted over 7,000 local time-series features using a wide range of operations based on time-series analysis (Fulcher and Jones, 2017; Fulcher et al., 2013). The extracted features include, but are not limited to, distributional properties, entropy and variability, autocorrelation, time-delay embeddings, and nonlinear properties of a given time-series (Fulcher, 2018; Fulcher et al., 2013).

The `hctsa` feature extraction analysis was performed on the parcellated fMRI time-series of each run and each participant separately (Figure 4.1). Following the feature extraction procedure, the outputs of the operations that produced errors were removed and the remaining features (6,441 features) were normalized across nodes using an outlier-robust sigmoidal transform. We used Pearson correlation coefficients to measure the pairwise similarity between the time-series features of all possible combinations of brain

areas. As a result, a temporal profile similarity network was constructed for each individual and each run, representing the strength of the similarity of the local temporal fingerprints of brain areas (Figure 4.1). The resulting similarity matrices were then compared to the underlying functional and structural brain networks.

4.6.6 Neurosynth

Functional activation probability maps were obtained for multiple psychological terms using Neurosynth (Yarkoni et al., 2011) (`https://github.com/neurosynth/neurosynth`). Probability maps were restricted to those for terms present in both Neurosynth and the Cognitive Atlas (Poldrack et al., 2011), yielding a total of 123 maps (Supplementary File S4.2). We used the volumetric "association test" (i.e. reverse inference) maps, which were projected to the FreeSurfer *fsaverage5* mid-grey surface with nearest neighbor interpolation using Freesurfer's `mri_vol2surf` function (v6.0.0; `http://surfer.nmr.mgh.harvard.edu/`). The resulting surface maps were then parcellated to 400 cortical regions using the Schaefer parcellation (Schaefer et al., 2018).

4.6.7 Null model

A consistent question in the present work is the topographic correlation between time-series features and other features of interest. To make inferences about these links, we implement a null model that systematically disrupts the relationship between two topographic maps but preserves their spatial autocorrelation (Alexander-Bloch et al., 2018; Markello and Misic, 2020) (see also (Burt et al., 2018, 2020) for an alternative approach). For the anatomical atlas, we first created a surface-based representation of the Cammoun atlas on the FreeSurfer fsaverage surface using the Connectome Mapper toolkit (`https://github.com/LTS5/cmp`; (Daducci et al., 2012)). For the functional atlas, we used the Schaefer-400 atlas in the HCP's fsLR32k grayordinate space (Schaefer et al., 2018; Van Essen et al., 2013). We then used the spherical projection of the surfaces to define spatial coordinates for each parcel by selecting the vertex closest to the center-of-mass of each parcel (Shafiei et al., 2020a; Vázquez-Rodríguez et al., 2019; Vazquez-Rodriguez et al., 2020). The resulting spatial coordinates were used to generate null models by applying randomly-sampled rotations and reassigning node values based on the closest resulting parcel (10,000 repetitions). The rotation was applied to one hemisphere and then mirrored to the other hemisphere.

4.7 Acknowledgments

We thank Vincent Bazinet, Justine Hansen, Estefany Suarez, Bertha Vazquez-Rodriguez and Zhen-Qi Liu for helpful comments and stimulating discussion. This research was undertaken thanks in part to funding from the Canada First Research Excellence Fund, awarded to McGill University for the Healthy Brains for Healthy Lives initiative. BM acknowledges support from the Natural Sciences and Engineering Research Council of Canada (NSERC Discovery Grant RGPIN #017-04265) and from the Canada Research Chairs Program. GS acknowledges support from the Natural Sciences and Engineering Research Council of Canada (NSERC).

4.8 Bibliography

Abeysuriya, R., C. Rennie, and P. Robinson (2015). "Physiologically based arousal state estimation and dynamics". *J Neurosci Meth*, 253, pp. 55–69.

Abraham, A. et al. (2014). "Machine learning for neuroimaging with scikit-learn". *Frontiers in neuroinformatics*, 8, p. 14.

Alexander-Bloch, A. F. et al. (2018). "On testing for spatial correspondence between maps of human brain structure and function". *Neuroimage*, 178, pp. 540–551.

Anderson, K. M. et al. (2018). "Gene expression links functional networks across cortex and striatum". *Nat Commun*, 9(1), pp. 1–14.

Anderson, K. M. et al. (2020). "Transcriptional and imaging-genetic association of cortical interneurons, brain function, and schizophrenia risk". *Nat Commun*, 11(1), pp. 1–15.

Arnatkevičiūtė, A., B. D. Fulcher, and A. Fornito (2019). "A practical guide to linking brain-wide gene expression and neuroimaging data". *Neuroimage*, 189, pp. 353–367.

Avena-Koenigsberger, A., B. Misic, and O. Sporns (2018). "Communication dynamics in complex brain networks". *Nat Rev Neurosci*, 19(1), p. 17.

Azen, R. and D. V. Budescu (2003). "The dominance analysis approach for comparing predictors in multiple regression." *Psychological methods*, 8(2), p. 129.

Baldassano, C. et al. (2017). "Discovering event structure in continuous narrative perception and memory". *Neuron*, 95(3), pp. 709–721.

Baum, G. L. et al. (2020). "Development of structure–function coupling in human brain networks during youth". *Proceedings of the National Academy of Sciences*, 117(1), pp. 771–778.

Bazinet, V. et al. (2020). "Multiscale communication in cortico-cortical networks". *bioRxiv*.

Benjamini, Y. and Y. Hochberg (1995). "Controlling the false discovery rate: a practical and powerful approach to multiple testing". *Journal of the Royal statistical society: series B (Methodological)*, 57(1), pp. 289–300.

Bertolero, M. A., B. T. Yeo, and M. D'Esposito (2017). "The diverse club". *Nature communications*, 8(1), pp. 1–11.

Betzel, R. F. and D. S. Bassett (2018). "Specificity and robustness of long-distance connections in weighted, interareal connectomes". *Proceedings of the National Academy of Sciences*, 115(21), E4880–E4889.

Betzel, R. F. et al. (2018). "Distance-dependent consensus thresholds for generating group-representative structural brain networks". *Network Neuroscience*, pp. 1–22.

Beul, S. F., H. Barbas, and C. C. Hilgetag (2017). "A predictive structural model of the primate connectome". *Sci Rep*, 7(1), pp. 1–12.

Bolt, T., M. L. Anderson, and L. Q. Uddin (2018). "Beyond the evoked/intrinsic neural process dichotomy". *Net Neurosci*, 2(1), pp. 1–22.

Breakspear, M. (2017). "Dynamic models of large-scale brain activity". *Nature neuroscience*, 20(3), pp. 340–352.

Budescu, D. V. (1993). "Dominance analysis: a new approach to the problem of relative importance of predictors in multiple regression." *Psychological bulletin*, 114(3), p. 542.

Burt, J. B. et al. (2018). "Hierarchy of transcriptomic specialization across human cortex captured by structural neuroimaging topography". *Nat Neurosci*, 21(9), pp. 1251–1259.

Burt, J. B. et al. (2020). "Generative modeling of brain maps with spatial autocorrelation". *NeuroImage*.

Burzynska, A. Z. et al. (2013). "A scaffold for efficiency in the human brain". *J Neurosci*, 33(43), pp. 17150–17159.

Chaudhuri, R. et al. (2015). "A large-scale circuit mechanism for hierarchical dynamical processing in the primate cortex". *Neuron*, 88(2), pp. 419–431.

Chien, H.-Y. S. and C. J. Honey (2020). "Constructing and forgetting temporal context in the human cerebral cortex". *Neuron*.

Cocchi, L. et al. (2016). "A hierarchy of timescales explains distinct effects of local inhibition of primary visual cortex and frontal eye fields". *eLife*, 5, e15252.

Coifman, R. R. et al. (2005). "Geometric diffusions as a tool for harmonic analysis and structure definition of data: Diffusion maps". *Proc Natl Acad Sci USA*, 102(21), pp. 7426–7431.

Daducci, A. et al. (2012). "The connectome mapper: an open-source processing pipeline to map connectomes with MRI". *PloS one*, 7(12).

Dale, A. M., B. Fischl, and M. I. Sereno (1999). "Cortical surface-based analysis: I. Segmentation and surface reconstruction". *Neuroimage*, 9(2), pp. 179–194.

Deco, G. et al. (2020). "Dynamical consequences of regional heterogeneity in the brains transcriptional landscape". *bioRxiv*.

Demirtaş, M. et al. (2019). "Hierarchical heterogeneity across human cortex shapes large-scale neural dynamics". *Neuron*, 101(6), pp. 1181–1194.

Desikan, R. S. et al. (2006). "An automated labeling system for subdividing the human cerebral cortex on MRI scans into gyral based regions of interest". *Neuroimage*, 31(3), pp. 968–980.

Dhollander, T., D. Raffelt, and A. Connelly (2016). "Unsupervised 3-tissue response function estimation from single-shell or multi-shell diffusion MR data without a co-registered T1 image". In: *ISMRM Workshop on Breaking the Barriers of Diffusion MRI*. Vol. 5.

Economo, C. F. von and G. N. Koskinas (1925). *Die cytoarchitektonik der hirnrinde des erwachsenen menschen*. J. Springer.

Economo, C. F. von, G. N. Koskinas, and L. C. Triarhou (2008). *Atlas of cytoarchitectonics of the adult human cerebral cortex*. Vol. 10. Karger Basel.

Fallon, J. et al. (2020). "Timescales of spontaneous fMRI fluctuations relate to structural connectivity in the brain". *Network Neuroscience*, 4(3), pp. 788–806.

Fischl, B., M. I. Sereno, and A. M. Dale (1999). "Cortical surface-based analysis: II: inflation, flattening, and a surface-based coordinate system". *Neuroimage*, 9(2), pp. 195–207.

Fulcher, B. D. (2018). "Feature-based time-series analysis". In: *Feature Engineering for Machine Learning and Data Analytics*. CRC Press, pp. 87–116.

Fulcher, B. D. and A. Fornito (2016). "A transcriptional signature of hub connectivity in the mouse connectome". *Proceedings of the National Academy of Sciences*, 113(5), pp. 1435–1440.

Fulcher, B. D. and N. S. Jones (2017). "hctsa: A computational framework for automated time-series phenotyping using massive feature extraction". *Cell systems*, 5(5), pp. 527–531.

Fulcher, B. D., M. A. Little, and N. S. Jones (2013). "Highly comparative time-series analysis: the empirical structure of time series and their methods". *Journal of the Royal Society Interface*, 10(83), p. 20130048.

Fulcher, B. D. et al. (2019). "Multimodal gradients across mouse cortex". *Proc Natl Acad Sci USA*, 116(10), pp. 4689–4695.

Gao, R. et al. (2020). "Neuronal timescales are functionally dynamic and shaped by cortical microarchitecture". *Elife*, 9, e61277.

Garrett, D., S. Epp, and U. Lindenberger (2017). "Local temporal variability reflects functional network integration in the human brain: On the crucial role of the thalamus". *NeuroImage*, p. 184739.

Garrett, D. D. et al. (2013). "Moment-to-moment brain signal variability: A next frontier in human brain mapping?" *Neuroscience & Biobehavioral Reviews*, 37(4), pp. 610–624.

Garrett, D. D. et al. (2018). "Local temporal variability reflects functional integration in the human brain". *Neuroimage*, 183, pp. 776–787.

Glasser, M. F. et al. (2013). "The minimal preprocessing pipelines for the Human Connectome Project". *Neuroimage*, 80, pp. 105–124.

Glasser, M. F. et al. (2016). "The human connectome project's neuroimaging approach". *Nature neuroscience*, 19(9), p. 1175.

Glasser, M. F. et al. (2018). "Using temporal ICA to selectively remove global noise while preserving global signal in functional MRI data". *NeuroImage*, 181, pp. 692–717.

Golesorkhi, M. et al. (2020). "Time meets space: brain dynamics drive spatial topography". *bioRxiv*.

Gollo, L. L. et al. (2015). "Dwelling quietly in the rich club: brain network determinants of slow cortical fluctuations". *Phil Trans R Soc B*, 370(1668), p. 20140165.

Gordon, E. M. et al. (2017). "Precision functional mapping of individual human brains". *Neuron*, 95(4), pp. 791–807.

Goulas, A. et al. (2019). "A blueprint of mammalian cortical connectomes". *PLoS Biol*, 17(3), e2005346.

Hansen, J. Y. et al. (2020). "Molecular signatures of cognition and affect". *bioRxiv*.

Hasson, U. et al. (2008). "A hierarchy of temporal receptive windows in human cortex". *J Neurosci*, 28(10), pp. 2539–2550.

Hawrylycz, M. et al. (2015). "Canonical genetic signatures of the adult human brain". *Nature neuroscience*, 18(12), p. 1832.

Hawrylycz, M. J. et al. (2012). "An anatomically comprehensive atlas of the adult human brain transcriptome". *Nature*, 489(7416), p. 391.

Hilgetag, C. C. and A. Goulas (2020). "'Hierarchy'in the organization of brain networks". *Philos Trans R Soc B*, 375(1796), p. 20190319.

Hilgetag, C. C. et al. (2019). "An architectonic type principle integrates macroscopic cortico-cortical connections with intrinsic cortical circuits of the primate brain". *Net Neurosci*, 3(4), pp. 905–923.

Hill, J. et al. (2010). "Similar patterns of cortical expansion during human development and evolution". *Proceedings of the National Academy of Sciences*, 107(29), pp. 13135–13140.

Honey, C. J. et al. (2012). "Slow cortical dynamics and the accumulation of information over long timescales". *Neuron*, 76(2), pp. 423–434.

Huntenburg, J. M., P.-L. Bazin, and D. S. Margulies (2018). "Large-scale gradients in human cortical organization". *Trends in cognitive sciences*, 22(1), pp. 21–31.

Huntenburg, J. M. et al. (2017). "A systematic relationship between functional connectivity and intracortical myelin in the human cerebral cortex". *Cereb Cortex*, 27(2), pp. 981–997.

Ito, T., L. J. Hearne, and M. W. Cole (2020). "A cortical hierarchy of localized and distributed processes revealed via dissociation of task activations, connectivity changes, and intrinsic timescales". *NeuroImage*, 221, p. 117141.

Jeurissen, B. et al. (2014). "Multi-tissue constrained spherical deconvolution for improved analysis of multi-shell diffusion MRI data". *NeuroImage*, 103, pp. 411–426.

Jones, E. and T. Powell (1970). "An anatomical study of converging sensory pathways within the cerebral cortex of the monkey". *Brain*, 93(4), pp. 793–820.

Keitel, A. and J. Gross (2016). "Individual human brain areas can be identified from their characteristic spectral activation fingerprints". *PLoS Biol*, 14(6), e1002498.

Khambhati, A. N. et al. (2018). "Modeling and interpreting mesoscale network dynamics". *NeuroImage*, 180, pp. 337–349.

Kiebel, S. J., J. Daunizeau, and K. J. Friston (2008). "A hierarchy of time-scales and the brain". *PLoS Comput BIol*, 4(11).

Langs, G., P. Golland, and S. S. Ghosh (2015). "Predicting activation across individuals with resting-state functional connectivity based multi-atlas label fusion". In: *International Conference on Medical Image Computing and Computer-Assisted Intervention*. Springer, pp. 313–320.

Li, J. et al. (2019). "Topography and behavioral relevance of the global signal in the human brain". *Scientific reports*, 9(1), pp. 1–10.

Lurie, D. J. and M. D'Esposito (2020). "Gradients of intrinsic dynamics follow connectomic, anatomical and microstructural hierarchies". In: *Annual Meeting of the Organization for Human Brain Mapping*.

Lurie, D. J. et al. (2020). "Questions and controversies in the study of time-varying functional connectivity in resting fMRI". *Net Neurosci*, 4(1), pp. 30–69.

Mahjoory, K. et al. (2019). "The frequency gradient of human resting-state brain oscillations follows cortical hierarchies". *BioRxiv*, p. 857656.

Marcus, D. et al. (2011). "Informatics and data mining tools and strategies for the human connectome project". *Frontiers in neuroinformatics*, 5, p. 4.

Margulies, D. S. et al. (2016). "Situating the default-mode network along a principal gradient of macroscale cortical organization". *Proceedings of the National Academy of Sciences*, 113(44), pp. 12574–12579.

Markello, R. and B. Misic (2020). "Comparing spatially-constrained null models for parcellated brain maps". *BioRxiv*.

Markicevic, M. et al. (2020). "Cortical excitation: inhibition imbalance causes abnormal brain network dynamics as observed in neurodevelopmental disorders". *Cereb Cortex*.

Mesulam, M.-M. (1998). "From sensation to cognition." *Brain*, 121(6), pp. 1013–1052.

Mesulam, M.-M. (2000). "Behavioral neuroanatomy". *Principles of behavioral and cognitive neurology*, 2, pp. 1–120.

Misic, B. et al. (2011). "Functional embedding predicts the variability of neural activity". *Front Syst Neurosci*, 5, p. 90.

Mišić, B. et al. (2014). "The functional connectivity landscape of the human brain". *PLoS ONE*, 9(10), e111007.

Mišić, B. et al. (2015). "Cooperative and competitive spreading dynamics on the human connectome". *Neuron*, 86(6), pp. 1518–1529.

Mišić, B. et al. (2018). "Network-based asymmetry of the human auditory system". *Cerebral Cortex*, 28(7), pp. 2655–2664.

Muller, E. J. et al. (2020). "Core and Matrix Thalamic Sub-Populations Relate to Spatio-Temporal Cortical Connectivity Gradients". *bioRxiv*.

Murray, J. D. et al. (2014). "A hierarchy of intrinsic timescales across primate cortex". *Nat Neurosci*, 17(12), p. 1661.

Paquola, C. et al. (2019). "Microstructural and functional gradients are increasingly dissociated in transmodal cortices". *PLoS Biol*, 17(5), e3000284.

Paquola, C. et al. (2020). "A cortical wiring space links cellular architecture, funtional dynamics and hierarchies in humans". *bioRxiv*.

Payeur, A., J.-C. Béïque, and R. Naud (2019). "Classes of dendritic information processing". *Curr Opin Neurobiol*, 58, pp. 78–85.

Pedregosa, F. et al. (2011). "Scikit-learn: Machine learning in Python". *the Journal of machine Learning research*, 12, pp. 2825–2830.

Poldrack, R. A. et al. (2011). "The cognitive atlas: toward a knowledge foundation for cognitive neuroscience". *Frontiers Neuroinform*, 5, p. 17.

Preti, M. G., T. A. Bolton, and D. Van De Ville (2017). "The dynamic functional connectome: State-of-the-art and perspectives". *Neuroimage*, 160, pp. 41–54.

Quackenbush, J. (2002). "Microarray data normalization and transformation". *Nature Genetics*, 32, p. 496.

Raut, R. V., A. Z. Snyder, and M. E. Raichle (2020). "Hierarchical dynamics as a macroscopic organizing principle of the human brain". *Proceedings of the National Academy of Sciences*, 117(34), pp. 20890–20897.

Richiardi, J. et al. (2015). "Correlated gene expression supports synchronous activity in brain networks". *Science*, 348(6240), pp. 1241–1244.

Romero-Garcia, R. et al. (2018). "Structural covariance networks are coupled to expression of genes enriched in supragranular layers of the human cortex". *Neuroimage*, 171, pp. 256–267.

Rubinov, M. and O. Sporns (2010). "Complex network measures of brain connectivity: uses and interpretations". *Neuroimage*, 52(3), pp. 1059–1069.

Salimi-Khorshidi, G. et al. (2014). "Automatic denoising of functional MRI data: combining independent component analysis and hierarchical fusion of classifiers". *Neuroimage*, 90, pp. 449–468.

Schaefer, A. et al. (2018). "Local-global parcellation of the human cerebral cortex from intrinsic functional connectivity MRI". *Cerebral cortex*, 28(9), pp. 3095–3114.

Scholtens, L. H. et al. (2014). "Linking macroscale graph analytical organization to microscale neuroarchitectonics in the macaque connectome". *Journal of Neuroscience*, 34(36), pp. 12192–12205.

Sethi, S. S. et al. (2017). "Structural connectome topology relates to regional BOLD signal dynamics in the mouse brain". *Chaos: An Interdisciplinary Journal of Nonlinear Science*, 27(4), p. 047405.

Shafiei, G. et al. (2019). "Dopamine signaling modulates the stability and integration of intrinsic brain networks". *Cerebral Cortex*, 29(1), pp. 397–409.

Shafiei, G. et al. (2020a). "Spatial patterning of tissue volume loss in schizophrenia reflects brain network architecture". *Biol Psychiat*.

Shafiei, G. et al. (2020b). "Topographic gradients of intrinsic dynamics across neocortex". *Elife*, 9, e62116.

Shine, J. M. et al. (2019). "The low-dimensional neural architecture of cognitive complexity is related to activity in medial thalamic nuclei". *Neuron*, 104(5), pp. 849–855.

Smith, R. E. et al. (2015). "SIFT2: Enabling dense quantitative assessment of brain white matter connectivity using streamlines tractography". *Neuroimage*, 119, pp. 338–351.

Sporns, O., G. Tononi, and R. Kötter (2005). "The human connectome: a structural description of the human brain". *PLoS computational biology*, 1(4), e42.

Straub, I. et al. (2020). "Gradients in the mammalian cerebellar cortex enable Fourier-like transformation and improve storing capacity". *eLife*, 9, e51771.

Suárez, L. E. et al. (2020). "Linking structure and function in macroscale brain networks". *Trends Cogn Sci*.

Tournier, J. D., F. Calamante, and A. Connelly (2010). "Improved probabilistic streamlines tractography by 2nd order integration over fibre orientation distributions". In: *Proceedings of the international society for magnetic resonance in medicine*. Vol. 18, p. 1670.

Tournier, J.-D. et al. (2019). "MRtrix3: A fast, flexible and open software framework for medical image processing and visualisation". *NeuroImage*, p. 116137.

Uddin, L. Q. (2020). "Bring the Noise: Reconceptualizing Spontaneous Neural Activity". *Trends in Cognitive Sciences*.

Van Essen, D. C. et al. (2013). "The WU-Minn human connectome project: an overview". *Neuroimage*, 80, pp. 62–79.

Vázquez-Rodríguez, B. et al. (2019). "Gradients of structure–function tethering across neocortex". *Proc Natl Acad Sci USA*, 116(42), pp. 21219–21227.

Vazquez-Rodriguez, B. et al. (2020). "Signal propagation via cortical hierarchies". *Net Neurosci*.

Vértes, P. E. et al. (2016). "Gene transcription profiles associated with inter-modular hubs and connection distance in human functional magnetic resonance imaging networks". *Philosophical Transactions of the Royal Society B: Biological Sciences*, 371(1705), p. 20150362.

Wael, R. Vos de et al. (2018). "Anatomical and microstructural determinants of hippocampal subfield functional connectome embedding". *Proceedings of the National Academy of Sciences*, 115(40), pp. 10154–10159.

Wagstyl, K. et al. (2015). "Cortical thickness gradients in structural hierarchies". *Neuroimage*, 111, pp. 241–250.

Wagstyl, K. et al. (2020). "BigBrain 3D atlas of cortical layers: Cortical and laminar thickness gradients diverge in sensory and motor cortices". *PLoS Biol*, 18(4), e3000678.

Wang, P. et al. (2019). "Inversion of a large-scale circuit model reveals a cortical hierarchy in the dynamic resting human brain". *Sci Adv*, 5(1), eaat7854.

Wang, X.-J. (2020). "Macroscopic gradients of synaptic excitation and inhibition in the neocortex". *Nat Rev Neurosci*, pp. 1–10.

Watanabe, T., G. Rees, and N. Masuda (2019). "Atypical intrinsic neural timescale in autism". *eLife*, 8, e42256.

Wei, Y. et al. (2018). "Multiscale examination of cytoarchitectonic similarity and human brain connectivity". *Net Neurosci*, 3(1), pp. 124–137.

Yarkoni, T. et al. (2011). "Large-scale automated synthesis of human functional neuroimaging data". *Nat Meth*, 8(8), p. 665.

Yeo, B. T. et al. (2011). "The organization of the human cerebral cortex estimated by intrinsic functional connectivity". *Journal of neurophysiology*, 106(3), p. 1125.

Zheng, Y.-Q. et al. (2019). "Local vulnerability and global connectivity jointly shape neurodegenerative disease propagation". *PLoS Biol*, 17(11).

Table S4.1: **Dominance analysis** | Dominance Analysis was used to quantify the distinct contributions of inter-regional distance, structural connectivity, and functional connectivity to temporal profile similarity (Azen and Budescu, 2003; Budescu, 1993) (https://github.com/dominance-analysis/dominance-analysis). Dominance analysis is a method for assessing the relative importance of predictors in regression or classification models. The technique estimates the relative importance of predictors by constructing all possible combinations of predictors and quantifying the relative contribution of each predictor as additional variance explained (i.e. gain in R^2) by adding that predictor to the models. Specifically, for p predictors we have $2^p - 1$ models that include all possible combinations of predictors. The incremental R^2 contribution of each predictor to a given subset model of all the other predictors is then calculated as the increase in R^2 due to the addition of that predictor to the regression model. Here we first constructed a multiple linear regression model with distance, structural connectivity and functional connectivity as independent variables and temporal profile similarity as the dependent variable to quantify the distinct contribution of each factor using dominance analysis. The total R^2 is 0.28 for the complete model that includes all variables. The relative importance of each factor is summarized in the table, where each column corresponds to: Interactional Dominance is the incremental R^2 contribution of the predictor to the complete model. For each variable, interactional dominance is measured as the difference between the R^2 of the complete model and the R^2 of the model with all other variables except that variable; Individual Dominance of a predictor is the R^2 of the model when only that predictor is included as the independent variable in the regression; Average Partial Dominance is the average incremental R^2 contributions of a given predictor to all possible subset of models except the complete model and the model that only includes that variable; Total Dominance is a summary measure that quantifies the additional contribution of each predictor to all subset models by averaging all the above measures for that predictor; Percentage Relative Importance is the percent value of the Total Dominance.

	Interactional Dominance	**Individual Dominance**	**Average Partial Dominance**	**Total Dominance**	**Percentage Relative Importance**
Euclidean distance	0.095	0.245	0.128	0.156	56.015
functional connectivity	0.030	0.130	0.038	0.066	23.591
structural connectivity	2.97e-05	0.142	0.029	0.057	20.393

Table S4.2: **List of terms used in Neurosynth analyses** | The overlapping terms between Neurosynth (Yarkoni et al., 2011) and Cognitive Atlas (Poldrack et al., 2011) corpuses used in the reported analyses are listed below.

action	encoding	loss	reward anticipation
adaptation	episodic memory	maintenance	rhythm
addiction	expectancy	manipulation	risk
anticipation	expertise	meaning	rule
anxiety	extinction	memory	salience
arousal	face recognition	memory retrieval	search
association	facial expression	mental imagery	selective attention
attention	familiarity	monitoring	semantic memory
autobiographical memory	fear	mood	sentence comprehension
balance	fixation	morphology	skill
belief	focus	motor control	sleep
categorization	gaze	movement	social cognition
cognitive control	goal	multisensory	spatial attention
communication	hyperactivity	naming	speech perception
competition	imagery	navigation	speech production
concept	impulsivity	object recognition	strategy
consciousness	induction	pain	strength
consolidation	inference	perception	stress
context	inhibition	planning	sustained attention
coordination	insight	priming	task difficulty
decision	integration	psychosis	thought
decision making	intelligence	reading	uncertainty
detection	intention	reasoning	updating
discrimination	interference	recall	utility
distraction	judgment	recognition	valence
eating	knowledge	rehearsal	verbal fluency
efficiency	language	reinforcement learning	visual attention
effort	language comprehension	response inhibition	visual perception
emotion	learning	response selection	word recognition
emotion regulation	listening	retention	working memory
empathy	localization	retrieval	

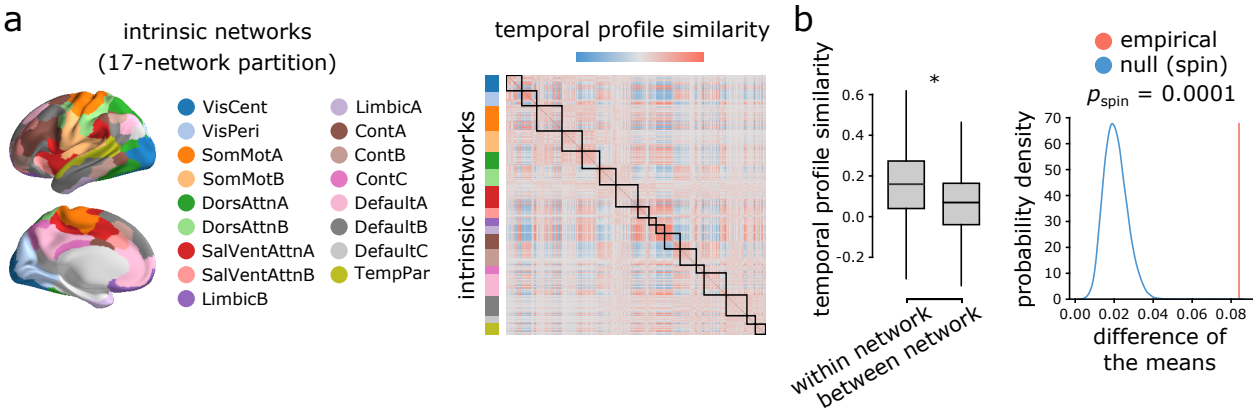

Figure S4.1: **Intrinsic networks: 17 network partition** | (a) Regional time-series features are compared between pairs of cortical areas using their functional connectivity profiles. Cortical areas are ordered based on their intrinsic network assignments (17-network partition) (Schaefer et al., 2018; Yeo et al., 2011). (b) Pairwise temporal profile similarity is significantly higher among regions that belong to the same intrinsic functional networks. Asterisk denotes a statistically significant difference of the mean temporal profile similarity (two-tailed t-test; $t(79,798) = 31.151$; $p \approx 0$). The results are consistent when the distance effect is regressed out from temporal profile similarity using the exponential trend identified in Figure 4.2b (two-tailed t-test; $t(79,798) = 21.193$; $p \approx 0$). Statistical significance of the difference of the mean temporal profile similarity of within and between intrinsic networks is also assessed against a null distribution of differences generated by spatial autocorrelation-preserving label permutation ("spin tests"; (Alexander-Bloch et al., 2018)) (10,000 spatial permutations; right-most panel).

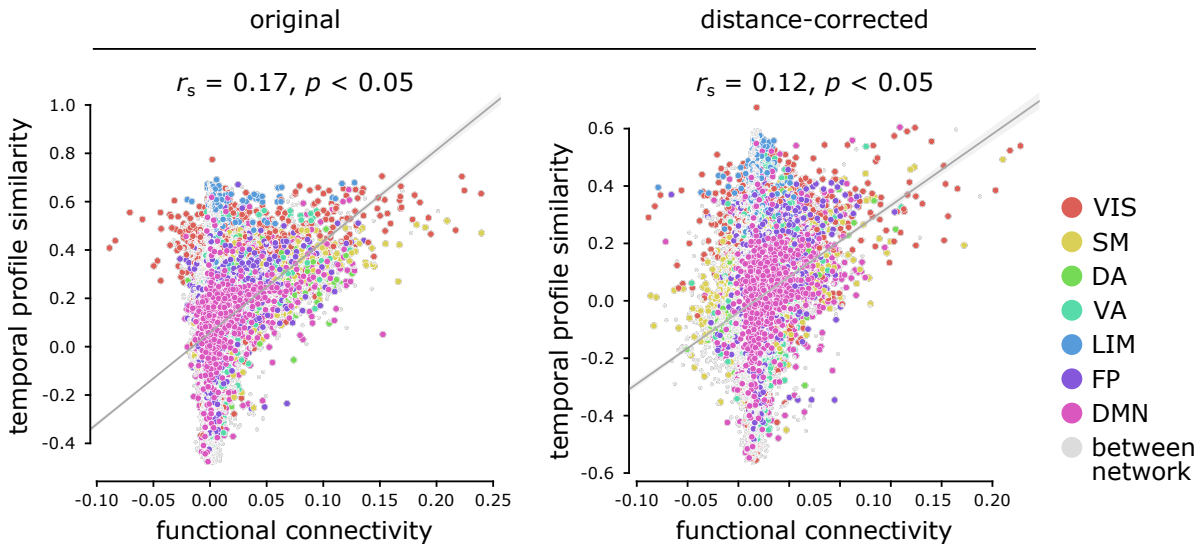

Figure S4.2: **Functional connectivity measured by partial correlations** | For completeness, all functional connectivity analyses were repeated using partial correlations, as implemented in `Nilearn` (Abraham et al., 2014). Temporal profile similarity is positively correlated with functional connectivity estimated using partial correlations. This relationship remains after partialling out Euclidean distance between regions from both measures using exponential trends. r_s denotes Spearman rank correlation coefficients; linear regression lines are added to the scatter plots for visualization purposes only. Connections are colour-coded based on the intrinsic network assignments (Schaefer et al., 2018; Yeo et al., 2011). VIS = visual, SM = somatomotor, DA = dorsal attention, VA = ventral attention, LIM = limbic, FP = fronto-parietal, DMN = default mode.

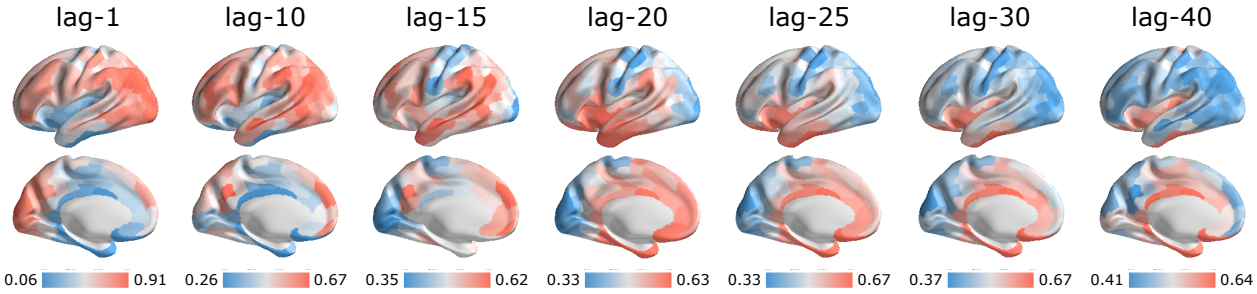

Figure S4.3: **Linear autocorrelation function** | Linear autocorrelation function is depicted on the brain surface at varying time lags. The autocorrelation values are normalized between 0 and 1 using an outlier-robust sigmoidal transform and spatial maps are depicted based on the standard deviation σ of their respective distributions. Short-lag autocorrelation measures load positively on PC1, while long-lag autocorrelation measures load negatively, consistent with the notion that autocorrelation decays with increasing time lag (Figure 4.3).

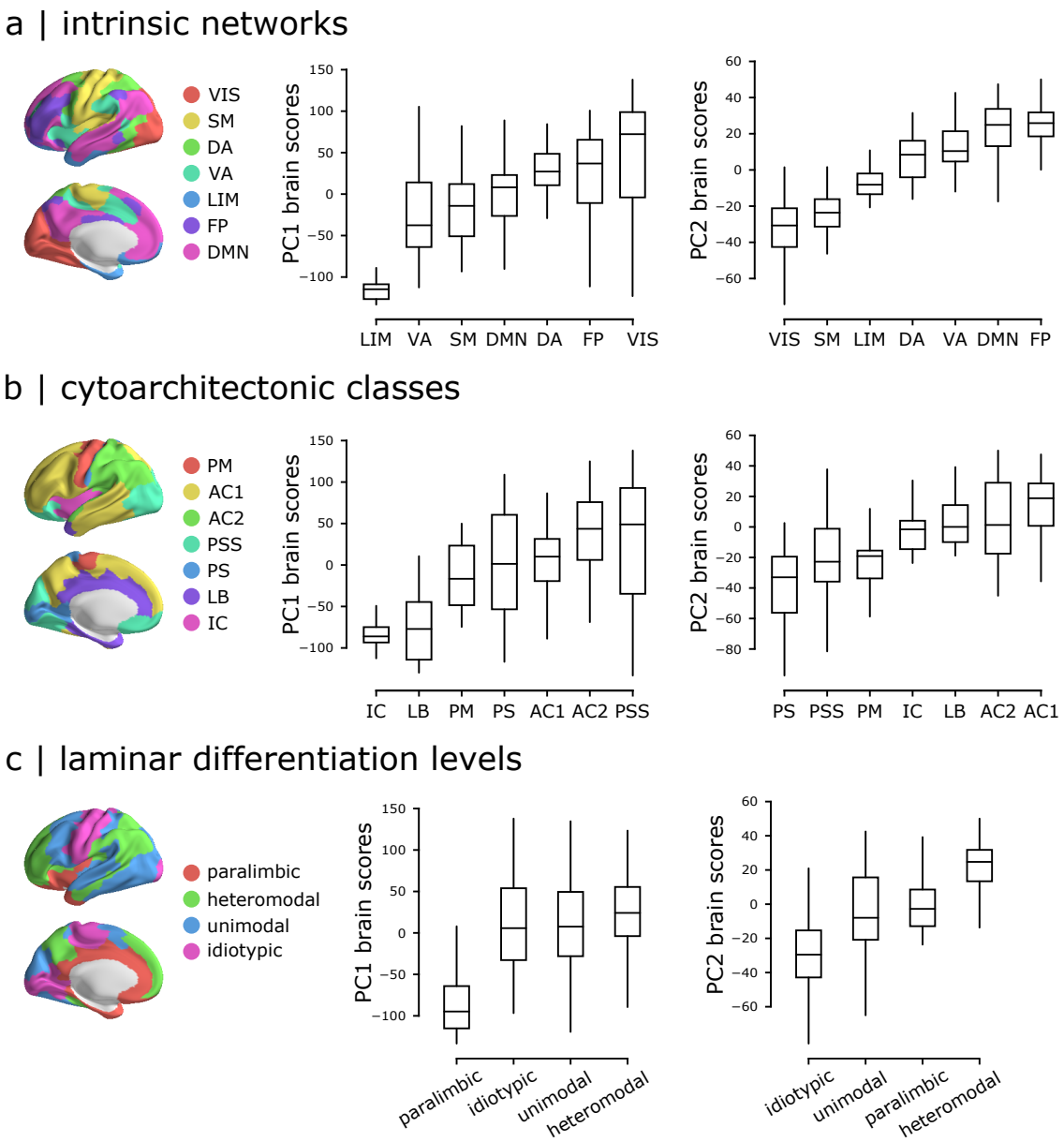

Figure S4.4: **Intrinsic dynamics across intrinsic networks, cytoarchitectonic classes and laminar differentiation levels** | Mean PC1 and PC2 scores were computed for the constituent classes in three commonly used anatomical and functional partitions of the brain: (a) intrinsic fMRI networks (Schaefer et al., 2018; Yeo et al., 2011), (b) cytoarchitectonic classes (Economo and Koskinas, 1925; Economo et al., 2008; Vértes et al., 2016), laminar differentiation levels (Mesulam, 2000). Intrinsic networks: VIS = visual, SM = somatomotor, DA = dorsal attention, VA = ventral attention, LIM = limbic, FP = fronto-parietal, DMN = default mode. Cytoarchitectonic classes: PM = primary motor cortex, AC1 = association cortex, AC2 = association cortex, PSS = primary/secondary sensory, PS = primary sensory cortex, LB = limbic regions, IC = insular cortex.

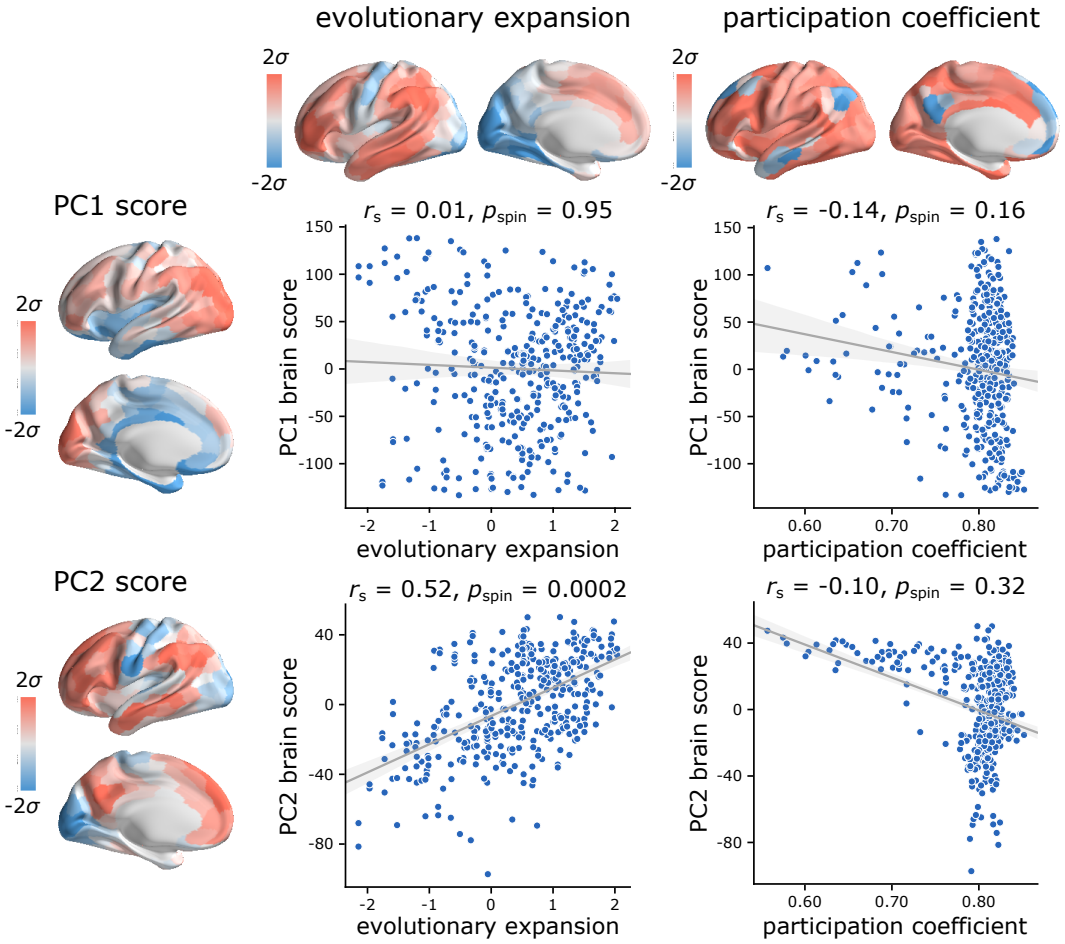

Figure S4.5: **Topographic organization of intrinsic dynamics compared to evolutionary expansion and participation coefficient** | The evolutionary expansion map (Baum et al., 2020; Hill et al., 2010) was obtained through `https://github.com/PennLINC/Brain_Organization` and parcellated into 400 cortical areas using the Schaefer parcellation (Schaefer et al., 2018). Regional weighted participation coefficients (Brain Connectivity Toolbox; (Rubinov and Sporns, 2010)) were estimated from functional connectivity graphs with respect to the 7-network partition of intrinsic networks (Schaefer et al., 2018; Yeo et al., 2011). We then compared the maps to the PC1 and PC2 brain score patterns. The evolutionary expansion map was significantly correlated with PC2 topography, but not PC1 topography. The regional participation coefficient map was not significantly correlated with either PC1 or PC2 topography. Statistical significance of the reported Spearman rank correlation r_s is assessed using 10,000 spatial permutations tests, preserving the spatial autocorrelation in the data ("spin tests"; (Alexander-Bloch et al., 2018)). Linear regression lines are added to the scatter plots for visualization purposes only.

Chapter 5

Neurophysiological signatures of cortical micro-architecture

Golia Shafiei[1], Sylvain Baillet[1], Ben D. Fulcher[2] & Bratislav Misic[1]

[1]McConnell Brain Imaging Centre, Montréal Neurological Institute, McGill University, Montréal, Canada

[2]School of Physics, The University of Sydney, NSW 2006, Australia

5.1 Preface

A large body of literature has used neural oscillations to characterize regional brain dynamics and neural communication patterns. Power spectral properties of neurophysiological activity are often used for this purpose. However, the dynamic signature of neurophysiological activity and its association with cortical micro-architecture have not been characterized with respect to the broader range of inter-disciplinary time-series analysis. The work presented here expands on Chapter 4 and examines regional neural dynamics using spontaneous neurophysiological activity with high temporal resolution instead of slower haemodynamic fluctuations. Resting-state magnetoencephalography (MEG) data is used here to quantify neurophysiological activity. MEG is a non-invasive neuroimaging technique that measures the magnetic fields generated by electrical currents from the ongoing neural activity and provides whole-brain maps of neural dynamics with high temporal resolution (below millisecond precision) (Baillet, 2017; Baillet et al., 2001; Hämäläinen et al., 1993). Using both conventional measures of neurophysiological

dynamics and data-driven, near-comprehensive lists of time-series properties, the goal of this study is to identify the dynamic fingerprint of neurophysiological activity and assess the relationship between fast-oscillating neural activity and cortical micro-architecture. This project will be submitted for publication in 2022.

5.2 Abstract

Systematic variations in cortical circuit properties are observed across the cortex. These microscale gradients are reflected in the neural activity, which can be captured by neurophysiological time-series. How the spontaneous neurophysiological dynamics are organized across the cortex and how they arise from the heterogeneous cortical micro-architecture remains unknown. Here we comprehensively assess intrinsic neural dynamics of magnetoencephalography (MEG) signal across the human brain. Applying massive temporal feature extraction to regional neurophysiological activity, we estimate over 6,800 time-series features across the neocortex. We identify dynamical signature of neurophysiological activity and map regional dynamics to cortical micro-architecture. We find that dynamic fingerprint of neurophysiological activity reflects characteristics of power spectrum density and long term memory of the signal, emphasizing the importance of conventional measures of electromagnetic dynamics while introducing novel ones. Moreover, the main axis of variation in neurophysiological activity reflects the anatomical hierarchy and cortical metabolic demands.

5.3 Introduction

Signals, in the form of electrical impulses, are perpetually generated, propagated and integrated via multiple types of neurons and neuronal populations (Bargmann and Marder, 2013; Swanson and Lichtman, 2016). The wiring of the brain guides the propagation of signals through networks of nested polyfunctional neural circuits (Avena-Koenigsberger et al., 2018; Bullmore and Sporns, 2009). The resulting fluctuations in membrane potentials and firing rates ultimately manifest as patterned neurophysiological activity (Baillet, 2017; Baillet et al., 2001; Hämäläinen et al., 1993).

A rich literature demonstrates links between cortical micro-architecture and dynamics. Numerous studies have investigated the cellular and laminar origins of cortical rhythms (Bastos et al., 2020; Buzsáki et al., 2012; Buzsaki and Draguhn, 2004; Buzsáki et al., 2013; Engel et al., 2001; Wang, 2020). For instance, electro- and magneto-encephalography

(EEG/MEG) signals appear to be more sensitive to dipoles originating from pyramidal cells of cortical layers II-III and V (Murakami and Okada, 2006; Zhu et al., 2009). Moreover, specific time-series features of neuronal electrophysiology depend on neuron type, morphology and local gene transcription, particularly genes associated with ion channel regulation (Bomkamp et al., 2019; Tripathy et al., 2015, 2017). However, many previous studies have focused on single or small sets of features-of-interest, often mapping single micro-architectural features to single dynamical features. Starting with the discovery of 8-12 Hz alpha rhythm in the electroencephalogram (Berger, 1929), conventional time-series analysis in neuroscience has typically focused on canonical electrophysiological rhythms (Donoghue and Voytek, 2022; Donoghue et al., 2020; Picton et al., 2000; Silva Castanheira et al., 2021; Wiesman et al., 2022). More recently, there has also been a growing interest in studying the intrinsic timescales that display a hierarchy of temporal processing from fast fluctuating activity in unimodal cortex to slower encoding of contextual information in transmodal cortex (Baldassano et al., 2017; Gao et al., 2020; Hasson et al., 2008; Honey et al., 2012; Ito et al., 2020; Kiebel et al., 2008; Mahjoory et al., 2020; Murray et al., 2014; Raut et al., 2020; Watanabe et al., 2019). How ongoing neurophysiological dynamics arise from specific features of neural circuit micro-architecture remains a key question in neuroscience (Bargmann and Marder, 2013; Swanson and Lichtman, 2016; Wang, 2020).

Recent analytic advances have opened new opportunities to perform neurophysiological time-series phenotyping by computing comprehensive feature sets that go beyond power spectral measures, including measures of signal amplitude distribution, entropy, fractal scaling and autocorrelation (Fulcher, 2018; Fulcher and Jones, 2017; Fulcher et al., 2013). Concomitant advances in imaging technologies and data sharing offer new ways to comprehensively measure brain structure with unprecedented detail and depth (Huntenburg et al., 2018; Markello et al., 2022; Sydnor et al., 2021), including gene expression (Hawrylycz et al., 2012), myelination (Glasser and Van Essen, 2011; Huntenburg et al., 2017), neurotransmitter receptors (Beliveau et al., 2017; Dukart et al., 2021; Hansen et al., 2022; Knudsen et al., 2020; Martins et al., 2021; Nørgaard et al., 2021; Norgaard et al., 2022; Zilles and Palomero-Gallagher, 2017), cytoarchitecture (Amunts et al., 2013; Finnema et al., 2018; Paquola et al., 2021), laminar differentiation (Amunts et al., 2013; Wagstyl et al., 2020), cell type composition (Di Biase et al., 2022; Hawrylycz et al., 2012; Seidlitz et al., 2020), metabolism (Raichle and Mintun, 2006; Vaishnavi et al., 2010) and evolutionary expansion (Hill et al., 2010; Reardon et al., 2018).

Here we comprehensively characterize the dynamical signature of neurophysiological

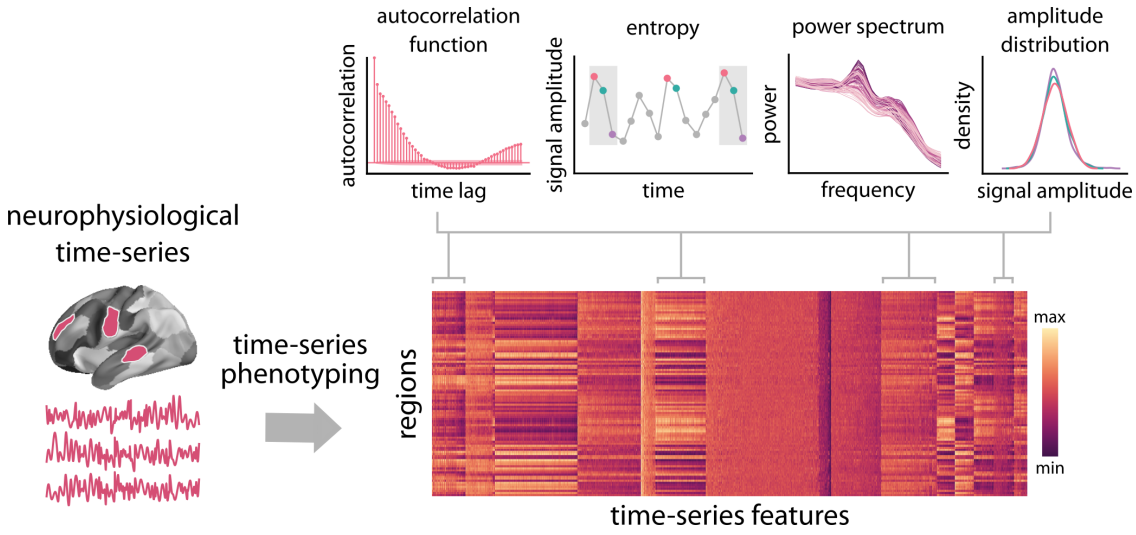

Figure 5.1: **Feature-based representation of neurophysiological time-series** | Highly comparative time-series analysis (`hctsa`; (Fulcher et al., 2013)) toolbox was used to perform time-series feature extraction on regional MEG time-series. This time-series phenotyping procedure generated 6,880 time-series features for each region, including measures of autocorrelation, entropy, power spectrum and amplitude distribution.

activity and relate it to the underlying micro-architecture. We first derive whole-brain spontaneous regional neurophysiological activity using source-resolved magnetoencephalography (MEG) from the Human Connectome Project (HCP; (Van Essen et al., 2013)). We then apply highly comparative time-series analysis (`hctsa`; (Fulcher and Jones, 2017; Fulcher et al., 2013)) to estimate a near-exhaustive set of $> 6,800$ time-series features for each brain region (Figure 4.1). At the same time, we construct a micro-architectural atlas of the brain using the `neuromaps` toolbox (Markello et al., 2022), including maps of microstructure, metabolism, neurotransmitter receptors, laminar differentiation and cell types (Figure 5.2). Finally, we map these extensive micro-architectural and dynamical atlases to one another.

5.4 Results

Regional neurophysiological time-series were estimated by applying locally constrained minimum variance (LCMV) beamforming to resting state MEG data from the Human Connectome Project (HCP; (Van Essen et al., 2013)) using `Brainstorm` software (Tadel et al., 2011)(see *Methods* for details). Highly comparative time-series analysis (`hctsa`) was then applied to regional time-series to estimate 6,880 time-series features for each region, including measures of autocorrelation, fluctuation analysis, entropy, power spectrum and amplitude distribution (Figure 4.1; (Fulcher et al., 2013)). This time-series phenotyping

procedure yields a comprehensive, data-driven dynamic "fingerprint" for each brain region.

To estimate a comprehensive set of multi-modal micro-architectural features, we used the recently-developed `neuromaps` toolbox to transform and compile a set of 45 features, including measures of microstructure, metabolism, cortical expansion, receptors and transporters, layer thickness and cell types (Markello et al., 2022) (Figure 5.2).

5.4.1 Topographic distribution of neurophysiological dynamics

The `hctsa` time-series phenotyping procedure generated 6,880 time-series features per brain region. Since many time-series measures and features potentially capture related dynamical behaviour, we first seek to identify dominant macroscopic patterns or gradients of neurophysiological dynamics (Shafiei et al., 2020b). Applying singular value decomposition to the region $\times$ feature matrix, we find evidence of a single dominant component that captures 48.7% of the variance in regional time-series features (Figure 5.3a). The dominant component or "gradient" of neurophysiological dynamics (PC1) mainly spans the posterior parietal cortex and sensory-motor cortices on one end and the anterior temporal, orbitofrontal and ventromedial cortices on the other end (Figure 5.3a). Focusing on intrinsic functional networks, we find that the topographic organization of the dominant neurophysiological dynamics varies along a sensory-fugal axis from dorsal attention, somatomotor and visual networks to limbic and default mode networks (Yeo et al., 2011) (Figure 5.3a).

We next investigate the top-loading time-series features on the first component, by correlating each of the original feature maps with the PC1 map. All correlations are statistically assessed using spatial autocorrelation-preserving null models ("spin tests" (Alexander-Bloch et al., 2018; Markello and Misic, 2021); see *Methods* for details). Figure 5.3b shows that numerous features are positively and negatively correlated with PC1; the full list of features, their correlation coefficient and p-values is available in the online Supplementary File S1. Inspection of the top loading features reveals that the majority are either direct measures of the power spectrum or measures closely related to the power spectrum. Examples include the area under the curve at different frequency bands, parameters of different model fits to the power spectrum, the aperiodic exponent of the power spectrum, and measures mathematically related to the power spectrum, such as the shape of the autocorrelation function and measures of fluctuation analysis. Figure 5.3b shows how the power spectrum varies across the cortex, with each line representing a brain

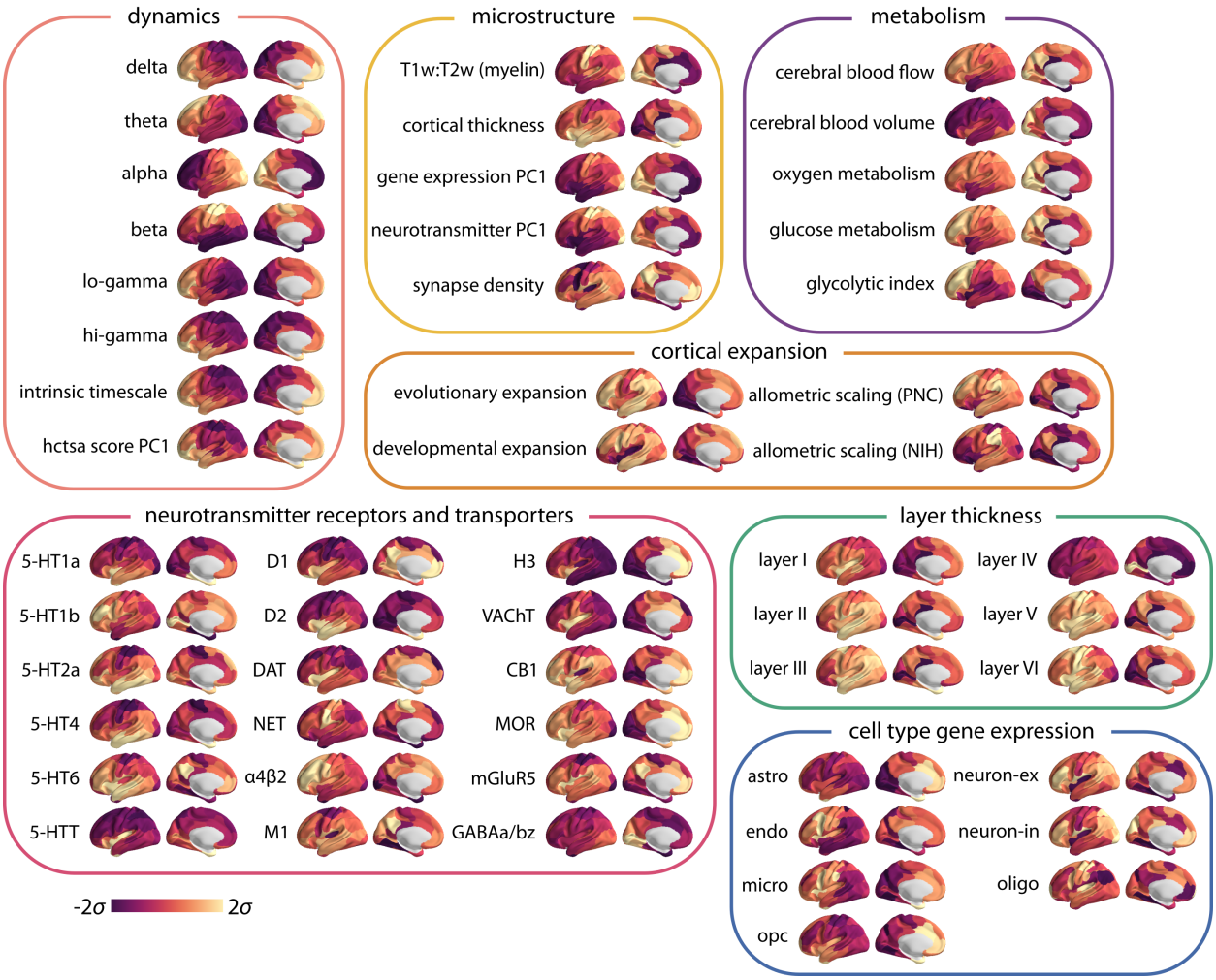

Figure 5.2: **Multimodal brain maps** | `neuromaps` toolbox was used to to transform and compile a set of 45 micro-architectural brain maps, including measures of microstructure, metabolism, cortical expansion, receptors and transporters, layer thickness and cell types (Markello et al., 2022) (see *Methods* for more details). Note that the microstructure maps include principal gradients of gene expression and neurotransmitter profiles, for which we have also separately included feature sub-sets (specific receptor maps and cell type specific gene expression). `Brainstorm` software was used to pre-process the resting-state MEG data and obtain power maps at six canonical electrophysiological bands (i.e., delta (δ: 2-4 Hz), theta (θ: 5-7 Hz), alpha (α: 8-12 Hz), beta (β: 15-29 Hz), low gamma (lo-γ: 30-59 Hz), and high gamma (hi-γ: 60-90Hz)) (Tadel et al., 2011) (see *Methods* for more details). FOOOF algorithm was used to parametrize power spectral density and estimate the intrinsic timescale (Donoghue et al., 2020; Gao et al., 2020) (see *Methods* for more details). Note that log-10 transformed intrinsic timescale map is shown here. Principal component analysis was used to estimate the principal component of the neurophysiological time-series features obtained from the `hctsa` toolbox (see Figure 5.3).

region. Regions are coloured by their position in the putative unimodal-transmodal hierarchy (Margulies et al., 2016); the variation suggests that unimodal regions display more prominent alpha and beta power peaks. Collectively, these results empirically demonstrate

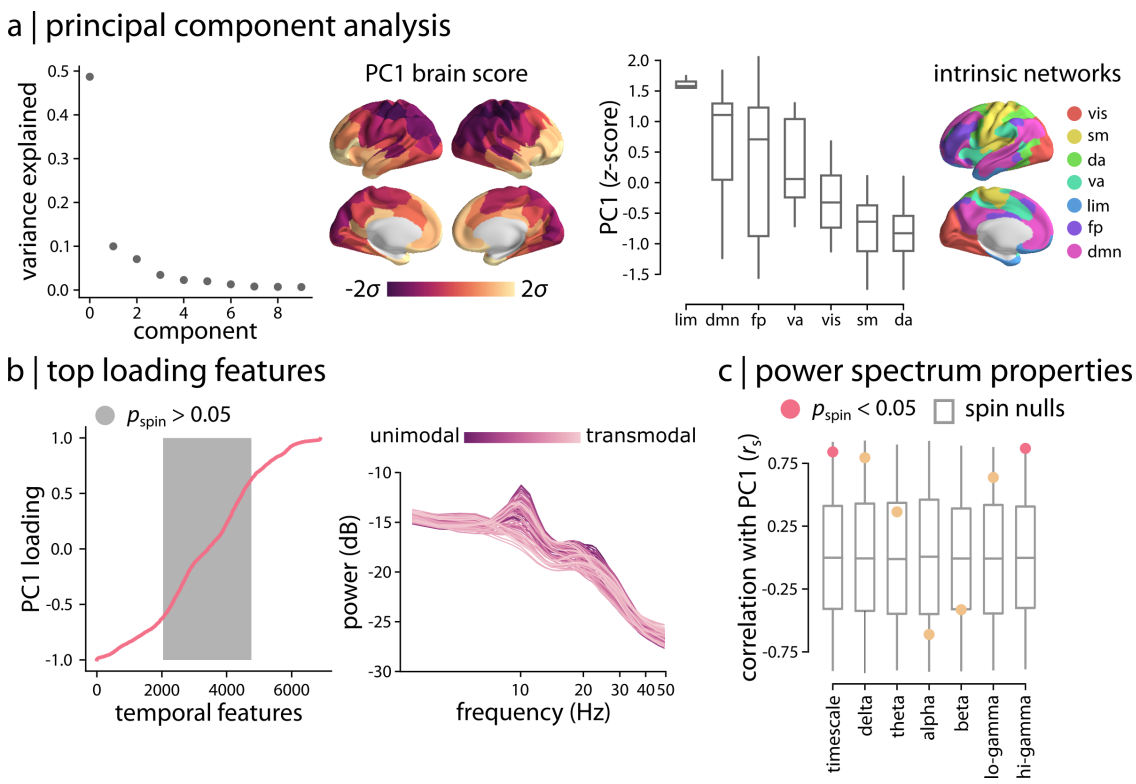

Figure 5.3: **Topographic distribution of neurophysiological dynamics** | (a) Principal component analysis (PCA) was used to identify linear combinations of MEG time-series features with maximum variance across the cortex. The fist principal component (PC1) accounts for 48.7% of the total variance in neurophysiological time-series features. The spatial organization of the dominant time-series features captured by PC1 is depicted across the cortex (95% confidence intervals). The distribution of PC1 brain score is also depicted for intrinsic functional networks (Yeo et al., 2011). (b) To examine the feature composition of the time-series features captured by PC1, feature loadings were estimated as the correlation coefficients between each `hctsa` time-series feature and PC1 brain score. Time-series features are ordered by their individual loadings. Grey indicates non-significant features based on 10 000 spatial autocorrelation-preserving permutation tests (FDR corrected). The top loading features were mainly related to the power spectrum of regional time-series and its organization. Regional power spectral densities are depicted, with each line representing a brain region. Regions are coloured by their position in the putative unimodal-transmodal hierarchy (Margulies et al., 2016). (c) To contextualize the principal component of variation in MEG time-series features, the PC1 brain score was correlated with MEG power maps at 6 canonical frequency bands and intrinsic timescale. PC1 score is significantly correlated with intrinsic timescale and hi-gamma power (FDR-corrected).

that the traditional focus on the power spectrum in electrophysiology is well-founded.

Given the hierarchical organization of PC1 and its close relationship with power spectral features, we directly tested the link between PC1 and conventional spectral measures (Donoghue et al., 2020; Silva Castanheira et al., 2021; Wiesman et al., 2022), as well as a measure of intrinsic timescale (Gao et al., 2020). Figure 5.3c shows the correlations between PC1 and delta (2-4 Hz), theta (5-7 Hz), alpha (8-12 Hz), beta (15-29 Hz), lo-gamma (30-59

Hz) and hi-gamma (60-90Hz) power maps, and intrinsic neural timescale (Gao et al., 2020; Ito et al., 2020; Mahjoory et al., 2020; Murray et al., 2014; Raut et al., 2020; Watanabe et al., 2019; Wolff et al., 2022). We find that PC1 displays large spatial correlations with most ($|r| > 0.36$), and significant correlations with intrinsic timescale ($r_s = 0.84$, $p_{spin} = 0.03$; FDR-corrected) and hi-gamma ($r_s = 0.87$, $p_{spin} = 0.005$; FDR-corrected). The fact that PC1 correlates with intrinsic timescale is consistent with the notion that both capture broad variations in the power spectrum.

5.4.2 Neurophysiological signature of micro-architecture

How do these regional neurophysiological time-series features map onto multi-modal micro-architectural features? To address this question, we implement a partial least squares analysis (PLS; (McIntosh and Mišić, 2013; McIntosh and Lobaugh, 2004)) that seeks to identify linear combinations of time-series features and linear combinations of micro-architectural features that optimally covary with one another. Figure 5.4a shows that the analysis identifies multiple such combinations, termed latent variables. Statistical significance of each latent variable was assessed using spatial autocorrelation-preserving permutation tests (Hansen et al., 2021). The first latent variable was statistically significant, capturing the greatest covariance between time-series and micro-architectural features (covariance explained $= 76.6\%$, $p_{spin} = 0.0069$).

Figure 5.4b shows the spatial topography of time-series features and micro-architectural scores for the first latent variable. These are the weighted sums of the original input features according to the weighting identified by the latent variable. The correlation between the score maps is maximized by the analysis ($r_s = 0.75$, $p_{spin} = 0.0033$). We therefore sought to estimate whether the same mapping between time-series and micro-architectural features (a) can be observed out-of-sample, and (b) goes beyond the background effect of spatial autocorrelation in the two maps. We therefore adopted a distance-dependent cross-validation procedure where "seed" regions were randomly chosen and the 75% most physically proximal regions were selected as the training set, while the remaining 25% most physically distal regions were selected as the test set (Hansen et al., 2021) (see *Methods* for more details). For each train-test split, we fit a PLS model to the train set and project the test set onto the weights (i.e. singular vectors) derived from the train set. The resulting test set scores are then correlated to estimate an out-of-sample correlation coefficient. The procedure is then repeated for $1,000$ randomly rotated (spin) nulls to estimate a null distribution for the out-of-sample correlation coefficients. Figure 5.4b shows that the mean

out-of-sample score correlation is $r = 0.55$ and statistically significant compared to the spatial autocorrelation-preserving null correlation coefficients ($p_{\text{spin}} = 0.03$).

We next examine the corresponding time-series and micro-architecture feature loadings and identify the most contributing factors to the spatial patterns captured by the first latent variable (Figure 5.4c,d). The top loading time-series features were mainly related to the long-term memory and self-affinity of the neurophysiological signal, quantified by fluctuation analysis (Figure 5.4c). Fluctuation analysis quantifies self-affinity and long-range autocorrelation of time-series (Bryce and Sprague, 2012; Hardstone et al., 2012; Talkner and Weber, 2000). For example, the Hurst exponent or the alpha parameter of the detrended fluctuation analysis, which is a measure of long-term memory of the time-series, is depicted across the cortex in Figure 5.4c (left panel). The spatial distribution of this measure shows that unimodal cortex, such as the area marked with the pink circle, has shorter long-term memory compared to transmodal cortex, such as the area marked with the purple circle. Long-term memory of the signal captured by the detrended fluctuation analysis is also reflected in the shape of the autocorrelation function, and more specifically, at the zero crossing point of the autocorrelation function (Figure 5.4c, left). For example, the autocorrelation function of unimodal cortex (pink circle) crosses zero autocorrelation earlier than the autocorrelation function of transmodal cortex (purple circle). A more direct example of the long-term memory of the signal is the linear autocorrelation estimated at longer lags. Autocorrelation at lag 24 is also depicted in Figure 5.4c (right panel), showing lower autocorrelation in unimodal cortex and higher autocorrelation in transmodal cortex. Although the Hurst exponent of the detrended fluctuation analysis and long-range autocorrelation are measures of long-term memory and are shown in Figure 5.4c as two examples of high loading features, they can both be related to the power spectral density and broader structure of the power spectrum (Talkner and Weber, 2000). The full list of time-series feature loadings for the first latent variable is available at the online Supplementary File S2.

Figure 5.4d shows the corresponding micro-architectural loadings. The most contributing micro-architectural factors to the spatial patterns captured by the first latent variable are the principal component of gene expression (gene expression PC1; a potential proxy for cell type distribution (Burt et al., 2018; Hansen et al., 2021; Hawrylycz et al., 2012)), T1w/T2w ratio (a proxy for intracortical myelin), principal component of neurotransmitter receptors and transporters (neurotransmitter PC1), and oxygen and glucose metabolism that have strong positive loadings. We also find high contributions (strong negative loadings) from specific neurotransmitter receptor and transporters, in particular metabotropic serotonergic and dopaminergic receptors, as well as from cell type-specific gene expression

of oligodendrocyte precursors (opc), which are involved in myelinogenesis (Bergles and Richardson, 2016; Bergles et al., 2000; Fernandez-Castaneda and Gaultier, 2016; Miller, 1996; Simons and Nave, 2016). Consistent findings were obtained when we used univariate analysis to relate regional time-series features and the top loading micro-architectural maps, in particular principal component of gene expression and T1w/T2w ratio, which have previously been extensively studied as archetypical micro-architectural gradients (Burt et al., 2018; Demirtaş et al., 2019; Fulcher et al., 2019; Gao et al., 2020; Huntenburg et al., 2018) (Figure S5.1). Altogether, this analysis provides a comprehensive chart or "lookup table" of how micro-architectural and time-series feature maps are associated with one another. These results demonstrate that cortical variation in multiple micro-architectural features manifests as a gradient of time-series properties of neurophysiological signals, particularly long-term memory and power spectral density.

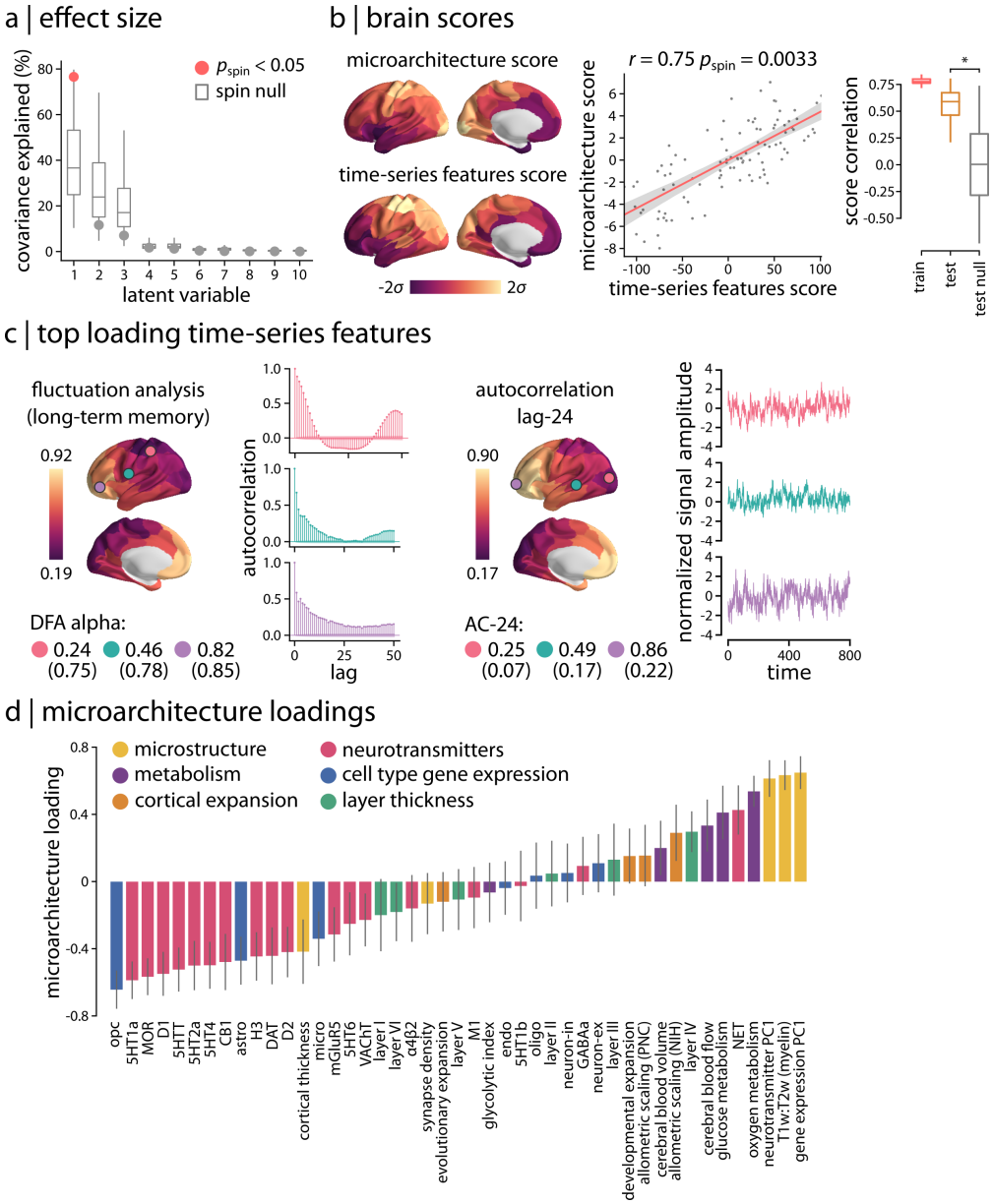

Figure 5.4: **Neurophysiological signature of micro-architecture** | (a) Partial least square (PLS) analysis was used to assess the multivariate relationship between micro-architectural and time-series features. PLS identified a single significant latent variable ($p_{\text{spin}} = 0.0069$, covariance explained = 76.6%). (b) Spatial patterns of micro-architecture and time-series features scores are depicted for the first latent variable. The two brain score maps are significantly correlated. To assess the out-of-sample correlation of brain scores, a distance-dependent cross-validation analysis with spatial autocorrelation-preserving nulls was used (see *Methods* for more details). Mean out-of-sample (test set) correlation was statistically significant compared to 1,000 null correlations (mean $r_{\text{test}} = 0.55$, $p_{\text{spin}} = 0.03$). (c) Top loading time-series features were related to the long-term memory of the signal. Hurst exponent or alpha parameter of the detrended fluctuation analysis (DFA), a measure of long-term memory of time-series (Talkner and Weber, 2000), is depicted as an example of top loading features. Fluctuation analysis also reflects the shape of the autocorrelation function. Lag-24 autocorrelation is depicted as another example (each time lag is 2 ms). For each map, three regions are selected based on the alpha parameter of DFA and lag-24 autocorrelation (circles on the brain surface: pink = 5^{th} percentile, green = 50^{th} percentile, purple = 95^{th} percentile). Values inside the parenthesis (bottom row) are the raw feature values and the ones on the top are the normalized ones. (d) Feature loadings are shown for micro-architectural brain maps.

5.5 Discussion

In the present study, we use time-series phenotyping analysis to comprehensively chart the dynamic fingerprint of neurophysiological activity from the resting-state MEG signal. We then map the resulting dynamical atlas to a micro-architectural atlas to identify the neurophysiological signatures of cortical micro-architecture. We demonstrate that cortical variation in neurophysiological time-series properties mainly reflects power spectral density and is closely associated with intrinsic timescale and long term memory of the signal. Moreover, the spatial organization of neurophysiological dynamics follows gradients of micro-architecture, such as neurotransmitter receptor and transporters, gene expression and T1w/T2w ratios, and reflects cortical metabolic demands.

Numerous studies have previously investigated neural oscillations and their relationship with neural communication patterns in the brain (Buzsaki and Draguhn, 2004; Buzsáki et al., 2013; Engel et al., 2001; Fries, 2005). Previous reports also suggest that neural oscillations influence behaviour and cognition (Engel et al., 1997; Fries, 2005; Voytek and Knight, 2015; Voytek et al., 2015; Wang, 2010) and are involved in multiple neurological diseases and disorders (Kopell et al., 2014; Voytek and Knight, 2015). Neural oscillations manifest as the variations of power amplitude of neurophysiological signal in the frequency domain (Buzsáki et al., 2013; Donoghue et al., 2020; Frauscher et al., 2018; He, 2014). Power spectral characteristics of the neurophysiological signal, such as mean power amplitude in canonical frequency bands, have previously been used to investigate the underlying mechanisms of large-scale brain activity and to better understand the individual differences in brain function (Das et al., 2022; Florin and Baillet, 2015; Mahjoory et al., 2020; Silva Castanheira et al., 2021; Voytek et al., 2015; Wiesman et al., 2022). Other time-series properties, that can be related to the power spectral density, have also been used to study neural dynamics, such as measures of intrinsic timescale and self-affinity or self-similarity of the signal (e.g. autocorrelation and fluctuation analysis) (Gao et al., 2020; Hardstone et al., 2012; Kiebel et al., 2008; Talkner and Weber, 2000).

The goal of this study was to expand on the previous literature and identify potentially relevant, but less-commonly used time-series properties of neurophysiological brain activity. Applying an unbiased, data-driven time-series feature extraction analysis, we find that the topographic organization of neurophysiological time-series signature follows a sensory-fugal axis, separating somatomotor, occipital and parietal cortices from anterior temporal, orbitofrontal and ventromedial cortices. This dynamic fingerprint of neurophysiological activity is characterized by measures of power spectrum and the broader structure

of power spectral density across the cortex. Interestingly, this dominant pattern resembles the spatial distribution of intrinsic timescale, which is also related to the characteristics of power spectral density (Gao et al., 2020; Ito et al., 2020; Murray et al., 2014). Altogether, while the findings highlight a few under-represented time-series features such as measures of fluctuation analysis, they are mostly confirmatory emphasizing the importance of conventional methods and the key role of power spectral properties in characterizing neurophysiological activity.

Earlier reports found that regional neural dynamics, including measures of power spectrum and intrinsic timescale, reflect the underlying circuit properties and cortical micro-architecture (Gao et al., 2020; Kiebel et al., 2008; Murray et al., 2014). The relationship between neural dynamics and cortical micro-architecture is often examined using a single, or a few microstructural features. Recent advances in data collection and integration and the increasing number of data sharing initiatives have provided a unique opportunity to comprehensively study cortical circuit properties and micro-architecture using a wide range of multimodal datasets (Amunts et al., 2013; Hansen et al., 2022; Hawrylycz et al., 2012; Markello et al., 2022; Paquola et al., 2021; Van Essen et al., 2013; Wagstyl et al., 2018). Here we use such datasets and compile multiple micro-architectural maps, including measures of microstructure, metabolism, cortical expansion, receptors and transporters, layer thickness and cell type-specific gene expressions, to chart the relationship between neurophysiological dynamics and cortical micro-architecture in a multivariate analysis.

Our findings build on previous reports by showing that neurophysiological dynamics follow the underlying cytoarchitectonic and microstructural gradients. In particular, our findings confirm that MEG intrinsic dynamics are associated with the heterogeneous distribution of gene expression and myelination (Demirtaş et al., 2019; Gao et al., 2020) and neurotransmitter receptors and transporters (Hansen et al., 2022), which are proxy measures for cellular and molecular circuit properties (Burt et al., 2018; Hansen et al., 2021; Hawrylycz et al., 2012). In addition, we link the dynamic signature of ongoing neurophysiological activity with multiple metabolic attributes (Raichle, 2015; Raichle and Mintun, 2006); for instance, we find that regions with greater oxygen and glucose metabolic metabolism tend to display lower temporal autocorrelation and therefore more variable moment-to-moment intrinsic activity. We also find a prominent association with cell type-specific gene expression of oligodendrocyte precursors (opc), potentially reflecting the contribution of these cells to myelin generation by giving rise to myelinating oligodendrocytes during development (Bergles and Richardson, 2016; Bergles et al., 2000; Fernandez-Castaneda and Gaultier, 2016; Miller, 1996; Simons and Nave, 2016) and to

myelin regulation and metabolic support of myelinated axons in the adult neural circuits (Bergles and Richardson, 2016; Simons and Nave, 2016; Xiao et al., 2022). Finally, we find that the dominant dynamic signature of neural activity covaries with the granular cortical layer IV, consistent with the idea that this layer receives prominent subcortical (including thalamic) feedforward projections (Douglas and Martin, 2004; Scheeringa and Fries, 2019).

The present findings must be interpreted with respect to several methodological considerations. First, we used MEG data from a subset of individuals with no familial relationships from the HCP dataset. Although all the presented analysis are performed using the group-level data, future work with larger sample sizes can provide more generalizable outcomes. Larger sample sizes will also help go beyond associative analysis and allow for predictive analysis of neural dynamics and micro-architecture in unseen datasets. Second, MEG is susceptible to low signal-to-noise ratio and has variable sensitivity to neural activity from different regions. Thus, electrophysiological recordings with higher spatial resolution, such as intracranial electroencephalography (iEEG and ECoG), may provide more precise measures of neural dynamics that can be examined with respect to cortical micro-architecture. Finally, despite the fact that we attempt to use a near-comprehensive list of time-series properties and multiple micro-architectural features, neither the time-series features nor the micro-architectural maps are exhaustive sets of measures. Moreover, micro-architectural features are group-average maps that are compiled from different datasets. Multi-modal datasets from the same individuals are required to perform individual-level comparisons between the dynamical and micro-architectural atlases.

Altogether, using an unbiased, data-driven approach, the present findings show that neurophysiological signatures of cortical micro-architecture are hierarchically organized across the cortex, reflecting the underlying circuit properties. Importantly, these findings highlight the importance of conventional approaches in studying the characteristics of neurophysiological activity, while also introducing less-commonly used time-series features that covary with cortical micro-architecture, such as fluctuation analysis. Collectively, this work opens new avenues for studying the anatomical basis of neurophysiological activity.

5.6 Methods

5.6.1 Dataset: Human Connectome Project (HCP)

Resting state magnetoencephalography (MEG) data from a sample of healthy young adults ($n = 33$; age range 22-35 years) with no familial relationships were obtained from Human Connectome Project (HCP; S900 release (Van Essen et al., 2013)). The data includes resting state scans of approximately 6 minutes long (sampling rate = 2034.5 Hz; anti-aliasing low-pass filter at 400 Hz) and noise recordings for all participants. MEG anatomical data and 3T structural magnetic resonance imaging (MRI) data of all participants were also obtained for MEG pre-processing.

5.6.2 Resting state magnetoencephalography (MEG)

Resting state MEG data was analyzed using `Brainstorm` software, which is documented and freely available for download online under the GNU general public license (Tadel et al., 2011; http://neuroimage.usc.edu/brainstorm). The MEG recordings were registered to the structural MRI scan of each individual using the anatomical transformation matrix provided by HCP for co-registration, following the procedure described in `Brainstorm`'s online tutorials for the HCP dataset (https://neuroimage.usc.edu/brainstorm/Tutorials/HCP-MEG). The data were downsampled to 1/4 of the original sampleing rate(i.e 509 Hz) to facilitate processing. The pre-processing was performed by applying notch filters at 60, 120, 180, 240, and 300 Hz, and was followed by a high-pass filter at 0.3 Hz to remove slow-wave and DC-offset artifacts. Bad channels were marked based on the information obtained through the data management platform of HCP for MEG data (ConnectomeDB; https://db.humanconnectome.org/). The artifacts (including heartbeats, eye blinks, saccades, muscle movements, and noisy segments) were then removed from the recordings using automatic procedures as proposed by `Brainstorm`. More specifically, electrocardiogram (ECG) and electrooculogram (EOG) recordings were used to detect heartbeats and blinks, respectively. We then used Signal-Space Projections (SSP) to automatically remove the detected artifacts. We also used SSP to remove saccades and muscle activity as low-frequency (1-7 Hz) and high-frequency (40-240 Hz) components, respectively.

The pre-processed sensor-level data was then used to obtain a source estimation on HCP's fsLR4k cortical surface for each participant. Head models were computed using overlapping spheres and the data and noise covariance matrices were estimated from the resting state MEG and noise recordings. Linearly constrained minimum variance (LCMV)

beamformering from `Brainstorm` was then used to obtain the source activity for each participant. We performed data covariance regularization to avoid the instability of data covariance inversion due to the smallest eigenvalues. Data covariance regularization was performed using the "median eigenvalue" method from Brainstorm (Tadel et al., 2011), such that the eigenvalues of the eigenspectrum of data covariance that were smaller than the median eigenvalue were replaced with the median eigenvalue itself. The estimated source variance was also normalized by the noise covariance matrix to reduce the effect of variable source depth. Source orientations were constrained to be normal to the cortical surface at each of the 8,000 vertex locations on the fsLR4k surface. Finally, source-level time-series were parcellated into 100 regions using the Schaefer-100 atlas (Schaefer et al., 2018), such that a given parcel's time series was estimated as the first principal component of its constituting sources' time series.

5.6.3 Power spectral analysis

Welch's method was used to estimate power spectrum density (PSD) from the source-level time-series, using overlapping windows of length 4 seconds with 50% overlap. Average power at each frequency band was then calculated for each vertex (i.e. source). Source-level power data were parcellated into 100 regions using the Schaefer-100 atlas (Schaefer et al., 2018) for each participant at six canonical electrophysiological bands (i.e., delta (δ: 2-4 Hz), theta (θ: 5-7 Hz), alpha (α: 8-12 Hz), beta (β: 15-29 Hz), low gamma (lo-γ: 30-59 Hz), and high gamma (hi-γ: 60-90Hz)). The vertex-level power maps are publicly available via the `neuromaps` toolbox on the fsLR4k surface (Markello et al., 2022).

5.6.4 Intrinsic timescale

The intrinsic timescale of each brain region was estimated using spectral parameterization with the FOOOF algorithm (Donoghue et al., 2020). Specifically, the source-level power spectral density were used to extract the neural timescale at each vertex and for each individual using the procedure described by (Gao et al., 2020). The FOOOF algorithm decomposes the power spectra into periodic (oscillatory) and aperiodic ($1/f$-like) components by fitting the power spectral density in the log-log space and identifying the oscillatory peaks as the periodic components and the "knee parameter" k that controls for the bend in the aperiodic component (Donoghue et al., 2020; Gao et al., 2020). The knee parameter k can then be used to calculate the "knee frequency" as $f_k = k^{1/2}$, which is the

frequency where a knee or a bend occurs in the power spectrum density (Gao et al., 2020). Finally, the intrinsic timescale τ is estimated as (Gao et al., 2020):

$$\tau = \frac{1}{2\pi f_k} \tag{5.1}$$

We used the FOOOF algorithm to fit the power spectral density with with "knee" aperiodic mode and maximum number of 2 peaks over the frequency range of 1-60 Hz. Note that since the first notch filter was applied at 60 Hz during the pre-processing analysis, we did not fit the model above 60 Hz. Intrinsic timescale τ was estimated for each vertex and was parcellated using the Schaefer-100 atlas (Schaefer et al., 2018). Vertex-level intrinsic timescale map is publicly available at the `neuromaps` toolbox on the fsLR4k surface (Markello et al., 2022).

5.6.5 Time-series feature extraction using `hctsa`

We used the highly comparative time-series analysis toolbox, `hctsa` (Fulcher and Jones, 2017; Fulcher et al., 2013), to perform a massive feature extraction of the time-series for each brain area for each participant. The `hctsa` package extracted over 7 000 local time-series features using a wide range of operations based on time-series analysis (Fulcher and Jones, 2017; Fulcher et al., 2013). The extracted features include, but are not limited to, measures of data distribution, temporal dependency and correlation properties, entropy and variability, parameters of time-series model fit, and nonlinear properties of a given time-series (Fulcher, 2018; Fulcher et al., 2013).

The `hctsa` feature extraction analysis was performed on the parcellated MEG time-series. Given that applying `hctsa` on the full time-series is computationally expensive, we used 80 seconds of data for feature extraction after dropping the first 30 seconds. Previous reports suggest that relatively short segments of about 30 to 120 seconds of resting-state data are sufficient to estimate robust properties of intrinsic brain activity (Wiesman et al., 2022). Nevertheless, to ensure that we can robustly estimate time-series features from 80 seconds of data, we calculated a subset of `hctsa` features using the `Catch-22` toolbox (Lubba et al., 2019) on subsequent segments of time-series with varying length for each participant. Specifically, we extracted time-series features from short segments of data ranging from 5 to 125 seconds in increments of 5 seconds. To identify the optimal time-series length required to estimate robust and stable features, we calculated the Pearson correlation coefficient between features of two subsequent segments (e.g. features estimated from 10 and 5 seconds of data). The correlation coefficient between the estimated

features started to stabilize at time-series segments of around 30 seconds, consistent with previous reports (Wiesman et al., 2022) (Figure S5.2). Following the feature extraction procedure, the outputs of the operations that produced errors were removed and the remaining features (6,880 features) were normalized across nodes using an outlier-robust sigmoidal transform.

5.6.6 `neuromaps` data

We used the `neuromaps` toolbox (https://github.com/netneurolab/neuromaps) (Markello et al., 2022) to obtain micro-architectural and neurotransmitter receptor and transporter maps in their native spaces. Details about all maps and their data sources are available in (Markello et al., 2022). Briefly, all data that were originally available in any surface space were transformed to the fsLR32k surface space using linear interpolation to resample data and were parcellated into 100 cortical regions using the Schaefer atlas in fsLR32k space (Schaefer et al., 2018). All volumetric data were retained in their native MNI152 volumetric space and were parcellated into 100 cortical regions using the volumetric Schaefer atlas in MNI152 space (Schaefer et al., 2018). Micro-architectural maps included T1w:T2w as a proxy measure of cortical myelin (Glasser et al., 2016), cortical thickness (Glasser et al., 2016), principal component of gene expression (Hawrylycz et al., 2012; Markello et al., 2021), principal component of neurotransmitter receptors and transporters (Hansen et al., 2022), synapse density (using $[^{11}C]$UCB-J PET tracer that binds to the synaptic vesicle glycoprotein 2A (SV2A)) (Bini et al., 2020; Chen et al., 2018, 2021; Finnema et al., 2016, 2018, 2019, 2020; Holmes et al., 2019; Mecca et al., 2020; O'Dell et al., 2021; Radhakrishnan et al., 2021; Smart et al., 2021; Weiss et al., 2021), metabolism (i.e. cerebral blood flow and volume, oxygen and glucose metabolism, glycolytic index) (Vaishnavi et al., 2010), evolutionary and developmental expansion (Hill et al., 2010), allometric scaling from Philadelphia Neurodevelopmental Cohort (PNC) and National Institutes of Health (NIH) (Reardon et al., 2018). Neurotransmitter maps included 18 different neurotransmitter receptors and transporters across 9 different neurotransmitter systems, namely serotonin (5-HT1a, 5-HT1b, 5-HT2a, 5-HT4, 5-HT6, 5-HTT), histamine (H3), dopamine (D1, D2, DAT), norepinephrine (NET), acetylcholine ($\alpha 4\beta 2$, M1, VAChT), cannabinoid (CB1), opioid (MOR), glutamate (mGluR5), and GABA (GABAa/bz) (Hansen et al., 2022).

5.6.7 BigBrain histological data

Layer thickness data for the 6 cortical layers (I-VI) were obtained from the BigBrain atlas, which is a volumetric, high-resolution ($20 \times 20 \times 20\mu m$) histological atlas of a post mortem human brain (Amunts et al., 2013; Paquola et al., 2021; Wagstyl et al., 2020). In the BigBrain atlas, sections of the post mortem brain are stained for cell bodies using Merker staining technique (Merker, 1983). These sections are then imaged and used to reconstruct a volumetric histological atlas of the human brain that reflects neuronal density and soma size and captures the regional differentiation of cytoarchitecture (Amunts et al., 2013; Paquola et al., 2019, 2021; Wagstyl et al., 2018, 2020). The approximate cortical layer thickness data obtained from the BigBrainWarp toolbox (Paquola et al., 2021), were originally generated using a convolutional neural network that automatically segments the cortical layers from the pial to white surfaces (Wagstyl et al., 2020). Full description of how the cortical layer thickness was approximated is available elsewhere (Wagstyl et al., 2020). The cortical layer thickness data for the 6 cortical layers were obtained on the *fsaverage* surface (164k vertices) from the BigBrainWarp toolbox (Paquola et al., 2021) and were parcellated into 100 cortical regions using the Schaefer-100 atlas (Schaefer et al., 2018).

5.6.8 Cell type-specific gene expression

Regional microarray expression data were obtained from 6 post-mortem brains (1 female, ages 24.0–57.0, 42.50 ± 13.38) provided by the Allen Human Brain Atlas (AHBA, https://human.brain-map.org; (Hawrylycz et al., 2012)). Data were processed with the abagen toolbox (version 0.1.3-doc; https://github.com/rmarkello/abagen; (Markello et al., 2021)) using the Schaefer-100 volumetric atlas in MNI space (Schaefer et al., 2018).

First, microarray probes were reannotated using data provided by (Arnatkevičiūtė et al., 2019); probes not matched to a valid Entrez ID were discarded. Next, probes were filtered based on their expression intensity relative to background noise (Quackenbush, 2002), such that probes with intensity less than the background in $\geq 50.00\%$ of samples across donors were discarded. When multiple probes indexed the expression of the same gene, we selected and used the probe with the most consistent pattern of regional variation across donors (i.e., differential stability; (Hawrylycz et al., 2015)), calculated with:

$$\Delta_S(p) = \frac{1}{\binom{N}{2}} \sum_{i=1}^{N-1} \sum_{j=i+1}^{N} \rho[B_i(p), B_j(p)] \tag{5.2}$$

where ρ is Spearman rank correlation of the expression of a single probe, p, across regions in two donors B_i and B_j, and N is the total number of donors. Here, regions correspond to the structural designations provided in the ontology from the AHBA.

The MNI coordinates of tissue samples were updated to those generated via non-linear registration using the Advanced Normalization Tools (ANTs; https://github.com/chrisfilo/alleninf). To increase spatial coverage, tissue samples were mirrored bilaterally across the left and right hemispheres (Romero-Garcia et al., 2018). Samples were assigned to brain regions in the provided atlas if their MNI coordinates were within 2 mm of a given parcel. If a brain region was not assigned a tissue sample based on the above procedure, every voxel in the region was mapped to the nearest tissue sample from the donor in order to generate a dense, interpolated expression map. The average of these expression values was taken across all voxels in the region, weighted by the distance between each voxel and the sample mapped to it, in order to obtain an estimate of the parcellated expression values for the missing region. All tissue samples not assigned to a brain region in the provided atlas were discarded.

Inter-subject variation was addressed by normalizing tissue sample expression values across genes using a robust sigmoid function (Fulcher et al., 2013):
where ρ is Spearman's rank correlation of the expression of a single probe, p, across regions in two donors B_i and B_j, and N is the total number of donors. Here, regions correspond to the structural designations provided in the ontology from the AHBA.

The MNI coordinates of tissue samples were updated to those generated via non-linear registration using the Advanced Normalization Tools (ANTs; https://github.com/chrisfilo/alleninf). To increase spatial coverage, tissue samples were mirrored bilaterally across the left and right hemispheres (Romero-Garcia et al., 2018). Samples were assigned to brain regions in the provided atlas if their MNI coordinates were within 2 mm of a given parcel. If a brain region was not assigned a tissue sample based on the above procedure, every voxel in the region was mapped to the nearest tissue sample from the donor in order to generate a dense, interpolated expression map. The average of these expression values was taken across all voxels in the region, weighted by the distance between each voxel and the sample mapped to it, in order to obtain an estimate of the parcellated expression values for the missing region. All tissue samples not assigned to a brain region in the provided atlas were discarded.

Inter-subject variation was addressed by normalizing tissue sample expression values across genes using a robust sigmoid function (Fulcher et al., 2013):

$$x_{norm} = \frac{1}{1 + \exp(-\frac{(x - \langle x \rangle)}{\text{IQR}_x})} \tag{5.3}$$

where $\langle x \rangle$ is the median and IQR_x is the normalized interquartile range of the expression of a single tissue sample across genes. Normalized expression values were then rescaled to the unit interval:

$$x_{scaled} = \frac{x_{norm} - \min(x_{norm})}{\max(x_{norm}) - \min(x_{norm})} \tag{5.4}$$

Gene expression values were then normalized across tissue samples using an identical procedure. Samples assigned to the same brain region were averaged separately for each donor and then across donors, yielding a regional expression matrix of 15,633 genes.

Finally, cell type-specific gene expression maps were calculated using gene sets identified by a cell type deconvolution analysis (Di Biase et al., 2022; Hansen et al., 2021; Seidlitz et al., 2020). Detailed description of the analysis is available at (Seidlitz et al., 2020). Briefly, cell-specific gene sets were compiled across 5 single-cell and single-nucleus RNA sequencing studies of adult human post-mortem cortical samples (Darmanis et al., 2015; Habib et al., 2017; Lake et al., 2018; Li et al., 2018; McKenzie et al., 2018; Zhang et al., 2016). Gene expression maps of the compiled study-specific cell types were obtained from AHBA. Unsupervised hierarchical clustering analysis was used to identify 7 canonical cell classes that included astrocytes (astro), endothelial cells (endo), microglia (micro), excitatory neurons (neuron-ex), inhibitory neurons (neuron-in), oligodendrocytes (oligo) and oligodendrocyte precursors (opc). We then used the resulting gene sets to obtain average cell type-specific expression maps for each of these 7 cell classes from the regional expression matrix of 15,633 genes.

5.6.9 Partial Least Squares (PLS)

Partial least squares (PLS) analysis was used to investigate the relationship between resting-state MEG time-series features and micro-architecture maps. PLS is a multivariate statistical technique that identifies mutually orthogonal, weighted linear combinations of the original variables in the two datasets that maximally covary with each other, namely the latent variables (McIntosh and Mišić, 2013; McIntosh and Lobaugh, 2004). In the present analysis, one dataset is the `hctsa` feature matrix (i.e. $\mathbf{X}_{n \times t}$) with $n = 100$ rows as brain regions and $t = 6880$ columns as time-series features. The other dataset is the compiled set of micro-architectural maps (i.e. $\mathbf{Y}_{n \times m}$) with $n = 100$ rows (brain regions)

and $m = 45$ columns (micro-architecture maps). To identify the latent variables, both data matrices were normalized column-wise (i.e. z-scored) and a singular value decomposition was applied to the correlation matrix $\mathbf{R} = \mathbf{X}'\mathbf{Y}$ as follows:

$$\mathbf{R} = \mathbf{X}'\mathbf{Y} = \mathbf{USV}' \tag{5.5}$$

where $\mathbf{U}_{t\times m}$ and $\mathbf{V}_{m\times m}$ are orthonormal matrices of left and right singular vectors and $\mathbf{S}_{m\times m}$ is the diagonal matrix of singular values. Each column of $\mathbf{U}$ and $\mathbf{V}$ matrices corresponds to a latent variable. Each element of the diagonal of $\mathbf{S}$ is the corresponding singular value. The singular values are proportional to the covariance explained by latent variable and can be used to calculate effect sizes as $\eta_i = s_i^2 / \sum_{j=1}^{J} s_j^2$ where η_i is the effect size for the i-th latent variable (LV_i), s_i is the corresponding singular value, and J is the total number of singular values (here $J = m$). The left and right singular vectors $\mathbf{U}$ and $\mathbf{V}$ demonstrate the extent to which the time-series features and micro-architectural maps contribute to latent variables, respectively. Time-series features with positive weights covary with micro-architectural maps with positive weights, while negatively weighted time-series features and micro-architectural maps covary together. Singular vectors can be used to estimate brain scores that demonstrate the extent to which each brain region expresses the weighted patterns identified by latent variables. Brain scores for time-series features and micro-architectural maps are calculated by projecting the original data onto the PLS-derived weights (i.e., $\mathbf{U}$ and $\mathbf{V}$):

$$\text{Brain scores for time-series features} = \mathbf{XU}$$
$$\text{Brain scores for micro-architecture} = \mathbf{YV}$$

Loadings for time-series features and micro-architectural maps are then computed as the Pearson correlation coefficient between the original data matrices and their corresponding brain scores. For example, time-series feature loadings are the correlation coefficients between the original `hctsa` time-series feature vectors and PLS-derived brain scores for time-series features.

The statistical significance of latent variables was assessed using 10,000 permutation tests, where the original data was randomized using spatial autocorrelation-preserving nulls (see *Null model* for more details). The PLS analysis was repeated for each permutation, resulting in a null distribution of singular values. The significance of the original singular values were then assessed against the permuted null distributions (Figure 5.4a). The

reliability of PLS loadings was estimated using bootstrap resampling (Efron and Tibshirani, 1986), where rows of the original data matrices **X** and **Y** are randomly resampled with replacement 10,000 times. The PLS analysis was then repeated for each resampled data, generating a sampling distribution for each time-series feature and micro-architectural map (i.e. generating 10,000 bootstrap-resampled loadings). The bootstrap-resampled loading distributions are then used to estimate 95% confidence intervals for loadings (e.g. see Figure 5.4d).

Finally, given that PLS-derived brain scores are by design highly correlated, we used a distance-dependent cross-validation analysis with spatial autocorrelation-preserving nulls to (a) assess the out-of-sample correlations between brain scores, and (b) ensure that the observed association between brain scores goes beyond the spatial autocorrelation inherent to the data (Hansen et al., 2021). Specifically, 75% of the closest brain regions in Euclidean distance to a random "seed" region were selected as training set, while the 25% remaining distant regions were selected as test set. We then re-ran the PLS analysis on the training set (i.e. 75% of regions) and used the resulting weights (i.e. singular values) to estimated brain scores for test set. The out-of-sample correlation was then calculated as the Pearson correlation coefficient between test set brain scores of time-series features and micro-architectural maps. We repeated this analysis 99 times, such that each time a random brain region was selected as the seed region, yielding distributions of training set brain scores correlations and test set (out-of-sample) correlations. Note that 99 is the maximum number of train-test splits here given that brain maps consist of 100 regions. The significance of the mean out-of-sample correlation was assessed against 1,000 permuted null models, where the cross-validation analysis was repeated using randomized data with preserved spatial autocorrelation and a null distribution of out-of-sample correlations were generated (Figure 5.4b).

5.6.10 Null model

To make inferences about the topographic correlations between any two brain maps, we implement a null model that systematically disrupts the relationship between two topographic maps but preserves their spatial autocorrelation (Alexander-Bloch et al., 2018; Markello and Misic, 2021; Váša and Mišić, 2022). We used the Schaefer-100 atlas in the HCP's fsLR32k grayordinate space (Schaefer et al., 2018; Van Essen et al., 2013). The spherical projection of the fsLR32k surface was used to define spatial coordinates for each parcel by selecting the vertex closest to the center-of-mass of each parcel (Shafiei et al., 2020a; Vázquez-Rodríguez et al., 2019; Vazquez-Rodriguez et al., 2020). The resulting spatial

coordinates were used to generate null models by applying randomly-sampled rotations and reassigning node values based on the closest resulting parcel (10,000 repetitions). The rotation was applied to one hemisphere and then mirrored to the other hemisphere.

5.6.11 Code and data availability

Code used to conduct the reported analyses is available on GitHub (https://github.com/netneurolab/shafiei_megtimeseries). Data used in this study were obtained from the Human Connectome Project (HCP) database (available at https://db.humanconnectome.org/).

5.7 Acknowledgments

BM acknowledges support from the Natural Sciences and Engineering Research Council of Canada (NSERC), Canadian Institutes of Health Research (CIHR), Brain Canada Foundation Future Leaders Fund, the Canada Research Chairs Program, the Michael J. Fox Foundation, and the Healthy Brains for Healthy Lives initiative. SB acknowledges support from the NIH (R01 EB026299), a Discovery grant from the Natural Science and Engineering Research Council of Canada (NSERC 436355-13), the CIHR Canada research Chair in Neural Dynamics of Brain Systems, the Brain Canada Foundation with support from Health Canada, and the Innovative Ideas program from the Canada First Research Excellence Fund, awarded to McGill University for the Healthy Brains for Healthy Lives initiative. GS acknowledges support from the Natural Sciences and Engineering Research Council of Canada (NSERC) and the Fonds de recherche du Québec - Nature et Technologies (FRQNT).

5.8 Bibliography

Alexander-Bloch, A. F. et al. (2018). "On testing for spatial correspondence between maps of human brain structure and function". *Neuroimage*, 178, pp. 540–551.

Amunts, K. et al. (2013). "BigBrain: an ultrahigh-resolution 3D human brain model". *Science*, 340(6139), pp. 1472–1475.

Arnatkevičiūtė, A., B. D. Fulcher, and A. Fornito (2019). "A practical guide to linking brain-wide gene expression and neuroimaging data". *Neuroimage*, 189, pp. 353–367.

Avena-Koenigsberger, A., B. Mišić, and O. Sporns (2018). "Communication dynamics in complex brain networks". *Nature Reviews Neuroscience*, 19(1), p. 17.

Baillet, S. (2017). "Magnetoencephalography for brain electrophysiology and imaging". *Nature neuroscience*, 20(3), pp. 327–339.

Baillet, S., J. C. Mosher, and R. M. Leahy (2001). "Electromagnetic brain mapping". *IEEE Signal processing magazine*, 18(6), pp. 14–30.

Baldassano, C. et al. (2017). "Discovering event structure in continuous narrative perception and memory". *Neuron*, 95(3), pp. 709–721.

Bargmann, C. I. and E. Marder (2013). "From the connectome to brain function". *Nature methods*, 10(6), pp. 483–490.

Bastos, A. M. et al. (2020). "Layer and rhythm specificity for predictive routing". *Proceedings of the National Academy of Sciences*, 117(49), pp. 31459–31469.

Beliveau, V. et al. (2017). "A high-resolution in vivo atlas of the human brain's serotonin system". *Journal of Neuroscience*, 37(1), pp. 120–128.

Berger, H. (1929). "Über das elektroenkephalogramm des menschen". *Archiv für psychiatrie und nervenkrankheiten*, 87(1), pp. 527–570.

Bergles, D. E. and W. D. Richardson (2016). "Oligodendrocyte development and plasticity". *Cold Spring Harbor perspectives in biology*, 8(2), a020453.

Bergles, D. E. et al. (2000). "Glutamatergic synapses on oligodendrocyte precursor cells in the hippocampus". *Nature*, 405(6783), pp. 187–191.

Bini, J. et al. (2020). "Human adult and adolescent biodistribution and dosimetry of the synaptic vesicle glycoprotein 2A radioligand 11 C-UCB-J". *EJNMMI research*, 10(1), pp. 1–8.

Bomkamp, C. et al. (2019). "Transcriptomic correlates of electrophysiological and morphological diversity within and across excitatory and inhibitory neuron classes". *PLoS computational biology*, 15(6), e1007113.

Bryce, R. and K. Sprague (2012). "Revisiting detrended fluctuation analysis". *Scientific reports*, 2(1), pp. 1–6.

Bullmore, E. and O. Sporns (2009). "Complex brain networks: graph theoretical analysis of structural and functional systems". *Nature Reviews Neuroscience*, 10(3), pp. 186–198.

Burt, J. B. et al. (2018). "Hierarchy of transcriptomic specialization across human cortex captured by structural neuroimaging topography". *Nat Neurosci*, 21(9), pp. 1251–1259.

Buzsáki, G., C. A. Anastassiou, and C. Koch (2012). "The origin of extracellular fields and currents—EEG, ECoG, LFP and spikes". *Nature reviews neuroscience*, 13(6), pp. 407–420.

Buzsaki, G. and A. Draguhn (2004). "Neuronal oscillations in cortical networks". *science*, 304(5679), pp. 1926–1929.

Buzsáki, G., N. Logothetis, and W. Singer (2013). "Scaling brain size, keeping timing: evolutionary preservation of brain rhythms". *Neuron*, 80(3), pp. 751–764.

Chen, M.-K. et al. (2018). "Assessing synaptic density in Alzheimer disease with synaptic vesicle glycoprotein 2A positron emission tomographic imaging". *JAMA neurology*, 75(10), pp. 1215–1224.

Chen, M.-K. et al. (2021). "Comparison of [11C] UCB-J and [18F] FDG PET in Alzheimer's disease: A tracer kinetic modeling study". *Journal of Cerebral Blood Flow & Metabolism*, p. 0271678X211004312.

Darmanis, S. et al. (2015). "A survey of human brain transcriptome diversity at the single cell level". *Proceedings of the National Academy of Sciences*, 112(23), pp. 7285–7290.

Das, A. et al. (2022). "Spontaneous neuronal oscillations in the human insula are hierarchically organized traveling waves". *eLife*, 11, e76702.

Demirtaş, M. et al. (2019). "Hierarchical heterogeneity across human cortex shapes large-scale neural dynamics". *Neuron*, 101(6), pp. 1181–1194.

Di Biase, M. A. et al. (2022). "Cell type-specific manifestations of cortical thickness heterogeneity in schizophrenia". *Molecular Psychiatry*, pp. 1–9.

Donoghue, T. and B. Voytek (2022). "Automated meta-analysis of the event-related potential (ERP) literature". *Scientific Reports*, 12(1), pp. 1–12.

Donoghue, T. et al. (2020). "Parameterizing neural power spectra into periodic and aperiodic components". *Nature neuroscience*, 23(12), pp. 1655–1665.

Douglas, R. J. and K. A. Martin (2004). "Neuronal circuits of the neocortex". *Annu. Rev. Neurosci.*, 27, pp. 419–451.

Dukart, J. et al. (2021). *JuSpace: A tool for spatial correlation analyses of magnetic resonance imaging data with nuclear imaging derived neurotransmitter maps*. Tech. rep. Wiley Online Library.

Efron, B. and R. Tibshirani (1986). "Bootstrap methods for standard errors, confidence intervals, and other measures of statistical accuracy". *Stat Sci*, pp. 54–75.

Engel, A. K., P. Fries, and W. Singer (2001). "Dynamic predictions: oscillations and synchrony in top–down processing". *Nature Reviews Neuroscience*, 2(10), pp. 704–716.

Engel, A. K. et al. (1997). "Role of the temporal domain for response selection and perceptual binding." *Cerebral cortex (New York, NY: 1991)*, 7(6), pp. 571–582.

Fernandez-Castaneda, A. and A. Gaultier (2016). "Adult oligodendrocyte progenitor cells–multifaceted regulators of the CNS in health and disease". *Brain, behavior, and immunity*, 57, pp. 1–7.

Finnema, S. J. et al. (2016). "Imaging synaptic density in the living human brain". *Science translational medicine*, 8(348), 348ra96–348ra96.

Finnema, S. J. et al. (2018). "Kinetic evaluation and test–retest reproducibility of [11C] UCB-J, a novel radioligand for positron emission tomography imaging of synaptic vesicle glycoprotein 2A in humans". *Journal of Cerebral Blood Flow & Metabolism*, 38(11), pp. 2041–2052.

Finnema, S. J. et al. (2019). "A single-center, open-label positron emission tomography study to evaluate brivaracetam and levetiracetam synaptic vesicle glycoprotein 2A binding in healthy volunteers". *Epilepsia*, 60(5), pp. 958–967.

Finnema, S. J. et al. (2020). "Reduced synaptic vesicle protein 2A binding in temporal lobe epilepsy: A [11C] UCB-J positron emission tomography study". *Epilepsia*, 61(10), pp. 2183–2193.

Florin, E. and S. Baillet (2015). "The brain's resting-state activity is shaped by synchronized cross-frequency coupling of neural oscillations". *Neuroimage*, 111, pp. 26–35.

Frauscher, B. et al. (2018). "High-frequency oscillations in the normal human brain". *Annals of neurology*, 84(3), pp. 374–385.

Fries, P. (2005). "A mechanism for cognitive dynamics: neuronal communication through neuronal coherence". *Trends in cognitive sciences*, 9(10), pp. 474–480.

Fulcher, B. D. (2018). "Feature-based time-series analysis". In: *Feature Engineering for Machine Learning and Data Analytics*. CRC Press, pp. 87–116.

Fulcher, B. D. and N. S. Jones (2017). "hctsa: A computational framework for automated time-series phenotyping using massive feature extraction". *Cell systems*, 5(5), pp. 527–531.

Fulcher, B. D., M. A. Little, and N. S. Jones (2013). "Highly comparative time-series analysis: the empirical structure of time series and their methods". *Journal of the Royal Society Interface*, 10(83), p. 20130048.

Fulcher, B. D. et al. (2019). "Multimodal gradients across mouse cortex". *Proc Natl Acad Sci USA*, 116(10), pp. 4689–4695.

Gao, R. et al. (2020). "Neuronal timescales are functionally dynamic and shaped by cortical microarchitecture". *Elife*, 9, e61277.

Glasser, M. F. and D. C. Van Essen (2011). "Mapping human cortical areas in vivo based on myelin content as revealed by T1-and T2-weighted MRI". *Journal of Neuroscience*, 31(32), pp. 11597–11616.

Glasser, M. F. et al. (2016). "A multi-modal parcellation of human cerebral cortex". *Nature*, 536(7615), pp. 171–178.

Habib, N. et al. (2017). "Massively parallel single-nucleus RNA-seq with DroNc-seq". *Nature methods*, 14(10), pp. 955–958.

Hämäläinen, M. et al. (1993). "Magnetoencephalography—theory, instrumentation, and applications to noninvasive studies of the working human brain". *Reviews of modern Physics*, 65(2), p. 413.

Hansen, J. et al. (2022). "Mapping neurotransmitter systems to the structural and functional organization of the human neocortex". *bioRxiv*.

Hansen, J. Y. et al. (2021). "Mapping gene transcription and neurocognition across human neocortex". *Nature Human Behaviour*, 5(9), pp. 1240–1250.

Hardstone, R. et al. (2012). "Detrended fluctuation analysis: a scale-free view on neuronal oscillations". *Frontiers in physiology*, 3, p. 450.

Hasson, U. et al. (2008). "A hierarchy of temporal receptive windows in human cortex". *J Neurosci*, 28(10), pp. 2539–2550.

Hawrylycz, M. et al. (2015). "Canonical genetic signatures of the adult human brain". *Nature neuroscience*, 18(12), pp. 1832–1844.

Hawrylycz, M. J. et al. (2012). "An anatomically comprehensive atlas of the adult human brain transcriptome". *Nature*, 489(7416), p. 391.

He, B. J. (2014). "Scale-free brain activity: past, present, and future". *Trends in cognitive sciences*, 18(9), pp. 480–487.

Hill, J. et al. (2010). "Similar patterns of cortical expansion during human development and evolution". *Proceedings of the National Academy of Sciences*, 107(29), pp. 13135–13140.

Holmes, S. E. et al. (2019). "Lower synaptic density is associated with depression severity and network alterations". *Nature communications*, 10(1), pp. 1–10.

Honey, C. J. et al. (2012). "Slow cortical dynamics and the accumulation of information over long timescales". *Neuron*, 76(2), pp. 423–434.

Huntenburg, J. M., P.-L. Bazin, and D. S. Margulies (2018). "Large-scale gradients in human cortical organization". *Trends in cognitive sciences*, 22(1), pp. 21–31.

Huntenburg, J. M. et al. (2017). "A systematic relationship between functional connectivity and intracortical myelin in the human cerebral cortex". *Cereb Cortex*, 27(2), pp. 981–997.

Ito, T., L. J. Hearne, and M. W. Cole (2020). "A cortical hierarchy of localized and distributed processes revealed via dissociation of task activations, connectivity changes, and intrinsic timescales". *NeuroImage*, 221, p. 117141.

Kiebel, S. J., J. Daunizeau, and K. J. Friston (2008). "A hierarchy of time-scales and the brain". *PLoS Comput BIol*, 4(11).

Knudsen, G. M. et al. (2020). "Guidelines for the content and format of PET brain data in publications and archives: A consensus paper". *Journal of Cerebral Blood Flow & Metabolism*, 40(8), pp. 1576–1585.

Kopell, N. J. et al. (2014). "Beyond the connectome: the dynome". *Neuron*, 83(6), pp. 1319–1328.

Lake, B. B. et al. (2018). "Integrative single-cell analysis of transcriptional and epigenetic states in the human adult brain". *Nature biotechnology*, 36(1), pp. 70–80.

Li, M. et al. (2018). "Integrative functional genomic analysis of human brain development and neuropsychiatric risks". *Science*, 362(6420), eaat7615.

Lubba, C. H. et al. (2019). "catch22: Canonical time-series characteristics". *Data Mining and Knowledge Discovery*, 33(6), pp. 1821–1852.

Mahjoory, K. et al. (2020). "The frequency gradient of human resting-state brain oscillations follows cortical hierarchies". *Elife*, 9, e53715.

Margulies, D. S. et al. (2016). "Situating the default-mode network along a principal gradient of macroscale cortical organization". *Proceedings of the National Academy of Sciences*, 113(44), pp. 12574–12579.

Markello, R. D. and B. Misic (2021). "Comparing spatial null models for brain maps". *NeuroImage*, 236, p. 118052.

Markello, R. D. et al. (2021). "Standardizing workflows in imaging transcriptomics with the abagen toolbox". *Elife*, 10, e72129.

Markello, R. D. et al. (2022). "Neuromaps: structural and functional interpretation of brain maps". *bioRxiv*.

Martins, D. et al. (2021). "Imaging transcriptomics: Convergent cellular, transcriptomic, and molecular neuroimaging signatures in the healthy adult human brain". *Cell reports*, 37(13), p. 110173.

McIntosh, A. R. and B. Mišić (2013). "Multivariate statistical analyses for neuroimaging data". *Annual review of psychology*, 64, pp. 499–525.

McIntosh, A. R. and N. J. Lobaugh (2004). "Partial least squares analysis of neuroimaging data: applications and advances". *Neuroimage*, 23, S250–S263.

McKenzie, A. T. et al. (2018). "Brain cell type specific gene expression and co-expression network architectures". *Scientific reports*, 8(1), pp. 1–19.

Mecca, A. P. et al. (2020). "In vivo measurement of widespread synaptic loss in Alzheimer's disease with SV2A PET". *Alzheimer's & Dementia*, 16(7), pp. 974–982.

Merker, B. (1983). "Silver staining of cell bodies by means of physical development". *Journal of neuroscience methods*, 9(3), pp. 235–241.

Miller, R. H. (1996). "Oligodendrocyte origins". *Trends in neurosciences*, 19(3), pp. 92–96.

Murakami, S. and Y. Okada (2006). "Contributions of principal neocortical neurons to magnetoencephalography and electroencephalography signals". *The Journal of physiology*, 575(3), pp. 925–936.

Murray, J. D. et al. (2014). "A hierarchy of intrinsic timescales across primate cortex". *Nat Neurosci*, 17(12), p. 1661.

Nørgaard, M. et al. (2021). "A high-resolution in vivo atlas of the human brain's benzodiazepine binding site of GABAA receptors". *NeuroImage*, 232, p. 117878.

Norgaard, M. et al. (2022). "PET-BIDS, an extension to the brain imaging data structure for positron emission tomography". *Scientific data*, 9(1), pp. 1–7.

O'Dell, R. S. et al. (2021). "Association of Aβ deposition and regional synaptic density in early Alzheimer's disease: a PET imaging study with [11 C] UCB-J". *Alzheimer's Research & Therapy*, 13(1), pp. 1–12.

Paquola, C. et al. (2019). "Microstructural and functional gradients are increasingly dissociated in transmodal cortices". *PLoS Biol*, 17(5), e3000284.

Paquola, C. et al. (2021). "The BigBrainWarp toolbox for integration of BigBrain 3D histology with multimodal neuroimaging". *eLife*, 10. Ed. by S. Jbabdi et al., e70119.

Picton, T. W. et al. (2000). "Guidelines for using human event-related potentials to study cognition: recording standards and publication criteria". *Psychophysiology*, 37(2), pp. 127–152.

Quackenbush, J. (2002). "Microarray data normalization and transformation". *Nature genetics*, 32(4), pp. 496–501.

Radhakrishnan, R. et al. (2021). "In vivo evidence of lower synaptic vesicle density in schizophrenia". *Molecular Psychiatry*, pp. 1–9.

Raichle, M. E. (2015). "The restless brain: how intrinsic activity organizes brain function". *Philosophical Transactions of the Royal Society B: Biological Sciences*, 370(1668), p. 20140172.

Raichle, M. E. and M. A. Mintun (2006). "Brain work and brain imaging". *Annu. Rev. Neurosci.*, 29, pp. 449–476.

Raut, R. V., A. Z. Snyder, and M. E. Raichle (2020). "Hierarchical dynamics as a macroscopic organizing principle of the human brain". *Proceedings of the National Academy of Sciences*, 117(34), pp. 20890–20897.

Reardon, P. et al. (2018). "Normative brain size variation and brain shape diversity in humans". *Science*, 360(6394), pp. 1222–1227.

Romero-Garcia, R. et al. (2018). "Structural covariance networks are coupled to expression of genes enriched in supragranular layers of the human cortex". *Neuroimage*, 171, pp. 256–267.

Schaefer, A. et al. (2018). "Local-global parcellation of the human cerebral cortex from intrinsic functional connectivity MRI". *Cerebral cortex*, 28(9), pp. 3095–3114.

Scheeringa, R. and P. Fries (2019). "Cortical layers, rhythms and BOLD signals". *NeuroImage*, 197, pp. 689–698.

Seidlitz, J. et al. (2020). "Transcriptomic and cellular decoding of regional brain vulnerability to neurogenetic disorders". *Nature communications*, 11(1), pp. 1–14.

Shafiei, G. et al. (2020a). "Spatial patterning of tissue volume loss in schizophrenia reflects brain network architecture". *Biol Psychiat*.

Shafiei, G. et al. (2020b). "Topographic gradients of intrinsic dynamics across neocortex". *Elife*, 9, e62116.

Silva Castanheira, J. da et al. (2021). "Brief segments of neurophysiological activity enable individual differentiation". *Nature communications*, 12(1), pp. 1–11.

Simons, M. and K.-A. Nave (2016). "Oligodendrocytes: myelination and axonal support". *Cold Spring Harbor perspectives in biology*, 8(1), a020479.

Smart, K. et al. (2021). "Binding of the synaptic vesicle radiotracer [11C] UCB-J is unchanged during functional brain activation using a visual stimulation task". *Journal of Cerebral Blood Flow & Metabolism*, 41(5), pp. 1067–1079.

Swanson, L. W. and J. W. Lichtman (2016). "From Cajal to connectome and beyond". *Annual review of neuroscience*, 39, pp. 197–216.

Sydnor, V. J. et al. (2021). "Neurodevelopment of the association cortices: Patterns, mechanisms, and implications for psychopathology". *Neuron*, 109(18), pp. 2820–2846.

Tadel, F. et al. (2011). "Brainstorm: a user-friendly application for MEG/EEG analysis". *Computational intelligence and neuroscience*, 2011.

Talkner, P. and R. O. Weber (2000). "Power spectrum and detrended fluctuation analysis: Application to daily temperatures". *Physical Review E*, 62(1), p. 150.

Tripathy, S. J. et al. (2015). "Brain-wide analysis of electrophysiological diversity yields novel categorization of mammalian neuron types". *Journal of Neurophysiology*, 113(10), pp. 3474–3489.

Tripathy, S. J. et al. (2017). "Transcriptomic correlates of neuron electrophysiological diversity". *PLoS computational biology*, 13(10), e1005814.

Vaishnavi, S. N. et al. (2010). "Regional aerobic glycolysis in the human brain". *Proceedings of the National Academy of Sciences*, 107(41), pp. 17757–17762.

Van Essen, D. C. et al. (2013). "The WU-Minn human connectome project: an overview". *Neuroimage*, 80, pp. 62–79.

Váša, F. and B. Mišić (2022). "Null models in network neuroscience". *Nature Reviews Neuroscience*.

Vázquez-Rodríguez, B. et al. (2019). "Gradients of structure–function tethering across neocortex". *Proc Natl Acad Sci USA*, 116(42), pp. 21219–21227.

Vazquez-Rodriguez, B. et al. (2020). "Signal propagation via cortical hierarchies". *Net Neurosci*.

Voytek, B. and R. T. Knight (2015). "Dynamic network communication as a unifying neural basis for cognition, development, aging, and disease". *Biological psychiatry*, 77(12), pp. 1089–1097.

Voytek, B. et al. (2015). "Oscillatory dynamics coordinating human frontal networks in support of goal maintenance". *Nature neuroscience*, 18(9), pp. 1318–1324.

Wagstyl, K. et al. (2018). "Mapping cortical laminar structure in the 3D BigBrain". *Cerebral cortex*, 28(7), pp. 2551–2562.

Wagstyl, K. et al. (2020). "BigBrain 3D atlas of cortical layers: Cortical and laminar thickness gradients diverge in sensory and motor cortices". *PLoS Biol*, 18(4), e3000678.

Wang, X.-J. (2010). "Neurophysiological and computational principles of cortical rhythms in cognition". *Physiological reviews*, 90(3), pp. 1195–1268.

— (2020). "Macroscopic gradients of synaptic excitation and inhibition in the neocortex". *Nat Rev Neurosci*, pp. 1–10.

Watanabe, T., G. Rees, and N. Masuda (2019). "Atypical intrinsic neural timescale in autism". *eLife*, 8, e42256.

Weiss, J. J. et al. (2021). "Preliminary in vivo evidence of reduced synaptic density in Human Immunodeficiency Virus (HIV) despite antiretroviral therapy". *Clinical Infectious Diseases*, 73(8), pp. 1404–1411.

Wiesman, A. I., J. da Silva Castanheira, and S. Baillet (2022). "Stability of spectral estimates in resting-state magnetoencephalography: Recommendations for minimal data duration with neuroanatomical specificity". *Neuroimage*, 247, p. 118823.

Wolff, A. et al. (2022). "Intrinsic neural timescales: temporal integration and segregation". *Trends in cognitive sciences*.

Xiao, Y. et al. (2022). "Oligodendrocyte precursor cells sculpt the visual system by regulating axonal remodeling". *Nature Neuroscience*, 25(3), pp. 280–284.

Yeo, B. T. et al. (2011). "The organization of the human cerebral cortex estimated by intrinsic functional connectivity". *Journal of neurophysiology*, 106(3), p. 1125.

Zhang, Y. et al. (2016). "Purification and characterization of progenitor and mature human astrocytes reveals transcriptional and functional differences with mouse". *Neuron*, 89(1), pp. 37–53.

Zhu, Z. et al. (2009). "The relationship between magnetic and electrophysiological responses to complex tactile stimuli". *BMC neuroscience*, 10(1), pp. 1–13.

Zilles, K. and N. Palomero-Gallagher (2017). "Multiple transmitter receptors in regions and layers of the human cerebral cortex". *Frontiers in neuroanatomy*, 11, p. 78.

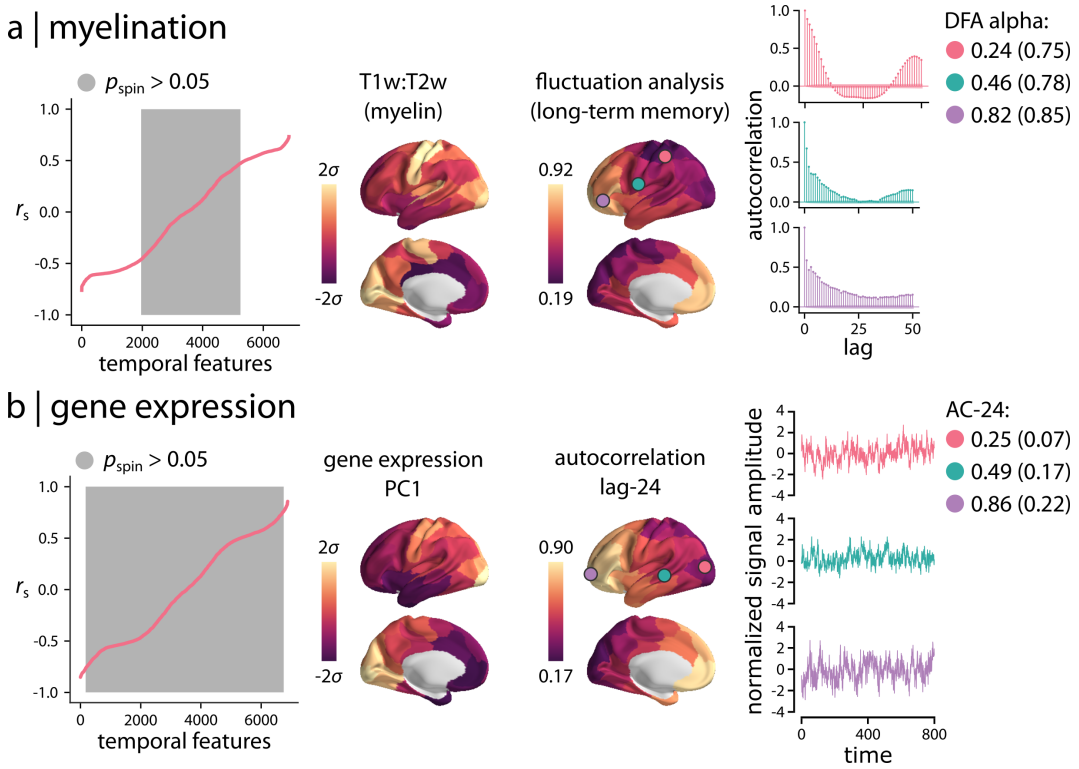

Figure S5.1: **Univariate analysis of neurophysiological time-series features** | Spearman's rank correlation coefficients (r_s) were used to investigate the univariate associations between `hctsa` time-series features of neurophysiological signal and two commonly-used micro-architectural maps: (a) T1w/Tw2 ratio as a proxy measure of myelination, and (b) principal component of gene expression. The resulting correlations were compared with null distributions of correlations obtained from 10,000 spatial autocorrelation-preserving nulls. Grey indicates non-significant time-series features (FDR corrected). Examples of high loading time-series features are shown for each micro-architectural map. Alpha parameter or Hurst exponent of detrended fluctuation analysis (DFA), a measure of long term memory of the signal, is shown for T1w/T2w ratio. The fluctuation analysis also reflects the shape of the autocorrelation function. Lag-24 autocorrelation is shown for principal component of gene expression (each time lag is 2 ms). For each map, three regions are selected based on the alpha parameter of DFA and lag-24 autocorrelation (circles on the brain surface: pink = 5^{th} percentile, green = 50^{th} percentile, purple = 95^{th} percentile). Values inside the parenthesis are the raw feature values while the ones outside the parenthesis are the normalized values. Full lists of features, their correlation coefficients and p-values are available for T1w/T2w ratio and gene expression in the online Supplementary Files S3,4.

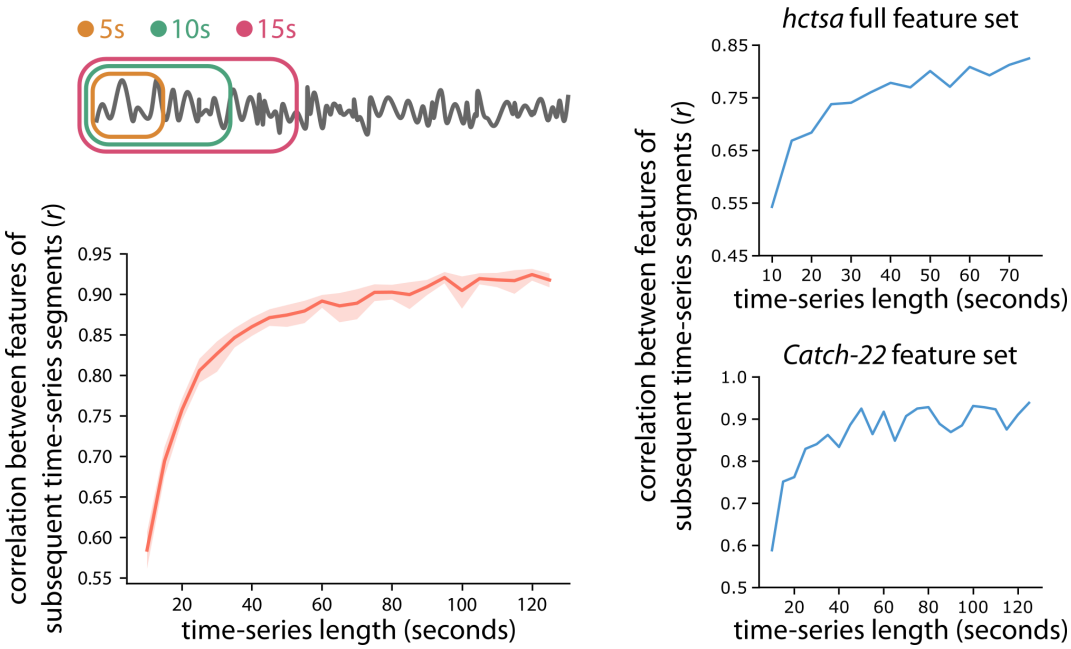

Figure S5.2: **Stability of time-series features** | To identify the time-series length required to robustly estimate the time-series features, we calculated a subset of `hctsa` features using the `Catch-22` toolbox (Lubba et al., 2019) on subsequent segments of time-series with varying length for each participant. We extracted time-series features from short segments of data ranging from 5 to 125 seconds in increments of 5 seconds. To identify the optimal time-series length required to estimate robust and stable features, we calculated the Pearson correlation coefficient r between features of two subsequent segments (e.g. features estimated from 10 and 5 seconds of data). The group-average correlation coefficient between the estimated features started to stabilize at time-series segments of around 30 seconds, consistent with previous reports (Wiesman et al., 2022) (left). To compare the stability analysis of `Catch-22` features with full `hctsa` features, the correlation coefficients between subsequent segments of time-series are shown for one random participant (right).

Chapter 6

Human electromagnetic and haemodynamic networks systematically converge in unimodal cortex and diverge in transmodal cortex

Golia Shafiei[1], Sylvain Baillet[1] & Bratislav Misic[1]

[1]McConnell Brain Imaging Centre, Montréal Neurological Institute, McGill University, Montréal, Canada

Published in:
PLOS Biology https://doi.org/10.1371/journal.pbio.3001735

6.1 Preface

Previous chapters investigated how temporal properties of regional neural activity are related to global network organization and cortical micro-architecture. Local neural activity can be measured at different timescales, from milliseconds to several seconds, using different neuroimaging modalities such as functional magnetic resonance imaging (MRI) and electromagnetic imaging (MEG/EEG). Despite complementary strengths to image spatiotemporal brain dynamics, the links between MEG and fMRI are not fully understood and the two fields have diverged. These imaging modalities are different in nature as they are sensitive to different mechanisms and measure neural activity at

slow and fast timescales (functional MRI and electromagnetic imaging, respectively). However, given that both types of signals are generated by the same underlying biological organization, some level of alignment is expected between the estimated dynamics from the two modalities (Sadaghiani et al., 2022). The work presented here quantifies the correspondence between inter-regional functional associations recovered from MEG and fMRI and bridges the two disciplines by comprehensively mapping haemodynamic and electromagnetic network architectures. This work was published in PLOS Biology in 2022 (Shafiei et al., 2022).

6.2 Abstract

Whole-brain neural communication is typically estimated from statistical associations among electromagnetic or haemodynamic time-series. The relationship between functional network architectures recovered from these two types of neural activity remains unknown. Here we map electromagnetic networks (measured using magnetoencephalography; MEG) to haemodynamic networks (measured using functional magnetic resonance imaging; fMRI). We find that the relationship between the two modalities is regionally heterogeneous and systematically follows the cortical hierarchy, with close correspondence in unimodal cortex and poor correspondence in transmodal cortex. Comparison with the BigBrain histological atlas reveals that electromagnetic-haemodynamic coupling is driven by laminar differentiation and neuron density, suggesting that the mapping between the two modalities can be explained by cytoarchitectural variation. Importantly, haemodynamic connectivity cannot be explained by electromagnetic activity in a single frequency band, but rather arises from the mixing of multiple neurophysiological rhythms. Correspondence between the two is largely driven by MEG functional connectivity at the beta (15-29 Hz) frequency band. Collectively, these findings demonstrate highly organized but only partly overlapping patterns of connectivity in MEG and fMRI functional networks, opening fundamentally new avenues for studying the relationship between cortical micro-architecture and multi-modal connectivity patterns.

6.3 Introduction

The structural wiring of the brain imparts a distinct signature on neuronal co-activation patterns. Inter-regional projections promote signaling and synchrony among distant neuronal populations, giving rise to coherent neural dynamics, measured as regional time series of

electromagnetic or haemodynamic neural activity (Fries, 2005). Systematic co-activation among pairs of regions can be used to map functional connectivity networks. Over the past decade, these dynamics are increasingly recorded without task instruction or stimulation; the resulting "intrinsic" functional connectivity is thought to reflect spontaneous neural activity.

The macro-scale functional architecture of the brain is commonly inferred from electromagnetic or haemodynamic activity. The former can be measured using electroencephalography (EEG) or magnetoencephalography (MEG), while the latter is measured using functional magnetic resonance imaging (fMRI). Numerous studies – using both MEG and fMRI – have reported evidence of intrinsic functional patterns that are highly organized (Baker et al., 2014; Bellec et al., 2006; Brookes et al., 2011a,b; De Pasquale et al., 2010; Power et al., 2011; Tewarie et al., 2014; Yeo et al., 2011), reproducible (Brookes et al., 2012; Colclough et al., 2016; Gordon et al., 2017; Noble et al., 2019) and comparable to task-driven co-activation patterns (Brookes et al., 2012; Cole et al., 2014; Smith et al., 2009).

How do electromagnetic and haemodynamic networks relate to one another? Although both modalities attempt to capture the same underlying biological process (neural activity), they are sensitive to different physiological mechanisms and ultimately reflect neural activity at fundamentally different time scales (Baillet, 2017; Hall et al., 2014; Hari and Parkkonen, 2015; Sadaghiani et al., 2022; Sadaghiani and Wirsich, 2020). Emerging theories emphasize a hierarchy of time scales of intrinsic fluctuations across the cortex (Gao et al., 2020; Murray et al., 2014; Raut et al., 2020; Shafiei et al., 2020b), where unimodal cortex is more sensitive to immediate changes in the sensory environment, while transmodal cortex is more sensitive to prior context (Baldassano et al., 2017; Chaudhuri et al., 2015; Chien and Honey, 2020; Hasson et al., 2008; Honey et al., 2012; Huntenburg et al., 2018). This raises the possibility that the alignment between the relatively slower functional architecture captured by fMRI and faster functional architecture captured by MEG may systematically vary across the cortex.

Previous reports have found some, but not complete, global overlap between the two modalities. Multiple MEG and fMRI independent components – representing spatiotemporal signatures of resting-state intrinsic networks – show similar spatial topography, particularly the visual, somatomotor and default mode components (Baker et al., 2014; Brookes et al., 2011a,b; Hipp et al., 2012). The spatial overlap between large-scale networks has also been reported in task-based studies and with networks recovered from other modalities, such as EEG and intracranial EEG (Das et al., 2022; Freeman et al., 2009; Liljeström et al., 2015; Menon et al., 1997; Musso et al., 2010). Moreover, fMRI

and MEG/EEG yield comparable fingerprinting accuracy, suggesting that they encode common information (Demuru and Fraschini, 2020; Fraschini et al., 2019; Sareen et al., 2021; Silva Castanheira et al., 2021). Finally, global edge-wise comparisons between fMRI networks and electrocorticography (ECoG) (Betzel et al., 2019), EEG (Deligianni et al., 2014; Wirsich et al., 2017, 2021) and MEG (Garcés et al., 2016; Hipp and Siegel, 2015; Tewarie et al., 2016) also yield moderate correlations. Although global comparisons are more common when different modalities are studied, regional and network-level relationships have also been explored using electrophysiological and intracranial EGG recordings (Das et al., 2022; Logothetis, 2003; Mukamel et al., 2005) as well as EEG and MEG recordings (Hipp and Siegel, 2015; Singh, 2012; Stevenson et al., 2012). Regional comparisons of electrophysiological and fMRI recordings also suggest that the relationship between the two may be affected by distinct cytoarchitecture and laminar structure of brain regions, particularly in visual and frontal cortex (Bastos et al., 2018; Bastos et al., 2015; Buffalo et al., 2011; Maier et al., 2011, 2010; Scheeringa and Fries, 2019; Scheeringa et al., 2016; Smith et al., 2013). How the coupling between fMRI and MEG connectivity profiles varies from region to region, and how this coupling reflects cytoarchitecture, is still not fully understood. Furthermore, previous studies have mostly assessed the association between haemodynamic and electromagnetic networks for separate frequency bands, investigating independent contributions of individual rhythms to haemodynamic connectivity. This effectively precludes the possibility that superposition and mixing of elementary electromagnetic rhythms manifests as patterns of haemodynamic connectivity (Hipp and Siegel, 2015; Mantini et al., 2007; Tewarie et al., 2016).

How regional connectivity profiles of MEG and fMRI functional networks are associated across the cortex and how their correspondence relates to the underlying cytoarchitecture, remains an exciting open question. Here, we use a linear multi-factor model that allows to represent the haemodynamic functional connectivity profile of a given brain region as a linear combination of its electromagnetic functional connectivity in multiple frequency bands. We then explore how the two modalities align across the neocortex and investigate the contribution of cytoarchitectonic variations to their alignment.

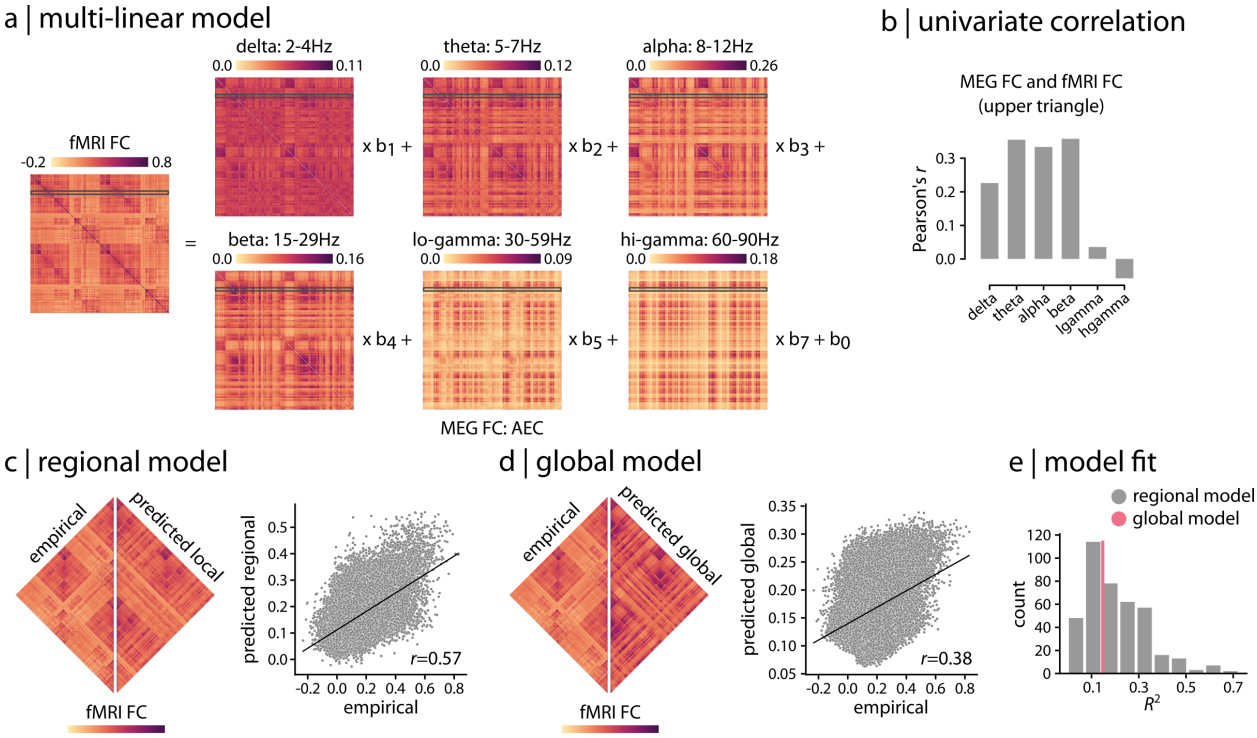

Figure 6.1: **Relating haemodynamic and electromagnetic connectivity** | (a) A multi-linear regression model was applied to predict resting state fMRI connectivity patterns from band-limited MEG functional connectivity (amplitude envelope correlation; AEC (Bruns et al., 2000)). The model is specified for each brain region separately, attempting to predict a region's haemodynamic connectivity profile from its electromagnetic connectivity profile. (b) The overall relationship between fMRI and MEG functional connectivity is estimated by correlating the upper triangle of fMRI FC (i.e. above diagonal) with the upper triangles of band-limited MEG FC, suggesting moderate relationship between the two across frequency bands. (c) Regional multi-linear model shown in panel (a) is used to predict fMRI FC from band-limited MEG FC for each brain region (i.e. row) separately. The empirical and predicted fMRI FC are depicted side-by-side for the regional model. The whole-brain edge-wise relationship between the empirical and predicted values is shown in the scatter plot. Each grey dot represents an edge (pairwise functional connection) from the upper triangles of empirical and predicted fMRI FC matrices. (d) A global multi-linear model is used to predict the entire upper triangle of fMRI FC from the upper triangles of the MEG FC matrices. The empirical and predicted fMRI FC are depicted side-by-side for the global model. The whole-brain edge-wise relationship between the empirical and predicted values is shown in the scatter plot. Each grey dot represents en edge from the upper triangles of empirical and predicted fMRI FC matrices. (e) The distribution of regional model fit quantified by R^2 is shown for regional model (grey histogram plot). The global model fit is also depicted for comparison (pink line). The data and code needed to generate this figure can be found in https://github.com/netneurolab/shafiei_megfmrimapping and https://zenodo.org/record/6728338.

6.4 Results

Data were derived using task-free MEG and fMRI recordings in the same unrelated participants from the Human Connectome Project (HCP (Van Essen et al., 2013); $n = 33$).

We first develop a simple regression-based model to map regional MEG connectivity to regional fMRI connectivity using group-average data. We then investigate how regionally heterogeneous the correspondence between the two is, and how different rhythms contribute to this regional heterogeneity. Finally, we conduct extensive sensitivity testing to demonstrate that the results are robust to multiple methodological choices.

6.4.1 Relating haemodynamic and electromagnetic connectivity

To relate fMRI and MEG functional connectivity patterns, we apply a multi-linear regression model (Vázquez-Rodríguez et al., 2019) (Figure 6.1). The model is specified for each brain region separately, attempting to predict a region's haemodynamic connectivity profile from its electromagnetic connectivity profile. The dependent variable is a row of the fMRI functional connectivity (FC) matrix and the independent variables are the corresponding rows of MEG FC matrices for six canonical electrophysiological bands, estimated using amplitude envelope correlation (AEC (Bruns et al., 2000)) with spatial leakage correction (see *Methods* for more details). For a model fitted for a given node i, the observations in the model are the connections of node i to the other $j \neq i$ regions (Figure 6.1a). The model predicts the fMRI FC profile of node i (i.e. i-th row) from a linear combination of MEG FC profiles of node i in the six frequency bands (i.e. i-th rows of MEG FC matrices). Collectively, the model embodies the idea that multiple rhythms could be superimposed to give rise to regionally heterogeneous haemodynamic connectivity.

Indeed, we find that the relationship between haemodynamic and electromagnetic connectivity is highly heterogeneous. Band-limited MEG connectivity matrices are moderately correlated with fMRI connectivity, ranging from $r = -0.06$ to $r = 0.36$ (Figure 6.1b; r denotes Pearson correlation coefficient). The regional multi-linear model fits range from adjusted-$R^2 = -0.002$ to adjusted-$R^2 = 0.72$ (R^2 denotes coefficient of determination; hereafter we refer to adjusted-R^2 as R^2), suggesting a close correspondence in some regions and poor correspondence in others (Figure 6.1c,e). Band-specific regional model fits are depicted in Figure S6.1, where each band-specific MEG connectivity is separately used as a single predictor in the model. For comparison, a single global model is fitted to the data, predicting the entire upper triangle of the fMRI FC matrix (i.e. all values above the diagonal) from a linear combination of the upper triangles of six MEG FC matrices (i.e. all values above the diagonal)(see *Methods* for more detail). The global model, which simultaneously relates whole-brain fMRI FC to the whole-brain MEG FC, yields an $R^2 = 0.15$ (Figure 6.1d,e). Importantly, the global model clearly obscures the wide range of correspondences, which can be considerably greater or smaller for individual regions.

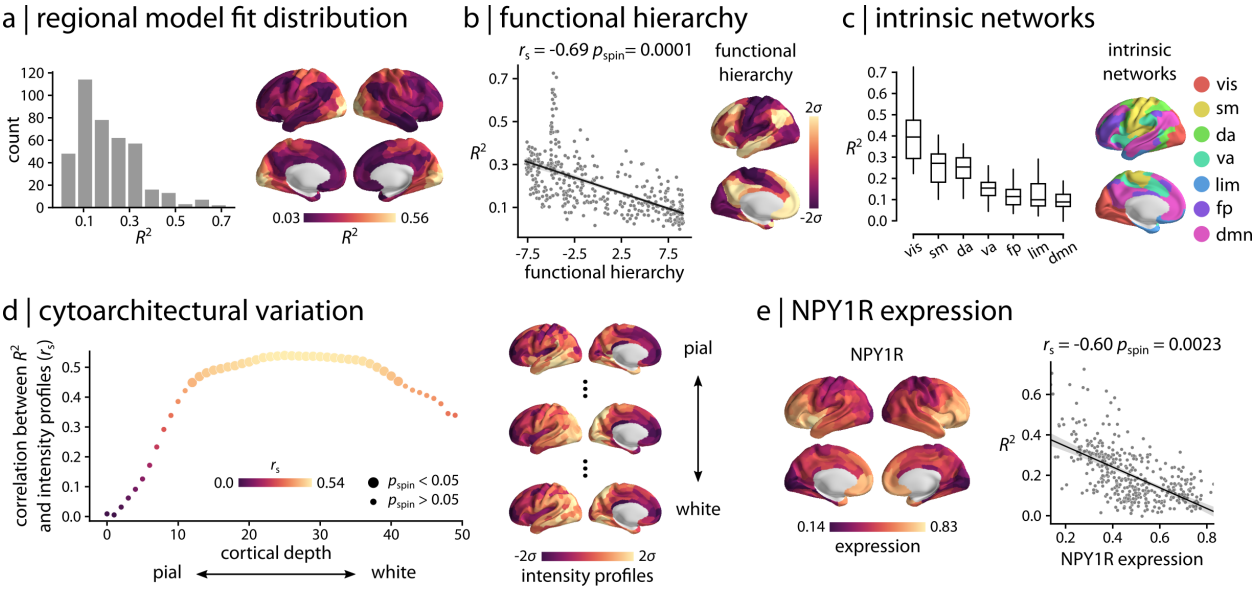

Figure 6.2: **Regional model fit** | (a) Spatial organization of fMRI-MEG correspondence is depicted for the regional model fit (95% interval). The cross-modal correspondence of connectivity profiles of brain regions is distributed heterogeneously across the cortex, representing regions with low or high correspondence. Strong cross-modal correspondence is observed in sensory areas whereas poor correspondence is observed for higher order regions. (b) Spatial organization of the cross-modal correspondence is compared with the functional hierarchical organization of cerebral cortex (Margulies et al., 2016). The two are significantly anti-correlated, confirming poor fMRI-MEG correspondence in connectivity profile of higher-order, transmodal areas compared to strong correspondence for sensory, unimodal regions. (c) Regions are stratified by their affiliation with macro-scale intrinsic networks (Yeo et al., 2011). The distribution of R^2 is depicted for each network, displaying a systematic gradient of cross-modal correspondence with the highest correspondence in the visual network and lowest correspondence in the default mode network. (d) The model fit is related to the cytoarchitectural variation of the cortex, estimated from the cell staining intensity profiles at various cortical depths obtained from the BigBrain histological atlas (Amunts et al., 2013; Paquola et al., 2021). Bigger circles denote statistically significant associations after correction for multiple comparisons by controlling the false discovery rate (FDR) at 5% alpha (Benjamini and Hochberg, 1995). The peak association between cross-modal correspondence and cytoarchitecture is observed approximately at cortical layer IV that has high density of granule cells. Staining intensity profiles are depicted across the cortex for the most pial, the middle and the white matter surfaces. (e) Microarray gene expression of vasoconstrictive NPY1R (Neuropeptide Y Receptor Y1) was estimated from the Allen Human Brain Atlas (AHBA; (Hawrylycz et al., 2012)). The MEG-fMRI cross-modal correspondence R^2 map (i.e. regional model fit) is compared with NPY1R gene expression. r_s denotes Spearman rank correlation. Intrinsic networks: vis = visual; sm = somatomotor; da = dorsal attention; va = ventral attention; lim = limbic; fp = frontoparietal; dmn = default mode. The data and code needed to generate this figure can be found in https://github.com/netneurolab/shafiei_megfmrimapping and https://zenodo.org/record/6728338.

6.4.2 Hierarchical organization of cross-modal correspondence

We next consider the spatial organization of fMRI-MEG correspondence. Figure 6.2a shows the spatial distribution of regional R^2 values, representing regions with low or

high correspondence. Regions with strong cross-modal correspondence include the visual, somato-motor and auditory cortex. Regions with low cross-modal correspondence include the posterior cingulate, lateral temporal and medial prefrontal cortex.

Collectively, the spatial layout of cross-modal correspondence bears a resemblance to the unimodal-transmodal cortical hierarchy observed in large-scale functional and microstructural organization of the cerebral cortex (Huntenburg et al., 2018). To assess this hypothesis, we first compared the cross-modal R^2 map with the principal functional hierarchical organization of the cortex, estimated using diffusion map embedding (Langs et al., 2015; Margulies et al., 2016) (Figure 6.2b; see *Methods* for more details). The two are significantly anti-correlated (Spearman rank correlation coefficient $r_s = -0.69$, $p_{spin} = 0.0001$), suggesting strong cross-modal correspondence in unimodal sensory cortex and poor correspondence in transmodal cortex. We then stratify regions by their affiliation with macro-scale intrinsic networks and computed the mean R^2 in each network (Yeo et al., 2011) (Figure 6.2c). Here we also observe a systematic gradient of cross-modal correspondence, with the strongest correspondence in the visual network and poorest correspondence in the default mode network.

We relate the cross-modal R^2 map to the cytoarchitectural variation of the cortex (Figure 6.2d). We use the BigBrain histological atlas to estimate granular cell density at multiple cortical depths (Amunts et al., 2013; Paquola et al., 2021). Cell-staining intensity profiles were sampled across 50 equivolumetric surfaces from the pial surface to the white matter surface to estimate laminar variation in neuronal density and soma size. Figure 6.2d shows the correlation between MEG-fMRI correspondence and cell density (y-axis) at different cortical depths (x-axis). Interestingly, the model fit is associated with cytoarchitectural variation of the cortex, with the peak association observed approximately at cortical layer IV that has high density of granular cells and separates supra- and infra-granular layers (Paquola et al., 2019, 2020; Wagstyl et al., 2020). Layer IV predominately receives feedforward projections and has high vascular density (Douglas and Martin, 2004; Harel et al., 2006; Schmid et al., 2019). We further assess the relationship between MEG-fMRI cross-modal correspondence and vascular attributes. We obtain the microarray gene expression of the vasoconstrictive NPY1R (Neuropeptide Y Receptor Y1) from Allen Human Brain Atlas (AHBA; Hawrylycz et al., 2012; see *Methods* for more details), given previous reports that the BOLD response is associated with the vasoconstrictive mechanism of Neuropeptide Y (NPY) acting on Y1 receptors (Uhlirova et al., 2016). We then compare the cross-modal association map with the expression of NPY1R and identify a significant association between the two (Figure 6.2e; $r_s = -0.60$, $p_{spin} = 0.0023$). This demonstrates that

regions with low cross-modal correspondence are enriched for NPY1R whereas areas with high cross-modal associations have less NPY-dependent vasoconstriction. Altogether, the results suggest that the greater coupling in unimodal cortex may be driven by the underlying cytoarchitecture, reflecting higher density of granular cells and distinct vascularization of cortical layer IV.

We also relate cross-modal R^2 map to the variation of structure-function coupling across the cortex, which has also been shown to follow the unimodal-transmodal hierarchy (Baum et al., 2020; Preti and Van De Ville, 2019; Suárez et al., 2020; Vázquez-Rodríguez et al., 2019; Zamani Esfahlani et al., 2022). We estimate structure-function coupling as the Spearman rank correlation between regional structural and functional connectivity profiles (Baum et al., 2020) (Figure S6.2; see *Methods* for more details). We then correlate the identified map with the regional model fit, identifying a significant association between the two (Figure S6.2; $r_s = 0.40$, $p_{spin} = 0.0025$). This is consistent with the notion that both haemodynamic and electromagnetic neural activity are constrained by the anatomical pathways and the underlying structural organization (Cabral et al., 2014; Sarwar et al., 2021; Sorrentino et al., 2021).

6.4.3 Heterogeneous contributions of multiple rhythms

How do different rhythms contribute to regional patterns of cross-modal correspondence? To address this question and to assess the effects of cross-correlation between MEG connectivity at different frequency bands (Figure S6.5), we perform a dominance analysis for every regional multi-linear model (Azen and Budescu, 2003; Budescu, 1993). Specifically, dominance analysis is used to examine the separate effects of each band-limited MEG functional connectivity, as well as the effects of all other possible combinations of band-limited MEG FC, on the regional model fit. This technique estimates the relative importance of predictors by constructing all possible combinations of predictors and re-fitting the multi-linear model for each combination. The possible combinations of predictors include sets of single predictors, all possible pairs of predictors, all possible combinations with 3 predictors, and so on. To assess the influence of each band on the model fit, dominance analysis re-fits the model for each combination and quantifies the relative contribution of each predictor as the increase in variance explained after adding that predictor to the models (i.e. gain in adjusted-R^2). Figure 6.3a shows the global dominance of each frequency band, where dominance is quantified as "percent relative importance" or "contribution percentage" of each band. Overall, we observe the greatest contributions from MEG

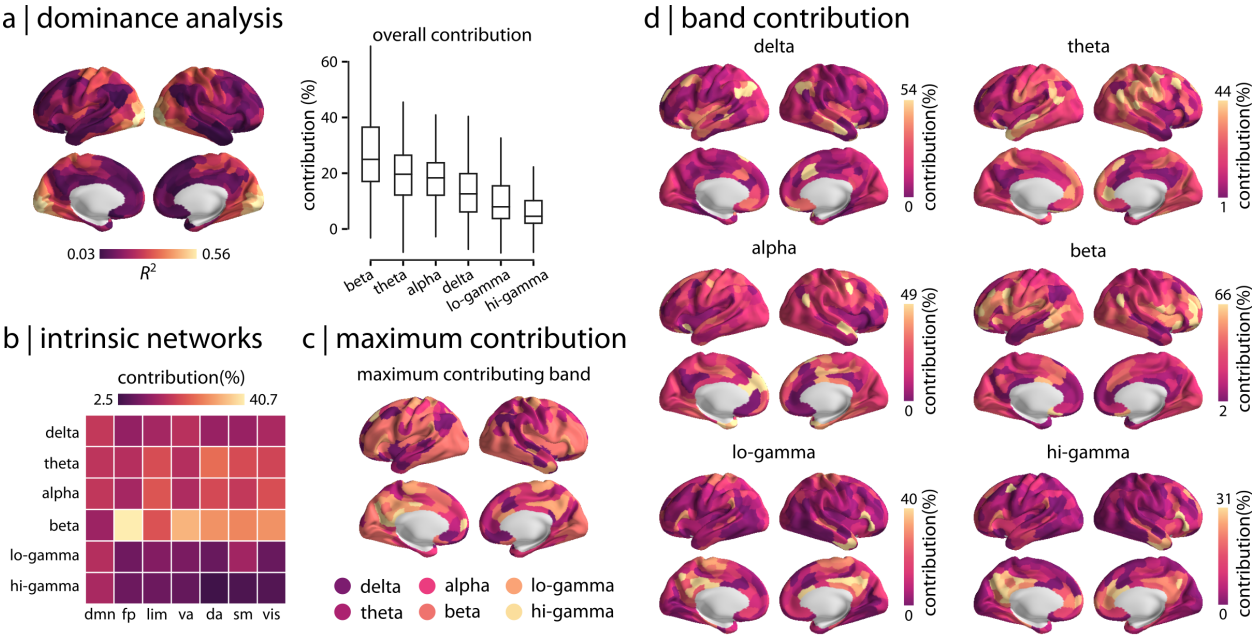

Figure 6.3: **Dominance analysis** | Dominance analysis is performed for each regional multi-linear model to quantify how MEG connectivity at different rhythms contribute to regional patterns of cross-modal correspondence (Azen and Budescu, 2003; Budescu, 1993). (a) The overall contribution of each frequency band is depicted for the regional model (box plots). Beta band connectivity, followed by theta and alpha bands, contribute the most to the model fit whereas low and high gamma bands contribute the least. (b) The mean contribution of different rhythms is estimated for the intrinsic networks. Consistent with the overall contributions depicted in panel (a), the greatest contribution is associated with beta band connectivity. (c) The most dominant predictor (frequency band) is depicted for each brain region, confirming overall higher contributions from beta band across the cortex. (d) Frequency band contribution to the regional cross-modal correspondence is shown separately for different rhythms across the cortex (95% intervals). The data and code needed to generate this figure can be found in https://github.com/netneurolab/shafiei_megfmrimapping and https://zenodo.org/record/6728338.

connectivity at beta band, followed by theta and alpha bands, and smallest contributions from low and high gamma bands.

Zooming in on individual regions and intrinsic networks, we find that the dominance pattern is also regionally heterogeneous. Namely, the make-up and contribution of specific MEG frequencies to a region's fMRI connectivity profile varies from region to region. Figure 6.3b shows the dominance of specific rhythms in each intrinsic network. Figure 6.3c shows the most dominant predictor for every brain region. We find that beta band contribution is highest in occipital and lateral frontal cortices. Sensorimotor cortex has high contributions from combinations of beta, alpha, and theta bands. Parietal and temporal areas are mostly dominated by delta and theta bands as well as some contribution from alpha band. Medial frontal cortex shows contributions from the alpha band, while low and high gamma bands contribute to posterior cingulate cortex and precuneus. Figure 6.3d

shows the dominance of specific rhythms separately for each region. Overall, we observe that beta connectivity has the highest contribution percentage (95% confidence interval: [2% 66%]), largely contributing to model prediction across the cortex. These findings are consistent with previous reports, demonstrating that haemodynamic connectivity is related to the superposition of band-limited electromagnetic connectivity and that band contributions vary across the cortex (Hipp and Siegel, 2015; Tewarie et al., 2016).

Finally, we used Analysis of Variance (ANOVA) to quantitatively assess the differences in band-specific contributions to the cross-modal correspondence map (Table S6.1). Specifically, we assessed the significance and effect size of differences in band-specific contributions for all possible pairs of frequency bands. We identify two main findings (for full results see Table S6.1): (1) Overall, the variability of band-specific contributions is significantly larger between groups (i.e. bands) compared to the variability within groups ($F(5, 2394) = 117.31$; $p < 0.0001$). (2) Band-specific contributions are significantly different from each other and are ranked in the same order as depicted in Figure 6.3a. Specifically, contribution of beta band is significantly larger than contribution of alpha band (difference of the means = 8.65, t-value = 9.46, p-value < 0.0001, Cohen's $d = 0.69$) and theta band (difference of the means = 7.56, t-value = 8.27, p-value < 0.0001, Cohen's $d = 0.58$). Also, the contribution from the delta band is significantly lower than beta (difference of the means = 12.37, t-value = 13.53, p-value < 0.0001, Cohen's $d = 0.96$), alpha (difference of the means = 3.72, t-value = 4.07, p-value = 0.0007, Cohen's $d = 0.29$), and theta (difference of the means = 4.81, t-value = 5.26, p-value < 0.0001, Cohen's $d = 0.37$). Note that although the difference between alpha and theta band contributions is not significant, both their contributions are significantly lower than beta band and larger than delta band. Moreover, delta band contribution is significantly larger than contribution of lo-gamma (difference of the means = 3.78, t-value = 4.14, p-value = 0.0005, Cohen's $d = 0.29$) and lo-gamma contribution is significantly larger than hi-gamma (difference of the means = 3.72, t-value = 4.07, p-value = 0.0007, Cohen's $d = 0.29$). Note that the values reported here are the absolute values for difference of the means, t-values, p-values and Cohen's d (effect size). All p-values are corrected for multiple comparisons using Bonferroni correction.

6.4.4 Sensitivity analysis

Finally, we note that the present report goes through several decision points that have equally-justified alternatives. Here we explore the other possible choices. First, rather than framing the report from an explanatory perspective (focusing on model fit), we instead derive an equivalent set of results using a predictive perspective (focusing on

out-of-sample prediction). We perform cross-validation at both the region- and subject-level (Figure 6.4a,b). For region-level cross-validation, we pseudorandomly split the connectivity profile of a given region into train and test sets based on spatial separation (inter-regional Euclidean distance), such that 75% of the closest regions to a random region are selected as the train set and the remaining 25% of the regions are selected as test set (399 repetitions; see *Methods* for more details) (Hansen et al., 2021a). We then train the multi-linear model using the train set and predict the connection strength of the test set for each region and each split. The mean regional model performance across splits is consistent for train and test sets (Figure 6.4a; $r = 0.78$, $p_{spin} = 0.0001$). For subject-level cross-validation, we use leave-one-out-cross validation, wherein we train the regional multi-linear models using data from $n - 1$ subjects and test each one on the held-out subject. The mean regional model performance is consistent for train and test sets (Figure 6.4b; $r = 0.90$, $p_{spin} = 0.0001$). Altogether, both analyses give similar, highly concordant results with the simpler model fit-based analysis, identifying strong cross-modal correspondence in unimodal sensory regions and poor correspondence in transmodal areas.

To consider the effect of spatial proximity on the findings, we remove the exponential inter-regional Euclidean distance trend from all connectivity matrices before fitting any model. The results are consistent with and without distance correction (Figure 6.4c; correlation with functional hierarchy: $r_s = -0.53$, $p_{spin} = 0.0001$; correlation with original R^2: $r_s = 0.67$, $p_{spin} = 0.0001$). We also obtain consistent findings when we repeat the analysis without accounting for spatial leakage effect in estimating MEG connectivity with AEC (Figure 6.4d; correlation with functional hierarchy: $r_s = -0.60$, $p_{spin} = 0.0001$; correlation with original R^2: $r_s = 0.84$, $p_{spin} = 0.0001$). Next, we use another source reconstruction method (standardized low resolution brain electromagnetic tomography; sLoreta (Pascual-Marqui et al., 2002)) instead of LCMV beamformers, as previous reports suggest that sLoreta improves source localization accuracy (Hauk et al., 2019, 2011). We then estimate MEG connectivity with AEC and repeat the multi-linear model analysis, identifying similar results as before (Figure 6.4e; correlation with functional hierarchy: $r_s = -0.80$, $p_{spin} = 0.0001$; correlation with original R^2: $r_s = 0.85$, $p_{spin} = 0.0002$). Next, we compute MEG connectivity using an alternative, phase-based connectivity measure (phase locking value; PLV (Lachaux et al., 1999; Mormann et al., 2000)), rather than the AEC. The two FC measures yield similar cross-modal correspondence maps (Figure 6.4f; correlation with functional hierarchy: $r_s = -0.53$, $p_{spin} = 0.0022$; correlation with original R^2: $r_s = 0.66$, $p_{spin} = 0.0001$). We also repeat the analysis using a low resolution parcellation (Schaefer-200 atlas (Schaefer et al., 2018)) to ensure that the findings are independent

from the choice of parcellation. As before, the results demonstrate similar cross-modal correspondence map (Figure 6.4g; correlation with functional hierarchy: $r_s = -0.70$, $p_{spin} = 0.0001$). To assess the extent to which the results are influenced by MEG source localization error, we compare the cross-modal correspondence pattern to peak localization error estimated using cross-talk function (CTF) (Hauk and Stenroos, 2014; Hauk et al., 2019, 2011; Liu et al., 2002; Molins et al., 2008). No significant association is observed between R^2 pattern and CTF for LCMV (Figure S6.3a; $r_s = -0.14$, $p_{spin} = 0.6$) and sLoreta (Figure S6.3b; $r_s = -0.04$, $p_{spin} = 0.9$) source reconstruction solutions. Finally, to confirm that the cross-modal correspondence pattern is independent from signal-to-noise ratio (SNR), we compare the regional model fit with the SNR map of the reconstructed sources, identifying no significant association between the two (Figure S6.4; $r_s = 0.32$, $p_{spin} = 0.25$)(see *Methods* for more details).

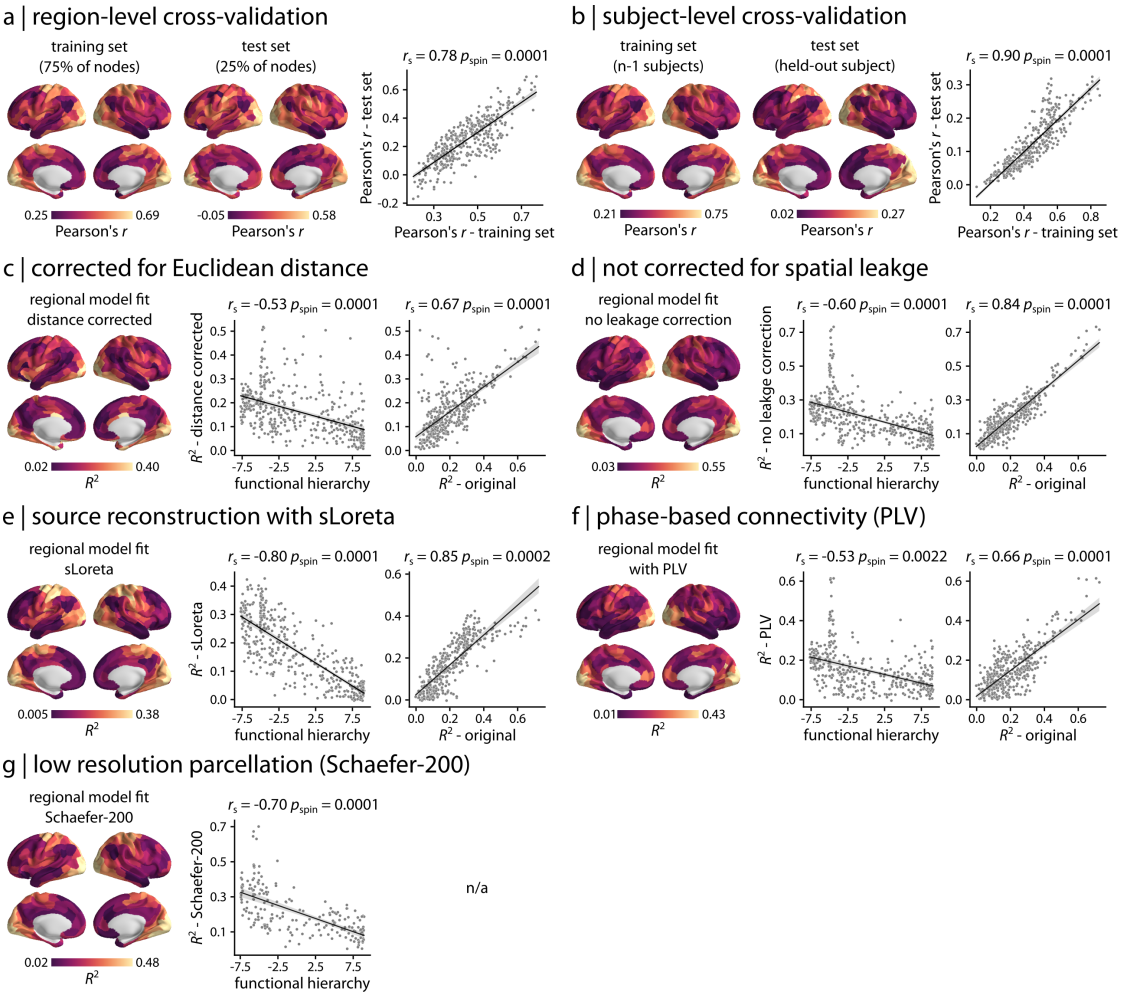

Figure 6.4: **Sensitivity analysis** | (a) A regional cross-validation was performed by pseudorandomly splitting the connectivity profile of a given region into train and test sets based on spatial separation (see *Methods* for more details). The multi-linear model is then fitted on the train set and is used to predict the connection strength of the test set for each region and each split. The mean regional model performance across splits is depicted for train and test sets, displaying consistent results between the two (scatter plot). The out-of-sample model performance is stronger in the sensory, unimodal areas compared to transmodal areas, consistent with original findings (Figure 6.2). (b) A subject-level cross-validation was performed using a leave-one-out approach. The regional multi-linear model is trained using data from $n-1$ subjects and is tested on the held-out subject for each region separately. The mean regional model performance is shown for train and test sets, displaying consistent results between the two (scatter plot). The out-of-sample model performance is stronger in the sensory, unimodal areas compared to transmodal areas, consistent with original findings (Figure 6.2). The analysis is also repeated for various processing choices: (c) after regressing out inter-regional Euclidean distance from connectivity matrices, (d) using MEG connectivity data without spatial leakage correction, (e) using another MEG source reconstruction method (standardized low resolution brain electromagnetic tomography; sLoreta (Pascual-Marqui et al., 2002)), (f) using a phase-based MEG connectivity measure (phase-locking value; PLV (Lachaux et al., 1999; Mormann et al., 2000)), and (g) at a low resolution parcellation (Schaefer-200 atlas (Schaefer et al., 2018)). The results are consistent across all control analyses, identifying similar cross-modal correspondence maps as the original analysis (Figure 6.2a). All brain maps are shown at 95% intervals. r_s denotes Spearman rank correlation. The data and code needed to generate this figure can be found in https://github.com/netneurolab/shafiei_megfmrimapping and https://zenodo.org/record/6728338.

6.5 Discussion

In the present report we map electromagnetic functional networks to haemodynamic functional networks in the human brain. We find two principal results. First, the relationship between the two modalities is regionally heterogeneous but systematic, reflecting the unimodal-transmodal cortical hierarchy and cytoarchitectural variation. Second, haemodynamic connectivity cannot be explained by electromagnetic connectivity in a single band, but rather reflects mixing and superposition of multiple rhythms.

The fact that the association between the two modalities follows a gradient from unimodal to transmodal cortex resonates with emerging work on cortical hierarchies (Huntenburg et al., 2018; Margulies et al., 2016; Mesulam, 1998). Indeed, similar spatial variations are observed for multiple micro-architectural features, such as gene expression (Burt et al., 2018; Fulcher et al., 2019; Hansen et al., 2021a), T1w/T2w ratio (Huntenburg et al., 2017), laminar differentiation (Wagstyl et al., 2020) and neurotransmitter receptor profiles (Froudist-Walsh et al., 2021; Goulas et al., 2021; Hansen et al., 2021b). Collectively, these studies point to a natural axis of cortical organization that encompasses variations in both structure and function across micro-, meso- and macro-scopic spatial scales.

Interestingly, we find the closest correspondence between fMRI and MEG functional connectivity in unimodal cortex (including the visual and somatomotor networks) and the poorest correspondence in transmodal cortex (default mode, limbic, fronto-parietal and ventral attention networks). In other words, the functional architectures of the two modalities are consistent early in the cortical hierarchy, presumably reflecting activity related to instantaneous changes in the external environment. Conversely, as we move up the hierarchy, there is a gradual separation between the two architectures, suggesting that they are differently modulated by endogenous inputs and contextual information. How the two types of functional connectivity are related to ongoing task demand is an exciting question for future research.

Why is there systematic divergence between the two modalities? Our findings suggest that topographic variation in MEG-fMRI coupling is due to variation in cytoarchitecture and neurovascular coupling. First, we observe greater MEG-fMRI coupling in regions with prominent granular layer IV. This result may reflect variation of microvascular density at different cortical layers (Drew, 2019; Scheeringa and Fries, 2019; Schmid et al., 2019). Namely, cortical layer IV is the most vascularized, and this is particularly prominent in primary sensory areas (Schmid et al., 2019). The BOLD response mainly reflects local field potentials arising from synaptic currents of feedforward input signals to cortical

layer IV (Douglas and Martin, 2004; Harel et al., 2006); as a result, the BOLD response is more sensitive to cortical layer IV with high vascular density (Uludağ and Blinder, 2018). Therefore, electromagnetic neuronal activity originating from layer IV should be accompanied by a faster and more prominent BOLD response. This is consistent with our finding that brain regions with more prominent granular layer IV (i.e. unimodal cortex) have greater correspondence between electromagnetic and haemodynamic functional architectures. In other words, heterogeneous cortical patterning of MEG-fMRI coupling may reflect heterogeneous patterning of underlying neurovascular coupling.

Second, we observe prominent anticorrelations between vasoconstrictive NPY1R-expressing neurons and MEG-fMRI coupling. Multiple studies of vasodilator and vasoconstrictor mechanisms involved in neural signaling have demonstrated links between microvasculature and the BOLD signal (Drew, 2019; Uhlirova et al., 2016). For example, an optogenetic and 2-photon mouse imaging study found that task-related negative BOLD signal is mainly associated with vasoconstrictive mechanism of Neuropeptide Y (NPY) acting on Y1 receptors, suggesting that neurovascular coupling is cell specific (Uhlirova et al., 2016). Interestingly, by comparing the cortical expression of NPY1R (Neuropeptide Y Receptor Y1) in the human brain with MEG-fMRI correspondence pattern identified here, we find that regions with low cross-modal correspondence are enriched for NPY1R whereas areas with high cross-modal associations have less NPY-dependent vasoconstriction. Collectively, these results suggest that MEG-fMRI correspondence is at least partly due to regional variation in cytoarchitecture and neurovascular coupling.

More generally, numerous studies have investigated the laminar origin of cortical rhythms. For example, animal electrophysiological recordings demonstrated that visual and frontal cortex gamma activity can be localized to superficial cortical layers (supragranular layers I-III and granular layer IV), whereas alpha and beta activity are localized to deep infragranular layers (layers V-VI) (Bastos et al., 2018; Bastos et al., 2015; Buffalo et al., 2011; Maier et al., 2011, 2010; Smith et al., 2013). Similar findings have been reported in humans using EEG and laminar-resolved BOLD recordings, demonstrating that gamma and beta band EEG power are associated with superficial and deep layer BOLD response, respectively, whereas alpha band EEG power is associated with BOLD response in both superficial and deep layers (Scheeringa et al., 2016). Laminar specificity of cortical rhythms is increasingly emphasized in contemporary accounts of predictive processing (Bastos et al., 2020). In the predictive coding framework, transmodal regions generate predictive signals that modulate the activity of sensory unimodal regions depending on context (Donhauser and Baillet, 2020). These top-down signals are relatively slow, as they evolve with the

context of exogenous (stimulation) inputs. The consequence on unimodal areas is a boost of their encoding gain, reflected in stronger, faster activity that tracks incoming stimuli. They in turn generate error signals that are slower and reflect the discrepancy between the predictions received and the actual external input. These slower error signals are then registered by higher-order transmodal regions. Specific cortical layers and rhythms contribute to this predictive coding (Bastos et al., 2020). For example, an unfamiliar, unpredicted stimulus is associated with increased gamma power that is fed forward up the cortical hierarchy (i.e. bottom-up from sensory to association cortices) through the superficial layers to transfer the prediction errors. This in turn results in low top-down, feedback predictions through deep cortical layers via alpha and beta rhythms. Conversely, predicted stimuli are associated with stronger feedback alpha and beta rhythms via deep layers, inhibiting the gamma activity for expected exogenous inputs (Bastos et al., 2020). This hierarchical predictive processing framework is also thought to underlie conscious perception by top-down transfer of perceptual predictions via alpha and beta rhythms through deep layers and bottom-up transfer of prediction errors via gamma rhythm through superficial layers, minimizing predictions errors (Bastos et al., 2020; Safron, 2020; Seth and Bayne, 2022). Our results, linking cytoarchitecture with rhythm-specific connectivity may help to further refine and develop this emerging framework.

Altogether, our findings suggest that the systemic divergence between MEG and fMRI connectivity patterns may reflect variations in cortical cytoarchitecture and vascular density of cortical layers. However, note that due to the low spatial resolution of fMRI and MEG data, haemodynamic and electromagnetic connectivity is not resolved at the level of cortical layers. Rather, comparisons with cytoarchitecture are made via proxy datasets, such as the BigBrain histological atlas (Amunts et al., 2013) and the Allen Human Brain Atlas (Hawrylycz et al., 2012). Future work is required to assess the laminar-specificity of the cross-modal association in a more direct and comprehensive manner (Finn et al., 2021, 2019; Huber et al., 2017, 2021).

Throughout the present report, we find that fMRI networks are best explained as arising from the superposition of multiple band-limited MEG networks. Although previous work has focused on directly correlating fMRI with MEG/EEG networks in specific bands, we show that synchronized oscillations in multiple bands could potentially combine to give rise to the well studied fMRI functional networks. Indeed, and as expected, the correlation between any individual band-specific MEG network and fMRI is substantially smaller than the multi-linear model that takes into account all bands simultaneously. Previous work on cross-frequency interactions (Florin and Baillet, 2015) and on multi-layer MEG

network organization (Brookes et al., 2016) has sought to characterize the participation of individual brain regions within and between multiple frequency networks. Our findings build on this literature, showing that the superimposed representation may additionally help to unlock the link between MEG and fMRI networks.

It is noteworthy that the greatest contributions to the link between the two modalities came from beta band connectivity. Multiple authors have reported that – since it captures slow haemodynamic co-activation – fMRI network connectivity would be mainly driven by slower rhythms (Brookes et al., 2011a; Deligianni et al., 2014; Florin and Baillet, 2015; Liljeström et al., 2015; Mantini et al., 2007; Sadaghiani et al., 2022). Our findings demonstrate that although all frequency bands contribute to the emergence of fMRI networks, the greatest contributions come from beta band connectivity, followed by theta and alpha connectivity.

The present results raise two important questions for future work. First, how does structural connectivity shape fMRI and MEG functional networks (Cabral et al., 2014; Suárez et al., 2020; Wirsich et al., 2017)? We find that cross-modal correspondence between MEG and fMRI functional networks is associated with structure-function coupling measured from MRI functional and structural connectivity networks, suggesting that the cross-modal map may be constrained by structural connectivity. Previous reports demonstrate that unimodal, sensory regions have lower neural flexibility compared to transmodal, association areas and are more stable during development and evolution (Safron et al., 2022; Shafiei et al., 2020b; Yin et al., 2020). This suggests that the underlying anatomical network constrains neural activity and functional flexibility in a nonuniform manner across the cortex, resulting in higher degrees of freedom in structure-function coupling in regions related to highly flexible cognitive processes. However, given that MEG and fMRI capture distinct neurophysiological mechanisms, it is possible that haemodynamic and electromagnetic architectures have a different relationship with structural connectivity and this could potentially explain why they systematically diverge through the cortical hierarchy (Baum et al., 2020; Preti and Van De Ville, 2019; Suárez et al., 2020; Vázquez-Rodríguez et al., 2019; Zamani Esfahlani et al., 2022). Second, the present results show how the two modalities are related in a task-free resting state, but what is the relationship between fMRI and MEG connectivity during cognitive tasks (Kujala et al., 2014)? Given that the two modalities become less correlated in transmodal cortex in the resting state, the relationship between them during task may depend on demand and cognitive functions required to complete the task.

Finally, the present results should be interpreted in light of several methodological

considerations. First, although we conduct extensive sensitivity testing, including multiple ways of defining functional connectivity, there exist many more ways in the literature to estimate both fMRI and MEG connectivity (Niso et al., 2013; Vinck et al., 2011). Second, to ensure that the analyses were performed in the same participants using both resting state fMRI and MEG, and that the participants have no familial relationships, we utilized a reduced version of the HCP sample. Third, in order to directly compare the contributions of multiple frequency bands, all were entered into the same model. As a result however, the observations in the linear models (network edges) are not independent, violating a basic assumption of these statistical models. For this reason, we only use model fits and dominance values to compare the correspondence of fMRI and MEG across a set of nodes, each of which is estimated under the same conditions. Finally, to ensure that the findings are independent from sensitivity of MEG to neural activity from different regions, we compared the cross-modal correspondence map with MEG signal-to-noise ratio and source localization error, where no significant associations were identified. However, MEG is still susceptible to such artifacts given that regions with lower signal-to-noise ratio (e.g. Sylvian fissure) are the ones where source reconstruction solutions have higher source localization errors (Goldenholz et al., 2009; Hauk et al., 2022).

Despite complementary strengths to image spatiotemporal brain dynamics, the links between MEG and fMRI are not fully understood and the two fields have diverged. The present report bridges the two disciplines by comprehensively mapping haemodynamic and electromagnetic network architectures. By considering the contributions of the canonical frequency bands simultaneously, we show that the superposition and mixing of MEG neurophysiological rhythms manifests as highly structured patterns of fMRI functional connectivity. Systematic convergence and divergence among the two modalities in different brain regions opens fundamentally new questions about the relationship between cortical hierarchies and multi-modal functional networks.

6.6 Methods

6.6.1 Dataset: Human Connectome Project (HCP)

Resting state magnetoencephalography (MEG) data of a set of healthy young adults ($n = 33$; age range 22-35 years) with no familial relationships were obtained from Human Connectome Project (HCP; S900 release (Van Essen et al., 2013)). The data includes resting state scans of about 6 minutes long (sampling rate = 2034.5 Hz; anti-aliasing filter low-pass

filter at 400 Hz) and noise recordings for all participants. MEG anatomical data and 3T structural magnetic resonance imaging (MRI) data of all participants were also obtained for MEG pre-processing. Finally, we obtained functional MRI data of the same $n = 33$ individuals from HCP dataset. All four resting state fMRI scans (two scans with R/L and L/R phase encoding directions on day 1 and day 2, each about 15 minutes long; $TR = 720$ ms) were available for all participants.

6.6.2 HCP Data Processing

6.6.2.1 Resting state magnetoencephalography (MEG)

Resting state MEG data was analyzed using Brainstorm software, which is documented and freely available for download online under the GNU general public license (Tadel et al., 2011; http://neuroimage.usc.edu/brainstorm). The MEG recordings were registered to the structural MRI scan of each individual using the anatomical transformation matrix provided by HCP for co-registration, following the procedure described in Brainstorm's online tutorials for the HCP dataset (https://neuroimage.usc.edu/brainstorm/Tutorials/HCP-MEG). The pre-processing was performed by applying notch filters at 60, 120, 180, 240, and 300 Hz, and was followed by a high-pass filter at 0.3 Hz to remove slow-wave and DC-offset artifacts. Bad channels were marked based on the information obtained through the data management platform of HCP for MEG data (ConnectomeDB; https://db.humanconnectome.org/). The artifacts (including heartbeats, eye blinks, saccades, muscle movements, and noisy segments) were then removed from the recordings using automatic procedures as proposed by Brainstorm. More specifically, electrocardiogram (ECG) and electrooculogram (EOG) recordings were used to detect heartbeats and blinks, respectively. We then used Signal-Space Projections (SSP) to automatically remove the detected artifacts. We also used SSP to remove saccades and muscle activity as low-frequency (1-7 Hz) and high-frequency (40-240 Hz) components, respectively.

The pre-processed sensor-level data was then used to obtain a source estimation on HCP's fsLR4k cortex surface for each participant. Head models were computed using overlapping spheres and the data and noise covariance matrices were estimated from the resting state MEG and noise recordings. Linearly constrained minimum variance (LCMV) beamformers method from Brainstorm was then used to obtain the source activity for each participant. We performed data covariance regularization and normalized the estimated source variance by the noise covariance matrix to reduce the effect of variable source depth. The L2 matrix norm (i.e. regularization parameter) of data covariance matrix is usually

defined as the largest eigenvalue of its eigenspectrum. However, the eigenspectrum of MEG data covariance can be ill-conditioned, such that the eigenvalues may span many decades where larger eigenvalues are overestimated and smaller eigenvalues are underestimated. In other words, the L2 norm of the data covariance matrix can be many times larger than the majority of eigenvalues, making it difficult to select a conventional regularization parameter. Following guidelines from Brainstorm (Tadel et al., 2011), we used the "median eigenvalue" method to regularize the data covariance matrix, where the eigenvalues smaller than the median eigenvalue are replaced with the median eigenvalue itself (i.e. flattening the tail of eigenvalues spectrum to the median). The covariance matrix is then reconstructed using the modified eigenspectrum. This helps to avoid the instability of data covariance inversion caused by the smallest eigenvalues and regularizes the data covariance matrix. Source orientations were constrained to be normal to the cortical surface at each of the 8,000 vertex locations on the fsLR4k surface. Source-level time-series were then parcellated into 400 regions using the Schaefer-400 atlas (Schaefer et al., 2018), such that a given parcel's time series was estimated as the first principal component of its constituting sources' time series.

Parcellated time-series were then used to estimate functional connectivity with an amplitude-based connectivity measure from Brainstorm (amplitude envelope correlation; AEC (Bruns et al., 2000)). An orthogonalization process was applied to correct for the spatial leakage effect by removing all shared zero-lag signals (Colclough et al., 2015). AEC functional connectivity were derived for each participant at six canonical electrophysiological bands (i.e., delta (δ: 2-4 Hz), theta (θ: 5-7 Hz), alpha (α: 8-12 Hz), beta (β: 15-29 Hz), low gamma (lo-γ: 30-59 Hz), and high gamma (hi-γ: 60-90Hz)). Group-average MEG functional connectivity matrices were constructed as the mean functional connectivity across all individuals for each frequency band. For comparison, band-limited group-average AEC matrices were also estimated without correcting for spatial leakage effect.

We also processed the MEG data using additional methodological choices. First, the LCMV source reconstructed and parcellated time-series were used to estimate functional connectivity with an alternative, phase-based connectivity measure (phase locking value; PLV (Lachaux et al., 1999; Mormann et al., 2000)) for each frequency band. Second, another source reconstruction method (standardized low resolution brain electromagnetic tomography; sLoreta (Pascual-Marqui et al., 2002)) was used instead of LCMV beamformers to obtain source-level time-series, given that previous reports suggest that sLoreta improves source localization accuracy (Hauk et al., 2019, 2011). Source-level time-series, obtained by sLoreta, were then parcellated into 400 regions and were used to estimate AEC matrices

with spatial leakage correction for the six frequency bands. Third, to ensure that the findings are independent from choice of parcellation, a low resolution atlas (Schaefer-200 (Schaefer et al., 2018)) was used to parcellate the original LCMV source-level time-series to 200 cortical regions and obtain spatial leakage corrected AEC connectivity matrices. Finally, we estimated MEG source localization errors for LCMV and sLoreta source reconstruction solutions using cross-talk functions (CTF) (Hauk and Stenroos, 2014; Hauk et al., 2019, 2022, 2011; Liu et al., 2002; Molins et al., 2008). CTF of a given source i is a measure of how activity from all other sources contributes to the activity estimated for the i-th source. Following guidelines from Brainstorm (Tadel et al., 2011) and MNE-Python software packages (Gramfort et al., 2013), we used CTF to calculate peak localization error of a given source i as the Euclidean distance between the peak location estimated for source i and the true source location i on the surface model (Hauk et al., 2019; Molins et al., 2008). Source-level CTF was then parcellated using the Schaefer-400 atlas. We also estimated source-level signal-to-noise ratio (SNR) for LCMV source reconstruction solution as follows (Goldenholz et al., 2009; Piastra et al., 2021):

$$\mathrm{SNR} = 10\log10(\frac{a^2}{N}\sum_{k=1}^{N}\frac{b_k^2}{s_k^2}) \tag{6.1}$$

where a is the source amplitude (i.e. typical strength of a dipole, which is 10 nAm (Hämäläinen et al., 1993)), N is the number of sensors, b_k is the signal at sensor k estimated by the forward model for a source with unit amplitude, and s_k^2 is the noise variance at sensor k. SNR was first calculated at the source level and was then parcellated using the Schaefer-400 atlas.

6.6.2.2 Resting state functional MRI

The functional MRI data were pre-processed using HCP minimal pre-processing pipelines (Glasser et al., 2013; Van Essen et al., 2013). Detailed information regarding data acquisition and pre-processing is available elsewhere (Glasser et al., 2013; Van Essen et al., 2013). Briefly, all 3T functional MRI time-series (voxel resolution of 2 mm isotropic) were corrected for gradient nonlinearity, head motion using a rigid body transformation, and geometric distortions using scan pairs with opposite phase encoding directions (R/L, L/R) (Wael et al., 2018). Further pre-processing steps include co-registration of the corrected images to the T1w structural MR images, brain extraction, normalization of whole brain intensity, high-pass filtering ($>$ 2000s FWHM; to correct for scanner drifts), and removing additional noise using the ICA-FIX process (Salimi-Khorshidi et al., 2014; Wael et al.,

2018). The pre-processed time-series were then parcellated into 400 cortical areas using Schaefer-400 parcellation (Schaefer et al., 2018). The parcellated time-series were used to construct functional connectivity matrices as Pearson correlation coefficients between pairs of regional time-series for each of the four scans and each participant. A group-average functional connectivity matrix was constructed as the mean functional connectivity across all individuals and scans.

6.6.2.3 Diffusion weighted imaging (DWI)

Diffusion weighted imaging (DWI) data was obtained for the same individuals from the HCP dataset. MRtrix3 package (Tournier et al., 2019) (`https://www.mrtrix.org/`) was used to pre-process the DWI data as described elsewhere (Shafiei et al., 2020b). In brief, multi-shell multi-tissue constrained spherical deconvolution algorithm from MRtrix was applied to generate fiber orientation distributions (Dhollander et al., 2016; Jeurissen et al., 2014). Probabilistic streamline tractography based on the generated fiber orientation distributions was used to reconstruct white matter edges (Tournier et al., 2010). The tract weights were optimized by estimating an appropriate cross-section multiplier for each streamline following the procedure proposed by Smith and colleagues (Smith et al., 2015). Structural connectivity matrices were then reconstructed for each participant using the Schaefer-400 atlas (Schaefer et al., 2018). Finally, a binary group-level structural connectivity matrix was constructed using a consensus approach that preserves the edge length distribution in individual participants (Betzel et al., 2018; Mišić et al., 2015). The binary consensus structural connectivity matrix was weighted by the average structural connectivity across individuals to obtain a weighted structural connectivity matrix.

6.6.3 BigBrain histological data

To characterize the cytoarchitectural variation across the cortex, cell-staining intensity profile data were obtained from the BigBrain atlas (Amunts et al., 2013; Paquola et al., 2021). The BigBrain is a high-resolution (20 μm) histological atlas of a post mortem human brain and includes cell-staining intensities that are sampled at each vertex across 50 equivolumetric surfaces from the pial to the white matter surface using the Merker staining technique (Amunts et al., 2013; Merker, 1983). The staining intensity profile data represent neuronal density and soma size at varying cortical depths, capturing the regional differentiation of cytoarchitecture (Amunts et al., 2013; Paquola et al., 2019, 2021; Wagstyl et al., 2018, 2020). Intensity profiles at various cortical depths can be used to approximately

identify boundaries of cortical layers that separate supragranular (cortical layers I-III), granular (cortical layer IV), and infragranular (cortical layers V-VI) layers (Paquola et al., 2021; Wagstyl et al., 2018, 2020). The data were obtained on *fsaverage* surface (164k vertices) from the BigBrainWarp toolbox (Paquola et al., 2021) and were parcellated into 400 cortical regions using the Schaefer-400 atlas (Schaefer et al., 2018).

The cross-modal correspondence map, estimated as adjusted-R^2 (see *Multi-linear model* for more details), was then compared with the parcellated cell-staining intensity data. Specifically, the regional model fit was correlated with cell-staining profiles at each cortical depth using Spearman rank correlation (r_s). 10,000 spatial-autocorrelation preserving nulls were used to construct a null distribution of correlation at each cortical depth (see *Null model* for more details on spatial-autocorrelation preserving nulls). Significance of the associations were estimated by comparing the empirical Spearman rank correlation with the distribution of null correlations at each cortical depth, identifying the number of null correlations that were equal to or greater than the empirical correlation (two-tailed test). Finally, Benjamini-Hochberg procedure (Benjamini and Hochberg, 1995) was used to correct for multiple comparisons by controlling the false discovery rate (FDR) at 5% across all 50 comparisons.

6.6.4 Allen Human Brain Atlas (AHBA)

Regional microarray expression data were obtained from 6 post-mortem brains (1 female, ages 24.0–57.0, 42.50 $\pm$ 13.38) provided by the Allen Human Brain Atlas (AHBA, `https://human.brain-map.org`; (Hawrylycz et al., 2012)). Data were processed with the `abagen` toolbox (version 0.1.3-doc; `https://github.com/rmarkello/abagen`; (Markello et al., 2021)) using the Schaefer-400 volumetric atlas in MNI space (Schaefer et al., 2018).

First, microarray probes were reannotated using data provided by (Arnatkevičiūtė et al., 2019); probes not matched to a valid Entrez ID were discarded. Next, probes were filtered based on their expression intensity relative to background noise (Quackenbush, 2002), such that probes with intensity less than the background in $\geq$ 50.00% of samples across donors were discarded. When multiple probes indexed the expression of the same gene, we selected and used the probe with the most consistent pattern of regional variation across donors (i.e., differential stability; (Hawrylycz et al., 2015)), calculated with:

$$\Delta_S(p) = \frac{1}{\binom{N}{2}} \sum_{i=1}^{N-1} \sum_{j=i+1}^{N} \rho[B_i(p), B_j(p)] \tag{6.2}$$

where ρ is Spearman rank correlation of the expression of a single probe, p, across regions in two donors B_i and B_j, and N is the total number of donors. Here, regions correspond to the structural designations provided in the ontology from the AHBA.

The MNI coordinates of tissue samples were updated to those generated via non-linear registration using the Advanced Normalization Tools (ANTs; https://github.com/chrisfilo/alleninf). To increase spatial coverage, tissue samples were mirrored bilaterally across the left and right hemispheres (Romero-Garcia et al., 2018). Samples were assigned to brain regions in the provided atlas if their MNI coordinates were within 2 mm of a given parcel. If a brain region was not assigned a tissue sample based on the above procedure, every voxel in the region was mapped to the nearest tissue sample from the donor in order to generate a dense, interpolated expression map. The average of these expression values was taken across all voxels in the region, weighted by the distance between each voxel and the sample mapped to it, in order to obtain an estimate of the parcellated expression values for the missing region. All tissue samples not assigned to a brain region in the provided atlas were discarded.

Inter-subject variation was addressed by normalizing tissue sample expression values across genes using a robust sigmoid function (Fulcher et al., 2013):

$$x_{norm} = \frac{1}{1 + \exp(-\frac{(x - \langle x \rangle)}{\mathrm{IQR}_x})} \tag{6.3}$$

where $\langle x \rangle$ is the median and IQR_x is the normalized interquartile range of the expression of a single tissue sample across genes. Normalized expression values were then rescaled to the unit interval:

$$x_{scaled} = \frac{x_{norm} - \min(x_{norm})}{\max(x_{norm}) - \min(x_{norm})} \tag{6.4}$$

Gene expression values were then normalized across tissue samples using an identical procedure. Samples assigned to the same brain region were averaged separately for each donor and then across donors, yielding a regional expression matrix of 15,633 genes. Expression of NPY1R (Neuropeptide Y Receptor Y1) was extracted from the regional expression matrix and was related to the cross-modal correspondence map, estimated as adjusted-R^2 (see *Multi-linear model* for more details), using 10,000 spatial-autocorrelation preserving nulls (see *Null model* for more details).

6.6.5 Multi-linear model

6.6.5.1 Regional model

A multiple linear regression model was used to assess regional associations between haemodynamic (fMRI) and electromagnetic (MEG) functional connectivity (Figure 6.1 (Vázquez-Rodríguez et al., 2019)). A separate multi-linear model is applied for each brain region from the parcellated data, predicting the region's fMRI functional connectivity profile from its band-limited MEG functional connectivity. The dependent variable is a row of the fMRI connectivity matrix and the independent variables (predictors) are the corresponding rows of MEG connectivity for the six canonical electrophysiological bands. The linear regression model for each brain region i is constructed as follows:

$$\begin{aligned} FC_i = & b_1 \times FC(\delta)_i + b_2 \times FC(\theta)_i + \\ & b_3 \times FC(\alpha)_i + b_4 \times FC(\beta)_i + \\ & b_5 \times FC(\text{lo},\gamma)_i + b_6 \times FC(\text{hi},\gamma)_i + b_0 \end{aligned} \tag{6.5}$$

where the dependant variable FC_i is the set of fMRI connections of node i to the other $j \neq i$ regions and the predictors are sets of MEG connections of node i to the other $j \neq i$ regions for the six frequency bands ($FC(\delta)_i$, $FC(\theta)_i$, $FC(\alpha)_i$, $FC(\beta)_i$, $FC(\text{lo},\gamma)_i$, $FC(\text{hi},\gamma)_i$). The regression coefficients $b_1, ..., b_6$ and the intercept b_0 are then optimized to yield maximum correlation between empirical and predicted fMRI connectivity for each brain region. Goodness of fit for each regional model is quantified using adjusted-R^2 (coefficient of determination).

6.6.5.2 Global model

For comparison with the regional model, a single global model was fitted to the data, predicting the whole-brain fMRI functional connectivity from the whole-brain band-limited MEG functional connectivity (Figure 6.1d). Specifically, rather than applying a multi-linear model for each region (i.e. each row) separately, we fit a single multi-linear model using the upper triangle of band-limited MEG connectivity (i.e. all values above the diagonal of MEG connectivity matrices) as predictors and predict the upper triangle of fMRI connectivity. The equation below describes the multi-linear global model:

$$\begin{aligned} FC_{UT} = & b_1 \times FC(\delta)_{UT} + b_2 \times FC(\theta)_{UT} + \\ & b_3 \times FC(\alpha)_{UT} + b_4 \times FC(\beta)_{UT} + \\ & b_5 \times FC(\text{lo},\gamma)_{UT} + b_6 \times FC(\text{hi},\gamma)_{UT} + b_0 \end{aligned} \tag{6.6}$$

where the dependent variable FC_{UT} is the vectorized upper triangle of fMRI functional connectivity (i.e. above diagonal values) and the predictors are the vectorized upper triangles of MEG functional connectivity for the six frequency bands. The regression coefficients $b_1, ..., b_6$ and the intercept b_0 are then optimized to yield maximum correlation between empirical and predicted fMRI connectivity. Similar to the regional model, the goodness of fit for the global model is quantified using adjusted-R^2 (coefficient of determination).

6.6.5.3 Region-level cross-validation

Region-level cross-validation was performed to assess out-of-sample model performance. Given the spatial autocorrelation inherent to the data, random splits of brain regions into train and test sets may result in out-of-sample correlations that are inflated due to spatial proximity (Markello and Misic, 2021). To take this into account, we used a distance-dependant cross-validation approach where we pseudorandomly split the connectivity profile of a given region (e.g. node i) into train and test sets based on spatial separation (Hansen et al., 2021a). We used inter-regional Euclidean distance to select 75% of the closest regions to a randomly selected source region as the train set and the remaining 25% of the regions as test set. The random source region can be any of the 399 regions connected to node i; hence, the connectivity profile of node i is split into 399 unique train and test sets. We then train the multi-linear model using the train set and predict functional connectivity of the test set for each region and each split. Finally, the model performance is quantified using Pearson correlation coefficient between empirical and predicted values. The cross-validated regional model performance is then estimated as the mean correlation coefficient between empirical and predicted values across splits for each brain region.

6.6.5.4 Subject-level cross-validation

Leave-one-out cross-validation was performed to assess model performance on held-out subjects. Briefly, the regional multi-linear model is trained using the group-average data from $n - 1$ subjects. The trained model is then used to predict fMRI connectivity profile of each region on the held-out subject (test set). The model performance is quantified as

the Pearson correlation coefficient between empirical and predicted connectivity of each region. The analysis is repeated for all subjects and the regional model performance is averaged across individuals.

6.6.6 Diffusion map embedding

Diffusion map embedding was used to identify the principal axis of variation in functional organization of the cortex (diffusion map embedding and alignment package; https://github.com/satra/mapalign) (Langs et al., 2015; Margulies et al., 2016). Diffusion map embedding is a nonlinear dimensionality reduction technique that generates a low-dimensional representation of high-dimensional data by projecting it into an embedding space, such that the areas with similar connectivity profiles will be closer in distance in the new common space compared to the areas with dissimilar connectivity profiles (Coifman et al., 2005; Langs et al., 2015; Margulies et al., 2016). In brief, following the procedure described by Margulies and colleagues (Margulies et al., 2016), each row of the group-average fMRI functional connectivity was thresholded at 90%, such that only the top 10% of functional connections was retained in the matrix. Next, a cosine-similarity matrix was estimated based on the remaining functional connections, where the resulting pairwise cosine distances represent the similarity between the connectivity profiles of cortical regions according to their strongest connections. Finally, the diffusion map embedding was applied to the resulting positive affinity matrix. This identifies the principal axis of variation in functional connectivity, along which cortical regions are ordered based on the similarity of their connectivity profiles. The identified functional gradient or hierarchy spans the unimodal-transmodal axis, separating primary sensory-motor cortices from association cortex. The functional gradient map is also available as part of the `neuromaps` toolbox (Markello et al., 2022). The functional gradient was used as a metric of hierarchical organization of the cortex and was compared with the regional model fit (Figure 6.2).

6.6.7 Structure-function coupling

Structure-function coupling was estimated following the procedure described by Baum and colleagues (Baum et al., 2020). Structural and functional connectivity profiles of each brain region (i.e. each row of the connectivity matrices) were extracted from the weighted group-level structural and functional connectivity matrices. Structure-function coupling of a given region was then estimated as the Spearman rank correlation between non-zero values of that region's structural and functional connectivity profiles. Finally,

the resulting whole-brain structure-function coupling map was compared with the cross-modal correspondence map (i.e. R^2 map from the regional model). Significance of the association between the two maps was assessed using 10,000 spatial-autocorrelation preserving nulls (see *Null model* for more details).

6.6.8 Dominance analysis

Dominance Analysis was used to quantify the distinct contributions of resting state MEG connectivity at different frequency bands to the prediction of resting state fMRI connectivity in the multi-linear model (Azen and Budescu, 2003; Budescu, 1993) (https://github.com/dominance-analysis/dominance-analysis). Dominance analysis estimates the relative importance of predictors by constructing all possible combinations of predictors and re-fitting the multi-linear model for each combination (a model with p predictors will have $2^p - 1$ models for all possible combinations of predictors). The relative contribution of each predictor is then quantified as increase in variance explained by adding that predictor to the models (i.e. gain in adjusted-R^2). Here we first constructed a multiple linear regression model for each region with MEG connectivity profile of that region at six frequency bands as independent variables (predictors) and fMRI connectivity of the region as the dependent variable to quantify the distinct contribution of each factor using dominance analysis. The relative importance of each factor is estimated as "percent relative importance", which is a summary measure that quantifies the percent value of the additional contribution of that predictor to all subset models.

6.6.9 Null model

To make inferences about the topographic correlations between any two brain maps, we implement a null model that systematically disrupts the relationship between two topographic maps but preserves their spatial autocorrelation (Alexander-Bloch et al., 2018; Markello and Misic, 2021). We used the Schaefer-400 atlas in the HCP's fsLR32k grayordinate space (Schaefer et al., 2018; Van Essen et al., 2013). The spherical projection of the fsLR32k surface was used to define spatial coordinates for each parcel by selecting the vertex closest to the center-of-mass of each parcel (Shafiei et al., 2020a; Vázquez-Rodríguez et al., 2019; Vazquez-Rodriguez et al., 2020). The resulting spatial coordinates were used to generate null models by applying randomly-sampled rotations and reassigning node values based on the closest resulting parcel (10,000 repetitions). The rotation was applied to one hemisphere and then mirrored to the other hemisphere.

6.6.10 Code and data availability

Code and data used to conduct the reported analyses is available on GitHub (https://github.com/netneurolab/shafiei_megfmrimapping). Data used in this study were obtained from the Human Connectome Project (HCP) database (original HCP Young Adult data available at https://db.humanconnectome.org/ via Amazon Web Services (AWS)). The data and code needed to generate all main and supplementary figures can be found in https://github.com/netneurolab/shafiei_megfmrimapping and https://zenodo.org/record/6728338.

6.7 Acknowledgments

We thank Ross Markello, Estefany Suarez, Bertha Vazquez-Rodriguez, Zhen-Qi Liu for their comments on the manuscript. This research was undertaken thanks in part to funding from the Canada First Research Excellence Fund, awarded to McGill University for the Healthy Brains for Healthy Lives initiative. BM acknowledges support from the Natural Sciences and Engineering Research Council of Canada (NSERC Discovery Grant RGPIN #017-04265) and from the Canada Research Chairs Program. SB is grateful for the support received from the NIH (R01 EB026299), a Discovery grant from the Natural Science and Engineering Research Council of Canada (NSERC 436355-13), the CIHR Canada research Chair in Neural Dynamics of Brain Systems, the Brain Canada Foundation with support from Health Canada, and the Innovative Ideas program from the Canada First Research Excellence Fund, awarded to McGill University for the Healthy Brains for Healthy Lives initiative. GS acknowledges support from the Natural Sciences and Engineering Research Council of Canada (NSERC) and the Fonds de recherche du Québec - Nature et Technologies (FRQNT).

6.8 Bibliography

Alexander-Bloch, A. F. et al. (2018). "On testing for spatial correspondence between maps of human brain structure and function". *Neuroimage*, 178, pp. 540–551.

Amunts, K. et al. (2013). "BigBrain: an ultrahigh-resolution 3D human brain model". *Science*, 340(6139), pp. 1472–1475.

Arnatkevičiūtė, A., B. D. Fulcher, and A. Fornito (2019). "A practical guide to linking brain-wide gene expression and neuroimaging data". *Neuroimage*, 189, pp. 353–367.

Azen, R. and D. V. Budescu (2003). "The dominance analysis approach for comparing predictors in multiple regression." *Psychological methods*, 8(2), p. 129.

Baillet, S. (2017). "Magnetoencephalography for brain electrophysiology and imaging". *Nature neuroscience*, 20(3), pp. 327–339.

Baker, A. P. et al. (2014). "Fast transient networks in spontaneous human brain activity". *Elife*, 3, e01867.

Baldassano, C. et al. (2017). "Discovering event structure in continuous narrative perception and memory". *Neuron*, 95(3), pp. 709–721.

Bastos, A. M. et al. (2018). "Laminar recordings in frontal cortex suggest distinct layers for maintenance and control of working memory". *Proceedings of the National Academy of Sciences*, 115(5), pp. 1117–1122.

Bastos, A. M. et al. (2020). "Layer and rhythm specificity for predictive routing". *Proceedings of the National Academy of Sciences*, 117(49), pp. 31459–31469.

Bastos, A. M. et al. (2015). "Visual areas exert feedforward and feedback influences through distinct frequency channels". *Neuron*, 85(2), pp. 390–401.

Baum, G. L. et al. (2020). "Development of structure–function coupling in human brain networks during youth". *Proceedings of the National Academy of Sciences*, 117(1), pp. 771–778.

Bellec, P. et al. (2006). "Identification of large-scale networks in the brain using fMRI". *Neuroimage*, 29(4), pp. 1231–1243.

Benjamini, Y. and Y. Hochberg (1995). "Controlling the false discovery rate: a practical and powerful approach to multiple testing". *Journal of the Royal statistical society: series B (Methodological)*, 57(1), pp. 289–300.

Betzel, R. F. et al. (2018). "Distance-dependent consensus thresholds for generating group-representative structural brain networks". *Network Neuroscience*, pp. 1–22.

Betzel, R. F. et al. (2019). "Structural, geometric and genetic factors predict interregional brain connectivity patterns probed by electrocorticography". *Nature biomedical engineering*, 3(11), pp. 902–916.

Brookes, M. J. et al. (2011a). "Investigating the electrophysiological basis of resting state networks using magnetoencephalography". *Proceedings of the National Academy of Sciences*, 108(40), pp. 16783–16788.

Brookes, M. J. et al. (2011b). "Measuring functional connectivity using MEG: methodology and comparison with fcMRI". *Neuroimage*, 56(3), pp. 1082–1104.

Brookes, M. J. et al. (2012). "Task induced modulation of neural oscillations in electrophysiological brain networks". *Neuroimage*, 63(4), pp. 1918–1930.

Brookes, M. J. et al. (2016). "A multi-layer network approach to MEG connectivity analysis". *Neuroimage*, 132, pp. 425–438.

Bruns, A. et al. (2000). "Amplitude envelope correlation detects coupling among incoherent brain signals". *Neuroreport*, 11(7), pp. 1509–1514.

Budescu, D. V. (1993). "Dominance analysis: a new approach to the problem of relative importance of predictors in multiple regression." *Psychological bulletin*, 114(3), p. 542.

Buffalo, E. A. et al. (2011). "Laminar differences in gamma and alpha coherence in the ventral stream". *Proceedings of the National Academy of Sciences*, 108(27), pp. 11262–11267.

Burt, J. B. et al. (2018). "Hierarchy of transcriptomic specialization across human cortex captured by structural neuroimaging topography". *Nat Neurosci*, 21(9), pp. 1251–1259.

Cabral, J. et al. (2014). "Exploring mechanisms of spontaneous functional connectivity in MEG: how delayed network interactions lead to structured amplitude envelopes of band-pass filtered oscillations". *Neuroimage*, 90, pp. 423–435.

Chaudhuri, R. et al. (2015). "A large-scale circuit mechanism for hierarchical dynamical processing in the primate cortex". *Neuron*, 88(2), pp. 419–431.

Chien, H.-Y. S. and C. J. Honey (2020). "Constructing and forgetting temporal context in the human cerebral cortex". *Neuron*.

Coifman, R. R. et al. (2005). "Geometric diffusions as a tool for harmonic analysis and structure definition of data: Diffusion maps". *Proc Natl Acad Sci USA*, 102(21), pp. 7426–7431.

Colclough, G. L. et al. (2015). "A symmetric multivariate leakage correction for MEG connectomes". *Neuroimage*, 117, pp. 439–448.

Colclough, G. L. et al. (2016). "How reliable are MEG resting-state connectivity metrics?" *Neuroimage*, 138, pp. 284–293.

Cole, M. W. et al. (2014). "Intrinsic and task-evoked network architectures of the human brain". *Neuron*, 83(1), pp. 238–251.

Das, A., C. de Los Angeles, and V. Menon (2022). "Electrophysiological foundations of the human default-mode network revealed by intracranial-EEG recordings during resting-state and cognition". *NeuroImage*, p. 118927.

De Pasquale, F. et al. (2010). "Temporal dynamics of spontaneous MEG activity in brain networks". *Proceedings of the National Academy of Sciences*, 107(13), pp. 6040–6045.

Deligianni, F. et al. (2014). "Relating resting-state fMRI and EEG whole-brain connectomes across frequency bands". *Frontiers in neuroscience*, 8, p. 258.

Demuru, M. and M. Fraschini (2020). "EEG fingerprinting: Subject-specific signature based on the aperiodic component of power spectrum". *Computers in Biology and Medicine*, 120, p. 103748.

Dhollander, T., D. Raffelt, and A. Connelly (2016). "Unsupervised 3-tissue response function estimation from single-shell or multi-shell diffusion MR data without a co-registered T1 image". In: *ISMRM Workshop on Breaking the Barriers of Diffusion MRI*. Vol. 5.

Donhauser, P. W. and S. Baillet (2020). "Two distinct neural timescales for predictive speech processing". *Neuron*, 105(2), pp. 385–393.

Douglas, R. J. and K. A. Martin (2004). "Neuronal circuits of the neocortex". *Annu. Rev. Neurosci.*, 27, pp. 419–451.

Drew, P. J. (2019). "Vascular and neural basis of the BOLD signal". *Current Opinion in Neurobiology*, 58, pp. 61–69.

Finn, E. S., L. Huber, and P. A. Bandettini (2021). "Higher and deeper: Bringing layer fMRI to association cortex". *Progress in Neurobiology*, 207, p. 101930.

Finn, E. S. et al. (2019). "Layer-dependent activity in human prefrontal cortex during working memory". *Nature neuroscience*, 22(10), pp. 1687–1695.

Florin, E. and S. Baillet (2015). "The brain's resting-state activity is shaped by synchronized cross-frequency coupling of neural oscillations". *Neuroimage*, 111, pp. 26–35.

Fraschini, M. et al. (2019). "Robustness of functional connectivity metrics for EEG-based personal identification over task-induced intra-class and inter-class variations". *Pattern Recognition Letters*, 125, pp. 49–54.

Freeman, W. J., S. P. Ahlfors, and V. Menon (2009). "Combining fMRI with EEG and MEG in order to relate patterns of brain activity to cognition". *International journal of psychophysiology*, 73(1), pp. 43–52.

Fries, P. (2005). "A mechanism for cognitive dynamics: neuronal communication through neuronal coherence". *Trends in cognitive sciences*, 9(10), pp. 474–480.

Froudist-Walsh, S. et al. (2021). "Gradients of receptor expression in the macaque cortex". *bioRxiv*.

Fulcher, B. D., M. A. Little, and N. S. Jones (2013). "Highly comparative time-series analysis: the empirical structure of time series and their methods". *Journal of the Royal Society Interface*, 10(83), p. 20130048.

Fulcher, B. D. et al. (2019). "Multimodal gradients across mouse cortex". *Proc Natl Acad Sci USA*, 116(10), pp. 4689–4695.

Gao, R. et al. (2020). "Neuronal timescales are functionally dynamic and shaped by cortical microarchitecture". *Elife*, 9, e61277.

Garcés, P. et al. (2016). "Multimodal description of whole brain connectivity: A comparison of resting state MEG, fMRI, and DWI". *Human brain mapping*, 37(1), pp. 20–34.

Glasser, M. F. et al. (2013). "The minimal preprocessing pipelines for the Human Connectome Project". *Neuroimage*, 80, pp. 105–124.

Goldenholz, D. M. et al. (2009). "Mapping the signal-to-noise-ratios of cortical sources in magnetoencephalography and electroencephalography". *Human brain mapping*, 30(4), pp. 1077–1086.

Gordon, E. M. et al. (2017). "Precision functional mapping of individual human brains". *Neuron*, 95(4), pp. 791–807.

Goulas, A. et al. (2021). "The natural axis of transmitter receptor distribution in the human cerebral cortex". *Proceedings of the National Academy of Sciences*, 118(3).

Gramfort, A. et al. (2013). "MEG and EEG data analysis with MNE-Python". *Frontiers in neuroscience*, 7, p. 267.

Hall, E. L. et al. (2014). "The relationship between MEG and fMRI". *Neuroimage*, 102, pp. 80–91.

Hämäläinen, M. et al. (1993). "Magnetoencephalography—theory, instrumentation, and applications to noninvasive studies of the working human brain". *Reviews of modern Physics*, 65(2), p. 413.

Hansen, J. Y. et al. (2021a). "Mapping gene transcription and neurocognition across human neocortex". *Nature Human Behaviour*, 5(9), pp. 1240–1250.

Hansen, J. Y. et al. (2021b). "Mapping neurotransmitter systems to the structural and functional organization of the human neocortex". *bioRxiv*.

Harel, N. et al. (2006). "Combined imaging–histological study of cortical laminar specificity of fMRI signals". *Neuroimage*, 29(3), pp. 879–887.

Hari, R. and L. Parkkonen (2015). "The brain timewise: how timing shapes and supports brain function". *Philosophical Transactions of the Royal Society B: Biological Sciences*, 370(1668), p. 20140170.

Hasson, U. et al. (2008). "A hierarchy of temporal receptive windows in human cortex". *J Neurosci*, 28(10), pp. 2539–2550.

Hauk, O. and M. Stenroos (2014). "A framework for the design of flexible cross-talk functions for spatial filtering of EEG/MEG data: DeFleCT". *Human brain mapping*, 35(4), pp. 1642–1653.

Hauk, O., M. Stenroos, and M. Treder (2019). "EEG/MEG source estimation and spatial filtering: the linear toolkit". *Magnetoencephalography: From Signals to Dynamic Cortical Networks*, pp. 167–203.

— (2022). "Towards an Objective Evaluation of EEG/MEG Source Estimation Methods-The Linear Approach". *NeuroImage*, p. 119177.

Hauk, O., D. G. Wakeman, and R. Henson (2011). "Comparison of noise-normalized minimum norm estimates for MEG analysis using multiple resolution metrics". *Neuroimage*, 54(3), pp. 1966–1974.

Hawrylycz, M. et al. (2015). "Canonical genetic signatures of the adult human brain". *Nature neuroscience*, 18(12), p. 1832.

Hawrylycz, M. J. et al. (2012). "An anatomically comprehensive atlas of the adult human brain transcriptome". *Nature*, 489(7416), p. 391.

Hipp, J. F. and M. Siegel (2015). "BOLD fMRI correlation reflects frequency-specific neuronal correlation". *Current Biology*, 25(10), pp. 1368–1374.

Hipp, J. F. et al. (2012). "Large-scale cortical correlation structure of spontaneous oscillatory activity". *Nature neuroscience*, 15(6), pp. 884–890.

Honey, C. J. et al. (2012). "Slow cortical dynamics and the accumulation of information over long timescales". *Neuron*, 76(2), pp. 423–434.

Huber, L. et al. (2017). "High-resolution CBV-fMRI allows mapping of laminar activity and connectivity of cortical input and output in human M1". *Neuron*, 96(6), pp. 1253–1263.

Huber, L. et al. (2021). "Layer-dependent functional connectivity methods". *Progress in Neurobiology*, 207, p. 101835.

Huntenburg, J. M., P.-L. Bazin, and D. S. Margulies (2018). "Large-scale gradients in human cortical organization". *Trends in cognitive sciences*, 22(1), pp. 21–31.

Huntenburg, J. M. et al. (2017). "A systematic relationship between functional connectivity and intracortical myelin in the human cerebral cortex". *Cereb Cortex*, 27(2), pp. 981–997.

Jeurissen, B. et al. (2014). "Multi-tissue constrained spherical deconvolution for improved analysis of multi-shell diffusion MRI data". *NeuroImage*, 103, pp. 411–426.

Kujala, J. et al. (2014). "Multivariate analysis of correlation between electrophysiological and hemodynamic responses during cognitive processing". *NeuroImage*, 92, pp. 207–216.

Lachaux, J.-P. et al. (1999). "Measuring phase synchrony in brain signals". *Human brain mapping*, 8(4), pp. 194–208.

Langs, G., P. Golland, and S. S. Ghosh (2015). "Predicting activation across individuals with resting-state functional connectivity based multi-atlas label fusion". In: *International*

Conference on Medical Image Computing and Computer-Assisted Intervention. Springer, pp. 313–320.

Liljeström, M. et al. (2015). "Task-and stimulus-related cortical networks in language production: Exploring similarity of MEG-and fMRI-derived functional connectivity". *NeuroImage*, 120, pp. 75–87.

Liu, A. K., A. M. Dale, and J. W. Belliveau (2002). "Monte Carlo simulation studies of EEG and MEG localization accuracy". *Human brain mapping*, 16(1), pp. 47–62.

Logothetis, N. K. (2003). "The underpinnings of the BOLD functional magnetic resonance imaging signal". *Journal of Neuroscience*, 23(10), pp. 3963–3971.

Maier, A., C. J. Aura, and D. A. Leopold (2011). "Infragranular sources of sustained local field potential responses in macaque primary visual cortex". *Journal of Neuroscience*, 31(6), pp. 1971–1980.

Maier, A. et al. (2010). "Distinct superficial and deep laminar domains of activity in the visual cortex during rest and stimulation". *Frontiers in systems neuroscience*, 4, p. 31.

Mantini, D. et al. (2007). "Electrophysiological signatures of resting state networks in the human brain". *Proceedings of the National Academy of Sciences*, 104(32), pp. 13170–13175.

Margulies, D. S. et al. (2016). "Situating the default-mode network along a principal gradient of macroscale cortical organization". *Proceedings of the National Academy of Sciences*, 113(44), pp. 12574–12579.

Markello, R. D. and B. Misic (2021). "Comparing spatial null models for brain maps". *NeuroImage*, 236, p. 118052.

Markello, R. D. et al. (2021). "Standardizing workflows in imaging transcriptomics with the abagen toolbox". *Elife*, 10, e72129.

Markello, R. D. et al. (2022). "Neuromaps: structural and functional interpretation of brain maps". *bioRxiv*.

Menon, V et al. (1997). "Combined event-related fMRI and EEG evidence for temporal—parietal cortex activation during target detection". *Neuroreport*, 8(14), pp. 3029–3037.

Merker, B. (1983). "Silver staining of cell bodies by means of physical development". *Journal of neuroscience methods*, 9(3), pp. 235–241.

Mesulam, M.-M. (1998). "From sensation to cognition." *Brain*, 121(6), pp. 1013–1052.

Mišić, B. et al. (2015). "Cooperative and competitive spreading dynamics on the human connectome". *Neuron*, 86(6), pp. 1518–1529.

Molins, A et al. (2008). "Quantification of the benefit from integrating MEG and EEG data in minimum l2-norm estimation". *Neuroimage*, 42(3), pp. 1069–1077.

Mormann, F. et al. (2000). "Mean phase coherence as a measure for phase synchronization and its application to the EEG of epilepsy patients". *Physica D: Nonlinear Phenomena*, 144(3-4), pp. 358–369.

Mukamel, R. et al. (2005). "Coupling between neuronal firing, field potentials, and FMRI in human auditory cortex". *Science*, 309(5736), pp. 951–954.

Murray, J. D. et al. (2014). "A hierarchy of intrinsic timescales across primate cortex". *Nat Neurosci*, 17(12), p. 1661.

Musso, F. et al. (2010). "Spontaneous brain activity and EEG microstates. A novel EEG/fMRI analysis approach to explore resting-state networks". *Neuroimage*, 52(4), pp. 1149–1161.

Niso, G. et al. (2013). "HERMES: towards an integrated toolbox to characterize functional and effective brain connectivity". *Neuroinformatics*, 11(4), pp. 405–434.

Noble, S., D. Scheinost, and R. T. Constable (2019). "A decade of test-retest reliability of functional connectivity: A systematic review and meta-analysis". *Neuroimage*, 203, p. 116157.

Paquola, C. et al. (2019). "Microstructural and functional gradients are increasingly dissociated in transmodal cortices". *PLoS Biol*, 17(5), e3000284.

Paquola, C. et al. (2020). "Convergence of cortical types and functional motifs in the human mesiotemporal lobe". *Elife*, 9, e60673.

Paquola, C. et al. (2021). "The BigBrainWarp toolbox for integration of BigBrain 3D histology with multimodal neuroimaging". *eLife*, 10. Ed. by S. Jbabdi et al., e70119.

Pascual-Marqui, R. D. et al. (2002). "Standardized low-resolution brain electromagnetic tomography (sLORETA): technical details". *Methods Find Exp Clin Pharmacol*, 24(Suppl D), pp. 5–12.

Piastra, M. C. et al. (2021). "A comprehensive study on electroencephalography and magnetoencephalography sensitivity to cortical and subcortical sources". *Human Brain Mapping*, 42(4), pp. 978–992.

Power, J. D. et al. (2011). "Functional network organization of the human brain". *Neuron*, 72(4), pp. 665–678.

Preti, M. G. and D. Van De Ville (2019). "Decoupling of brain function from structure reveals regional behavioral specialization in humans". *Nature communications*, 10(1), pp. 1–7.

Quackenbush, J. (2002). "Microarray data normalization and transformation". *Nature genetics*, 32(4), pp. 496–501.

Raut, R. V., A. Z. Snyder, and M. E. Raichle (2020). "Hierarchical dynamics as a macroscopic organizing principle of the human brain". *Proceedings of the National Academy of Sciences*, 117(34), pp. 20890–20897.

Romero-Garcia, R. et al. (2018). "Structural covariance networks are coupled to expression of genes enriched in supragranular layers of the human cortex". *Neuroimage*, 171, pp. 256–267.

Sadaghiani, S., M. J. Brookes, and S. Baillet (2022). "Connectomics of human electrophysiology". *NeuroImage*, 247, p. 118788.

Sadaghiani, S. and J. Wirsich (2020). "Intrinsic connectome organization across temporal scales: New insights from cross-modal approaches". *Network Neuroscience*, 4(1), pp. 1–29.

Safron, A. (2020). "An Integrated World Modeling Theory (IWMT) of consciousness: combining integrated information and global neuronal workspace theories with the free energy principle and active inference framework; toward solving the hard problem and characterizing agentic causation". *Frontiers in artificial intelligence*, 3, p. 30.

Safron, A., V. Klimaj, and I. Hipólito (2022). "On the importance of being flexible: dynamic brain networks and their potential functional significances". *Frontiers in Systems Neuroscience*, p. 149.

Salimi-Khorshidi, G. et al. (2014). "Automatic denoising of functional MRI data: combining independent component analysis and hierarchical fusion of classifiers". *Neuroimage*, 90, pp. 449–468.

Sareen, E. et al. (2021). "Exploring MEG brain fingerprints: Evaluation, pitfalls, and interpretations". *NeuroImage*, 240, p. 118331.

Sarwar, T. et al. (2021). "Structure-function coupling in the human connectome: A machine learning approach". *NeuroImage*, 226, p. 117609.

Schaefer, A. et al. (2018). "Local-global parcellation of the human cerebral cortex from intrinsic functional connectivity MRI". *Cerebral cortex*, 28(9), pp. 3095–3114.

Scheeringa, R. and P. Fries (2019). "Cortical layers, rhythms and BOLD signals". *NeuroImage*, 197, pp. 689–698.

Scheeringa, R. et al. (2016). "The relationship between oscillatory EEG activity and the laminar-specific BOLD signal". *Proceedings of the National Academy of Sciences*, 113(24), pp. 6761–6766.

Schmid, F. et al. (2019). "Vascular density and distribution in neocortex". *Neuroimage*, 197, pp. 792–805.

Seth, A. K. and T. Bayne (2022). "Theories of consciousness". *Nature Reviews Neuroscience*, pp. 1–14.

Shafiei, G., S. Baillet, and B. Misic (2022). "Human electromagnetic and haemodynamic networks systematically converge in unimodal cortex and diverge in transmodal cortex". *PLOS Biology*, 20(8), pp. 1–27.

Shafiei, G. et al. (2020a). "Spatial patterning of tissue volume loss in schizophrenia reflects brain network architecture". *Biol Psychiat*.

Shafiei, G. et al. (2020b). "Topographic gradients of intrinsic dynamics across neocortex". *Elife*, 9, e62116.

Silva Castanheira, J. da et al. (2021). "Brief segments of neurophysiological activity enable individual differentiation". *Nature communications*, 12(1), pp. 1–11.

Singh, K. D. (2012). "Which "neural activity" do you mean? fMRI, MEG, oscillations and neurotransmitters". *Neuroimage*, 62(2), pp. 1121–1130.

Smith, M. A. et al. (2013). "Laminar dependence of neuronal correlations in visual cortex". *Journal of neurophysiology*, 109(4), pp. 940–947.

Smith, R. E. et al. (2015). "SIFT2: Enabling dense quantitative assessment of brain white matter connectivity using streamlines tractography". *Neuroimage*, 119, pp. 338–351.

Smith, S. M. et al. (2009). "Correspondence of the brain's functional architecture during activation and rest". *Proceedings of the national academy of sciences*, 106(31), pp. 13040–13045.

Sorrentino, P. et al. (2021). "The structural connectome constrains fast brain dynamics". *Elife*, 10, e67400.

Stevenson, C. M. et al. (2012). "Paired pulse depression in the somatosensory cortex: associations between MEG and BOLD fMRI". *Neuroimage*, 59(3), pp. 2722–2732.

Suárez, L. E. et al. (2020). "Linking structure and function in macroscale brain networks". *Trends Cogn Sci*.

Tadel, F. et al. (2011). "Brainstorm: a user-friendly application for MEG/EEG analysis". *Computational intelligence and neuroscience*, 2011.

Tewarie, P. et al. (2014). "Structural degree predicts functional network connectivity: a multimodal resting-state fMRI and MEG study". *NeuroImage*, 97, pp. 296–307.

Tewarie, P. et al. (2016). "Predicting haemodynamic networks using electrophysiology: The role of non-linear and cross-frequency interactions". *Neuroimage*, 130, pp. 273–292.

Tournier, J. D., F. Calamante, and A. Connelly (2010). "Improved probabilistic streamlines tractography by 2nd order integration over fibre orientation distributions". In: *Proceedings of the international society for magnetic resonance in medicine*. Vol. 18, p. 1670.

Tournier, J.-D. et al. (2019). "MRtrix3: A fast, flexible and open software framework for medical image processing and visualisation". *NeuroImage*, p. 116137.

Uhlirova, H. et al. (2016). "Cell type specificity of neurovascular coupling in cerebral cortex". *elife*, 5, e14315.

Uludağ, K. and P. Blinder (2018). "Linking brain vascular physiology to hemodynamic response in ultra-high field MRI". *Neuroimage*, 168, pp. 279–295.

Van Essen, D. C. et al. (2013). "The WU-Minn human connectome project: an overview". *Neuroimage*, 80, pp. 62–79.

Vázquez-Rodríguez, B. et al. (2019). "Gradients of structure–function tethering across neocortex". *Proc Natl Acad Sci USA*, 116(42), pp. 21219–21227.

Vazquez-Rodriguez, B. et al. (2020). "Signal propagation via cortical hierarchies". *Net Neurosci*.

Vinck, M. et al. (2011). "An improved index of phase-synchronization for electrophysiological data in the presence of volume-conduction, noise and sample-size bias". *Neuroimage*, 55(4), pp. 1548–1565.

Wael, R. Vos de et al. (2018). "Anatomical and microstructural determinants of hippocampal subfield functional connectome embedding". *Proceedings of the National Academy of Sciences*, 115(40), pp. 10154–10159.

Wagstyl, K. et al. (2018). "Mapping cortical laminar structure in the 3D BigBrain". *Cerebral cortex*, 28(7), pp. 2551–2562.

Wagstyl, K. et al. (2020). "BigBrain 3D atlas of cortical layers: Cortical and laminar thickness gradients diverge in sensory and motor cortices". *PLoS Biol*, 18(4), e3000678.

Wirsich, J. et al. (2017). "Complementary contributions of concurrent EEG and fMRI connectivity for predicting structural connectivity". *Neuroimage*, 161, pp. 251–260.

Wirsich, J. et al. (2021). "The relationship between EEG and fMRI connectomes is reproducible across simultaneous EEG-fMRI studies from 1.5 T to 7T". *NeuroImage*, 231, p. 117864.

Yeo, B. T. et al. (2011). "The organization of the human cerebral cortex estimated by intrinsic functional connectivity". *Journal of neurophysiology*, 106(3), p. 1125.

Yin, W. et al. (2020). "The emergence of a functionally flexible brain during early infancy". *Proceedings of the National Academy of Sciences*, 117(38), pp. 23904–23913.

Zamani Esfahlani, F. et al. (2022). "Local structure-function relationships in human brain networks across the lifespan". *Nature communications*, 13(1), pp. 1–16.

Table S6.1: **Analysis of Variance (ANOVA) for dominance analysis** | To quantitatively assess the differences in band-specific contributions to the cross-modal correspondence map, contributions estimated from dominance analysis were compared for all possible pairs of frequency bands using Analysis of Variance (ANOVA). All reported *p*-values are from two-tailed tests and are corrected for multiple comparisons using Bonferroni correction. Cohen's *d* denotes effect size.

Band A	**Band B**	**mean(A)**	**mean(B)**	**difference**	***t*-value**	***p*-value**	**Cohen's *d***
delta	theta	15.06	19.87	-4.81	-5.26	<0.0001	-0.37
delta	alpha	15.06	18.79	-3.72	-4.07	0.00073	-0.29
delta	beta	15.06	27.44	-12.37	-13.53	<0.0001	-0.96
delta	lo-gamma	15.06	11.28	3.78	4.14	0.00055	0.29
delta	hi-gamma	15.06	7.56	7.51	8.21	<0.0001	0.58
theta	alpha	19.87	18.79	1.08	1.19	1	0.08
theta	beta	19.87	27.44	-7.56	-8.27	<0.0001	-0.58
theta	lo-gamma	19.87	11.28	8.59	9.39	<0.0001	0.66
theta	hi-gamma	19.87	7.56	12.32	13.46	<0.0001	0.95
alpha	beta	18.79	27.44	-8.65	-9.46	<0.0001	-0.69
alpha	lo-gamma	18.79	11.28	7.51	8.21	<0.0001	0.58
alpha	hi-gamma	18.79	7.56	11.23	12.28	<0.0001	0.87
beta	lo-gamma	27.44	11.28	16.16	17.66	<0.0001	1.25
beta	hi-gamma	27.44	7.56	19.88	21.73	<0.0001	1.54
lo-gamma	hi-gamma	11.28	7.56	3.72	4.07	0.00072	0.29

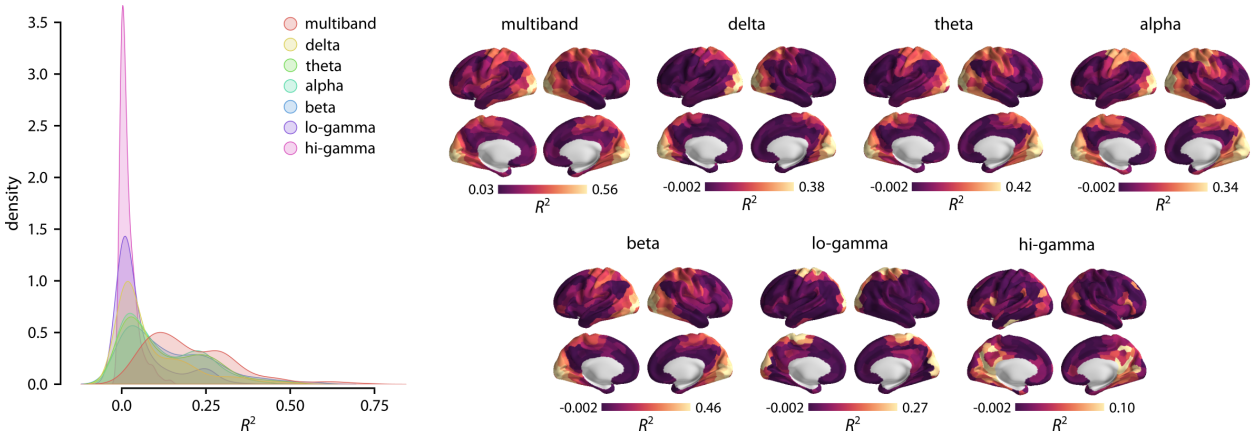

Figure S6.1: **Band-specific regional model fit** | Separate regional regression models were applied to map MEG functional connectivity (AEC) to fMRI functional connectivity at each frequency band. Distributions of adjusted-R^2 are depicted for band-specific regional model fits and for the multiband model fit obtained by the original analysis. The multi-linear regional model that combines MEG connectivity at multiple rhythms to predict regional fMRI connectivity profiles performs better than the band-specific models. The data and code needed to generate this figure can be found in https://github.com/netneurolab/shafiei_megfmrimapping and https://zenodo.org/record/6728338.

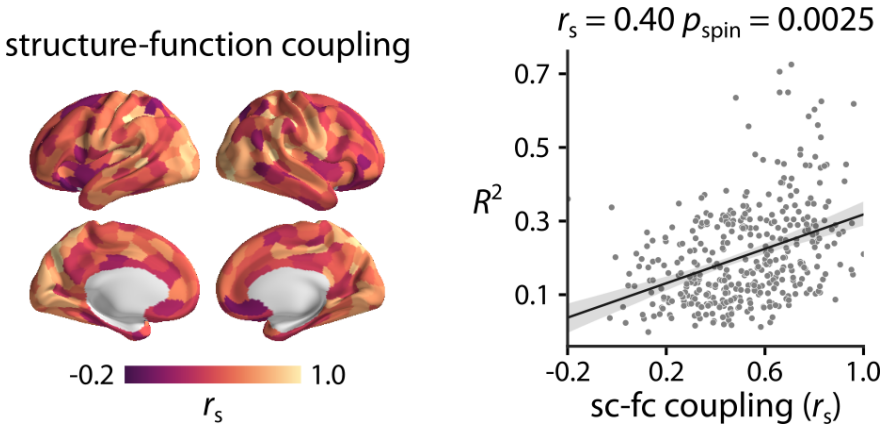

Figure S6.2: **Structure-function coupling** | Structure-function coupling was estimated as the Spearman rank correlation (r_s) between regional structural and functional connectivity profiles (Baum et al., 2020). The cross-modal R^2 map (i.e. regional model fit) is then compared with the structure-function coupling across the cortex. The data and code needed to generate this figure can be found in https://github.com/netneurolab/shafiei_megfmrimapping and https://zenodo.org/record/6728338.

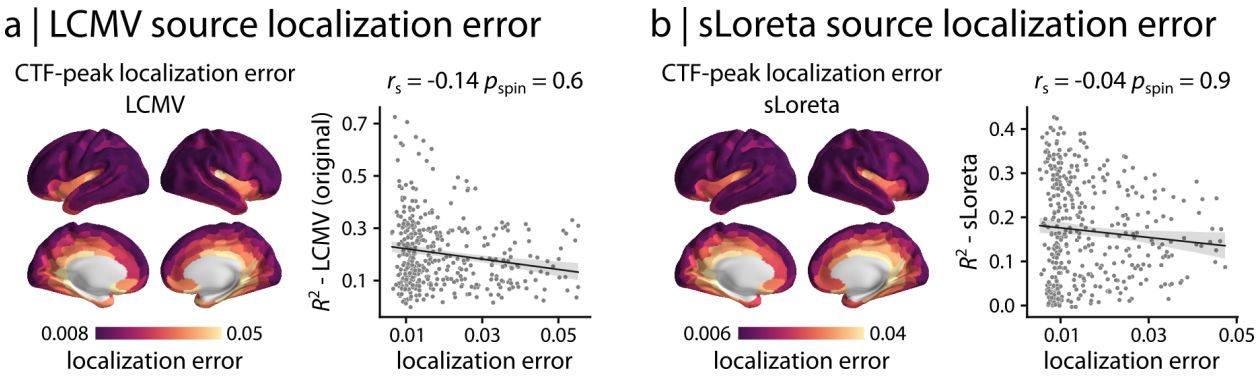

Figure S6.3: **Source localization error** | MEG source localization error is estimated for (a) LCMV and (b) sLoreta source reconstruction solutions using cross-talk functions (CTF) (Hauk and Stenroos, 2014; Hauk et al., 2019, 2011; Liu et al., 2002; Molins et al., 2008). CTF is used to calculate peak localization error of a given source i as the Euclidean distance between the peak location estimated for source i and the true source location i on the surface model (Hauk et al., 2019; Molins et al., 2008). No significant association is observed between the cross-modal correspondence R^2 map and peak localization error for LCMV and sLoreta. The data and code needed to generate this figure can be found in https://github.com/netneurolab/shafiei_megfmrimapping and https://zenodo.org/record/6728338.

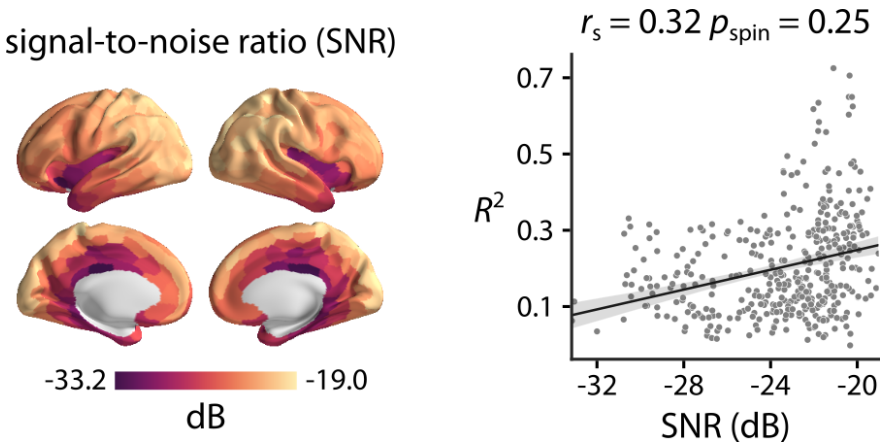

Figure S6.4: **Signal-to-noise ratio** | MEG signal-to-noise ratio (SNR) was estimated at the source level. Parcellated, group-average SNR map is depicted across the cortex. The cross-modal correspondence R^2 map (i.e. regional model fit) is then compared with the SNR map. The data and code needed to generate this figure can be found in https://github.com/netneurolab/shafiei_megfmrimapping and https://zenodo.org/record/6728338.

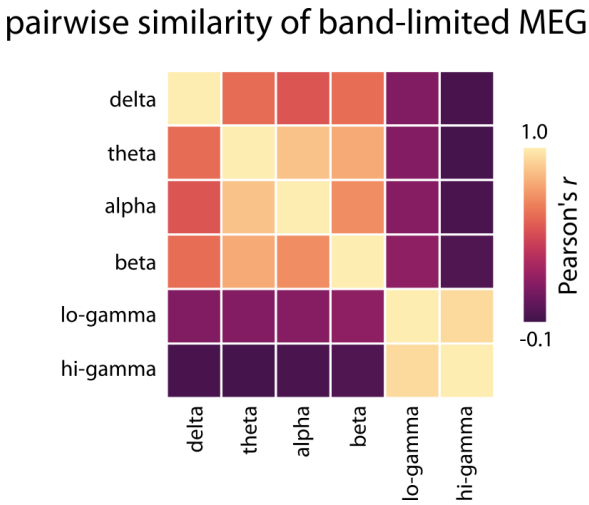

Figure S6.5: **Pairwise similarity of band-limited MEG functional connectivity** | Pearson correlation coefficient is calculated between upper triangles (i.e. values above diagonal) of band-limited MEG AEC functional connectivity to assess the pairwise similarity between MEG connectivity maps. The data and code needed to generate this figure can be found in https://github.com/netneurolab/shafiei_megfmrimapping and https://zenodo.org/record/6728338.

Chapter 7

Discussion

7.1 Summary of findings and contributions

Using a wide range of analytical and computational approaches and multimodal, multiscale datasets, this thesis studies regional brain dynamics and its relationship with microscale gradients and macroscale network embedding. Altogether, the findings build on previous research and advance our understanding of the interplay between regional dynamics and large-scale network organization. Unbiased, data-driven analysis of spontaneous neural activity identifies dynamical signatures of cortical micro-architecture and functional specialization in neocortex. Moreover, comprehensive mapping between haemodynamic and electromagnetic networks helps bridge the two disciplines, while highlighting the importance of multimodal imaging in capturing distinct aspects of brain function. Below, I highlight main scientific findings and distinct contributions of each chapter.

Chapter 3 demonstrates that regional neural activity is inexorably linked with large-scale brain network organization. Using fMRI data from three independently collected datasets, I investigate the effects of dopamine precursor depletion on local and global functional brain architecture in a sample of healthy young adults. The results show that dopamine depletion changes neural dynamics, increasing regional signal variability in specific intrinsic networks, primarily related to motor control and attention. In addition, increased signal variability is concomitant with reduced functional connectivity in those networks. Overall, the findings indicate that regional brain dynamics are inseparable from large-scale network embedding and highlights the stabilizing influence of dopamine signaling at the systems level.

Chapter 4 investigates how intrinsic brain dynamics are associated with systematic

variations in molecular and microstructural properties and macroscale network organization. Using time-series analyses and computational techniques, I comprehensively chart intrinsic dynamics across the cerebral cortex using regional haemodynamic activity in human brain. I identify two robust topographic gradients of intrinsic dynamics, distinct in terms of their temporal composition. These gradients follow microstructural hierarchies, such as myelination, microarray gene expression and cell type composition, and reflect macroscale anatomical and functional network embedding. Importantly, each dynamical pattern encodes a distinct psychological axis, namely a cognitive–affective axis and a sensory–higher order cognitive axis. Collectively, this study identifies a link between intrinsic dynamical properties and microscale and macroscale brain architecture and cognition. More generally, this study demonstrates that haemodynamic activity has a much richer dynamic repertoire than previously appreciated.

Chapter 5 presents a comprehensive study of neurophysiological intrinsic dynamics and their association with micro- and macro-scale architecture. Expanding on the previous chapter, I use time-series phenotyping analysis to extract a comprehensive list of time-series properties from neurophysiological activity. I find that dynamical signature of neurophysiological activity is dominated by measures related to the structure of the power spectrum density. Moreover, the results show that the dominant axis of variation in neurophysiological dynamics follows the micro-architectural gradients and is associated with metabolic demands across the cortex. Specifically, neurophysiological intrinsic dynamics reflect the cellular and molecular composition of the underlying cortical circuits, estimated using proxy measures such as microarray gene expression and neurotransmitter receptor and transporter profiles. Altogether, this study uses near-comprehensive and unbiased sets of time-series features and micro-architectural brain organization to identify the neurophysiological signatures of cortical micro-architecture. Although the findings of this study are mostly confirmatory, emphasizing the importance of conventional measures of neurophysiological dynamics, they introduce novel, less commonly-used neurophysiological time-series properties and provide a data-driven mapping between micro-architectural and dynamical atlases in the human brain.

Finally, Chapter 6 examines the extent to which the electrophysiological and haemodynamic network architectures correspond between two neuroimaging modalities, namely magnetoencephalography (MEG) and functional magnetic resonance imaging (fMRI). Specifically, I use a multiplexed model to directly investigate the cross-modal correspondence between high-resolution MEG and fMRI functional networks in the human brain.

The results show that the relationship between the two modalities is regionally heterogeneous but systematic, reflecting the unimodal-transmodal cortical hierarchy and cytoarchitectural variation. Moreover, haemodynamic connectivity cannot be explained by electromagnetic connectivity in a single frequency band, but rather reflects superposition of multiple rhythms. Altogether, the findings of this study demonstrate that the mixing of MEG neurophysiological rhythms manifests as highly structured patterns of fMRI functional connectivity. This project conceptually links haemodynamic and electromagnetic brain architectures, bridging the two disciplines and opening new avenues for investigating the association between cortical microstructure and multimodal functional networks.

Collectively, these findings demonstrate that regional dynamics of spontaneous neural activity are highly organized across the cortex. Regional intrinsic dynamics are constrained by macroscale network embedding and reflect the microscale, heterogeneous local circuit properties, such as cytoarchitecture and laminar differentiation, gene expression, and myelination. The work presented in this thesis is directly built upon previous research on intrinsic dynamics and while confirming the findings from previous literature, opens new avenues to examine the relationship between neural dynamics and gradients of micro-architectural features and macroscale network organization using multimodal brain data.

7.2 Future work

7.2.1 Bridging neural dynamics and cognition

Multiple lines of evidence, including the work presented in this thesis, demonstrate that local temporal properties are highly organized and aligned with gradients of micro-architecture and network organization of the brain. Previous reports also suggest that measures of neural variability are associated with inter-individual differences in behaviour and cognitive performance (Garrett et al., 2011, 2013b; Mišić et al., 2010; Waschke et al., 2021). Moreover, regional neural activity varies across the adult lifespan and these changes are associated with cognitive dysfunction in normal aging (Garrett et al., 2013a, 2015, 2022; Grady and Garrett, 2018; Reinhart and Nguyen, 2019; Uddin, 2020; Voytek et al., 2015; Waschke et al., 2017, 2021). Individual variation in cognitive performance and behavioural measures has been related to neural activity and dynamics, using measures such as signal variability (Garrett et al., 2015; McIntosh et al., 2008; Mišić et al., 2010)

and power spectral properties (Gao et al., 2020; Voytek et al., 2015). Although the focus of most of the previous studies has been to relate the brain function and structure to behaviour in an explanatory manner, there has been recent attempts to study the brain-behaviour relationship using predictive modeling with functional connectivity (Kashyap et al., 2019; Shen et al., 2017). Predictive modeling of human behaviour can broaden our understanding of brain-behaviour relationship and provide mechanistic accounts and generalizable theories regarding the inter-individual differences in flexible cognitive operations and complex behaviour (Varoquaux and Poldrack, 2019; Yarkoni and Westfall, 2017). Using predictive modeling based on regional intrinsic dynamics can help elucidate the brain-behaviour relationship. However, in order to go beyond associative brain-behaviour analysis and perform predictive modeling, and importantly, reproducible and generalizable analysis of brain-behaviour relationships, high quality brain data and well-defined cognitive and behavioural data from large samples of individuals are required (Buzsáki, 2020; Marek et al., 2022). Recent technological advances and data collection and data sharing efforts have made this more accessible by providing cross-sectional and longitudinal data from a large number of individuals (Feczko et al., 2021; Sudlow et al., 2015; Van Essen et al., 2013), offering new opportunities for generalizable and reproducible research on the relationship between brain activity and complex behaviour and cognition.

7.2.2 Neural dynamics during naturalistic stimulus

As mentioned above, a large body of research is available on inter-individual differences in regional neural dynamics and the relationship between neural variability and cognition both in young adults and across the lifespan. However, most previous reports rely on either task-based approaches or resting-state functional neuroimaging. These studies suggest that intrinsic neural activity is inexorably linked with microscale and macroscale brain organization, reflects inter-individual differences in behaviour and cognition, and evolves during healthy aging. Task-based paradigms are mainly used to study brain function in highly controlled setups, focusing on specific tasks and cognitive processes. While task-based experimental designs have proven to be useful in studying the brain function and its influence on cognition, they potentially miss on broader characteristics of spontaneous neural activity and their relationship with behaviour and cognitive function. On the other hand, resting-state studies that measure brain activity without any external stimuli or task-based manipulations are commonly used to assess the intrinsic neural dynamics and ongoing brain function. However, resting-state research only focuses on spontaneous brain activity and does not allow for any control over ongoing cognition.

More recently, there has been a growing evidence that new experimental paradigms, such as naturalistic stimuli that incorporate task-like manipulations while preserving properties of spontaneous neural activity, are required to better understand brain function and integration (Finn, 2021). Naturalistic paradigms impose constraints on brain activity and cognition, offering an unprecedented opportunity to study individualized neural dynamics. Given the growing demand, naturalistic datasets have become increasingly available over recent years (DuPre et al., 2020). Previous reports suggest that naturalistic settings are well suited for studying brain-behavior relationship as they amplify individual differences in brain activity (Finn and Bandettini, 2021). However, it remains unclear whether unconstrained "resting" designs, constrained "task" designs, or naturalistic designs are more optimal for capturing inter-individual heterogeneity in brain function. Another exciting open question is to determine how regional neural activity during naturalistic stimuli evolves across the lifespan, and how age-related changes in regional brain dynamics translate to individual differences in cognitive function. Naturalistic stimuli datasets are well suited for this purpose, as such paradigms enhance signals that are unique and sensitive to individuals, allowing us to map individualized neural dynamics to cognition in a controlled setting. Future work is required to use multimodal datasets and integrate novel scientific disciplines to characterize regional neural activity during naturalistic stimuli and identify individualized neural dynamics that manifest as individual differences in cognitive function and complex behaviour. Using naturalistic paradigm provides complementary information to our understanding of brain function at rest and opens new opportunities to investigate the mechanistic links between neural dynamics and cognition.

7.3 Conclusions

This thesis explores the link between regional neural dynamics and global organization of the human brain. There is a large body of literature available on how the underlying cellular and molecular properties of local cortical circuits give rise to neural activity, captured by a wide range of measurement techniques and imaging modalities at different scales. This thesis is built on and is inspired by earlier work on neural dynamics and years of research on this topic. The work presented in this thesis aims to bring multiple, multimodal datasets together and investigate the association between local brain dynamics and microarchitecture and macroscale network embedding in a data-driven, comprehensive manner. Collectively, this body of work emphasizes how data-driven approaches can be applied in

future research to study multi-scale network dynamics and fundamental aspect of brain function and integration using multiple data modalities and modern analytic tools.

Bibliography

Amunts, K. et al. (2013). "BigBrain: an ultrahigh-resolution 3D human brain model". *Science*, 340(6139), pp. 1472–1475.

Anderson, K. M. et al. (2018). "Gene expression links functional networks across cortex and striatum". *Nat Commun*, 9(1), pp. 1–14.

Anderson, K. M. et al. (2020). "Transcriptional and imaging-genetic association of cortical interneurons, brain function, and schizophrenia risk". *Nat Commun*, 11(1), pp. 1–15.

Avena-Koenigsberger, A., B. Misic, and O. Sporns (2018). "Communication dynamics in complex brain networks". *Nat Rev Neurosci*, 19(1), p. 17.

Baillet, S. (2017). "Magnetoencephalography for brain electrophysiology and imaging". *Nature neuroscience*, 20(3), pp. 327–339.

Baillet, S., J. C. Mosher, and R. M. Leahy (2001). "Electromagnetic brain mapping". *IEEE Signal processing magazine*, 18(6), pp. 14–30.

Baker, A. P. et al. (2014). "Fast transient networks in spontaneous human brain activity". *Elife*, 3, e01867.

Baldassano, C. et al. (2017). "Discovering event structure in continuous narrative perception and memory". *Neuron*, 95(3), pp. 709–721.

Baracchini, G. et al. (2021). "Inter-regional BOLD signal variability is an organizational feature of functional brain networks". *NeuroImage*, 237, p. 118149.

Bassett, D. S., P. Zurn, and J. I. Gold (2018). "On the nature and use of models in network neuroscience". *Nature Reviews Neuroscience*, 19(9), pp. 566–578.

Bassett, D. S. et al. (2011). "Dynamic reconfiguration of human brain networks during learning". *Proceedings of the National Academy of Sciences*, 108(18), pp. 7641–7646.

Bassett, D. S. and E. Bullmore (2006). "Small-world brain networks". *The neuroscientist*, 12(6), pp. 512–523.

Bastos, A. M. et al. (2018). "Laminar recordings in frontal cortex suggest distinct layers for maintenance and control of working memory". *Proceedings of the National Academy of Sciences*, 115(5), pp. 1117–1122.

Bastos, A. M. et al. (2020). "Layer and rhythm specificity for predictive routing". *Proceedings of the National Academy of Sciences*, 117(49), pp. 31459–31469.

Bastos, A. M. et al. (2015). "Visual areas exert feedforward and feedback influences through distinct frequency channels". *Neuron*, 85(2), pp. 390–401.

Baum, G. L. et al. (2020). "Development of structure–function coupling in human brain networks during youth". *Proceedings of the National Academy of Sciences*, 117(1), pp. 771–778.

Bazinet, V. et al. (2021). "Multiscale communication in cortico-cortical networks". *NeuroImage*, 243, p. 118546.

Bellec, P. et al. (2006). "Identification of large-scale networks in the brain using fMRI". *Neuroimage*, 29(4), pp. 1231–1243.

Bettinardi, R. G. et al. (2017). "How structure sculpts function: unveiling the contribution of anatomical connectivity to the brain's spontaneous correlation structure". *Chaos: An Interdisciplinary Journal of Nonlinear Science*, 27(4), p. 047409.

Betzel, R. F. and D. S. Bassett (2018). "Specificity and robustness of long-distance connections in weighted, interareal connectomes". *Proceedings of the National Academy of Sciences*, 115(21), E4880–E4889.

Betzel, R. F., J. D. Medaglia, and D. S. Bassett (2018). "Diversity of meso-scale architecture in human and non-human connectomes". *Nature communications*, 9(1), pp. 1–14.

Betzel, R. F. et al. (2017). "The modular organization of human anatomical brain networks: Accounting for the cost of wiring". *Network Neuroscience*, 1(1), pp. 42–68.

Beul, S. F., H. Barbas, and C. C. Hilgetag (2017). "A predictive structural model of the primate connectome". *Sci Rep*, 7(1), pp. 1–12.

Biswal, B. et al. (1995). "Functional connectivity in the motor cortex of resting human brain using echo-planar MRI". *Magnetic resonance in medicine*, 34(4), pp. 537–541.

Breakspear, M. (2017). "Dynamic models of large-scale brain activity". *Nature neuroscience*, 20(3), pp. 340–352.

Brookes, M. J. et al. (2011a). "Investigating the electrophysiological basis of resting state networks using magnetoencephalography". *Proceedings of the National Academy of Sciences*, 108(40), pp. 16783–16788.

Brookes, M. J. et al. (2011b). "Measuring functional connectivity using MEG: methodology and comparison with fcMRI". *Neuroimage*, 56(3), pp. 1082–1104.

Brookes, M. J. et al. (2012). "Task induced modulation of neural oscillations in electrophysiological brain networks". *Neuroimage*, 63(4), pp. 1918–1930.

Buffalo, E. A. et al. (2011). "Laminar differences in gamma and alpha coherence in the ventral stream". *Proceedings of the National Academy of Sciences*, 108(27), pp. 11262–11267.

Bullmore, E. and O. Sporns (2009). "Complex brain networks: graph theoretical analysis of structural and functional systems". *Nature Reviews Neuroscience*, 10(3), pp. 186–198.

Burt, J. B. et al. (2018). "Hierarchy of transcriptomic specialization across human cortex captured by structural neuroimaging topography". *Nat Neurosci*, 21(9), pp. 1251–1259.

Burt, J. B. et al. (2021). "Transcriptomics-informed large-scale cortical model captures topography of pharmacological neuroimaging effects of LSD". *Elife*, 10, e69320.

Burzynska, A. Z. et al. (2013). "A scaffold for efficiency in the human brain". *J Neurosci*, 33(43), pp. 17150–17159.

Buzsáki, G. (2020). "The brain–cognitive behavior problem: a retrospective". *Eneuro*, 7(4).

Cabral, J. et al. (2014). "Exploring mechanisms of spontaneous functional connectivity in MEG: how delayed network interactions lead to structured amplitude envelopes of band-pass filtered oscillations". *Neuroimage*, 90, pp. 423–435.

Chaudhuri, R. et al. (2015). "A large-scale circuit mechanism for hierarchical dynamical processing in the primate cortex". *Neuron*, 88(2), pp. 419–431.

Chien, H.-Y. S. and C. J. Honey (2020). "Constructing and forgetting temporal context in the human cerebral cortex". *Neuron*.

Cocchi, L. et al. (2016). "A hierarchy of timescales explains distinct effects of local inhibition of primary visual cortex and frontal eye fields". *eLife*, 5, e15252.

Colclough, G. L. et al. (2016). "How reliable are MEG resting-state connectivity metrics?" *Neuroimage*, 138, pp. 284–293.

Cole, M. W. et al. (2014). "Intrinsic and task-evoked network architectures of the human brain". *Neuron*, 83(1), pp. 238–251.

Damoiseaux, J. S. and M. D. Greicius (2009). "Greater than the sum of its parts: a review of studies combining structural connectivity and resting-state functional connectivity". *Brain structure and function*, 213(6), pp. 525–533.

Dave, S, T. Brothers, and T. Swaab (2018). "1/f neural noise and electrophysiological indices of contextual prediction in aging". *Brain research*, 1691, pp. 34–43.

De Pasquale, F. et al. (2010). "Temporal dynamics of spontaneous MEG activity in brain networks". *Proceedings of the National Academy of Sciences*, 107(13), pp. 6040–6045.

Deco, G. and V. K. Jirsa (2012). "Ongoing cortical activity at rest: criticality, multistability, and ghost attractors". *Journal of Neuroscience*, 32(10), pp. 3366–3375.

Deco, G. et al. (2014a). "How local excitation–inhibition ratio impacts the whole brain dynamics". *Journal of Neuroscience*, 34(23), pp. 7886–7898.

Deco, G. et al. (2014b). "Identification of optimal structural connectivity using functional connectivity and neural modeling". *Journal of Neuroscience*, 34(23), pp. 7910–7916.

Deco, G. et al. (2021). "Dynamical consequences of regional heterogeneity in the brain's transcriptional landscape". *Science Advances*, 7(29), eabf4752.

Demirtaş, M. et al. (2019). "Hierarchical heterogeneity across human cortex shapes large-scale neural dynamics". *Neuron*, 101(6), pp. 1181–1194.

Douglas, R. J. and K. A. Martin (2004). "Neuronal circuits of the neocortex". *Annu. Rev. Neurosci.*, 27, pp. 419–451.

Drew, P. J. (2019). "Vascular and neural basis of the BOLD signal". *Current Opinion in Neurobiology*, 58, pp. 61–69.

DuPre, E., M. Hanke, and J.-B. Poline (2020). "Nature abhors a paywall: How open science can realize the potential of naturalistic stimuli". *Neuroimage*, 216, p. 116330.

Eickhoff, S. B., B. Yeo, and S. Genon (2018). "Imaging-based parcellations of the human brain". *Nature Reviews Neuroscience*, 19(11), pp. 672–686.

Fallon, J. et al. (2020). "Timescales of spontaneous fMRI fluctuations relate to structural connectivity in the brain". *Network Neuroscience*, 4(3), pp. 788–806.

Feczko, E. et al. (2021). "Adolescent Brain Cognitive Development (ABCD) Community MRI Collection and Utilities". *bioRxiv*.

Finn, E. S. (2021). "Is it time to put rest to rest?" *Trends in cognitive sciences*, 25(12), pp. 1021–1032.

Finn, E. S. and P. A. Bandettini (2021). "Movie-watching outperforms rest for functional connectivity-based prediction of behavior". *NeuroImage*, 235, p. 117963.

Frauscher, B. et al. (2018). "High-frequency oscillations in the normal human brain". *Annals of neurology*, 84(3), pp. 374–385.

Fries, P. (2005). "A mechanism for cognitive dynamics: neuronal communication through neuronal coherence". *Trends in cognitive sciences*, 9(10), pp. 474–480.

Fulcher, B. D. (2018). "Feature-based time-series analysis". In: *Feature Engineering for Machine Learning and Data Analytics*. CRC Press, pp. 87–116.

Fulcher, B. D. and A. Fornito (2016). "A transcriptional signature of hub connectivity in the mouse connectome". *Proceedings of the National Academy of Sciences*, 113(5), pp. 1435–1440.

Fulcher, B. D. et al. (2019). "Multimodal gradients across mouse cortex". *Proc Natl Acad Sci USA*, 116(10), pp. 4689–4695.

Gao, R. et al. (2020). "Neuronal timescales are functionally dynamic and shaped by cortical microarchitecture". *Elife*, 9, e61277.

Garrett, D. D., A. R. McIntosh, and C. L. Grady (2013a). "Brain signal variability is parametrically modifiable". *Cerebral Cortex*, 24(11), pp. 2931–2940.

Garrett, D. D. et al. (2011). "The importance of being variable". *J Neurosci*, 31(12), pp. 4496–4503.

Garrett, D. D. et al. (2013b). "Moment-to-moment brain signal variability: A next frontier in human brain mapping?" *Neuroscience & Biobehavioral Reviews*, 37(4), pp. 610–624.

Garrett, D. D. et al. (2015). "Amphetamine modulates brain signal variability and working memory in younger and older adults". *Proc Natl Acad Sci USA*, 112(24), pp. 7593–7598.

Garrett, D. D. et al. (2018). "Local temporal variability reflects functional integration in the human brain". *Neuroimage*, 183, pp. 776–787.

Garrett, D. D. et al. (2022). "Dynamic regulation of neural variability during working memory reflects dopamine, functional integration, and decision-making". *bioRxiv*.

Glasser, M. F. et al. (2016). "A multi-modal parcellation of human cerebral cortex". *Nature*, 536(7615), pp. 171–178.

Gollo, L. L. et al. (2015). "Dwelling quietly in the rich club: brain network determinants of slow cortical fluctuations". *Phil Trans R Soc B*, 370(1668), p. 20140165.

Gordon, E. M. et al. (2017). "Precision functional mapping of individual human brains". *Neuron*, 95(4), pp. 791–807.

Goulas, A. et al. (2019). "A blueprint of mammalian cortical connectomes". *PLoS Biol*, 17(3), e2005346.

Grady, C. L. and D. D. Garrett (2018). "Brain signal variability is modulated as a function of internal and external demand in younger and older adults". *Neuroimage*, 169, pp. 510–523.

Griffa, A, Y Alemán-Gómez, and P Hagmann (2019). "Structural and functional connectome from 70 young healthy adults [Data set]". *Zenodo*.

Hagmann, P. et al. (2007). "Mapping human whole-brain structural networks with diffusion MRI". *PloS one*, 2(7), e597.

Hagmann, P. et al. (2008). "Mapping the structural core of human cerebral cortex". *PLoS biology*, 6(7), e159.

Hämäläinen, M. et al. (1993). "Magnetoencephalography—theory, instrumentation, and applications to noninvasive studies of the working human brain". *Reviews of modern Physics*, 65(2), p. 413.

Hansen, J. Y. et al. (2020). "Molecular signatures of cognition and affect". *bioRxiv*.

Hansen, J. Y. et al. (2021). "Mapping neurotransmitter systems to the structural and functional organization of the human neocortex". *bioRxiv*.

Harel, N. et al. (2006). "Combined imaging–histological study of cortical laminar specificity of fMRI signals". *Neuroimage*, 29(3), pp. 879–887.

Hasson, U. et al. (2008). "A hierarchy of temporal receptive windows in human cortex". *J Neurosci*, 28(10), pp. 2539–2550.

Hawrylycz, M. J. et al. (2012). "An anatomically comprehensive atlas of the adult human brain transcriptome". *Nature*, 489(7416), p. 391.

Hilgetag, C. C. and A. Goulas (2020). "'Hierarchy'in the organization of brain networks". *Philos Trans R Soc B*, 375(1796), p. 20190319.

Hilgetag, C. C. et al. (2019). "An architectonic type principle integrates macroscopic cortico-cortical connections with intrinsic cortical circuits of the primate brain". *Net Neurosci*, 3(4), pp. 905–923.

Honey, C. J., J.-P. Thivierge, and O. Sporns (2010). "Can structure predict function in the human brain?" *Neuroimage*, 52(3), pp. 766–776.

Honey, C. J. et al. (2007). "Network structure of cerebral cortex shapes functional connectivity on multiple time scales". *Proceedings of the National Academy of Sciences*, 104(24), pp. 10240–10245.

Honey, C. J. et al. (2012). "Slow cortical dynamics and the accumulation of information over long timescales". *Neuron*, 76(2), pp. 423–434.

Honey, C. et al. (2009). "Predicting human resting-state functional connectivity from structural connectivity". *Proceedings of the National Academy of Sciences*, 106(6), pp. 2035–2040.

Huntenburg, J. M., P.-L. Bazin, and D. S. Margulies (2018). "Large-scale gradients in human cortical organization". *Trends in cognitive sciences*, 22(1), pp. 21–31.

Huntenburg, J. M. et al. (2017). "A systematic relationship between functional connectivity and intracortical myelin in the human cerebral cortex". *Cereb Cortex*, 27(2), pp. 981–997.

Ito, T., L. J. Hearne, and M. W. Cole (2020). "A cortical hierarchy of localized and distributed processes revealed via dissociation of task activations, connectivity changes, and intrinsic timescales". *NeuroImage*, 221, p. 117141.

Jones, E. and T. Powell (1970). "An anatomical study of converging sensory pathways within the cerebral cortex of the monkey". *Brain*, 93(4), pp. 793–820.

Kandel, E. R. et al. (2000). *Principles of neural science*. Vol. 4. McGraw-hill New York.

Kashyap, R. et al. (2019). "Individual-specific fMRI-Subspaces improve functional connectivity prediction of behavior". *NeuroImage*, 189, pp. 804–812.

Keitel, A. and J. Gross (2016). "Individual human brain areas can be identified from their characteristic spectral activation fingerprints". *PLoS Biol*, 14(6), e1002498.

Khambhati, A. N. et al. (2018). "Modeling and interpreting mesoscale network dynamics". *NeuroImage*, 180, pp. 337–349.

Kiebel, S. J., J. Daunizeau, and K. J. Friston (2008). "A hierarchy of time-scales and the brain". *PLoS Comput BIol*, 4(11).

Liu, Z.-Q., R. F. Betzel, and B. Misic (2021). "Benchmarking functional connectivity by the structure and geometry of the human brain". *Network Neuroscience*, pp. 1–21.

Mahjoory, K. et al. (2020). "The frequency gradient of human resting-state brain oscillations follows cortical hierarchies". *Elife*, 9, e53715.

Maier, A., C. J. Aura, and D. A. Leopold (2011). "Infragranular sources of sustained local field potential responses in macaque primary visual cortex". *Journal of Neuroscience*, 31(6), pp. 1971–1980.

Maier, A. et al. (2010). "Distinct superficial and deep laminar domains of activity in the visual cortex during rest and stimulation". *Frontiers in systems neuroscience*, 4, p. 31.

Marek, S. et al. (2022). "Reproducible brain-wide association studies require thousands of individuals". *Nature*, 603(7902), pp. 654–660.

Margulies, D. S. et al. (2016). "Situating the default-mode network along a principal gradient of macroscale cortical organization". *Proceedings of the National Academy of Sciences*, 113(44), pp. 12574–12579.

Markello, R. D. et al. (2022). "Neuromaps: structural and functional interpretation of brain maps". *bioRxiv*.

Markicevic, M. et al. (2020). "Cortical excitation: inhibition imbalance causes abnormal brain network dynamics as observed in neurodevelopmental disorders". *Cereb Cortex*.

McIntosh, A. R., N. Kovacevic, and R. J. Itier (2008). "Increased brain signal variability accompanies lower behavioral variability in development". *PLoS Comput Biol*, 4(7), e1000106.

Mesulam, M.-M. (1998). "From sensation to cognition." *Brain*, 121(6), pp. 1013–1052.

Miller, K. L. et al. (2016). "Multimodal population brain imaging in the UK Biobank prospective epidemiological study". *Nature neuroscience*, 19(11), pp. 1523–1536.

Mirchi, N. et al. (2018). "Tracking mood fluctuations with functional network patterns". *Social cognitive and affective neuroscience*, 14(1), pp. 47–57.

Mišić, B. and O. Sporns (2016). "From regions to connections and networks: new bridges between brain and behavior". *Current opinion in neurobiology*, 40, pp. 1–7.

Mišić, B. et al. (2010). "Brain noise is task dependent and region specific". *J Neurophysiol*, 104(5), pp. 2667–2676.

Misic, B. et al. (2011). "Functional embedding predicts the variability of neural activity". *Front Syst Neurosci*, 5, p. 90.

Mišić, B. et al. (2015). "Cooperative and competitive spreading dynamics on the human connectome". *Neuron*, 86(6), pp. 1518–1529.

Mišic, B. et al. (2015). "Coordinated information generation and mental flexibility: large-scale network disruption in children with autism". *Cereb Cortex*, 25(9), pp. 2815–2827.

Mišić, B. et al. (2016). "Network-level structure-function relationships in human neocortex". *Cerebral Cortex*, 26(7), pp. 3285–3296.

Müller, E. J. et al. (2020). "Core and matrix thalamic sub-populations relate to spatio-temporal cortical connectivity gradients". *NeuroImage*, 222, p. 117224.

Murphy, A. C. et al. (2016). "Explicitly linking regional activation and function connectivity: community structure of weighted networks with continuous annotation". *arXiv preprint arXiv:1611.07962*.

Murray, J. D., M. Demirtaş, and A. Anticevic (2018). "Biophysical modeling of large-scale brain dynamics and applications for computational psychiatry". *Biological Psychiatry: Cognitive Neuroscience and Neuroimaging*, 3(9), pp. 777–787.

Murray, J. D. et al. (2014). "A hierarchy of intrinsic timescales across primate cortex". *Nat Neurosci*, 17(12), p. 1661.

Niedermeyer, E. and F. L. da Silva (2005). *Electroencephalography: basic principles, clinical applications, and related fields*. Lippincott Williams & Wilkins.

Niso, G. et al. (2016). "OMEGA: the open MEG archive". *Neuroimage*, 124, pp. 1182–1187.

Noble, S., D. Scheinost, and R. T. Constable (2019). "A decade of test-retest reliability of functional connectivity: A systematic review and meta-analysis". *Neuroimage*, 203, p. 116157.

Paquola, C. et al. (2019). "Microstructural and functional gradients are increasingly dissociated in transmodal cortices". *PLoS Biol*, 17(5), e3000284.

Paquola, C. et al. (2021). "The BigBrainWarp toolbox for integration of BigBrain 3D histology with multimodal neuroimaging". *eLife*, 10. Ed. by S. Jbabdi et al., e70119.

Payeur, A., J.-C. Béïque, and R. Naud (2019). "Classes of dendritic information processing". *Curr Opin Neurobiol*, 58, pp. 78–85.

Poldrack, R. A. and M. J. Farah (2015). "Progress and challenges in probing the human brain". *Nature*, 526(7573), pp. 371–379.

Power, J. D. et al. (2011). "Functional network organization of the human brain". *Neuron*, 72(4), pp. 665–678.

Preti, M. G. and D. Van De Ville (2019). "Decoupling of brain function from structure reveals regional behavioral specialization in humans". *Nature communications*, 10(1), pp. 1–7.

Raichle, M. E. (2009). "A brief history of human brain mapping". *Trends in neurosciences*, 32(2), pp. 118–126.

Raut, R. V., A. Z. Snyder, and M. E. Raichle (2020). "Hierarchical dynamics as a macroscopic organizing principle of the human brain". *Proceedings of the National Academy of Sciences*, 117(34), pp. 20890–20897.

Reinhart, R. M. and J. A. Nguyen (2019). "Working memory revived in older adults by synchronizing rhythmic brain circuits". *Nature neuroscience*, 22(5), pp. 820–827.

Richiardi, J. et al. (2015). "Correlated gene expression supports synchronous activity in brain networks". *Science*, 348(6240), pp. 1241–1244.

Roberts, J. A. et al. (2016). "The contribution of geometry to the human connectome". *Neuroimage*, 124, pp. 379–393.

Rosenberg, M. D. et al. (2016). "A neuromarker of sustained attention from whole-brain functional connectivity". *Nature neuroscience*, 19(1), p. 165.

Sadaghiani, S., M. J. Brookes, and S. Baillet (2022). "Connectomics of human electrophysiology". *NeuroImage*, 247, p. 118788.

Schaefer, A. et al. (2018). "Local-global parcellation of the human cerebral cortex from intrinsic functional connectivity MRI". *Cerebral cortex*, 28(9), pp. 3095–3114.

Scheeringa, R. and P. Fries (2019). "Cortical layers, rhythms and BOLD signals". *NeuroImage*, 197, pp. 689–698.

Scheeringa, R. et al. (2016). "The relationship between oscillatory EEG activity and the laminar-specific BOLD signal". *Proceedings of the National Academy of Sciences*, 113(24), pp. 6761–6766.

Schmid, F. et al. (2019). "Vascular density and distribution in neocortex". *Neuroimage*, 197, pp. 792–805.

Scholtens, L. H. et al. (2014). "Linking macroscale graph analytical organization to microscale neuroarchitectonics in the macaque connectome". *Journal of Neuroscience*, 34(36), pp. 12192–12205.

Seidlitz, J. et al. (2018). "Morphometric similarity networks detect microscale cortical organization and predict inter-individual cognitive variation". *Neuron*, 97(1), pp. 231–247.

Sethi, S. S. et al. (2017). "Structural connectome topology relates to regional BOLD signal dynamics in the mouse brain". *Chaos: An Interdisciplinary Journal of Nonlinear Science*, 27(4), p. 047405.

Shafiei, G. et al. (2019). "Dopamine signaling modulates the stability and integration of intrinsic brain networks". *Cerebral Cortex*, 29(1), pp. 397–409.

Shafiei, G. et al. (2020). "Topographic gradients of intrinsic dynamics across neocortex". *Elife*, 9, e62116.

Shen, X. et al. (2017). "Using connectome-based predictive modeling to predict individual behavior from brain connectivity". *nature protocols*, 12(3), pp. 506–518.

Shine, J. M. et al. (2019). "The low-dimensional neural architecture of cognitive complexity is related to activity in medial thalamic nuclei". *Neuron*, 104(5), pp. 849–855.

Silva Castanheira, J. da et al. (2021). "Brief segments of neurophysiological activity enable individual differentiation". *Nature communications*, 12(1), pp. 1–11.

Smith, M. A. et al. (2013). "Laminar dependence of neuronal correlations in visual cortex". *Journal of neurophysiology*, 109(4), pp. 940–947.

Smith, S. M. et al. (2009). "Correspondence of the brain's functional architecture during activation and rest". *Proceedings of the national academy of sciences*, 106(31), pp. 13040–13045.

Smith, S. M. et al. (2015). "A positive-negative mode of population covariation links brain connectivity, demographics and behavior". *Nature neuroscience*, 18(11), pp. 1565–1567.

Sorrentino, P. et al. (2021). "The structural connectome constrains fast brain dynamics". *Elife*, 10, e67400.

Sporns, O. (2011). "The human connectome: a complex network". *Annals of the New York Academy of Sciences*, 1224(1), pp. 109–125.

Sporns, O. and R. F. Betzel (2016). "Modular brain networks". *Annual review of psychology*, 67, pp. 613–640.

Sporns, O., G. Tononi, and R. Kötter (2005). "The human connectome: a structural description of the human brain". *PLoS computational biology*, 1(4), e42.

Straub, I. et al. (2020). "Gradients in the mammalian cerebellar cortex enable Fourier-like transformation and improve storing capacity". *eLife*, 9, e51771.

Suárez, L. E. et al. (2020). "Linking structure and function in macroscale brain networks". *Trends Cogn Sci*.

Sudlow, C. et al. (2015). "UK biobank: an open access resource for identifying the causes of a wide range of complex diseases of middle and old age". *PLoS medicine*, 12(3), e1001779.

Taylor, J. R. et al. (2017). "The Cambridge Centre for Ageing and Neuroscience (Cam-CAN) data repository: structural and functional MRI, MEG, and cognitive data from a cross-sectional adult lifespan sample". *Neuroimage*, 144, pp. 262–269.

Tournier, J.-D. et al. (2019). "MRtrix3: A fast, flexible and open software framework for medical image processing and visualisation". *NeuroImage*, p. 116137.

Uddin, L. Q. (2020). "Bring the Noise: Reconceptualizing Spontaneous Neural Activity". *Trends in Cognitive Sciences*.

Uludağ, K. and P. Blinder (2018). "Linking brain vascular physiology to hemodynamic response in ultra-high field MRI". *Neuroimage*, 168, pp. 279–295.

Van Den Heuvel, M. P. et al. (2009a). "Efficiency of functional brain networks and intellectual performance". *Journal of Neuroscience*, 29(23), pp. 7619–7624.

Van Den Heuvel, M. P. et al. (2009b). "Functionally linked resting-state networks reflect the underlying structural connectivity architecture of the human brain". *Human brain mapping*, 30(10), pp. 3127–3141.

Van Den Heuvel, M. P. et al. (2012). "High-cost, high-capacity backbone for global brain communication". *Proceedings of the National Academy of Sciences*, 109(28), pp. 11372–11377.

Van Essen, D. C. et al. (2013). "The WU-Minn human connectome project: an overview". *Neuroimage*, 80, pp. 62–79.

Varoquaux, G. and R. A. Poldrack (2019). "Predictive models avoid excessive reductionism in cognitive neuroimaging". *Current opinion in neurobiology*, 55, pp. 1–6.

Vázquez-Rodríguez, B. et al. (2019). "Gradients of structure–function tethering across neocortex". *Proc Natl Acad Sci USA*, 116(42), pp. 21219–21227.

Vinck, M. and C. A. Bosman (2016). "More gamma more predictions: gamma-synchronization as a key mechanism for efficient integration of classical receptive field inputs with surround predictions". *Frontiers in systems neuroscience*, 10, p. 35.

Voytek, B. et al. (2015). "Age-related changes in 1/f neural electrophysiological noise". *Journal of Neuroscience*, 35(38), pp. 13257–13265.

Wagstyl, K. et al. (2015). "Cortical thickness gradients in structural hierarchies". *Neuroimage*, 111, pp. 241–250.

Wagstyl, K. et al. (2020). "BigBrain 3D atlas of cortical layers: Cortical and laminar thickness gradients diverge in sensory and motor cortices". *PLoS Biol*, 18(4), e3000678.

Wang, P. et al. (2019). "Inversion of a large-scale circuit model reveals a cortical hierarchy in the dynamic resting human brain". *Sci Adv*, 5(1), eaat7854.

Wang, X.-J. (2020). "Macroscopic gradients of synaptic excitation and inhibition in the neocortex". *Nat Rev Neurosci*, pp. 1–10.

Waschke, L., M. Wöstmann, and J. Obleser (2017). "States and traits of neural irregularity in the age-varying human brain". *Scientific reports*, 7(1), pp. 1–12.

Waschke, L. et al. (2021). "Behavior needs neural variability". *Neuron*, 109(5), pp. 751–766.

Watts, D. J. and S. H. Strogatz (1998). "Collective dynamics of 'small-world'networks". *nature*, 393(6684), pp. 440–442.

Wei, Y. et al. (2018). "Multiscale examination of cytoarchitectonic similarity and human brain connectivity". *Net Neurosci*, 3(1), pp. 124–137.

Yarkoni, T. and J. Westfall (2017). "Choosing prediction over explanation in psychology: Lessons from machine learning". *Perspectives on Psychological Science*, 12(6), pp. 1100–1122.

Yeo, B. T. et al. (2011). "The organization of the human cerebral cortex estimated by intrinsic functional connectivity". *Journal of neurophysiology*, 106(3), p. 1125.

Zamani Esfahlani, F. et al. (2022). "Local structure-function relationships in human brain networks across the lifespan". *Nature communications*, 13(1), pp. 1–16.

Zheng, Y.-Q. et al. (2019). "Local vulnerability and global connectivity jointly shape neurodegenerative disease propagation". *PLoS Biol*, 17(11).